Electronic Thesis and Dissertation Repository

7-14-2021 1:00 PM

Study on graphene-based nanocomposites with special magnetoresistance properties

Songlin Yang, *The University of Western Ontario*

Supervisor: Dr. Zhang, Jin, *The University of Western Ontario*
A thesis submitted in partial fulfillment of the requirements for the Doctor of Philosophy degree
in Chemical and Biochemical Engineering
© Songlin Yang 2021

Recommended Citation

Abstract

Magnetoresistance (MR) refers to the change of a material's electrical resistance under the presence of an external magnetic field. The discovery of new MR phenomena (e.g., giant magnetoresistance (GMR) and tunneling magnetoresistance (TMR)) since the 1980s initiates the revolution of novel electric devices in the fields of data storage, position sensing, current sensing, non-destructive monitoring, biomedical sensing systems, etc. However, current devices display inadequate MR at the low magnetic field/room temperature, limited working range, and bulky size, which hinders the further application of MR sensors/devices. Therefore, the main goal of this thesis is to develop two-dimensional MR materials with high performance and their potential applications.

First, a new hybrid nanosheet was designed and developed by integrating reduced graphene oxide (rGO) and FeCo nanoparticles (NPs). A facile solvothermal process was developed to produce FeCo/rGO hybrid nanosheets with significant MR ($21 \pm 6\%$) at the low magnetic field (10 kOe) and room temperature. In addition, we demonstrated that the wireless magnetic field sensing system with FeCo/rGO hybrid nanosheets and ZigBee radio modules was able to achieve real-time detection and data collection of a working mobile phone. By adjusting the mass ratio of rGO adding to the system, we obtained the tunable MR of FeCo/rGO hybrid nanosheets. On the other hand, it was found that the formation of Co-Mn oxides NPs on rGO hybrid nanosheets was increased as the mass ratio of rGO added in the reaction exceeded 50 wt.%. The effects of imported ions on the MR of hybrid nanosheets were investigated. The formation of Co-Mn oxides NPs on hybrid nanosheets in this solvothermal process could lead to relatively high MR (3.5% ~ 4.5%) compared with other structures containing Co and Mn under the same conditions.

In addition to the chemical synthesis, we constructed FeCo/rGO hybrid nanosheets by using a laser-assisted physical deposition process, i.e., the matrix-assisted pulsed laser evaporation (MAPLE). The FeCo/rGO hybrid nanosheets prepared by MAPLE displayed MR with a level of 0.7% at ambient temperature and low magnetic fields (10 kOe), which is larger than or close to the reported MR of physically prepared FeCo-based granular materials/structures with higher FeCo ratios.

Finally, a mechanically flexible nanocomposite hydrogel with MR properties was developed. FeCo/rGO hybrid nanosheets were incorporated with the hydrogel matrix by using a photo-initiated polymerization process. The significant enhancements in mechanical properties compared with hydrogel matrix (toughness (0.11 MPa, 2.0x higher), Young's modulus (0.48 MPa, 1.5x higher), and maximal tensile stress (0.22 MPa, 1.7x higher)) and negative MR (-$1.4 \pm 0.3\%$) at room temperature and low magnetic fields were observed.

This work provides the solution to the challenges of developing ideal MR materials/structures and offers a better understanding of designing graphene-based nanocomposites with large MR. We believe that the flexibility and integrability of FeCo/rGO hybrid nanosheets not only benefit the design of MR sensors but also pave the way for extending the application of MR devices in the foreseeable future.

Keywords

Magnetoresistance (MR), reduced graphene oxide (rGO), magnetic field sensor, FeCo nanoparticles, nanocomposite hydrogel

Summary of Lay Audience

Magnetoresistance (MR) can be defined as the variation of a material's electrical resistance under the presence of an external magnetic field. Nowadays, MR sensors and devices are employed in magnetic storage (recording), position sensing, current sensing, non-destructive monitoring, biomedical sensing systems, etc. The performance of MR sensors at room temperature and low magnetic fields is important in these applications. However, current devices display inadequate MR at the low magnetic field/room temperature, limited working range, and bulky size. Therefore, the main goal of this thesis is to design and construct ideal MR materials/structures with large MR under these conditions.

We designed and developed a hybrid nanosheet based on reduced graphene oxide (rGO) and FeCo nanoparticles (NPs). The chemically synthesized FeCo/rGO hybrid nanosheets displayed significant MR at the low magnetic field and room temperature. A hybrid nanosheets-based wireless magnetic field sensing system was constructed, which achieved real-time detection and data collection of a working mobile phone. Meanwhile, we discovered the formation of Co-Mn oxides NPs on rGO hybrid nanosheets as the mass ratio of rGO added in the reaction exceeded 50 wt.%. The hybrid nanosheets with Co-Mn oxides NPs displayed relatively high MR compared with other structures containing Co and Mn under similar conditions.

In addition to the chemical path, we constructed FeCo/rGO hybrid nanosheets with a laser-assisted physical deposition process, i.e., the matrix-assisted pulsed laser evaporation (MAPLE). The MAPLE-prepared FeCo/rGO hybrid nanosheets exhibited MR close to or larger than the MR of other physically prepared FeCo-based granular materials/structures in previous works. Finally, by combining FeCo/rGO hybrid nanosheets with the hydrogel matrix, we developed a nanocomposite hydrogel with significant enhancements in mechanical properties and negative MR. The studies in this thesis provide a better understanding of designing and developing graphene-based nanocomposites with large MR. We believe that the findings in this thesis could be applied to overcome the obstacles of MR sensors and devices regarding sensitivity and cost-efficiency and benefit the future applications of MR devices.

Co-Authorship Statement

This thesis has been prepared by Songlin Yang with the suggestion, revision, and supervision of Dr. Jin Zhang. Guidance and aid were provided by Dr. Jin Zhang, the Principle Investigator and Supervisor, in study design/planning and data acquisition/interpretation. The thesis has been arranged according to the regulations for an integrated-article format thesis stipulated by the Faculty of Graduate and Postdoctoral Studies at Western University. The co-authors and their specific contributions are listed below.

Chapter 3: Developing FeCo/reduced graphene oxide (rGO) hybrid nanosheets with special magnetoresistance used for wireless magnetic field sensor

The experiments, characterizations, and data analysis were mainly performed by Songlin Yang. Mingyan Tan and Dr. Xu Li assisted with the XPS measurement and analysis. Dr. Tianqi Yu and Dr. Xianbin Wang helped in developing the wireless sensing system. Dr. Jin Zhang conceived and helped with the design of the experiments. Songlin Yang wrote the first draft of the manuscript under the supervision of Dr. Jin Zhang. This manuscript co-authored by S. Yang, M. Tan, T. Yu, X. Li, X. Wang, and J. Zhang was published in *Nano-Micro Letters* in March 2020.

Chapter 4: Investigation of the effect of increasing the mass ratio of rGO adding in the reaction and the formation of Co-Mn oxides

The experiments, characterizations, and data analysis were mainly performed by Songlin Yang. Mingyan Tan and Dr. Xu Li assisted with the XPS measurement and analysis. Dr. Jin Zhang conceived and helped with the design of the experiments. Songlin Yang wrote the first draft of the manuscript under the supervision of Dr. Jin Zhang. This manuscript co-authored by S. Yang, M. Tan, X. Li, and J. Zhang is to be submitted.

Chapter 5: Fabrication of FeCo/rGO hybrid nanosheets with the physical deposition process

The experiments, characterizations, and data analysis were mainly performed by Songlin Yang. Dr. Longyi Chen assisted with the experimental preparation and characterization. Dr. Jin Zhang conceived and helped with the design of the experiments. Songlin Yang wrote the first draft of the manuscript under the supervision of Dr. Jin Zhang. This manuscript co-authored by S. Yang, L. Chen, and J. Zhang is to be submitted.

Chapter 6: Developing FeCo/rGO hybrid nanosheets reinforced p(HEMA-co-AEMA) nanocomposite hydrogel with enhanced mechanical properties and magnetoresistances

The experiments, characterizations, and data analysis were mainly performed by Songlin Yang. Dr. Jin Zhang conceived and helped with the design of the experiments. Songlin Yang wrote the first draft of the manuscript under the supervision of Dr. Jin Zhang. This manuscript co-authored by S. Yang and J. Zhang is to be submitted.

Acknowledgments

Firstly, I want to express my deepest gratitude to my supervisor, Dr. Jin Zhang for allowing me to pursue my Ph.D. under her supervision. I really appreciate the continuous support, enlightening guidance, and insightful advice from her. I also want to thank her for her kindness and patience throughout my Ph.D. period. She provided me countless opportunities and encouragements that pushed me beyond my boundaries, which profoundly shaped myself and my lifestyle today. I couldn't be more grateful for her help and trust in both my research and life since I started my study at the University of Western Ontario. Her mentorship and support are crucial for me to overcome all these obstacles in my research work and my life.

I would like to thank my supervisor committees, Drs. Chunbao (Charles) Xu and Jose Herrera for their kindly guidance and encouragement. I also wish to thank Mingyan Tan and Dr. Xu Li for their assistance on XPS characterization and analysis. I am also grateful to Dr. Tianqi Yu and Dr. Xianbin Wang for the help in constructing the wireless sensing system.

I also had the great pleasure of working with all my past and present colleagues in the Zhang research group. Special thanks to Drs. Andrew (Wai Hei) Tse, Longyi Chen, and Longyan Chen for constructive suggestions. Thanks should also go to Eugene Hwang, Dr. Xueqin Zhao, Chao Lu, Yingqi Zhang, Jisu Song, Michelle Lee, Deepthi Muraleedharan, and Aditya Balaji for the friendship and collaboration.

Many thanks to Karen Nygard, Dr. Richard Gardiner, Kim Law, Souheil Afara, Dr. William Xu, Xuejie Gao, Yang Bai, Dr. Xingxing Liu, and Dr. Dongxing Zhang for their kind assistance and advice. I am also grateful to all my friends for their understanding and support throughout these years.

I must also sincerely thank my family for their understanding and encouragement that relieved my struggles in this journey. I truly appreciate their trust and support that helped me both mentally and physically.

Finally, I would like to thank the National Sciences and Engineering Research Council of Canada (NSERC) and the University of Western Ontario for their support and funding.

Table of Contents

List of Tables

List of Figures

List of Abbreviations

AEMA	2-aminoethyl methacrylate hydrochloride
AFP	Alpha-fetoprotein
AC	Alternating current
AMR	Anisotropic magnetoresistance
AFM	Atomic force microscope
BCC	Body-centered cubic
CA125 II	Cancer antigen 125
CCD	Charge-coupled device
CVD	Chemical vapor deposition
CFU	Colony-forming unit
CMR	Colossal magnetoresistance
CGR	Compound growth rate
COVID-19	Coronavirus disease 2019
CIP	Current in plane
CPP	Current perpendicular to plane
DNA	Deoxyribonucleic acid
DMSO	Dimethyl sulfoxide
DC	Direct current
DMPA	2,2-dimethoxy-2-phenylacetophenone
DRAM	Dynamic random access memory
EGDMA	Ethylene glycol dimethacrylate
EMF	Electromagnetic field
EDX	Energy-dispersive X-ray spectra
ELISA	Enzyme-linked immunosorbent assay
E. coli	*Escherichia coli*
EG	Ethylene glycol
ECM	Extracellular matrix
EMR	Extraordinary magnetoresistance
G-p(HEMA-co-AEMA)	FeCo/rGO hybrid nanosheets reinforced nanocomposite hydrogel
FDA	The United States Food and Drug Administration
FT-IR	Fourier-transform infrared spectroscopy
FWHM	Full width at half maximum
GMR	Giant magnetoresistance
GB	Gigabyte
GF	Graphene foam
GO	Graphene oxide

HDD	Hard disk drive
HEMA	2-hydroxyethyl methacrylate
HBV	Hepatitis B virus
HEV	Hepatitis E virus
HRTEM	High-resolution transmission electron microscopy
hCG	Human chorionic gonadotropin
HE4	Human epididymis protein 4
HIV	Human immunodeficiency virus
IgG	Immunoglobulin G
IgM	Immunoglobulin M
IC	Integrated circuits
IL6	Interleukin 6
IoT	Internet-of-things
kb	Kilobit
LED	Light-emitting diode
LOD	Limit of detection
MFM	Magnetic force microscope
MNPs	Magnetic nanoparticles
MRAM	Magnetic random access memory
MTJ	Magnetic tunnel junction
MR	Magnetoresistance
MAPLE	Matrix-assisted pulsed laser evaporation
MB	Megabyte
MAA	Methacrylic acid
MBE	Molecular beam epitaxy
NPs	Nanoparticles
Nd:YAG	Neodymium-doped yttrium aluminum garnet
NMR	Negative magnetoresistance
NVP	N-vinylpyrolidinone
OMR	Ordinary magnetoresistance
OER	Oxygen evolution reaction
ORR	Oxygen reduction reaction
PMLSM	Permanent magnet linear synchronous motor
PVD	Physical vapor deposition
POC	Point-of-care
pHEMA	Poly(2-Hydroxyethyl methacrylate)
p(HEMA-co-AEMA)	Copolymer of 2-hydroxyethyl methacrylate and 2-aminoethyl methacrylate
PMMA	Poly(methyl methacrylate)

PDMS	Polydimethylsiloxane
PMR	Positive magnetoresistance
PDF	Powder diffraction file
PAPP-A	Pregnancy-associated plasma protein-A
PCSK9	Proprotein convertase subtilisin/kexin type 9
PLD	Pulsed laser deposition
QMR	Quantum magnetoresistance
RF	Radiofrequency
RF-EMF	Radiofrequency electromagnetic field
RAM	Random access memory
rGO	Reduced graphene oxide
SEM	Scanning electron microscope
SAED	Selected area electron diffraction
SARS-CoV-2	Severe acute respiratory syndrome coronavirus 2
Tb	Terabit
TB	Terabyte
TT	Thymine-thymine
TEM	Transmission electron microscope
ST2	Tumorigenicity 2
TMR	Tunneling magnetoresistance
UTI	Urinary tract infection
UV	Ultraviolet
UV-Vis	Ultraviolet-visible
VSM	Vibrating sample magnetometer
WHO	World health organization
XRD	X-ray diffraction spectra
XPS	X-ray photoelectron spectra

Chapter 1

1   Introduction and Motivation

Magnetoresistance (MR) is defined as the variation of a material's electrical resistivity under the presence of external magnetic fields. In 1857, Lord Kelvin (William Thomson) first observed MR [1]. In the late 1980s, two scientists discovered that the multilayer system consists of Fe/Cr thin layers could display large MR at low temperature [2]. The MR of this Fe/Cr multilayer system at low temperature was later known as the giant magnetoresistance (GMR) [3]. The discovery of GMR has dramatically boosted the development of the magnetic recording industry since IBM applied GMR reading heads in the hard disk drive (HDD) [4]. Nowadays, MR devices/sensors have been broadly applied in various fields including data storage, position sensing, current sensing, non-destructive monitoring, and biomedical sensing systems [4-7].

In recent years, the demands on highly-sensitive and cost-effective MR devices/sensors raised. Improvements in the sensitivity and production process are important to the further applications of MR devices/sensors. The theme of this thesis is to develop a novel material with the enhanced MR and facile preparation process, which meets the requirements of highly-sensitive and cost-effective MR devices/sensors. Specifically, the aim is to construct a novel MR nanomaterial with minimum requirements on extreme conditions (e.g., low temperatures) and large magnetic fields (> 10 kOe). The investigations and discussions of the possible origin of the MR are included in this thesis. In addition, multifunctional MR devices/sensors were developed with the as-prepared novel MR nanomaterials. This chapter will provide an overview of the MR phenomena and applications of MR sensors. Meanwhile, current challenges in producing ideal MR devices/sensors and the possible solution to existing difficulties will be discussed. Research objectives and the outline of this thesis will be identified and listed.

1.1 A Brief Introduction of Magnetoresistance

MR is defined as a material's electrical resistance change under the presence of an external magnetic field. It was first observed by Lord Kelvin (William Thomson) in 1857 [1]. Since the discovery of GMR in the 1980s, numerous studies have been performed to investigate MR effects and MR materials/structures [3]. In specific, MR can be classified as several distinct types (**Figure 1.1**) including ordinary magnetoresistance (OMR), anisotropic magnetoresistance (AMR), giant magnetoresistance (GMR), tunneling magnetoresistance (TMR), colossal magnetoresistance (CMR), and extraordinary magnetoresistance (EMR).
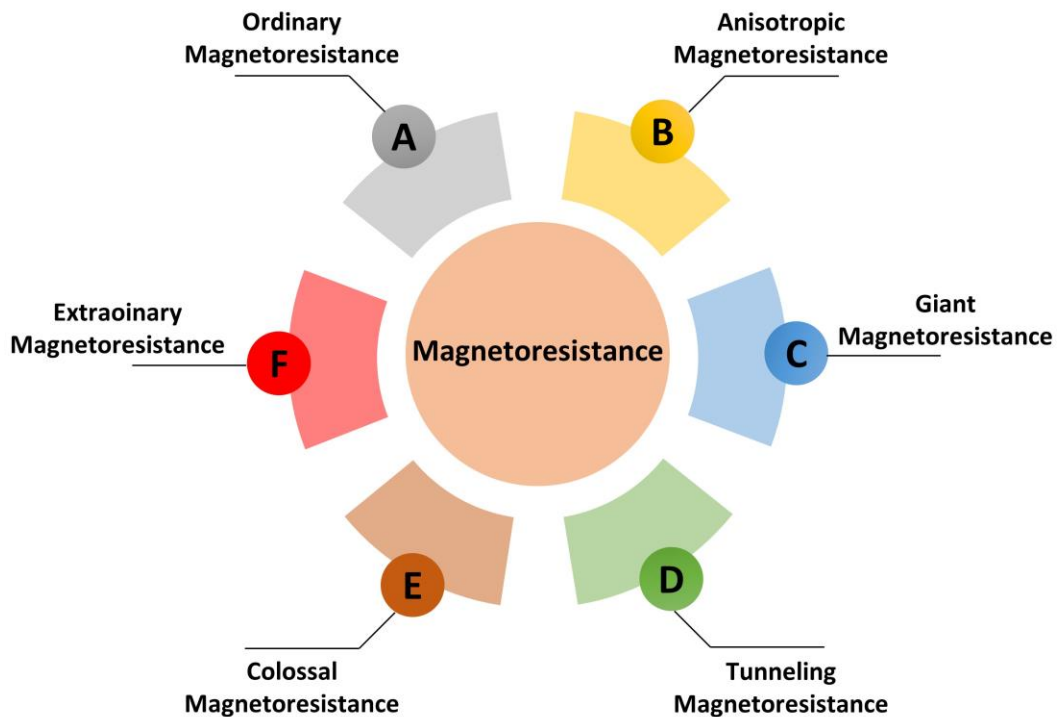
Figure 1.1 Different types of magnetoresistance (MR).

1.1.1 Ordinary Magnetoresistance

Ordinary magnetoresistance (OMR) is related to the (electrical) resistance change (ΔR) of metals under the presence of an external magnetic field (**Figure 1.2**). The OMR arises from the cyclic motion of electrons, and the MR of this phenomenon is relatively small

[8]. The magnitude of OMR can be increased by raising the intensity of external magnetic fields [9].
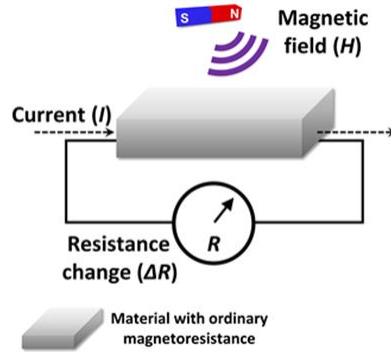
Figure 1.2 Schematic diagram of ordinary magnetoresistance (OMR).

1.1.2 Anisotropic Magnetoresistance (AMR)

In anisotropic magnetoresistance (AMR), the resistance change (ΔR) depends on the angle (θ) between the electric current and the magnetization of the material [10]. The AMR is triggered by the anisotropy of electron scattering effects in the material. Researchers observed AMR in the alloys (based on iron, cobalt, and nickel) in the 1970s [11, 12]. For AMR in ferromagnetic metals, the high resistance appears when the magnetization direction is parallel to the current direction. On the contrary, the low resistance appears when magnetization is perpendicular to the current direction (**Figure 1.3**) [10]. The magnitude of AMR can be calculated by the equation (1.1)

$$AMR = \frac{\rho_\parallel - \rho_\perp}{\rho_\perp} \qquad (1.1)$$

where $\rho_\parallel$ is the resistivity when the current is parallel to the magnetization direction, and $\rho_\perp$ the is resistivity when the current is perpendicular to the magnetization direction.
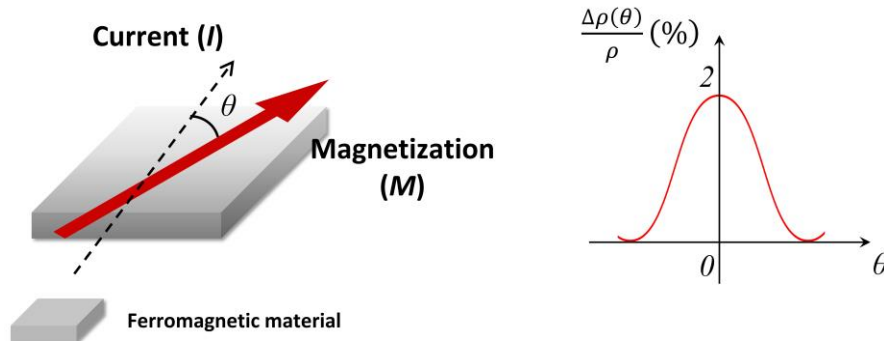
Figure 1.3 Schematic diagram of anisotropic magnetoresistance (AMR).

1.1.3   Giant Magnetoresistance (GMR)

In 1988, giant magnetoresistance (GMR) was discovered in the multilayer system of Fe and Cr [2]. GMR offers larger MR at a relatively small magnetic field, although it may require extreme conditions such as low temperatures [2, 3]. As shown in **Figure 1.4**, the sandwich structure of GMR includes two ferromagnetic layers and one non-magnetic (or non-ferromagnetic) layer. The GMR effect is related to the spin-dependent scattering of electrons [13]. Normally, the high resistance can be observed when the magnetization directions of two ferromagnetic layers are anti-parallel. On the other hand, the low resistance can be observed at the parallel state. The discovery of GMR has significantly increased the storage capacity of magnetic storage devices such as hard disk drives (HDDs) [4].
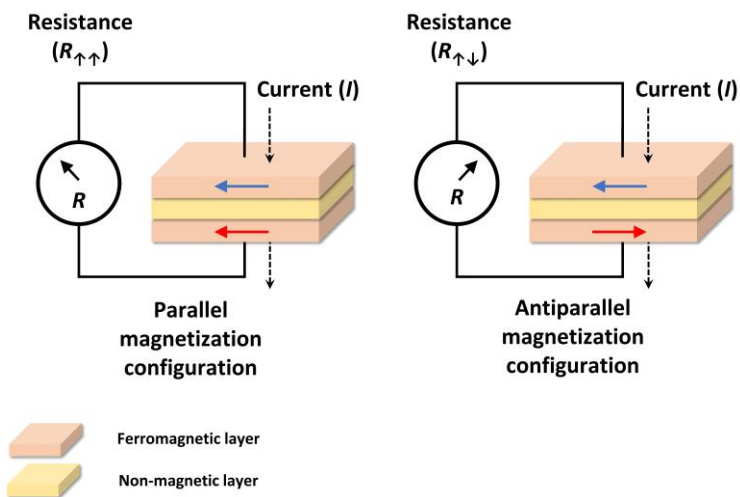
Figure 1.4 Schematic diagram of giant magnetoresistance (GMR).

1.1.4　Tunneling Magnetoresistance (TMR)

Tunneling magnetoresistance (TMR) adopts a similar multilayer configuration as the GMR. The basic unit of the TMR device is the magnetic tunnel junction (MTJ). The MTJ follows the structure of the ferromagnetic metal layer/insulator layer/ferromagnetic metal layer (**Figure 1.5**) [14]. In this system, electrons tunnel through the insulator layer due to the quantum tunnelling phenomenon [15]. TMR is generated by spin-dependent tunneling of electrons, which is related to the magnetization directions of ferromagnetic layers. The high resistance can be observed at the anti-parallel state. On the contrary, the low resistance can be obtained at the parallel state. TMR reading heads have been widely applied in HDDs since 2006 [16]. In addition, TMR sensors were used in position sensing and non-destructive monitoring to perform position measurement and defect detection [17-19].
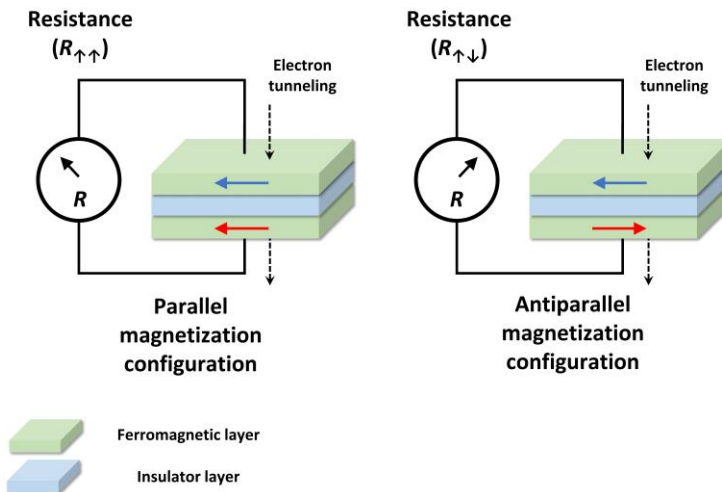
Figure 1.5 Schematic diagram of tunneling magnetoresistance (TMR).

1.1.5　Colossal Magnetoresistance (CMR)

In the 1990s, researchers discovered colossal magnetoresistance (CMR) in manganese-based perovskite oxides [20]. Various theories have been applied to explain the origin of CMR [21-23]. The magnitude of MR in CMR materials can be large (150% at 6×10^1 kOe. The Oersted (Oe, CGS) and A/m (SI) are units for magnetic field intensity (H). The Gauss (G, CGS) and Tesla (T, SI) are units for magnetic flux density. $B = \mu H$) [23-26].

Moreover, some CMR materials exhibit insulator-to-metal transfer at increasing temperature or external magnetic fields [23]. CMR materials are expected to become an important type of material for the production of MR devices/sensors. However, the future applications of CMR materials remain limited and unclear due to the prerequisites such as low temperature, large magnetic field, and complicated fabrication processes.

1.1.6   Extraordinary Magnetoresistance (EMR)

Extraordinary magnetoresistance (EMR) has been discovered in the hybrid structure of semiconductors and metals [27]. EMR effect can provide significant MR ($> 10^4$%) at relatively low magnetic fields (3×10^1 kOe) [28]. The origin of EMR is related to the changing ratio between currents flowing through the metal parts and the semiconductor parts [27]. The EMR sensor is expected to be applied in the reading heads of future HDDs [29]. However, the disadvantages of EMR devices are also obvious. The EMR devices require precise control on the layer thickness and complicated preparation processes. In addition, EMR devices experience difficulties in increasing the signal output and reducing the dimension [27].

1.2   Developing Magnetoresistance Materials/Structures

Since the discovery of MR, various MR materials/structures have been developed to achieve ideal performance under different conditions. Due to the special anisotropic property, AMR materials are applied in designing memory sensors and angle sensors [30, 31]. However, the MR of AMR materials is relatively low (2.5%). Currently, multilayer systems with GMR or TMR effects are widely employed in commercial applications [32-34]. In recent years, emerging nanotechnology has offered various options for constructing ideal MR materials/structures. Instead of the bulk layer, the granular MR system was developed with pressed small granules of magnetic materials. Granular MR systems are designed to reduce the complexity and improve the efficiency of the preparation [35-37].

Due to its unique physical/chemical properties, graphene has soon attracted the attention of researchers [38]. Multilayered graphene, graphene foams, and hybrid graphene

nanocomposites have been introduced in the development of MR materials/structures [39-41]. Layered graphene MR systems are constructed by introducing disorders into monolayer/multilayer graphene or combining graphene layers in multilayer devices [42-47]. Graphene foams (GF) are three-dimensional arranged graphene structures with good biocompatibility and MR property [48-54]. Hybrid graphene nanocomposites with MR are constructed with graphene and reduced graphene oxide (rGO) [41, 55-62]. A brief review of MR materials/structures is provided in Chapter 2.

1.3   Current Applications of Magnetoresistance Sensors

The study of William Thomson set the cornerstone for the future developments of MR devices [1]. However, few research attempts were put into the investigations of MR due to the small magnitude of the MR effect (less than 2%) [63]. The situation was changed when Grünberg and Fert discovered the GMR in 1988. In the meantime, the demands for magnetic sensors raised due to the surge of magnetic data storage systems since the early 70s. This led to a significant boost of studies on MR sensors/devices [2, 3]. In 1990, the GMR multilayer system was successfully prepared by IBM Almaden Research Center with high-vacuum DC magnetron sputtering. This result reveals the possibility to produce sensitive MR sensors for improving the storage capacity of magnetic storage devices [64]. After IBM introduced the first GMR reading head in HDD, more and more studies have focused on developing MR sensors for different applications [65].

MR sensors have been employed in different applications including biophysics and the automotive industry since the first commercial GMR sensor came to the market in 1994 [34]. Currently, the major applications of MR sensors include magnetic storage (recording), position sensing, current sensing, non-destructive monitoring, and biomedical sensing systems [66-72]. MR sensors have also been applied in producing antilock brakes, magnetocardiography, and galvanic isolators [73-79]. The total value of the magnetic sensor market is expected to exceed 2.0 billion US dollars in 2022 due to the brooming of the modern electronic industry [80]. As shown in **Figure 1.6**, the number of the published papers on MR sensors has increased since 1995, which indicates the growing scientific interest in this topic.
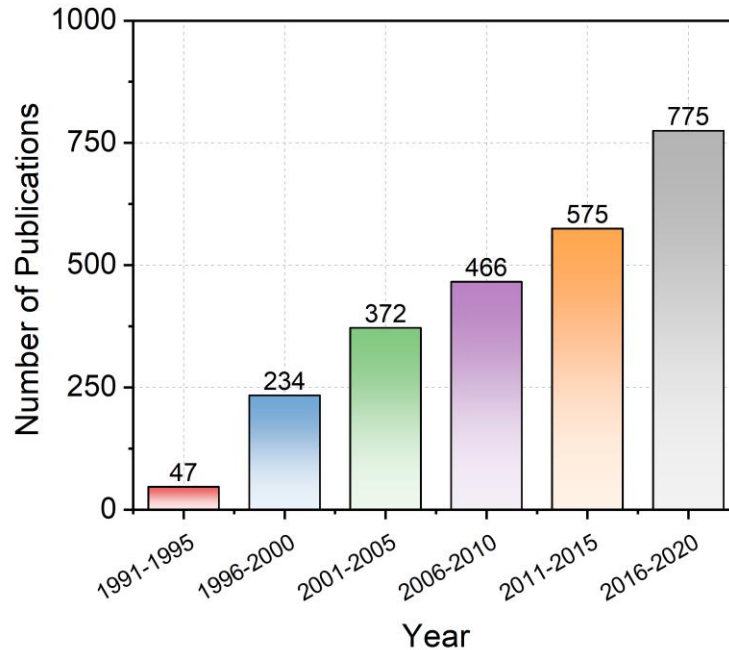
Figure 1.6 The number of publications on MR sensors from 1991 to 2020. The data were obtained from the Web of Science core collection with the keyword "magnetoresistance sensor".

1.4 The Demands on Highly-sensitive and Cost-effective MR Materials/Devices

The seeking of ideal MR sensors in various applications has raised the demands of highly-sensitive and cost-effective MR sensors. Since the discovery of MR, the study has never stopped for developing ideal MR materials/devices with large MR at room temperature/low magnetic fields and simplified preparation processes. Currently, GMR and TMR multilayer systems could provide applicable MR sensors and devices. However, these multilayer systems display drawbacks including large time and equipment cost in production, relatively low MR value at room temperature/low magnetic fields, and limited working range. The highly-sensitive and cost-effective MR materials/devices are in high demand to meet the specific requirements for different applications and broaden the industrial implementations of the MR sensors/devices (**Figure 1.7**).
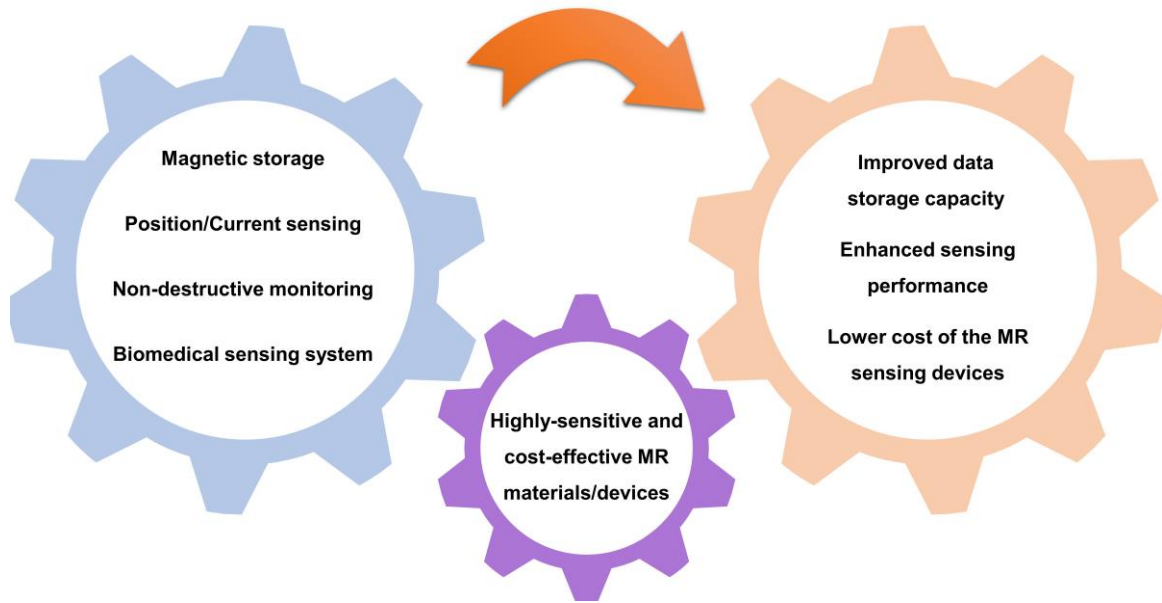
Figure 1.7 Schematic diagram of the potential impacts of highly-sensitive and cost-effective MR materials/devices on current applications.

For data storage, the highly-sensitive MR materials/devices can enhance the sensitivity of MR reading heads in HDDs. The area size of data bits can be minimized with the highly-sensitive MR reading head. This leads to a higher areal density of data and a larger storage capacity of HDDs. In addition, the highly-sensitive MR materials can contribute to decreasing the size of current TMR sensors. The cost-effective feature can help to reduce the production cost of MR reading heads. Therefore, these improvements could trigger a dramatic decline in the average retail price of magnetic storage devices with increased storage capacity. The decrease of average retail price could benefit the development of the electronics industry, which has been demonstrated by the prevalence of MR reading heads since the emergence of AMR, GMR, and TMR reading heads in the market.

The sensitivity of the MR sensor is crucial for position sensing, current sensing, and non-destructive monitoring. The targets' stray magnetic fields could be relatively low for detection (such as electrical currents in the integrated circuits or eddy currents of the defect area). Meanwhile, the structures above or close to the detection targets can obstruct the sensing process. Thus, MR sensors with higher sensitivity are required for

these applications especially for the low magnetic fields and room temperatures. Although GMR/TMR multilayer systems exhibit enhancements on sensitivity and reliability over the traditional Hall effect sensors, improvements are required to strengthen the sensitivity and working range of the multilayer systems [81]. The highly-sensitive MR sensors could offer more details and higher resolution in the applications such as position sensing, current sensing, and non-destructive monitoring [82]. The GMR/TMR multilayer systems increase the production cost of devices in these applications. Applying cost-effective MR materials could reduce the economic cost for the MR sensor-based position/current sensors and non-destructive monitor systems, which increases the profit and broadens the commercial application.

The sensitivity of magnetic field sensors is directly related to the limit of detection (LOD) in magnetic biomedical sensing platforms/systems. Magnetic nanoparticle (MNP) is the most adopted magnetic label for biomedical sensing platforms based on MR sensors. Hence, MNPs with higher magnetic moments are preferred as the stronger magnetic signals can be picked up by MR sensors. A higher signal-to-noise ratio can be achieved since the biological matrix exhibits low magnetic backgrounds. However, the detection process is still strongly influenced by built-in MR sensors' sensitivity and working range. Meanwhile, it is challenging for MR biomedical sensing systems to collect signals since the magnetic signal of MNPs are relatively low compared with bulk targets. This requires MR sensors to display larger signal outputs at relatively low magnetic fields [83].

Currently, GMR/TMR multilayer systems show disadvantages in MR at low magnetic fields and limited working ranges [84]. In addition, GMR/TMR multilayer systems increase the price of MR biomedical sensing platforms due to the high economic and time costs of the preparation process [84]. Therefore, the ideal MR materials/devices not only improve the sensitivity but also reduce the production cost of the biomedical sensing systems for potential applications such as point-of-care (POC) testing, which benefits the development of the next generation MR biomedical sensing platform [85].

Furthermore, increasing concerns appear on detections and quantifications of electromagnetic radiations nowadays due to the fast developments of communication

technology and personal electronic devices [86-88]. The world health organization (WHO) has already classified the radiofrequency electromagnetic field (RF-EMF) radiation as "possibly carcinogenic to humans" (Group 2B) [89]. WHO increases the priority of the researches about the effects of RF-EMF exposure on the human body due to the concerns of potential adverse effects on the brain and other organs (particularly in children) [90]. The detection of magnetic fields is an appliable method to detect and quantify electromagnetic radiations [91]. Hall effect sensors and MR sensors are two major types of magnetic field sensors. MR sensors display superiorities over traditional Hall-effect sensors in energy consumption, physical size, sensitivity, and temperature stability [92, 93]. In addition, current MR sensors could be improved in sensitivity, integrability, and cost-efficiency to meet the demands of possible massive usage of MR sensors for detecting electromagnetic radiations. Therefore, further studies are required for developing highly-sensitive and cost-effective MR materials/devices in RF-EMF detections.

1.5 Current Challenges in Constructing Ideal MR Materials/Devices

AMR was introduced in scientific and industrial fields by the discovery of AMR in 1857 and the application of AMR reading head of HDDs in 1991 [1, 94]. AMR materials have been applied in constructing angular sensors and displacement sensors. The variations of MR are related to the angle between the direction of magnetization and electrical current in the AMR materials [95]. However, AMR displays the low magnitude of MR outputs ($< 2.5\%$) and the bulk effect nature, which limit the applications of AMR materials-based sensors and hinder the miniaturization of AMR reading heads in HDDs [16, 34].

GMR and TMR sensors are the major types of MR sensors in the commercial market. Currently, GMR/TMR multilayer systems have become dominant in most of the MR sensors' applications (i.e., magnetic storage, position sensing, current sensing, non-destructive monitoring, and biomedical sensing system) [84, 96]. Although GMR/TMR sensors can achieve relatively high sensitivity in contrast with AMR sensors, the production process of multilayer systems is complicated and time-consuming. Moreover,

GMR/TMR multilayer systems require more layer repetitions and precise layer thickness control to improve the performance. Various preparation techniques are employed with requirements on special instruments (such as electron beam evaporation, magnetron sputtering, cathodic arc deposition, molecular beam epitaxy (MBE), pulsed laser deposition, and chemical vapor deposition (CVD)) [97-103]. In some circumstances, the total thickness of the GMR multilayer is required to be within 20 ~ 30 nm [104].

GMR/TMR multilayer systems demand high accuracy layer thickness control since the thickness limitations are strict. This leads to increased investments in equipment and complicated fabrication processes. The specifications on annealing temperature (> 250 °C) of multilayer systems introduce further requirements on the instruments and procedures [33, 105]. GMR/TMR multilayer systems can accomplish large MR at a high magnetic field. The resistance variation range is limited for some GMR sensors and most TMR sensors. This means that the resistance would soon reach a stable value as the magnetic field's intensity increases, which leads to a limited working range for magnetic field sensing [106, 107]. In conclusion, the major drawbacks of GMR/TMR multilayer systems include the high economic and time costs for preparation, limited working range, and relatively low MR value at room temperature, which hinder their future applications.

In recent two decades, nanoconstructed MR materials/structures are introduced by fast-developing nanotechnology. Granular MR systems were developed by dividing the bulk layers of magnetic materials into small magnetic particles. The magnetic particles are pressed together or embedded in the non-magnetic medium [35-37]. The granular MR systems exhibit superiorities in reducing the cost and complexity of the fabrication process compared with the multilayer configuration. However, granular MR systems require high magnetic fields ($\geqslant$ 50 kOe) and low temperature to achieve satisfactory resistance changes. Consequently, the MR of granular MR systems is relatively low at room temperature and low magnetic fields. In addition, complicated fabrication methods are involved in the production of granular MR systems (such as magnetron sputtering) [108-112].

The discovery of graphene offers a material with unique physical and chemical properties [113, 114]. MR is one of the most interesting transport phenomena in graphene-based materials, which allows graphene-based materials to be applied in constructing MR sensors/devices [115, 116]. Monolayer/multilayer graphene devices displayed large MR effects (up to 100%), and studies were performed for developing potential applications of graphene MR devices [39, 117]. However, the layered graphene requires special preparation techniques (such as chemical vapor deposition (CVD). In the meantime, it is challenging to achieve precise control of layer number/position [39]. Demands on specific substrates increase the production cost and complexity of layered graphene MR systems' preparation processes. In addition, most layered graphene MR systems exhibit small MR at room temperature, while high magnetic fields are necessary in most cases to reach the large MR [118]. Although many attempts have been made to enhance the performance of layered graphene MR systems, their current applications are limited by low cost-efficiency, complicated fabrication processes, and inadequate MR at ambient temperature/low magnetic fields.

Graphene foams have been introduced in developing MR materials due to their special physical/chemical properties. The advantages of graphene foams include good biocompatibility, the combination of intrinsic properties of graphene, pore size adjustability, three-dimensional morphology, and potential for mass production. Graphene foams achieve a large MR at high magnetic fields (50 ~ 60 kOe) by incorporating nanoparticle/polymers or introducing disorders [52-54]. However, graphene foams require complicated preparation methods (such as CVD) and specific techniques for introducing disorders (such as inductively coupled plasma systems). These procedures are not friendly for mass production and increase the investments in equipment. Furthermore, graphene foams display inadequate MR at low magnetic fields (< 10 kOe), and extreme temperature (~ 5 K) is required in some cases to obtain satisfactory MR responses [40, 119].

Hybrid graphene nanocomposites have been investigated for various applications since graphene offers a large surface-to-volume ratio and high carrier mobility [120]. Hybrid graphene nanocomposites have been introduced in developing graphene-based MR

materials/devices. Two different routes were applied in constructing hybrid graphene nanocomposites. In the first route, graphene layers are prepared by chemical vapor deposition (CVD) or mechanical exfoliation. These graphene layers are later decorated by nanoparticles/adatoms clusters *via* physical process [55-59]. The product of this method can achieve large MR at low temperatures (~ 10 K). Meanwhile, the drawbacks of this route include demands on specific fabrication equipment, requirements on specific substrates, and a relatively small magnitude of MR at room temperature. In addition, the decoration process involves techniques such as thermal evaporation and electron beam deposition, which further increase the cost and complexity of the production.

Reduced graphene oxide (rGO) is more friendly and cost-effective for mass production and constructing hybrid nanocomposites [121]. In the meantime, rGO offers a large surface area for nanoparticle modification [122]. It is applicable and accessible to produce rGO hybrid nanocomposites with chemical modification. rGO hybrid nanocomposites could improve the MR of graphene-based materials without increasing the investments in specific equipment. Some results indicate that rGO hybrid nanocomposites can achieve a large MR. However, the prerequisites include high magnetic fields or low temperature. In addition, few attempts have been made to improve the performance of rGO hybrid nanocomposites. Currently, rGO hybrid nanocomposites hardly meet the requirements of ideal MR materials due to the issues such as small MR at low magnetic fields and room temperatures. Therefore, further investigations are required to increase the MR of rGO hybrid nanocomposites, which could provide a solution to current challenges faced by MR materials/devices.

Table 1.1 summarized the advantages and disadvantages of currently developed MR materials/devices. In conclusion, further investigations are required to push the limit of the MR materials/devices and meet the demands of the highly-sensitive and cost-effective MR materials. Currently, most MR materials exhibit inadequate MR at low magnetic fields and room temperature. Therefore, breakthroughs are expected in constructing the next-generation MR sensors with high sensitivity and low cost, which will significantly boost the developments of the industrial application.

Table 1.1 Summary of current magnetoresistance (MR) materials/devices.

Type of magnetoresistance (MR) devices	Advantages	Disadvantages
Anisotropic magnetoresistance (AMR) materials/devices	Anisotropic properties of AMR materials/devices have advantages in position sensing and navigation (angular and displacement sensing)	The low magnitude of AMR outputs ($\Delta R/R_0 < 2.5\%$) Difficult to reduce the size and hard for miniaturization
Multilayer systems based on giant magnetoresistance (GMR) and tunneling magnetoresistance (TMR)	GMR/TMR multilayer systems exhibit high sensitivity for low magnetic fields GMR/TMR multilayer systems can be integrated with the electronic circuit easily	Multilayer structures require complicated fabrication processes and specific equipment due to the strict limitations of layer thickness (increasing cost on equipment and extending the fabrication process lead to expensive products) GMR/TMR multilayer systems exhibit limited resistance variation range (working range, especially for TMR) and relatively low MR at room temperature (mostly for GMR)

Type of magnetoresistance (MR) devices	Advantages	Disadvantages
Granular MR systems	Granular MR systems bring simplified fabrication procedures and reduced investments in instruments Relatively large MR at room temperature can be achieved by some specific designed granular MR systems	Magnetic field $\geq$ 50 kOe is the prerequisite to achieve large MR at ambient temperature (relatively small resistance change for low magnetic fields at room temperature) Some granular MR systems require extremely low temperatures for large MR Although granular MR systems can reduce the complexity of the fabrication process, the dependence on specific fabrication techniques (such as magnetron sputtering) remains

Type of magnetoresistance (MR) devices	Advantages	Disadvantages
Layered graphene MR systems	Layered graphene MR systems exhibit large MR value and potential to be applied on fabricating next-generation spintronics based on layered graphene	Most layered graphene MR systems require extremely low temperatures to achieve large MR Special designed substrates/circuits are required Precise control of layer number and positions is challenging Special fabrication techniques are required for preparing layered graphene, which further increases the production costs and the complexity
Graphene foam MR systems	Graphene foam MR systems display relatively large MR at room temperature and offer unique 3-D structures for potential applications	Large magnetic fields (≥ 50 kOe) are required for graphene foams to reach considerable MR (the magnitude of resistance change shrinks rapidly as the magnetic field reduce to the level of 10 kOe) Graphene foams require complicated fabrication processes (such as CVD) and specific defects-introducing instruments

Type of magnetoresistance (MR) devices		Advantages	Disadvantages
Hybrid graphene nanocomposites	Based on CVD/mechan-ical exfoliation produced graphene	Relatively large values were achieved for both positive and negative MR Future applications in fabricating graphene-based circuits	Special designed substrate/circuits are required for CVD/mechanical exfoliation produced graphene leads to complicated fabrication processes with more investments and time costs Exhibiting small magnitude of MR at room temperature
	Based on reduced graphene oxide (rGO)	rGO and rGO hybrid nanocomposites can be both obtained with facile preparation processes leads to lesser requirements on special equipment Reduced investments in instruments and simplified production process (cost-effective and friendly for mass production) Large MR was achieved by the rGO hybrid nanocomposites	Current results of rGO hybrid nanocomposites show relatively small MR at the low magnetic field (< 10 kOe) and room temperature Few investigations have been performed to develop and improve the MR of rGO hybrid nanocomposites

1.6 Motivations, Objectives, and Outcomes

Currently, the demand arises in developing highly-sensitive and cost-effective MR materials. The complicated preparation processes lead to the escalation of MR sensors/devices' prices, which obstructs the further application of MR sensors. Thus, the facile preparation process can reduce the investments and time costs of future mass production. In the meantime, the enhancement of MR can bring enormous improvements in data storage capacity, signal resolution, signal-to-noise ratio, and device miniaturization of industrial applications [66-72].

The major motivation of my work is to develop the highly-sensitive and cost-effective MR materials and devices. The objectives are to enhance the performance at low magnetic fields and room temperature and to overcome the obstacles of reducing the complexity of the fabrication process. The investigations of graphene have revealed unique physical and chemical properties [113, 114]. Developing graphene nanocomposites can be considered as a possible route to construct ideal MR materials. However, the preparation of layered graphene is challenging, complicated, and expensive due to the requirements for special preparation techniques and instruments. Reduced graphene oxide (rGO) can be applied to reduce the cost and complexity of the preparation processes. rGO is facile to produce, and it is favorable for mass production [123]. rGO offers a large surface area and functional groups, which are suitable for the modification of nanoparticles [122]. Therefore, it is possible to develop MR materials based on rGO hybrid nanocomposites, which exhibit enhanced MR at low magnetic fields and room temperature.

Ferromagnetic transition metals have been widely applied in the fabrication of GMR/TMR multilayer systems due to the spin-dependent scattering effects [97-103]. Ferromagnetic nanoparticles are adopted in constructing granular MR systems [124-126]. In addition to the single ferromagnetic metal, FeCo, FeNi, and FeGa have been applied in the production of GMR/TMR multilayer systems [127-129]. FeCo is an important type of ferromagnetic layer due to high saturation magnetization, high curie temperature, good mechanical strength, and spin-dependent scattering feature [130, 131]. FeCo

nanoparticles (NPs) are applied as the building blocks in various magnetic nanoparticle-based devices [132, 133]. In addition, FeCo granular MR systems exhibit considerable MR at large magnetic fields, which incorporate FeCo granules with the non-magnetic matrix [108-112]. Thus, FeCo NPs can be considered as one of the promising candidates for developing ideal nanoconstructed MR materials/devices.

In addition, A. A. Abrikosov pointed out that the inhomogeneous materials can display large positive MR, which contain layered materials with relatively small electron concentration and embedded metallic clusters/atoms [134, 135]. This theory later adopted graphite as an example of the layered substrate. Abrikosov proposed this theory in 1998 ~ 2000 when the era of graphene didn't come yet. It is possible to construct ideal MR materials/structures with graphene or rGO since graphene has been extensively studied nowadays. Therefore, rGO is applied as the substrate for developing materials with ideal MR performance in this thesis, which reduces the investments and complexity of the preparation process. FeCo NPs are applied to construct the hybrid nanocomposites with enhanced MR due to the unique magnetic properties and strong spin-dependent scattering effects. The expected outcome is to produce MR materials with improved performance based on rGO nanocomposites (i.e., FeCo/rGO hybrid nanosheets), which meet the requirements of cost-effective and highly-sensitive MR materials. Both chemical and physical routes are utilized to construct hybrid nanocomposites. In addition, FeCo/rGO hybrid nanosheets are applied in developing novel MR sensors and composite materials.

The main goals of this thesis are summarized to the objectives listed below:

- To develop the FeCo/rGO hybrid nanosheets with the chemical synthesis process.

- To construct the FeCo/rGO hybrid nanosheets with the laser-assisted physical deposition process.

- To study the chemical and physical properties of FeCo/rGO hybrid nanosheets and investigate the possible origin of the special MR of FeCo/rGO hybrid nanosheets.

- To develop novel MR sensors and composite materials based on FeCo/rGO hybrid nanosheets for potential applications.

1.7 Thesis Outline

In what follows, the dissertation will be organized in an outline as:

In Chapter 1, an overview of the research background is provided regarding magnetoresistance (MR), developments of MR materials/structures, and applications of MR sensors. This chapter mentioned the demands on highly-sensitive and cost-effective MR materials and revealed current challenges in constructing ideal MR materials/devices. This chapter identified the research motivations, objectives and outcomes of this thesis.

In Chapter 2, a brief review is provided in respect of the current progress on developing MR materials/structures. In addition, this chapter reviewed the major applications of MR sensors (including magnetic storage, position sensing, current sensing, non-destructive monitoring, and biomedical sensing systems). This chapter also mentioned the current advancements of MR sensors in these applications.

In Chapter 3, we designed and developed a new hybrid nanosheet with FeCo NPs and rGO. The FeCo/rGO hybrid nanosheets were successfully produced with the facile polyol process as FeCo NPs *in-situ* grown on the rGO. The FeCo/rGO hybrid nanosheets exhibit significant MR ($21 \pm 6\%$) at low magnetic fields and room temperature. Meanwhile, the tunable MR was achieved by adjusting the ratio of reaction materials. The possible origin of the MR was discussed by using the quantum magnetoresistance (QMR) model. Moreover, FeCo/rGO hybrid nanosheets were applied in constructing a wireless magnetic field sensing system, which finished the real-time detection of magnetic fields.

In Chapter 4, we investigated the influences of increasing the mass ratio of rGO in the reaction. Co-Mn oxides NPs were observed on rGO as the rGO mass ratio surpassed 60 wt.% in the reaction. The rGO with Co-Mn oxides NPs achieved large MR ($3.5\% \sim 4.5\%$) at low magnetic fields and the room temperature in contrast with other reported structures containing Co and Mn. This study reveals the effects of increasing the rGO mass ratio in

the reaction. It suggests a facile route to produce the nanocomposites with Co-Mn oxides and rGO, which can help the further investigations of the potential applications.

In Chapter 5, the objective is to construct FeCo/rGO hybrid nanosheets with the laser-assisted physical deposition technique (i.e., matrix-assisted pulsed laser evaporation (MAPLE)). The MAPLE technique was applied to stoichiometrically transfer FeCo NPs on rGO substrates. We successfully deposited FeCo NPs on rGO with MAPLE, and the influences were investigated regarding the deposition duration. The MAPLE-prepared FeCo/rGO hybrid nanosheets displayed positive MR (~ 0.7%) at the low magnetic field and room temperature. This MR is close to or relatively larger than the MR of other physically prepared FeCo-based granular systems with higher FeCo ratios.

In Chapter 6, we developed a mechanically flexible nanocomposite hydrogel with MR properties. This nanocomposite hydrogel was constructed by incorporating FeCo/rGO hybrid nanosheets with the copolymer of 2-hydroxyethyl methacrylate and 2-aminoethyl methacrylate (p(HEMA-co-AEMA)). The nanocomposite hydrogel offers outstanding mechanical properties (2.0x higher toughness, 1.5x higher Young's modulus, and 1.7x higher maximal tensile stress). In addition, a negative MR (-1.4 ± 0.3%) was observed in the nanocomposite hydrogel at room temperature and low magnetic fields.

In Chapter 7, the summary and conclusions were provided regarding the important findings of this thesis. This chapter discussed the challenges and limitations of the current investigations. Chapter 7 also identified perspectives for future studies based on this thesis.

1.8 References

[1] W. Thomson, XIX. On the electro-dynamic qualities of metals:—Effects of magnetization on the electric conductivity of nickel and of iron. *Proc. R. Soc. London* **1857**, (8), 546-550.

[2] M.N. Baibich, J.M. Broto, A. Fert, F.N. Van Dau, F. Petroff, P. Etienne*, et al.*, Giant Magnetoresistance of (001)Fe/(001)Cr Magnetic Superlattices. *Phys. Rev. Lett.* **1988**, *61* (21), 2472-2475.

[3] G. Binasch, P. Grünberg, F. Saurenbach, W. Zinn, Enhanced magnetoresistance in layered magnetic structures with antiferromagnetic interlayer exchange. *Phys. Rev. B* **1989**, *39* (7), 4828-4830.

[4] C. Chappert, A. Fert, F.N. Van Dau, The emergence of spin electronics in data storage. *Nat. Mater.* **2007**, *6*, 813.

[5] V. Kartik, A. Sebastian, T. Tuma, A. Pantazi, H. Pozidis, D.R. Sahoo, High-bandwidth nanopositioner with magnetoresistance based position sensing. *Mechatronics* **2012**, *22* (3), 295-301.

[6] R. Hamia, C. Cordier, C. Dolabdjian, Eddy-current non-destructive testing system for the determination of crack orientation. *NDT E Int.* **2014**, *61*, 24-28.

[7] V.D. Krishna, K. Wu, A.M. Perez, J.-P. Wang, Giant Magnetoresistance-based Biosensor for Detection of Influenza A Virus. *Front. Microbiol.* **2016**, *7*, 400.

[8] D. Feng, G. Jin, Introduction To Condensed Matter Physics, Volume 1, World Scientific Publishing Company, 2005.

[9] J. Nickel, Magnetoresistance overview, Hewlett-Packard Laboratories, Technical Publications Department, 1995.

[10] J. Velev, R.F. Sabirianov, S.S. Jaswal, E.Y. Tsymbal, Ballistic Anisotropic Magnetoresistance. *Phys. Rev. Lett.* **2005**, *94* (12), 127203.

[11] R.C. O'handley, Modern magnetic materials: principles and applications, Wiley, 2000.

[12] T. McGuire, R. Potter, Anisotropic magnetoresistance in ferromagnetic 3d alloys. *IEEE Trans. Magn.* **1975**, *11* (4), 1018-1038.

[13] P. Zahn, J. Binder, I. Mertig, R. Zeller, P.H. Dederichs, Origin of Giant Magnetoresistance: Bulk or Interface Scattering. *Phys. Rev. Lett.* **1998**, *80* (19), 4309-4312.

[14] S. Maekawa, U. Gafvert, Electron tunneling between ferromagnetic films. *IEEE Trans. Magn.* **1982**, *18* (2), 707-708.

[15] J. Inoue, S. Maekawa, Theory of tunneling magnetoresistance in granular magnetic films. *Phys. Rev. B* **1996**, *53* (18), R11927-R11929.

[16] E.E. Fullerton, J.R. Childress, Spintronics, Magnetoresistive Heads, and the Emergence of the Digital World. *Proc. IEEE* **2016**, *104* (10), 1787-1795.

[17] K.B. Klaassen, X. Xinzhi, J.C.L.v. Peppen, Signal and noise aspects of magnetic tunnel junction sensors for data storage. *IEEE Trans. Magn.* **2004**, *40* (1), 195-202.

[18] K.B. Nandapurkar, A.C. Sreekantan, P.K. Dutta, Performance Investigation of a Simplified TMR-Based Rotary Position Sensing System. *IEEE Trans. Instrum. Meas.* **2021**, *70*, 1-8.

[19] B. Wu, Y.J. Wang, X.C. Liu, C.F. He, A novel TMR-based MFL sensor for steel wire rope inspection using the orthogonal test method. *Smart Mater. Struct.* **2015**, *24* (7), 075007.

[20] J. Fontcuberta, B. Martínez, A. Seffar, S. Piñol, J.L. García-Muñoz, X. Obradors, Colossal Magnetoresistance of Ferromagnetic Manganites: Structural Tuning and Mechanisms. *Phys. Rev. Lett.* **1996**, *76* (7), 1122-1125.

[21] P.G. de Gennes, Effects of Double Exchange in Magnetic Crystals. *Phys. Rev.* **1960**, *118* (1), 141-154.

[22] A.R. Bishop, H. Röder, Theory of colossal magnetoresistance. *Curr. Opin. Solid State Mater. Sci.* **1997**, *2* (2), 244-251.

[23] E.L. Nagaev, Colossal-magnetoresistance materials: manganites and conventional ferromagnetic semiconductors. *Phys. Rep.* **2001**, *346* (6), 387-531.

[24] Z. Qiu, D. Hou, J. Barker, K. Yamamoto, O. Gomonay, E. Saitoh, Spin colossal magnetoresistance in an antiferromagnetic insulator. *Nat. Mater.* **2018**, *17* (7), 577-580.

[25] A.P. Ramirez, Colossal magnetoresistance. *J. Phys.: Condens. Matter* **1997**, *9* (39), 8171-8199.

[26] Y. Tokura, Critical features of colossal magnetoresistive manganites. *Rep. Prog. Phys.* **2006**, *69* (3), 797-851.

[27] J. Sun, J. Kosel, Extraordinary Magnetoresistance in Semiconductor/Metal Hybrids: A Review. *Materials* **2013**, *6* (2), 500-516.

[28] S.A. Solin, T. Thio, D.R. Hines, J.J. Heremans, Enhanced Room-Temperature Geometric Magnetoresistance in Inhomogeneous Narrow-Gap Semiconductors. *Science* **2000**, *289* (5484), 1530-1532.

[29] S.A. Solin, Magnetic field nanosensors. *Sci. Am.* **2004**, *291* (1), 70-77.

[30] E. Demirci, Magnetic and Magnetotransport Properties of Memory Sensors Based on Anisotropic Magnetoresistance. *J. Supercond. Novel Magn.* **2020**, *33* (12), 3835-3840.

[31] P.V. Sreevidya, U.P. Borole, R. Kadam, J. Khan, H.C. Barshilia, P. Chowdhury, A novel AMR based angle sensor with reduced harmonic errors for automotive applications. *Sens. Actuators, A* **2021**, 112573.

[32] Y. Ouyang, Z. Wang, G. Zhao, J. Hu, S. Ji, J. He*, et al.*, Current sensors based on GMR effect for smart grid applications. *Sens. Actuators, A* **2019**, *294*, 8-16.

[33] L. Schnitzspan, J. Cramer, J. Kubik, M. Tarequzzaman, G. Jakob, M. Kläui, Impact of Annealing Temperature on Tunneling Magnetoresistance Multilayer Stacks. *IEEE Magn. Lett.* **2020**, *11*, 1-5.

[34] S. Tumanski, Thin film magnetoresistive sensors, CRC Press, 2001.

[35] A.E. Berkowitz, J.R. Mitchell, M.J. Carey, A.P. Young, S. Zhang, F.E. Spada*, et al.*, Giant magnetoresistance in heterogeneous Cu-Co alloys. *Phys. Rev. Lett.* **1992**, *68* (25), 3745-3748.

[36] J.Q. Xiao, J.S. Jiang, C.L. Chien, Giant magnetoresistance in nonmultilayer magnetic systems. *Phys. Rev. Lett.* **1992**, *68* (25), 3749-3752.

[37] B.H. Zhou, J.D. Rinehart, A Size Threshold for Enhanced Magnetoresistance in Colloidally Prepared $CoFe_2O_4$ Nanoparticle Solids. *ACS Cent. Sci.* **2018**, *4* (9), 1222-1227.

[38] K.S. Novoselov, V.I. Fal′ko, L. Colombo, P.R. Gellert, M.G. Schwab, K. Kim, A roadmap for graphene. *Nature* **2012**, *490* (7419), 192-200.

[39] J.-J. Chen, J. Meng, Y.-B. Zhou, H.-C. Wu, Y.-Q. Bie, Z.-M. Liao*, et al.*, Layer-by-layer assembly of vertically conducting graphene devices. *Nat. Commun.* **2013**, *4* (1), 1921.

[40] R.U.R. Sagar, H.I.A. Qazi, M.H. Zeb, F.J. Stadler, B. Shabbir, X. Wang*, et al.*, Tunable sign of magnetoresistance in graphene foam – Ecoflex® composite for wearable magnetoelectronic devices. *Mater. Lett.* **2019**, *253*, 166-170.

[41] J. Zhu, Z. Luo, S. Wu, N. Haldolaarachchige, D.P. Young, S. Wei*, et al.*, Magnetic graphene nanocomposites: electron conduction, giant magnetoresistance and tunable negative permittivity. *J. Mater. Chem.* **2012**, *22* (3), 835-844.

[42] M. Rein, N. Richter, K. Parvez, X. Feng, H. Sachdev, M. Kläui*, et al.*, Magnetoresistance and Charge Transport in Graphene Governed by Nitrogen Dopants. *ACS Nano* **2015**, *9* (2), 1360-1366.

[43] Y.-B. Zhou, B.-H. Han, Z.-M. Liao, H.-C. Wu, D.-P. Yu, From positive to negative magnetoresistance in graphene with increasing disorder. *Appl. Phys. Lett.* **2011**, *98* (22), 222502.

[44] K. Gopinadhan, Y.J. Shin, R. Jalil, T. Venkatesan, A.K. Geim, A.H.C. Neto*, et al.*, Extremely large magnetoresistance in few-layer graphene/boron–nitride heterostructures. *Nat. Commun.* **2015**, *6* (1), 8337.

[45] P.U. Asshoff, J.L. Sambricio, A.P. Rooney, S. Slizovskiy, A. Mishchenko, A.M. Rakowski*, et al.*, Magnetoresistance of vertical Co-graphene-NiFe junctions controlled by charge transfer and proximity-induced spin splitting in graphene. *2D Mater.* **2017**, *4* (3), 031004.

[46] H. Huang, H. Guan, M. Su, X. Zhang, Y. Liu, C. Liu, *et al.*, Gate-tunable linear magnetoresistance in molybdenum disulfide field-effect transistors with graphene insertion layer. *Nano Res.* **2020**, *14* (7), 1814–1818.

[47] E.D. Cobas, O.M.J. van 't Erve, S.-F. Cheng, J.C. Culbertson, G.G. Jernigan, K. Bussman, *et al.*, Room-Temperature Spin Filtering in Metallic Ferromagnet–Multilayer Graphene–Ferromagnet Junctions. *ACS Nano* **2016**, *10* (11), 10357-10365.

[48] R.U.R. Sagar, N. Mahmood, F.J. Stadler, T. Anwar, S.T. Navale, K. Shehzad, *et al.*, High Capacity Retention Anode Material for Lithium Ion Battery. *Electrochim. Acta* **2016**, *211*, 156-163.

[49] Z. Chen, W. Ren, L. Gao, B. Liu, S. Pei, H.-M. Cheng, Three-dimensional flexible and conductive interconnected graphene networks grown by chemical vapour deposition. *Nat. Mater.* **2011**, *10* (6), 424-428.

[50] Y. Ma, Y. Chen, Three-dimensional graphene networks: synthesis, properties and applications. *Natl. Sci. Rev.* **2015**, *2* (1), 40-53.

[51] E. Krueger, A.N. Chang, D. Brown, J. Eixenberger, R. Brown, S. Rastegar, *et al.*, Graphene Foam as a Three-Dimensional Platform for Myotube Growth. *ACS Biomater. Sci. Eng.* **2016**, *2* (8), 1234-1241.

[52] M.H. Zeb, B. Shabbir, R.U.R. Sagar, N. Mahmood, K. Chen, I. Qasim, *et al.*, Superior Magnetoresistance Performance of Hybrid Graphene Foam/Metal Sulfide Nanocrystal Devices. *ACS Appl. Mater. Interfaces* **2019**, *11* (21), 19397-19403.

[53] R.U.R. Sagar, M. Galluzzi, A. García-Peñas, M.A. Bhat, M. Zhang, F.J. Stadler, Large unsaturated room temperature negative magnetoresistance in graphene foam composite for wearable and flexible magnetoelectronics. *Nano Res.* **2019**, *12* (1), 101-107.

[54] R.U.R. Sagar, M. Galluzzi, C. Wan, K. Shehzad, S.T. Navale, T. Anwar, *et al.*, Large, Linear, and Tunable Positive Magnetoresistance of Mechanically Stable Graphene Foam–Toward High-Performance Magnetic Field Sensors. *ACS Appl. Mater. Interfaces* **2017**, *9* (2), 1891-1898.

[55] C.-Y. Cai, J.-H. Chen, Electronic transport properties of Co cluster-decorated graphene. *Chin. Phys. B* **2018**, *27* (6), 067304.

[56] U. Chandni, E.A. Henriksen, J.P. Eisenstein, Transport in indium-decorated graphene. *Phys. Rev. B* **2015**, *91* (24), 245402.

[57] J.A. Elias, E.A. Henriksen, Electronic transport and scattering times in tungsten-decorated graphene. *Phys. Rev. B* **2017**, *95* (7), 075405.

[58] Z. Jia, R. Zhang, Q. Han, Q. Yan, R. Zhu, D. Yu*, et al.*, Large tunable linear magnetoresistance in gold nanoparticle decorated graphene. *Appl. Phys. Lett.* **2014**, *105* (14), 143103.

[59] Y. Wang, M. Jaiswal, M. Lin, S. Saha, B. Özyilmaz, K.P. Loh, Electronic Properties of Nanodiamond Decorated Graphene. *ACS Nano* **2012**, *6* (2), 1018-1025.

[60] G. Abellán, H. Prima-García, E. Coronado, Graphene enhances the magnetoresistance of FeNi$_3$ nanoparticles in hierarchical FeNi$_3$–graphene nanocomposites. *J. Mater. Chem. C* **2016**, *4* (11), 2252-2258.

[61] C. Majumder, S. Bhattacharya, S.K. Saha, Anomalous large negative magnetoresistance in transition-metal decorated graphene: Evidence for electron-hole puddles. *Phys. Rev. B* **2019**, *99* (4), 045408.

[62] Z. Sheykhifard, S.M. Mohseni, B. Tork, M.R. Hajiali, L. Jamilpanah, B. Rahmati*, et al.*, Magnetic graphene/Ni-nano-crystal hybrid for small field magnetoresistive effect synthesized via electrochemical exfoliation/deposition technique. *J. Mater. Sci.: Mater. Electron.* **2018**, *29* (5), 4171-4178.

[63] R. Weiss, R. Mattheis, G. Reiss, Advanced giant magnetoresistance technology for measurement applications. *Meas. Sci. Technol.* **2013**, *24* (8), 082001.

[64] S.S.P. Parkin, N. More, K.P. Roche, Oscillations in exchange coupling and magnetoresistance in metallic superlattice structures: Co/Ru, Co/Cr, and Fe/Cr. *Phys. Rev. Lett.* **1990**, *64* (19), 2304-2307.

[65] J.F. Gregg, I. Petej, E. Jouguelet, C. Dennis, Spin electronics-a review. *J. Phys. D: Appl. Phys.* **2002**, *35* (18), R121-R155.

[66] S.S.P. Parkin, M. Hayashi, L. Thomas, Magnetic Domain-Wall Racetrack Memory. *Science* **2008**, *320* (5873), 190-194.

[67] U. Ausserlechner, The Optimum Layout for Giant Magneto-Resistive Angle Sensors. *IEEE Sens. J.* **2010**, *10* (10), 1571-1582.

[68] S. Wu, J. Chen, S. Wu, A Rotary Encoder With an Eccentrically Mounted Ring Magnet. *IEEE Trans. Instrum. Meas.* **2014**, *63* (8), 1907-1915.

[69] R. Hahn, T. Schmidt, R. Slatter, B. Olberts, F. Romera, Magnetoresistive angular sensors for space applications: Results of breadboard and EQM testing and lessons learned. *Proc. ESMATS* **2017**, 1-6.

[70] R. Rempt, Scanning with magnetoresistive sensors for subsurface corrosion. *AIP Conf. Proc.* **2002**, *615* (1), 1771-1778.

[71] B. Wincheski, J. Simpson, M. Namkung, D. Perey, E. Scales, R. Louie, Development of Giant Magnetoresistive inspection system for detection of deep fatigue cracks under airframe fasteners. *AIP Conf. Proc.* **2002**, *615* (1), 1007-1014.

[72] R.S. Gaster, D.A. Hall, C.H. Nielsen, S.J. Osterfeld, H. Yu, K.E. Mach*, et al.*, Matrix-insensitive protein assays push the limits of biosensors in medicine. *Nat. Med.* **2009**, *15* (11), 1327-1332.

[73] C. Giebeler, D.J. Adelerhof, A.E.T. Kuiper, J.B.A. van Zon, D. Oelgeschläger, G. Schulz, Robust GMR sensors for angle detection and rotation speed sensing. *Sens. Actuators, A* **2001**, *91* (1), 16-20.

[74] G. Rieger, K. Ludwig, J. Hauch, W. Clemens, GMR sensors for contactless position detection. *Sens. Actuators, A* **2001**, *91* (1), 7-11.

[75] T.M. Hermann, W.C. Black, S. Hui, Magnetically coupled linear isolator. *IEEE Trans. Magn.* **1997**, *33* (5), 4029-4031.

[76] J.C. Rife, M.M. Miller, P.E. Sheehan, C.R. Tamanaha, M. Tondra, L.J. Whitman, Design and performance of GMR sensors for the detection of magnetic microbeads in biosensors. *Sens. Actuators, A* **2003**, *107* (3), 209-218.

[77] D.A. Hall, R.S. Gaster, T. Lin, S.J. Osterfeld, S. Han, B. Murmann*, et al.*, GMR biosensor arrays: A system perspective. *Biosens. Bioelectron.* **2010**, *25* (9), 2051-2057.

[78] M. Pannetier-Lecoeur, L. Parkkonen, N. Sergeeva-Chollet, H. Polovy, C. Fermon, C. Fowley, Magnetocardiography with sensors based on giant magnetoresistance. *Appl. Phys. Lett.* **2011**, *98* (15), 153705.

[79] Y. Shirai, K. Hirao, T. Shibuya, S. Okawa, Y. Hasegawa, Y. Adachi*, et al.*, Magnetocardiography Using a Magnetoresistive Sensor Array. *Int. Heart J.* **2019**, *60* (1), 50-54.

[80] R. Dixon Magnetic Sensors Report. https://cdn.ihs.com/www/pdf/1118/ABSTRACT-Magnetic-Sensors%20Report-2017.pdf (accessed Aug. 27, 2020).

[81] C.H. Smith, R.W. Schneider, T. Dogaru, S.T. Smith, Eddy‑Current Testing with GMR Magnetic Sensor Arrays. *AIP Conf. Proc.* **2004**, *700* (1), 406-413.

[82] H. Ehlers, M. Pelkner, R. Thewes, Heterodyne Eddy Current Testing Using Magnetoresistive Sensors for Additive Manufacturing Purposes. *IEEE Sens. J.* **2020**, *20* (11), 5793-5800.

[83] S.X. Wang, G. Li, Advances in Giant Magnetoresistance Biosensors With Magnetic Nanoparticle Tags: Review and Outlook. *IEEE Trans. Magn.* **2008**, *44* (7), 1687-1702.

[84] C. Ren, Q. Bayin, S. Feng, Y. Fu, X. Ma, J. Guo, Biomarkers detection with magnetoresistance-based sensors. *Biosens. Bioelectron.* **2020**, *165*, 112340.

[85] D.H. Blohm, A. Guiseppi-Elie, New developments in microarray technology. *Curr. Opin. Biotechnol.* **2001**, *12* (1), 41-47.

[86] D. Belpomme, L. Hardell, I. Belyaev, E. Burgio, D.O. Carpenter, Thermal and non-thermal health effects of low intensity non-ionizing radiation: An international perspective. *Environ. Pollut.* **2018**, *242*, 643-658.

[87] S. Engels, N.-L. Schneider, N. Lefeldt, C.M. Hein, M. Zapka, A. Michalik*, et al.*, Anthropogenic electromagnetic noise disrupts magnetic compass orientation in a migratory bird. *Nature* **2014**, *509* (7500), 353-356.

[88] M. Markov, Y. Grigoriev, Protect children from EMF. *Electromagn. Biol. Med.* **2015**, *34* (3), 251-256.

[89] R. Baan, Y. Grosse, B. Lauby-Secretan, F. El Ghissassi, V. Bouvard, L. Benbrahim-Tallaa*, et al.*, Carcinogenicity of radiofrequency electromagnetic fields. *Lancet Oncol.* **2011**, *12* (7), 624-626.

[90] E. van Deventer, E. van Rongen, R. Saunders, WHO research agenda for radiofrequency fields. *Bioelectromagnetics* **2011**, *32* (5), 417-421.

[91] B.B.B. Levitt, H. Lai, Biological effects from exposure to electromagnetic radiation emitted by cell tower base stations and other antenna arrays. *Environ. Rev.* **2010**, *18* (NA), 369-395.

[92] S. Parkin, J. Xin, C. Kaiser, A. Panchula, K. Roche, M. Samant, Magnetically engineered spintronic sensors and memory. *Proc. IEEE* **2003**, *91* (5), 661-680.

[93] J.S. Moodera, L.R. Kinder, T.M. Wong, R. Meservey, Large Magnetoresistance at Room Temperature in Ferromagnetic Thin Film Tunnel Junctions. *Phys. Rev. Lett.* **1995**, *74* (16), 3273-3276.

[94] C. Tsang, M. Chen, T. Yogi, K. Ju, Gigabit density recording using dual-element MR/inductive heads on thin-film disks. *IEEE Trans. Magn.* **1990**, *26* (5), 1689-1693.

[95] D.J. Adelerhof, W. Geven, New position detectors based on AMR sensors. *Sens. Actuators, A* **2000**, *85* (1), 48-53.

[96] G. Su, X. Wu, W. Tong, C. Duan, Two-Dimensional Layered Materials-Based Spintronics. *SPIN* **2015**, *05* (04), 1540011.

[97] M. Kąc, J. Morgiel, A. Polit, Y. Zabila, M. Marszałek, Atomic scale structure investigations of epitaxial Fe/Cr multilayers. *Appl. Surf. Sci.* **2014**, *305*, 154-159.

[98] M. Kąc, A. Polit, A. Dobrowolska, Y. Zabila, M. Krupiński, M. Marszałek, Surfactant influence on interface roughness and magnetoresistance value in Fe/Cr multilayers. *Thin Solid Films* **2013**, *542*, 199-203.

[99] C.-L. Chang, T.-H. Chiou, P.-H. Chen, W.-C. Chen, C.-T. Ho, W.-Y. Wu, Characteristics of TiN/W_2N multilayers prepared using magnetron sputter deposition with dc and pulsed dc powers. *Surf. Coat. Technol.* **2016**, *303*, 25-31.

[100] N. Saoula, S. Djerourou, K. Yahiaoui, K. Henda, R. Kesri, R.M. Erasmus, *et al.*, Study of the deposition of Ti/TiN multilayers by magnetron sputtering. *Surf. Interface Anal.* **2010**, *42* (6‑7), 1176-1179.

[101] E. Schubert, F. Frost, B. Ziberi, G. Wagner, H. Neumann, B. Rauschenbach, Ion beam sputter deposition of soft x-ray Mo∕Si multilayer mirrors. *J. Vac. Sci. Technol., B: Microelectron. Nanometer Struct.--Process., Meas., Phenom.* **2005**, *23* (3), 959-965.

[102] P.-K. Chiu, C.-T. Lee, D. Chiang, W.-H. Cho, C.-N. Hsiao, Y.-Y. Chen, *et al.*, Conductive and transparent multilayer films for low-temperature $TiO_2/Ag/SiO_2$ electrodes by E-beam evaporation with IAD. *Nanoscale Res. Lett.* **2014**, *9* (1), 35.

[103] M. Kąc, J. Żukrowski, M. Toulemonde, R. Kruk, V. Tokman, A. Polit, *et al.*, Swift iodine ion modification of the structural and magnetotransport properties of Fe/Cr systems. *Nucl. Instrum. Methods Phys. Res. B* **2009**, *267* (6), 925-930.

[104] V.S. Luong, Y. Su, C. Lu, J. Jeng, J. Hsu, M. Liao, *et al.*, Planarization, Fabrication, and Characterization of Three-Dimensional Magnetic Field Sensors. *IEEE Trans. Nanotechnol.* **2018**, *17* (1), 11-25.

[105] C.B. Ene, G. Schmitz, R. Kirchheim, A. Hütten, Stability and thermal reaction of GMR NiFe/Cu thin films. *Acta Mater.* **2005**, *53* (12), 3383-3393.

[106] L. Liu, Y. Yang, B. Yang, Non-contact and high-precision displacement measurement based on tunnel magnetoresistance. *Meas. Sci. Technol.* **2020**, *31* (6), 065102.

[107] M. Kac, A. Dobrowolska, A. Polit, J. Żukrowski, M. Marszalek, The influence of the atomic scale interface roughness on the GMR effect in Fe/Cr multilayers. *J. Alloys Compd.* **2020**, *824*, 153877.

[108] Y.P. Zeng, Z.W. Liu, H.Y. Yu, Z.G. Zheng, D.C. Zeng, X.S. Gao, Large positive room temperature magnetoresistance in nanogranular FeCo–Si–N thin films. *Mater. Lett.* **2013**, *110*, 27-30.

[109] Y.P. Zeng, Z.W. Liu, E. Mikmeková, Magnetoresistance effects associated with various electric conduction mechanisms in nanostructured $[C/FeCo]_n$ multilayers. *J. Magn. Magn. Mater.* **2017**, *421*, 39-43.

[110] C. Wang, X. Xiao, Y. Rong, T.Y. Hsu, The effect of substrate temperature on the microstructure and tunnelling magnetoresistance of FeCo–Al_2O_3 nanogranular films. *J. Mater. Sci.* **2006**, *41* (12), 3873-3879.

[111] S.-h. Ge, Z.-z. Zhang, Y.-y. Lu, C.-x. Li, G. Run-jin, Influence of annealing condition on giant magnetoresistance of FeCo–Cu granular films. *Thin Solid Films* **1997**, *311* (1), 33-37.

[112] C. Wang, X. Xiao, Y. Rong, H.Y. Hsu, Nanoparticle morphology in FeCo–SiO_2 granular films with tunneling giant magnetoresistance. *Mater. Sci. Eng., B* **2007**, *141* (3), 126-131.

[113] K.S. Novoselov, A.K. Geim, S.V. Morozov, D. Jiang, Y. Zhang, S.V. Dubonos*, et al.*, Electric Field Effect in Atomically Thin Carbon Films. *Science* **2004**, *306* (5696), 666-669.

[114] H.-C. Wu, A.N. Chaika, M.-C. Hsu, T.-W. Huang, M. Abid, M. Abid*, et al.*, Large positive in-plane magnetoresistance induced by localized states at nanodomain boundaries in graphene. *Nat. Commun.* **2017**, *8* (1), 14453.

[115] B. Song, K. Moon, C. Wong, Recent Developments in Design and Fabrication of Graphene-Based Interdigital Micro-Supercapacitors for Miniaturized Energy Storage Devices. *IEEE Trans. Compon., Packag., Manuf. Technol.* **2016**, *6* (12), 1752-1765.

[116] M.S. Purewal, Y. Zhang, P. Kim, Unusual transport properties in carbon based nanoscaled materials: nanotubes and graphene. *Phys. Status Solidi B* **2006**, *243* (13), 3418-3422.

[117] Y. Liu, I. Yudhistira, M. Yang, E. Laksono, Y.Z. Luo, J. Chen*, et al.*, Phonon-Mediated Colossal Magnetoresistance in Graphene/Black Phosphorus Heterostructures. *Nano Lett.* **2018**, *18* (6), 3377-3383.

[118] A.L. Friedman, J.L. Tedesco, P.M. Campbell, J.C. Culbertson, E. Aifer, F.K. Perkins*, et al.*, Quantum Linear Magnetoresistance in Multilayer Epitaxial Graphene. *Nano Lett.* **2010**, *10* (10), 3962-3965.

[119] R.U. Rehman Sagar, K. Shehzad, A. Ali, F.J. Stadler, Q. Khan, J. Zhao*, et al.*, Defect-induced, temperature-independent, tunable magnetoresistance of partially fluorinated graphene foam. *Carbon* **2019**, *143*, 179-188.

[120] Y. Liu, X. Dong, P. Chen, Biological and chemical sensors based on graphene materials. *Chem. Soc. Rev.* **2012**, *41* (6), 2283-2307.

[121] R. Tarcan, O. Todor-Boer, I. Petrovai, C. Leordean, S. Astilean, I. Botiz, Reduced graphene oxide today. *J. Mater. Chem. C* **2020**, *8* (4), 1198-1224.

[122] S. Repp, E. Harputlu, S. Gurgen, M. Castellano, N. Kremer, N. Pompe*, et al.*, Synergetic effects of Fe^{3+} doped spinel $Li_4Ti_5O_{12}$ nanoparticles on reduced graphene

oxide for high surface electrode hybrid supercapacitors. *Nanoscale* **2018**, *10* (4), 1877-1884.

[123] J.I. Paredes, S. Villar-Rodil, M.J. Fernández-Merino, L. Guardia, A. Martínez-Alonso, J.M.D. Tascón, Environmentally friendly approaches toward the mass production of processable graphene from graphite oxide. *J. Mater. Chem.* **2011**, *21* (2), 298-306.

[124] Z.W. Fan, P. Li, E.Y. Jiang, H.L. Bai, Evolution of magnetoresistance mechanisms in granular Co/C films with different conduction regimes. *J. Phys. D: Appl. Phys.* **2013**, *46* (6), 065002.

[125] Z. Quan, X. Zhang, W. Liu, X. Li, K. Addison, G.A. Gehring*, et al.*, Enhanced Room Temperature Magnetoresistance and Spin Injection from Metallic Cobalt in Co/ZnO and Co/ZnAlO Films. *ACS Appl. Mater. Interfaces* **2013**, *5* (9), 3607-3613.

[126] A. Gerber, A. Milner, B. Groisman, M. Karpovsky, A. Gladkikh, A. Sulpice, Magnetoresistance of granular ferromagnets. *Phys. Rev. B* **1997**, *55* (10), 6446-6452.

[127] L. Liu, Q. Zhan, H. Yang, H. Li, S. Zhang, Y. Liu*, et al.*, Magnetostrictive GMR spin valves with composite FeGa/FeCo free layers. *AIP Adv.* **2016**, *6* (3), 035206.

[128] X.G. Zhang, W.H. Butler, Large magnetoresistance in bcc Co/MgO/Co and FeCo/MgO/FeCo tunnel junctions. *Phys. Rev. B* **2004**, *70* (17), 172407.

[129] S.A. Sharko, A.I. Serokurova, T.I. Zubar, S.V. Trukhanov, D.I. Tishkevich, A.A. Samokhvalov*, et al.*, Multilayer spin-valve CoFeP/Cu nanowires with giant magnetoresistance. *J. Alloys Compd.* **2020**, *846*, 156474.

[130] H.N. Fuke, S. Hashimoto, M. Takagishi, H. Iwasaki, S. Kawasaki, K. Miyake*, et al.*, Magnetoresistance of FeCo Nanocontacts With Current-Perpendicular-to-Plane Spin-Valve Structure. *IEEE Trans. Magn.* **2007**, *43* (6), 2848-2850.

[131] R.S. Sundar, S.C. Deevi, Soft magnetic FeCo alloys: alloy development, processing, and properties. *Int. Mater. Rev.* **2005**, *50* (3), 157-192.

[132] G.S. Chaubey, C. Barcena, N. Poudyal, C. Rong, J. Gao, S. Sun*, et al.*, Synthesis and Stabilization of FeCo Nanoparticles. *J. Am. Chem. Soc.* **2007**, *129* (23), 7214-7215.

[133] P. Gould, Nanomagnetism shows *in vivo* potential. *Nano Today* **2006**, *1* (4), 34-39.

[134] A.A. Abrikosov, Quantum magnetoresistance of layered semimetals. *Phys. Rev. B* **1999**, *60* (6), 4231-4234.

[135] A.A. Abrikosov, Quantum linear magnetoresistance. *EPL* **2000**, *49* (6), 789-793.

Chapter 2

2 Background and Literature Review

2.1 Review of Current Progress on Developing Magnetoresistance Materials/Structures

2.1.1 GMR and TMR Multilayer Systems

The multilayer configuration was adopted in the production of MR sensors since the discovery of giant magnetoresistance (GMR) and tunneling magnetoresistance (TMR). The GMR effect was observed in the Fe/Cr multilayer system, and the TMR effect was discovered in Fe/Ge/Co multilayer system at low temperature (4.2 K) [1-3]. As mentioned previously, these multilayer systems consist of ferromagnetic material layers and non-magnetic material layers (GMR) or insulator layers (TMR). Two different configurations were involved in the fabrication of multilayer systems: current in plane (CIP) and current perpendicular to plane (CPP) (**Figure 2.1**) [4]. In the CIP configuration, the electrodes are placed on the side of the multilayer with the current flowing along with the multilayer system. The current flows perpendicular to the multilayer system in the CPP configuration, which achieves a higher MR value in contrast with the CIP configuration [5, 6]. In multilayer systems, the magnitude of the MR is related to various factors such as layer thickness, number of layer repetitions, layer crystallinity, interface roughness, and band/lattice matching between layers [7].

Accurate control of the layer thickness is crucial for the MR values. Various preparation processes (**Figure 2.2**) have been involved in the construction of multilayer systems including electron beam evaporation, magnetron sputtering, cathodic arc deposition, molecular beam epitaxy (MBE), pulsed laser deposition (PLD), and chemical vapor deposition (CVD) [8-14]. These techniques provide precise control on the layer thickness and layer repetitions. However, most of these techniques required prolonged/complicated

preparation processes and specific equipment/instruments, which leads to increasing economic costs and time costs for production.
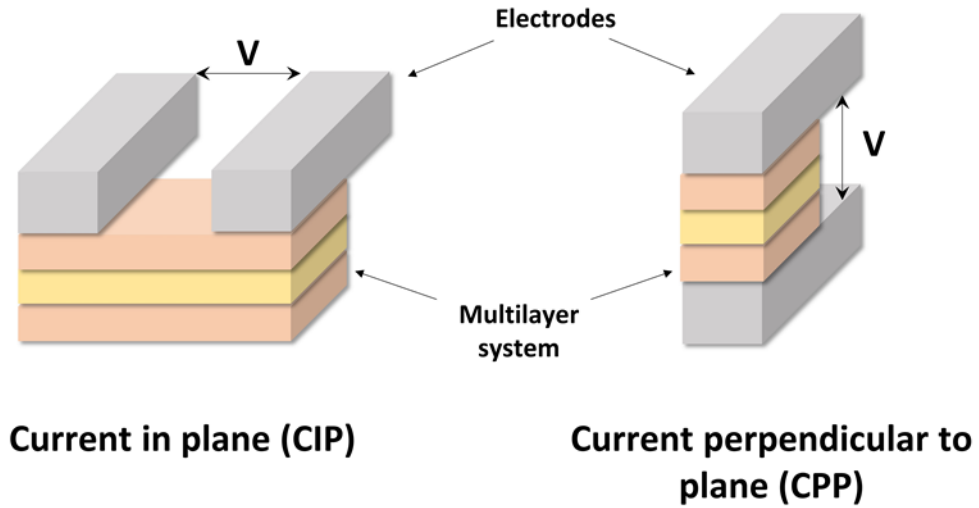
Figure 2.1 Schematic diagram of current in plane (CIP) configuration and current perpendicular to plane (CPP) configuration.
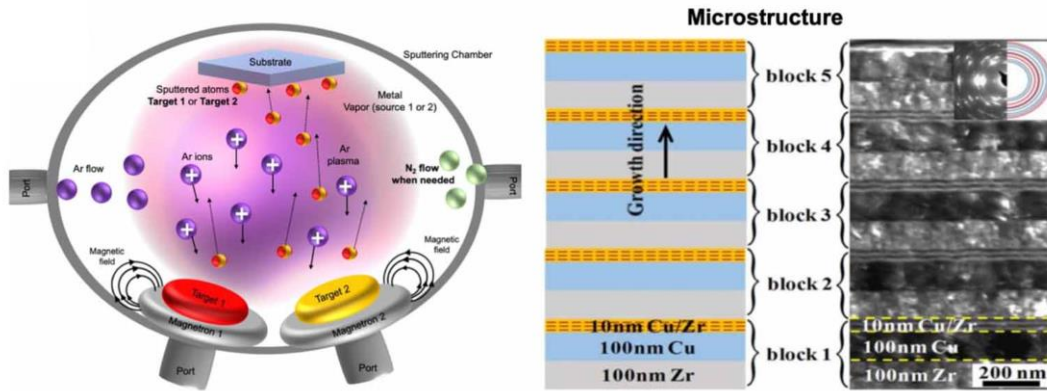
Figure 2.2 Schematic diagram of magnetron sputtering (left) and Cu-based metal multilayer fabricated by magnetron sputtering (right). Reprinted with permission from ref. [15].

Ferromagnetic metals (such as Fe, Co, and Ni) are involved in the fabrication of the ferromagnetic layer in multilayer systems. Meanwhile, non-magnetic layers (Cu, Cr, Ag, Au, Ru, etc.) are applied in the construction of multilayer systems [16]. Alloys such as FeCo (**Figure 2.3**) and FeNi are adopted in the production of both GMR and TMR multilayer systems due to their strong spin-dependent scattering properties [17, 18]. FeCo possesses unique properties such as high saturation magnetization, high Curie temperature, and good strength, which are ideal for constructing multilayer systems [19].
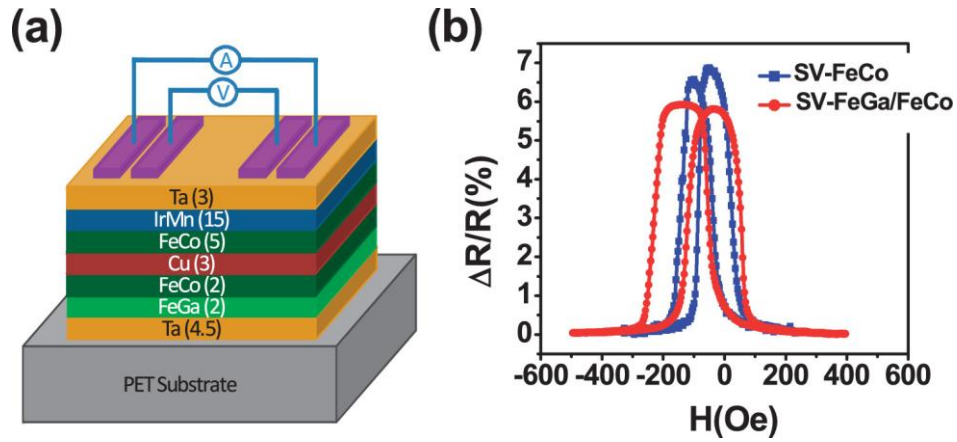
Figure 2.3 (a) Schematic diagram of multilayer system with FeGa/FeCo. (b) MR performance of the multilayer system with FeGa/FeCo. Reprinted with permission from ref. [17].

In engineering applications, the GMR multilayer systems normally consist of ferromagnetic layers with 4 ~ 6 nm thickness and 35 nm non-magnetic conductive spacer layer. The GMR and TMR multilayers exhibit good compatibility for integrating with electronic devices (**Figure 2.4**) [20]. GMR and some TMR multilayer systems display inadequate MR at the low magnetic field and room temperature. In addition, their applications are hindered by the limited working range (especially for TMR multilayer systems, shown in **Figure 2.5**) and complicated fabrication processes, which require further investigation to overcome current challenges [21].
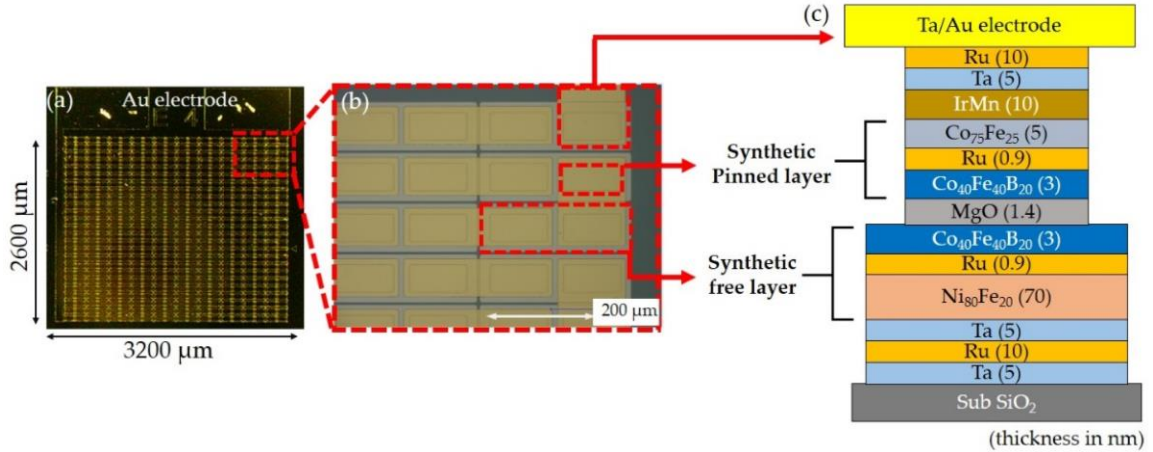
Figure 2.4 (a, b) Microscopy of TMR multilayer system consists of 500 MTJs. (c) Schematic diagram of TMR multilayer system. Reprinted with permission from ref. [21].
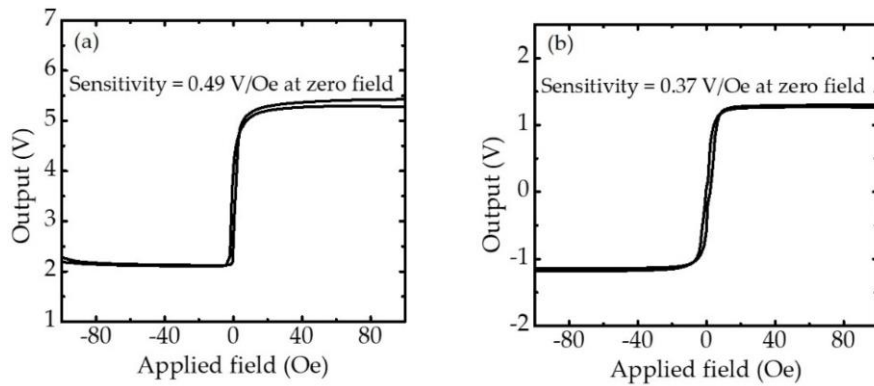
Figure 2.5 Outputs of TMR multilayer sensor array (MTJs) for (a) one and (b) four connected in serial. Reprinted with permission from ref. [21].

2.1.2   Nanoconstructed MR Systems

2.1.2.1   Granular MR Systems

Various methods have been developed to increase the sensitivity of the conventional GMR and TMR multilayer systems. One route is to maximize the layer numbers of the multilayer system. Although it is possible to achieve this architecture *via* the physical/chemical deposition processes mentioned previously, this route significantly increases the complexity and decreases the efficiency of the production process. The

granular MR systems (**Figure 2.6**) are developed to replace the multilayer configuration, which can increase the sensitivity and reduce the potential economic costs and time costs.
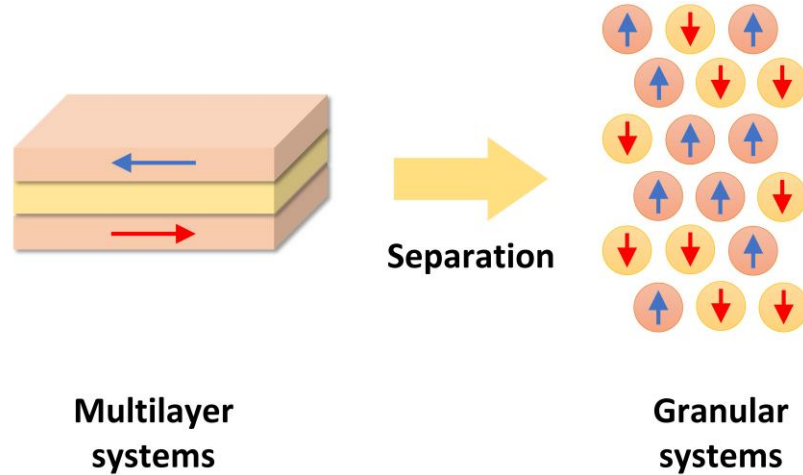
Figure 2.6 Schematic diagram of granular MR systems.

The small grains are pressed together to construct the granular MR system in the first geometry [22]. Another geometry is constructed by embedding the magnetic particles in the non-magnetic matrix (conducting or insulating) [23, 24]. The hypothesis suggests that these geometries can improve the magnitude of the MR since every boundary between the granular particles can become a spin-selecting junction [22]. In contrast with the conventional multilayer systems, granular MR systems reduce the investment in instruments and the complexity of the production process. Granular MR systems suffered from non-uniform distributions and poor grain boundaries in the early stages. Chemically/physically prepared nanoparticles have been applied to construct the granular MR systems since emerging nanotechnology provides uniformly dispersed nanoparticles.

Similar to the multilayer systems, nanoparticles containing Fe and Co are employed in the granular MR systems. Chemically synthesized Fe_3O_4 nanoparticles are adopted in constructing granular MR systems because of their accessibility, stability, and large magnetization. The Fe_3O_4 granular MR systems achieved -1.6% and -1.2% of resistance change at 5 kOe for thin film and pressed powder [25]. Various granular MR systems were developed based on core-shell structures of Fe_3O_4 including $Fe_3O_4@SiO_2$,

Fe$_3$O$_4$@ZnS, Fe$_3$O$_4$@ZrO$_2$ and MgO@Fe$_3$O$_4$ [22, 26-28]. These granular systems achieved a large linear working range (~ 2 T) and relatively large negative MR responses (-4% ~ -8%). However, most of them require low temperatures to obtain satisfactory MR values.

In the meantime, Co is widely applied in constructing granular MR systems. The investigations were performed on Co-Cu, Co-Ag, Co-Ni, and ZnO/ZnO-Co granular MR systems [29-31]. It should be noted that electrodeposition is applied in producing Co-based granular MR systems, which may slightly increase the cost of specific instruments in the preparation. In addition, the chemically synthesized CoFe$_2$O$_4$ nanoparticles (**Figure 2.7**) exhibited a large negative MR (-18% ~ -19%), which was obtained at a high magnetic field (70 kOe) [22].
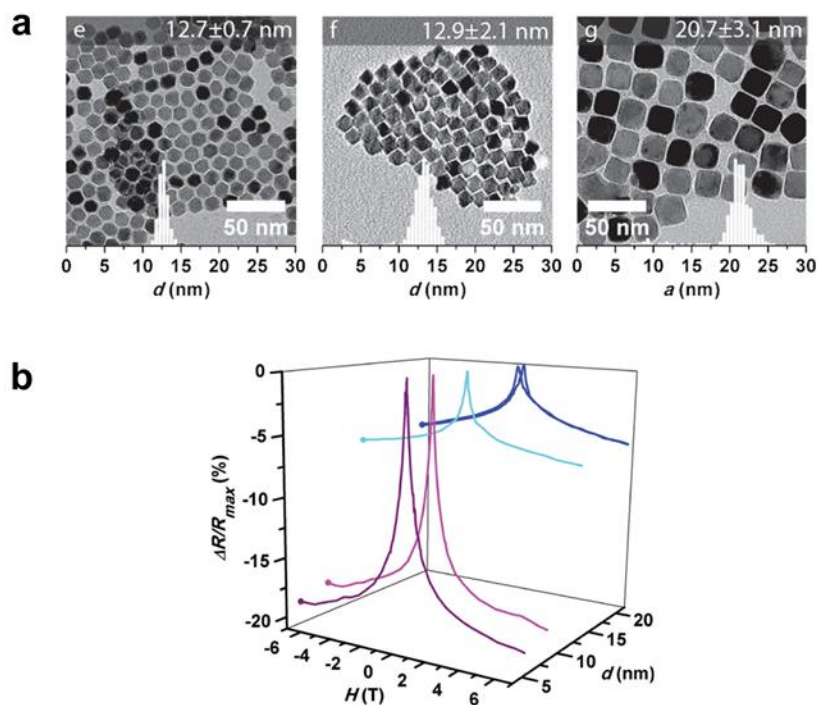
Figure 2.7 (a) TEM micrographs of CoFe$_2$O$_4$ nanoparticles. (b) MR of CoFe$_2$O$_4$ nanoparticles with different diameters. Reprinted with permission from ref. [22] (https://pubs.acs.org/doi/10.1021/acscentsci.8b00399, further permissions related to the material excerpted should be directed to the ACS).

Another geometry of granular MR systems is based on embedding nanoparticles in the non-magnetic matrix (**Figure 2.8**). Fe nanoparticles were deposited on the SiO_2 matrix with the ion beam, which achieved a positive MR at 40% at a large magnetic field (80 kOe) and room temperature [32]. Meanwhile, FeCo exhibits good compatibility with the granular MR system that consists of magnetic nanoparticles and the non-magnetic matrix. FeCo processes high saturation magnetization and strong spin-dependent scattering properties, which are favoured in MR materials [33-35].
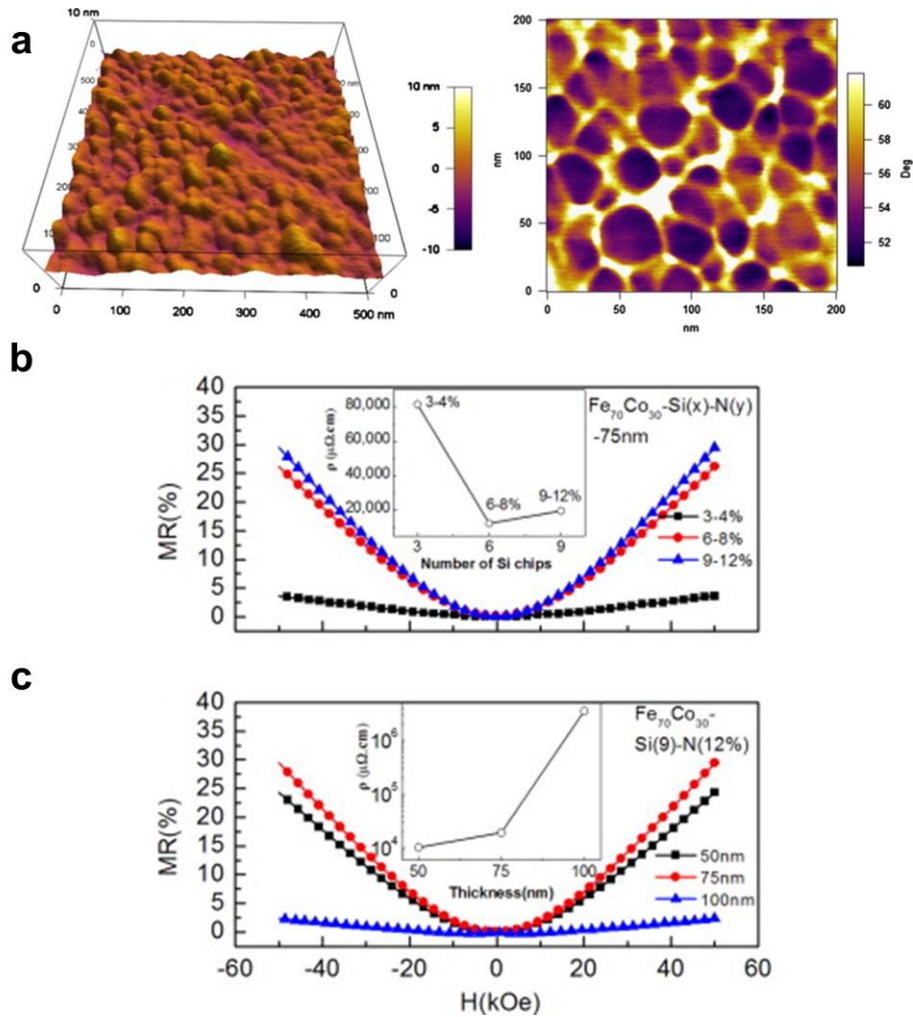
Figure 2.8 (a) 3-D AFM (left) and MFM images (right) of nanogranular FeCo–Si–N film. (b) MR of 75 nm thick FeCo–Si–N films at room temperature (different Si and N ratio). (c) MR of FeCo–Si (9%)–N (12%) with different thicknesses at room temperature. Reprinted with permission from ref. [33].

FeCo granules/particles have been embedded in Si-N, SiO_2, Al_2O_3, Cu, and carbon matrix by magnetron sputtering technique [33, 36-39]. In these studies, FeCo granular systems achieved the MR up to 30% at room temperature (**Figure 2.8**). However, the high magnetic field (50 kOe) is the prerequisite for FeCo granular systems to achieve large MR at ambient temperature. Therefore, although granular MR systems can reduce the cost and complexity in producing MR structures/devices with enhanced sensitivity, the granular systems still display inadequate MR at the low magnetic field ($\leq$ 10 kOe). In some cases, granular MR systems may require special conditions (i.e., low temperatures, large magnetic fields, etc.) to achieve proper performances.

2.1.2.2   Graphene-based MR Systems

2.1.2.2.1   Layered Graphene MR Systems

The discovery of graphene provided a powerful tool for developing MR materials as graphene possesses unique physical and chemical properties [40, 41]. The high electron mobility of graphene is promising for constructing spintronics [42, 43]. Large MR has been observed on MR systems based on monolayer graphene, bilayer graphene, and multilayer graphene (**Figure 2.9**) at room temperature or extremely low temperatures (1.9 K) [41, 44-46]. The results indicate the feasibility to design MR sensors with layered graphene systems, although specific substrates/preparation techniques are required in most circumstances.

Various methods were developed to enhance the MR of layered graphene systems. Normally, two different routes are applied. The first method relies on introducing disorder into the graphene layers. This method employs the monolayer or multilayer graphene produced by mechanical exfoliation or chemical vapor deposition (CVD) [47, 48]. The disorders are introduced by Ga^+ ion irradiation or nitrogen doping [47, 48]. The origin of the MR improvements is attributed to the increasing diffuse scattering at crystallite boundaries after the increase of disorders [47, 48]. Although this process can improve the performance of layered graphene systems, it requires specific substrate and

instrument, which leads to the increase in complexity and investment of the preparation process.
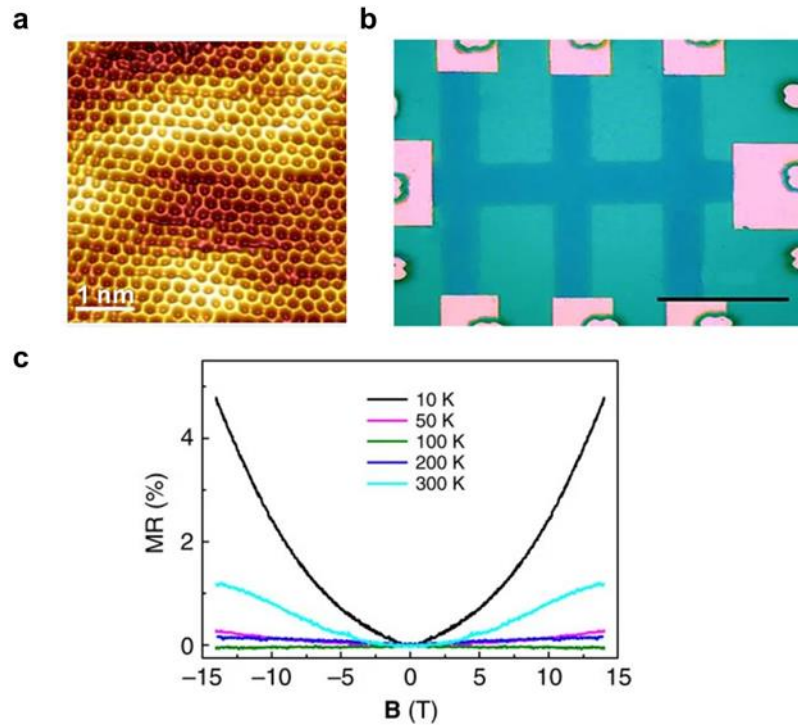
Figure 2.9 (a) STM micrograph showing honeycomb structure of graphene grown on SiC substrate. (b) Picture of graphene MR device (scale bar: 40 μm). (c) MR of the layered graphene-based systems at different temperatures (10 K ~ 300 K). Reprinted with permission from ref. [41].

The second method incorporates graphene layers into the multilayer systems. This method combines graphene layers with the other layered materials including using graphene as the inset layer for the multilayer systems or combining graphene with other two-dimensional materials [49-52]. Although some studies achieved significant improvement of MR performance for layered graphene systems, the issues can't be ignored regarding the requirements on specific instruments for producing mono/multilayer graphene and other layered materials.

The layered graphene system is one of the promising materials for developing future MR devices. However, it is noted that preparing layered graphene systems require specific substrates/circuits and instruments (for precise control of layer number), which increases

the cost and complexity of production processes. This hinders the further applications of layered graphene MR systems. Extreme conditions are required to achieve proper MR performances (such as low temperatures). Although various methods were developed to improve the performance of layered graphene systems at room temperature, these methods still rely on specific instruments, which result in prolong processes and low cost-efficiency. Moreover, some layered graphene systems display relatively small MR at the low magnetic field ($\leq$ 10 kOe), and higher magnetic fields are required to obtain large MR values in most circumstances.

2.1.2.2.2 Graphene Foam MR Systems

Graphene foam (GF) attracts the interest of researchers as it provides a solution to transfer two-dimensional material into a three-dimensional architecture. The advantages of graphene foams include biocompatibility, the combination of intrinsic properties of graphene, pore size adjustability, three-dimensional morphology, and potential for mass production [53-56]. Currently, graphene foams have been applied in designing gas sensors, lithium-ion batteries, and supercapacitors [53, 57, 58]. In addition, graphene foam can also be applied in the production of shapable electronic devices, although it suffers from the problems such as non-flexible structure and unstable mechanical strength.

Recently, researchers discovered interesting magneto-transport properties of graphene foams since three-dimensional graphene foams exhibit different morphology in contrast with two-dimensional graphene [59]. The magneto-transport properties are related to the size of graphene sheets, connections between graphene sheets, the edge boundaries of graphene sheets, and the layer number of graphene sheets in the graphene foams [60-64]. The trajectories of charge carriers are affected by the morphology of graphene in graphene foams under the presence of external magnetic fields [59]. Graphene foams produced by CVD exhibited large MR (80% ~ 90%) at the high magnetic field (> 50 kOe) and room temperature (**Figure 2.10**) [59, 65, 66].
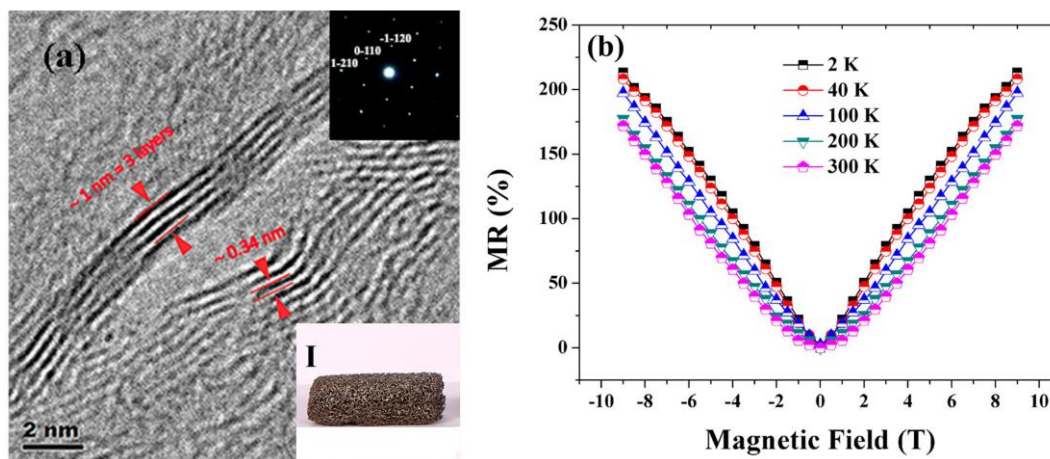
Figure 2.10 (a) HRTEM and SAED of graphene foam (prepared by CVD, inset: picture of as-prepared graphene foam). (b) MR of graphene foam at different temperatures. Reprinted with permission from ref. [59]. Copyright (2017) American Chemical Society.

The disorder and inhomogeneity are considered as the crucial factors for MR in graphene foams [65]. Two major routes are applied to further improve the performance of graphene foam MR systems. The first route is to introduce disorder to graphene foam. On the other hand, the second route is to incorporate other nanostructures/nanomaterials with graphene foam. Graphene foams were combined with polydimethylsiloxane (PDMS), poly(methyl methacrylate) (PMMA), and Cu_2ZnSnS_4 nanocrystals to enhance the MR performances or achieve tunable MR (**Figure 2.11**) [59, 66, 67]. In another approach, the inductively coupled plasma system was applied to perform the fluorination of graphene foams for introducing disorders [68].

Currently, graphene foams have exhibited potentials in developing future MR devices. However, graphene foams require complicated preparation processes that rely on specific equipment for producing graphene foams and introducing disorders. Meanwhile, graphene foams display inadequate MR at low magnetic fields ($\leq$ 10 kOe), and most of the results indicate that graphene foams exhibit large MR at the high magnetic field ($\geq$ 50 kOe). In addition, extreme temperatures (~ 5 K) are required in some circumstances to obtain satisfactory MR values for graphene foams. Therefore, further investigations could focus on enhancing the MR performance and reducing the complexity of production

processes. This would undoubtedly boost the applications of graphene foams for producing future MR devices/sensors.
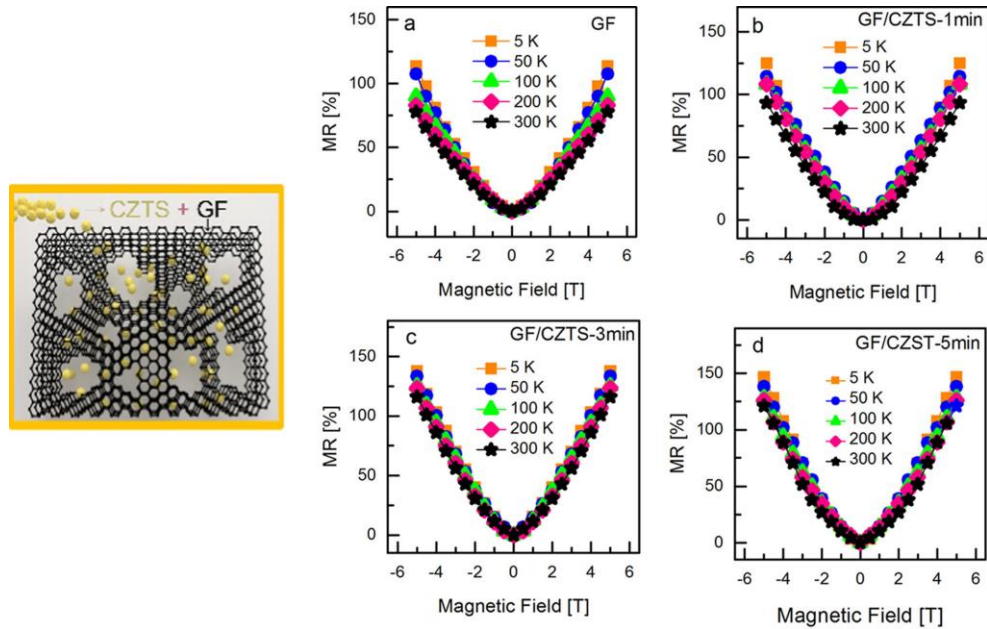
Figure 2.11 The schematic diagram of graphene foam combining with Cu₂ZnSnS₄ nanocrystals (left). The MR of (a) CVD prepared graphene foam and (b-d) Cu₂ZnSnS₄ nanocrystals modified graphene foams at different temperatures. Reprinted with permission from ref. [67]. Copyright (2019) American Chemical Society.

2.1.2.2.3   Hybrid Graphene Nanocomposites MR Systems

Graphene offers unique features such as high carrier mobility, high thermal conductivity, and a large surface-to-volume ratio [69]. The large surface area of graphene allows modifications for different applications (such as polymers, biomolecules, and nanoparticles) [70-72]. The nanoparticles modified graphene has been extensively investigated for various applications including biological medicine, biosensing, gas sensing, catalysis, microwave absorption, and energy storage. [73-78] Hybrid graphene nanocomposites provide outstanding outputs and promising properties in these areas. Therefore, it is possible to applied heterostructures based on hybrid graphene nanocomposites in the fabrication of MR devices.

Two different routes are adopted to achieve large MR values for hybrid graphene nanocomposites. In the first route, nanoparticles/adatoms clusters are decorated on the surface of CVD/mechanical exfoliation prepared graphene layers by thermal evaporation or electron beam deposition [79-83]. Both positive and negative MR were obtained in this route. Some studies suggested that relatively large MR could be achieved at low magnetic fields (-9% at ~ 7 kOe). However, this negative MR was reached at an extremely low temperature (10 K), and the MR deteriorated significantly to -3% as the temperature slightly increased to 50 K (**Figure 2.12**). Moreover, the physical deposition processes need specific preparation techniques. Specific substrates are required by CVD/mechanical exfoliation-produced graphene. These drawbacks increase the time and equipment investments of the production process, which hinders the possible applications in the future.
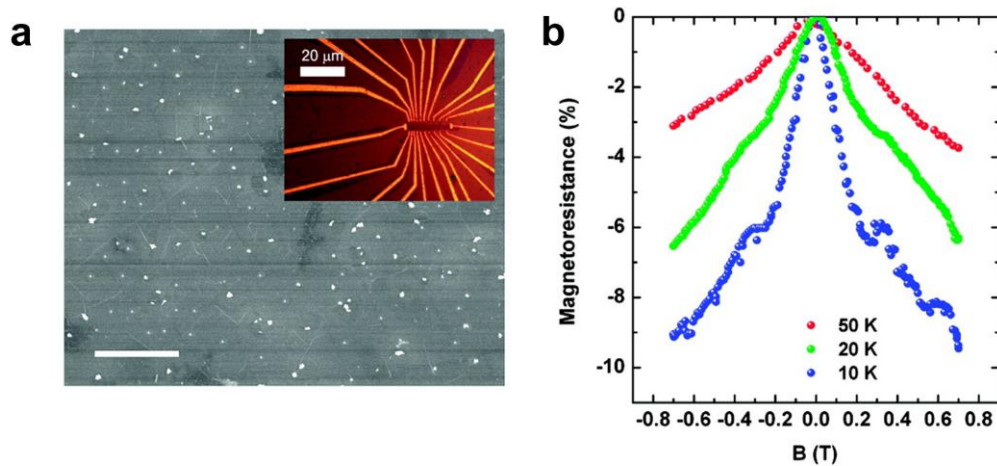
Figure 2.12 (a) SEM micrograph of graphene/nanodiamond film (scale bar: 1 μm, inset: as-prepared graphene/nanodiamond device). (b) MR of graphene/nanodiamond device at different temperatures. Reprinted with permission from ref. [83]. Copyright (2019) American Chemical Society.

Reduced graphene oxide (rGO) was employed by another route to decrease the equipment/time investments. rGO is facile to produce, and it is favourable for mass production [84]. Meanwhile, rGO is an appropriate substrate for nanoparticles due to the large surface area and functional groups on its surface. Therefore, it is possible to modify nanoparticles on the surface of rGO for developing MR materials. The rGO hybrid

nanocomposites can significantly decrease the requirements on specific instruments in the preparation process and reduce the complexity of the production process, which is promising for the mass production of future MR devices. Relatively large MR can be achieved by rGO hybrid nanocomposites (**Figure 2.13**) [85-88]. However, few attempts were made to develop ideal MR devices based on rGO hybrid nanocomposites. Currently, rGO hybrid nanocomposites display inadequate MR at the low magnetic field (≤ 10 kOe) and room temperature, which is not suitable for future applications.
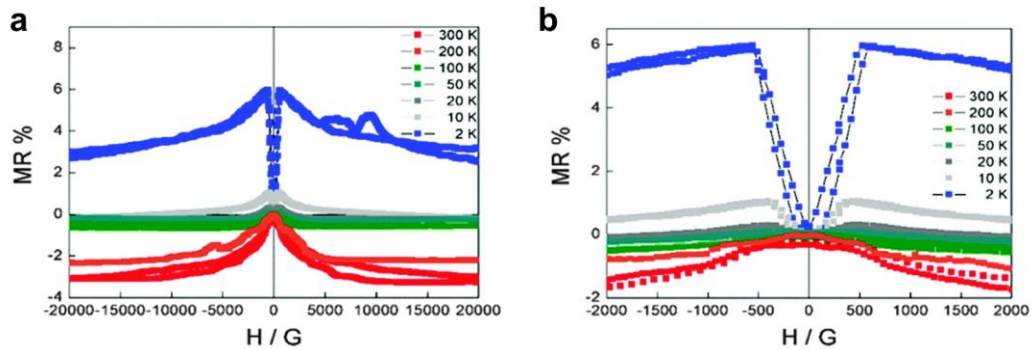
Figure 2.13 (a) MR of FeNi₃/graphene hybrid nanocomposites at different temperatures. (b) Zoom-in view of low magnetic fields (≤ 20 kOe). Reproduced from ref. [85] with permission from The Royal Society of Chemistry.

2.2 Review of Current Applications of Magnetoresistance Sensors

2.2.1 MR Sensors in Magnetic Storage

The anisotropic magnetoresistance (AMR) sensor was utilized as the reading head in hard disk drives (HDDs) by IBM since the 1990s [89]. Later, the reading heads were designed on GMR and TMR sensors, which led to the rapid development of the HDDs' storage capacity. The first HDD, IBM 350, can store 4.4 MB of data with 2 kb/in^2 areal density [90]. In contrast with IBM 350, current HDDs can be 2×10^6 higher in data storage (10 TB) with the areal density reaching 1 Tb/in^2. Meanwhile, the average retail price of HDDs has decreased dramatically as a result of the huge advance in the areal density of

data [89]. The cost of storing digital data is close to 10^6 per GB in IBM 350, and it is $0.01 per GB for modern HDDs (**Figure 2.14**).
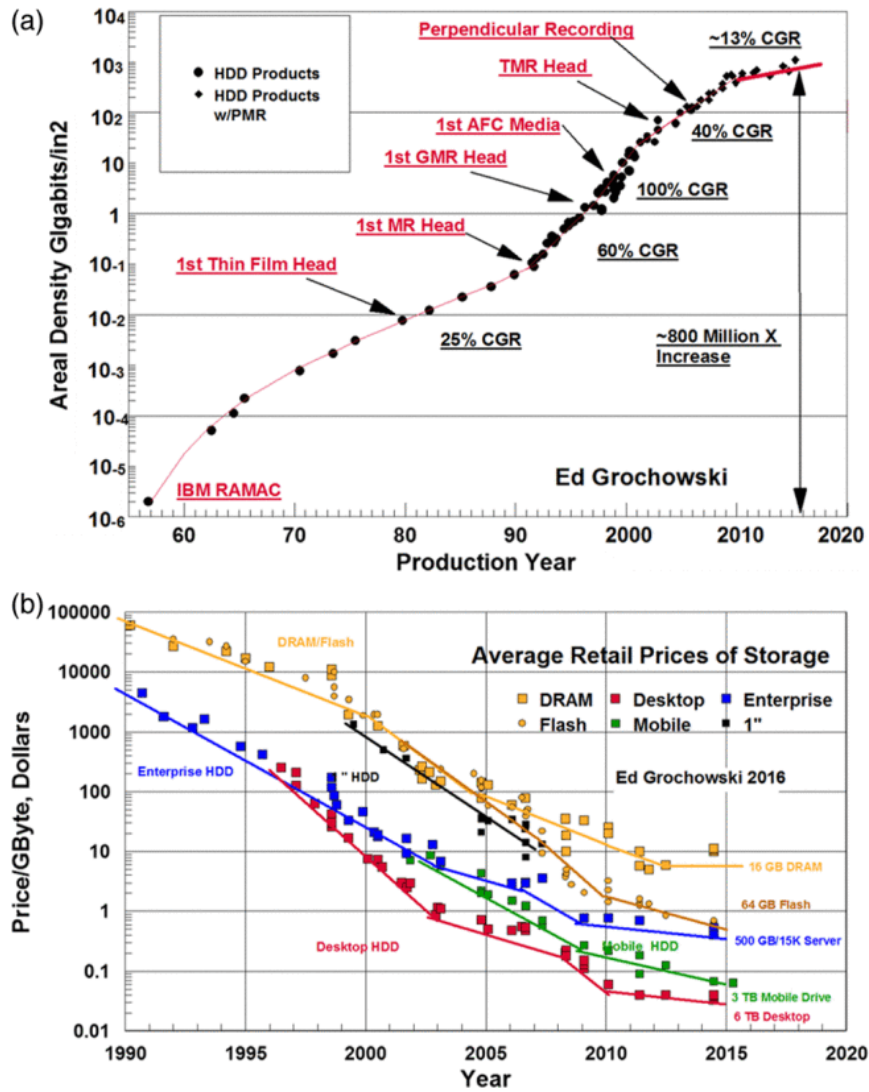
Figure 2.14 (a) Areal density of HDDs vs. year with the corresponding compound growth rate (CGR) of the areal density. (b) Average retail price of digital data storage per GB of storage vs. year. Reprinted with permission from ref. [89]. © [2016] IEEE.

The emergence of the MR sensor has introduced the AMR reading head, GMR reading head, and TMR reading head in 1991, 1997, and 2006, respectively [91-93]. **Figure 2.14** displays the compound growth rate (CGR) of HDDs' storage densities. A significant improvement of CGR (from 25% per year to 60% per year) occurred in 1991 as IBM

47

introduced the MR reading head in HDDs. The CGR was further improved to 100% after introducing the GMR reading head. Although the AMR reading head significantly boosts the development of the HDDs, further applications are hindered by the low MR performance and difficulties in reducing the size. Therefore, GMR and TMR sensors have become the mainstream MR reading heads applied in HDDs.

As shown in **Figure 2.15**, the read-write head of HDD consists of a traditional coil-structure writing head and a GMR or TMR reading head. The traditional coil structure writing head is used to adjust the magnetization of data bits. In the meantime, The MR reading head is applied to detect the magnetic field of data bits. The variation of magnetic fields can influence the resistance of the MR reading head. The signals of resistance change will be collected by electronic devices.
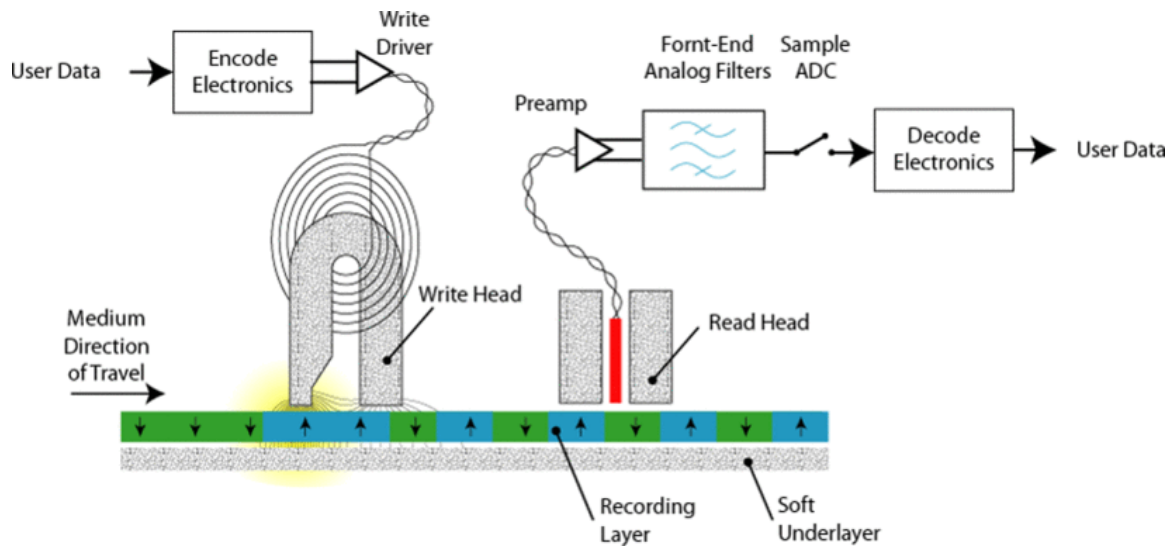
Figure 2.15 Schematic diagram of the modern read-write head for HDDs. The data bits are displayed in the recording layer. Reprinted with permission from ref. [89]. © [2016] IEEE.

GMR reading heads are considered as the starting point of the era of modern spintronics, which increase the MR responses and decrease the device dimensions [4]. The TMR effect exhibits a large MR within a small range of the magnetic field, which is appropriate for sensing the data bits since the outputs are "0" and "1". It is challenging to

further decrease the size of TMR reading heads due to the obstacles for reducing the thickness of the insulator layer. Studies are performed to seek MR materials that can replace the current TMR sensors [93].

Another important application is magnetic random access memory (MRAM). MRAM requires less static power consumption since the data can be stored by magnetization [94, 95]. Random access memory (RAM) is an important component of modern electronic devices. Nowadays, electronic devices mainly employ dynamic random access memory (DRAM) in production, which bases on semiconductor technologies. The key feature of DRAM is volatile property. DRAM may lose all the data after power-off as it is constructed on the circuits with capacitors. Currently, the semiconductor-based DRAMs are facing difficulties to keep the significant growth rate for the storage capacity due to the increased power consumption, which is triggered by the charge leakage problem in reducing the dimension of DRAMs. Therefore, non-volatile memories attract the interest of researchers due to their low power consumption.

MRAM is one of the candidates with features including non-volatility, unlimited read and writes cycles, and high-speed operation [96]. Magnetic tunnel junction (MTJ) is the major component for data storage in MRAMs. As shown in **Figure 2.16**, the MTJ displays low resistance under the parallel magnetization directions of the fixed layer and the free layer. It exports a high resistance output at the anti-parallel state. The data stability of MRAMs is not influenced by the measurement and power cut-off in contrast with DRAMs. Although MRAMs exhibit better scalability and relatively low writing current compared with other RAMs, the reliability issues of MRAMs can't be ignored, which can be caused by oxide barrier breakdown and barrier thickness variability [97]. Therefore, further investigations are required for MRAMs to meet the demands of ideal RAM in the future [98].
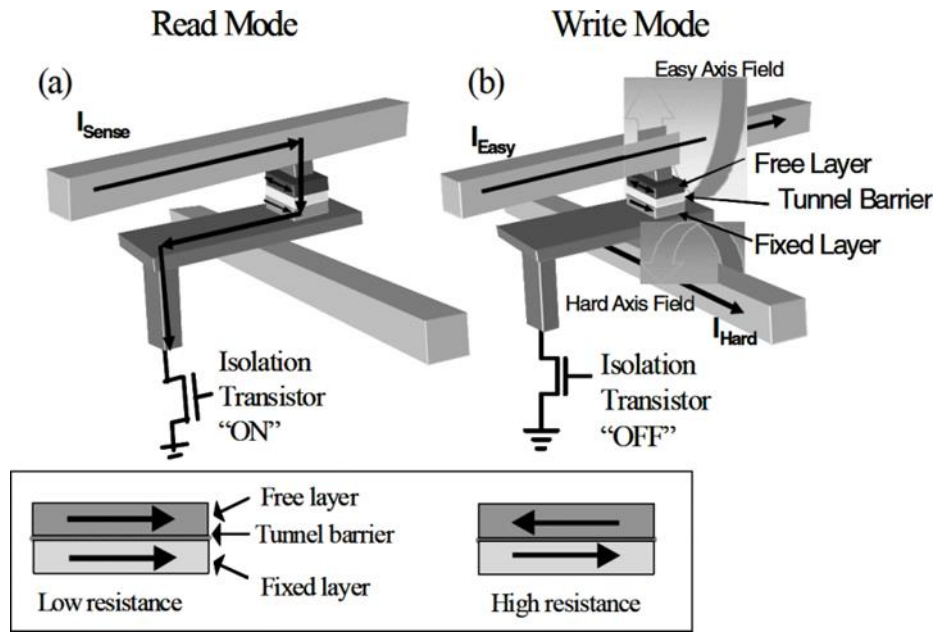
Figure 2.16 Schematic diagram of field-switched MRAM cell during (a) read and (b) write operations (Inset: magnetization of the TMR multilayer system). Reprinted with permission from ref. [96]. © [2006] IEEE.

2.2.2 MR Sensors in Position Sensing, Current Sensing, and Non-destructive Monitoring

Magnetic sensors (including MR sensors) have been widely applied in position sensing, current sensing, and non-destructive monitoring [99-101]. In these applications, magnetic sensors are applied to detect the magnetic fields generated by the targets. The magnetic signals are subsequently transferred to other outputs (such as voltage changes, current changes, and resistance changes). Magnetic displacement sensors have been broadly applied in position sensing. Magnetic sensors are cost-effective, stable, and contact-free compared with other sensors in this field [102, 103]. Magnetic field sensors are crucial parts of magnetic position sensing systems. In position sensing, two major categories of magnetic sensors are Hall effect sensors and MR sensors [104-106]. MR sensors are more suitable for position sensing because of the high sensitivity, low power consumption, and larger detection range in contrast with traditional Hall effect sensors.

TMR multilayer systems have been applied in producing commercial position sensing devices by Multidimension Technology Co., Ltd and NVE Corporation [107, 108]. The exported sine/cosine signals are transferred to position information in this sensing process. Meanwhile, a newly designed position sensing system embedded TMR magnetic field sensors into the permanent magnet linear synchronous motor (PMLSM). The position sensing was finished by the detection of permanent magnets in the PMLSM systems [100].

Sensor arrays are designed and constructed with GMR/TMR multilayer system (**Figure 2.17**) to achieve the two-dimensional and three-dimensional detections [109, 110]. The close-packed MR sensor array was built to dynamically detect magnetic microparticles with high precision. This sensor array can detect the magnetic field in the range of ± 500 Oe due to the limitation on the detection range of TMR. Despite the limited working range, it still set a good example to detect travelling particles with the MR sensor array. Another route integrates multiple GMR/TMR sensors with specifically designed circuits. The output signals are analyzed with computer-based driving/detection systems to obtain the magnetic field components at x-, y-, and z-axis.
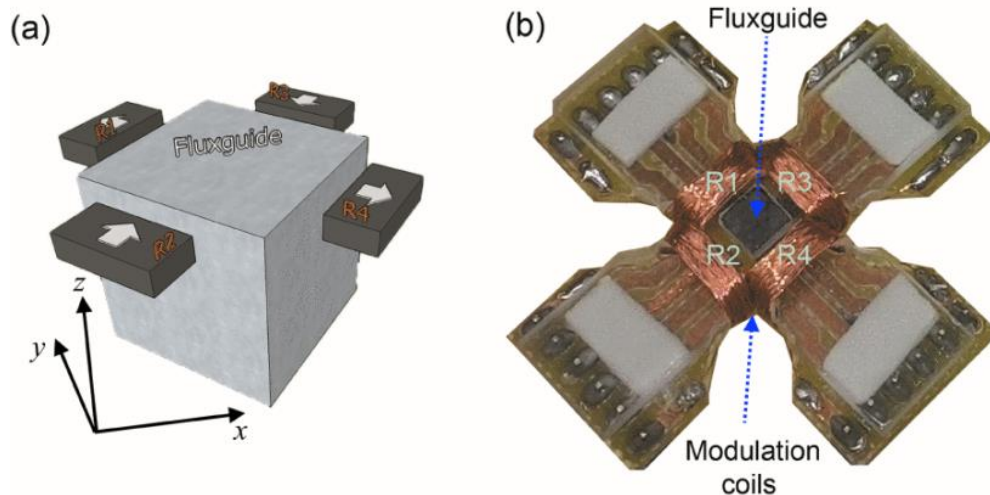
Figure 2.17 (a) Schematic diagram of the design of the three-dimensional field sensor based on GMR multilayer system. (b) Picture of the three-dimensional field sensor based on GMR multilayer system. Reprinted with permission from ref. [110] © [2015] IEEE.

The detection target is the magnetic field generated by the electrical current in (electrical) current sensing and non-destructive monitoring. GMR/TMR sensors are applied in constructing magnetic electrical current sensing systems. The MR current sensing system is employed in differentiating currents, switching regulators, wattmeters, independent voltage/current measurement, and voltage/current measurement multiplying. Meanwhile, MR sensors are adopted in current sensing devices for integrated circuits (IC) monitoring (such as miliwattmeters and electrical isolators) [60]. The smart grid is another important field for MR sensors in electrical current sensing. Special designed MR sensors are applied since various types of currents need to be measured in the smart grid [111].

Non-destructive monitoring (or non-destructive testing) is a crucial tool to inspect the defects in metallic materials. Non-destructive monitoring is applied in large metallic structures such as storage tanks and pipes for oil and gas delivery (in the petroleum industry) [112]. Two different sensing routes are adopted for non-destructive monitoring with magnetic field sensors: magnetic flux leakage testing and eddy current testing. The first route utilizes the breaks of magnetic field lines caused by the surface breaking [113]. Eddy current testing is a more commonly applied testing route for probes equipped with MR sensors (**Figure 2.18**) [114]. Eddy current is introduced by the external magnetic field source. The inspection is performed to detect both surface and subsurface defects. Compared with the conventional probes, the GMR and TMR sensors exhibit significant increases in efficiency during the inspection of eddy currents due to improvements in the sensitivity of the probe. The accuracy can be increased to 98.2% and 99.4% for reading excitation magnetic fields in the detection of subsurface defects (DC excitation and AC excitation). Therefore, MR sensors are promising for the eddy current testing, and they can certainly benefit the future industrial applications of non-destructive monitoring.
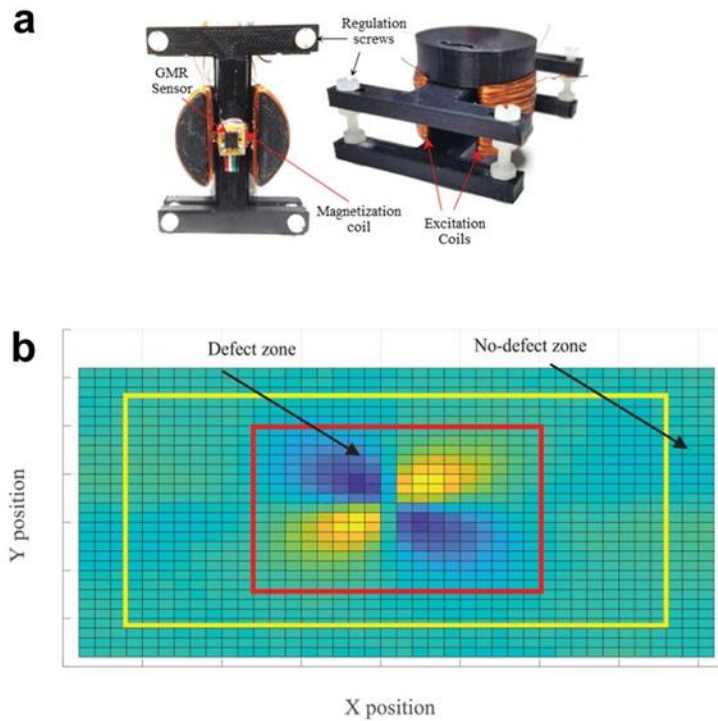
Figure 2.18 (a) Picture of eddy current probe with GMR sensor. (b) Typical color map response of the non-destructive monitoring. Reprinted with permission from ref.[114]. © [2019] IEEE.

2.2.3 MR Sensors in Biomedical Sensing Systems

The development of biomedical sensing platforms has been boosted in the past decade thanks to nanobiotechnology. The MR sensor-based biomedical sensing platforms have attracted the interest of researchers since they are sensitive, compact, user-friendly, and cost-effective. MR biosensors experience low background noise in contrast to other biosensors (optical, plasmonic, and electrochemical) since most of the biological environments are nonmagnetic. Therefore, the target's medium triggers limited negative effects, which leads to the reliable and high-precision detection of magnetic labels [115].

In the typical sensing process, the functionalized magnetic nanoparticles (MNPs) are adopted as the magnetic labels (**Figure 2.19**). The sensing process is performed by detecting the stray magnetic fields of MNPs with MR sensors. Variations of the magnetic field's intensity are related to quantity differences of MNPs. Magnetic signals are

transferred to other processable signals such as resistance change or current change [116]. Compared with other nanomaterials, the advantages of MNPs include high stability, less operating difficulty, and a high signal-to-noise ratio.

The capture probes are firstly immobilized on the surface of MR sensors [117]. The analytes attached with MNPs can be grubbed by capture probes on the surface of MR sensors for sequential magnetic field sensing [118]. The MR sensor-based biological sensing platforms have attracted the interest of researchers since the first GMR biosensor array was developed in 1998 [119]. Currently, MR biosensors are applied in three major categories of biomedical applications: biomedical diagnosis, food safety, and environmental monitoring [120-122].
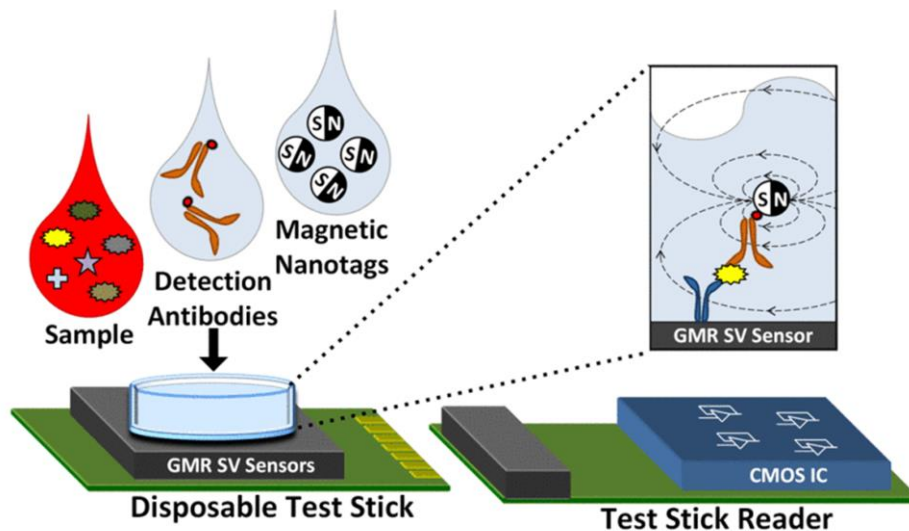
Figure 2.19 Schematic diagram of the sensing process of the MR biosensing platform. Reprinted with permission from ref. [117]. © [2013] IEEE.

MR sensors-based biomedical sensing platforms are suitable for diagnosis applications. The precise and robust diagnosis technique is decisive for treating patients and restricting the spread of the diseases [123]. Various proof-of-concept MR biosensors were designed for diagnosis even in the early stages of MR devices' development [124, 125]. GMR and TMR sensors were applied in the direct detection of proteins and antigens such as endoglin, pregnancy-associated plasma protein-A (PAPP-A), proprotein convertase

subtilisin/kexin type 9 (PCSK9), and suppression of tumorigenicity 2 (ST2) [126, 127]. In these biosensing platforms, the nano-sized MR sensors were applied for real-time monitoring and quantitative detection of the targets in the human serum, which were used to construct the array of GMR sensors. The limit of detection (LOD) reached 40 pg/mL in this process.

Other important topics of biosensing include early detection and diagnosis of cancers and the monitoring of tumors for therapeutic goals. These applications demand enhanced sensitivity and specificity for cancer diagnosis. The GMR biosensing platforms successfully detected cancer antigens including interleukin 6 (IL6), human epididymis protein 4 (HE4), and cancer antigen 125 (CA125 II). GMR biosensors achieved the LODs at the level of 7.4 pg/mL, 3.7 U/mL, and 7.4 pg/mL in these applications [128]. Meanwhile, the GMR biosensing platform was combined with microfluidics for simultaneous detection of 12 tumor markers including human chorionic gonadotropin (free β-hCG) and alpha-fetoprotein (AFP) [129]. This system achieved multi-analyte detection with the LOD at ng/mL level, which can significantly reduce the complexity of the conventional test process.

Currently, demands have been raised regarding the fast and accurate detection of viruses and antibodies due to the global pandemic of COVID-19 [116]. The world health organization (WHO) estimated that up to 82% of COVID-19 patients developed very mild symptoms. A robust approach is crucial for the early detection of virus/antibody to control this global pandemic [130, 131]. The MR biosensing platform is considered to be a potential solution since MR biosensors exhibited high accuracy and high stability in the detection of viruses and antibodies of other diseases.

MR biosensing platforms successfully detected influenza viruses including H1N1 and H3N2v in solution and nasal swab [132, 133]. A portable device was developed to meet the requirements of point-of-care (POC) applications (**Figure 2.20**). The LODs for H1N1 and H3N2v are both 250 $TCID_{50}$/mL. Meanwhile, the MR immunoassay achieved LODs at the level of 10 ng/mL and 50 ng/mL for detection of human immunoglobulins G and M

(IgG and IgM) [134]. MR biosensors were also applied in detecting hepatitis B virus (HBV), hepatitis E virus (HEV), and human immunodeficiency virus (HIV) [135-137].
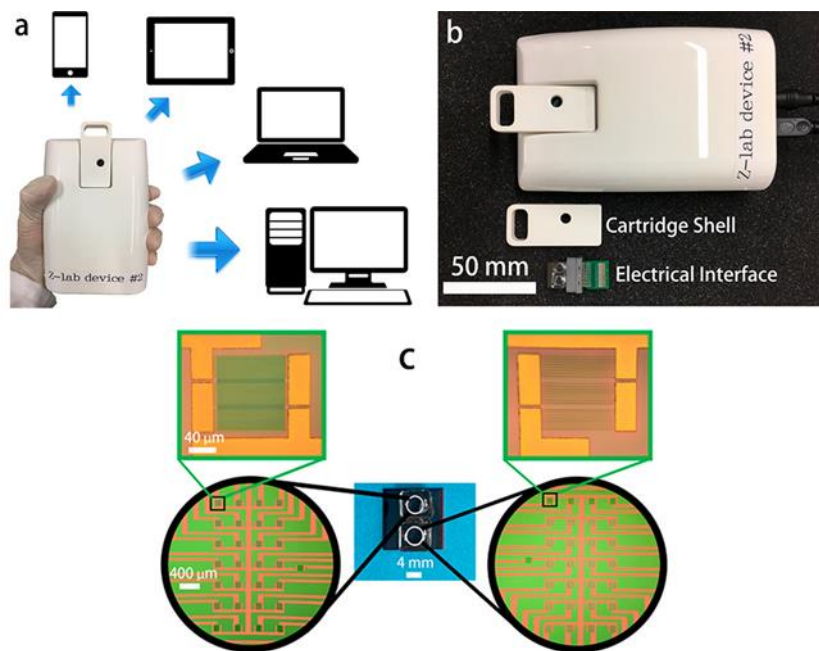
Figure 2.20 (a) Schematic diagram real-time data collection and data transmission of the portable biosensing platform based on MR sensors for the detection of influenza viruses. (b) Picture of the portable devices. (c) Picture of the GMR sensor array. Reprinted with permission from ref. [133]. Copyright (2017) American Chemical Society.

The detection of bacteria is another important topic due to the serious consequences of bacterial infections. For example, *Escherichia coli (E. coli)* can trigger diseases such as urinary tract infection (UTI). In the meantime, food safety is another application that requires the detection of bacteria. The pathogenic bacteria in food have become one of the major health and public concerns nowadays. The detection of bacteria with MR biosensors follows a similar mechanism with the previously discussed MR biosensing platforms. The TMR sensor array has been applied in the detection of *E. coli* O157:H7 with a LOD at 10^2 CFU/mL [138]. Meanwhile, microfluidics was employed in the GMR biosensing platform for *E.coli* detection (**Figure 2.21**) [139]. Moreover, the GMR

biosensing platform accomplished the detection of the *Salmonella*'s (another food pathogen) DNA [140].
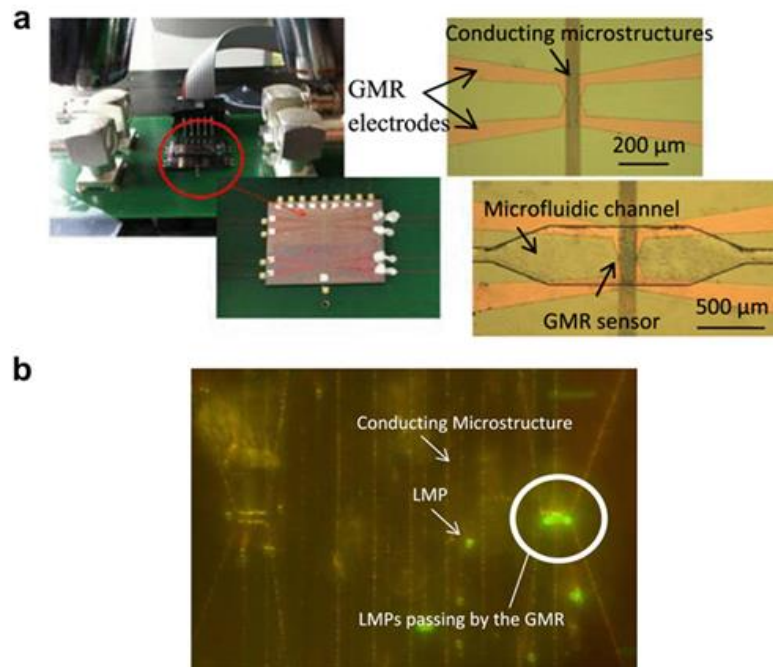
Figure 2.21 (a) Pictures of the MR biosensing platform for *E.coli* detection (b) The *E.coli* inside the detection microchannel bind with the MNPs (captured by fluorescent microscope.) Reprinted with permission from ref. [139]. © [2014] IEEE.

In the meantime, the detections of mycotoxins and allergens are important for food safety. The GMR sensor array was applied in the detection of various mycotoxins such as aflatoxins B1 and zearalenone with a LOD at 50 pg/ml. This array achieved simultaneous detection for various mycotoxins [141]. MR biosensing platforms are capable of detecting major peanut allergens ara h1, ara h2, and gliadin, which can trigger a serious response. The LODs of these allergens can reach 7.0 ng/mL, 0.2 ng/mL, and 1.5 ng/mL [142]. Although MR biosensing platforms exhibit low LODs, the 96 well ELISAs still display a higher sensitivity in terms of the allergens testing. Further studies are required in this area to improve the sensitivity [123].

Environmental monitoring is another major application of MR sensor-based biosensing platforms. This application analyzes the hazardous contents and pollutants in the environment as they can accumulate in the human body through the food chain. The

GMR biosensing platform was modified with thymine-thymine (TT) molecules, which achieved precise detection of mercury ions (Hg^{2+}) in the natural environment [143]. The LOD is at the level of 10 nM for buffer and natural water. In another study, the ricin toxins were detected by the TMR biosensing platform in polluted water. The TMR biosensing platform completed the quantitative detection of ricin toxins with a LOD at 1 ng/mL [144]. The TMR biosensing platform experiences minimum interferences from the other contents and environmental factors. These results indicate the possibility for the MR biosensing platform to finish detections of hazard contents in other complex samples such as soil, food, and blood.

Further improvements are required for MR biosensing platforms to meet the demands of clinical implements. Meanwhile, MR biosensing platforms display superiorities such as simultaneous detection, user-friendly procedures, and simple integration with electronic devices. MR biosensing platform is a promising candidate for the development of ideal next-generation biosensing systems. Currently, MR biosensing platforms experience difficulties in the magnitude of MR (especially for low magnetic fields), sensing range, and investments for commercially accessible MR sensors [123]. Moreover, the performance of multilayer systems is inadequate at room temperature [123]. Although the TMR multilayer system could display a large MR, the limited working range can't be ignored. GMR/TMR multilayer systems could be expensive compared with traditional testing approaches due to the complicated preparation processes. The price of MR sensors limits the commercial applications of MR biomedical sensing platforms. Therefore, further investigations are required on developing cost-effective MR materials/devices with enhanced MR response at low magnetic field/room temperature, which can benefit the future commercial applications of MR biomedical sensing systems.

2.3 Summary

Since the first observation of MR, more and more attempts have been put into the development of ideal MR sensors for various applications. Meanwhile, many studies were performed to extend the application of MR sensors [145-151]. The major applications of MR sensors include magnetic storage, position sensing, current sensing,

non-destructive monitoring, and biomedical sensing system. Meanwhile, MR sensors were applied in antilock brakes, magnetocardiography, and galvanic isolators [122, 152-157]. The expansion of the electronic industry leads to the significant growth of commercial magnetic sensors. The total value of the market is expected to surpass 2.0 billion US dollars in 2022 [158].

The sensitivity and efficiency are crucial to commercial MR sensors in terms of improving the performance of the devices. Ideal MR sensors require enhanced MR at low magnetic fields and room temperature, reduced time/equipment cost, and enlarged working range, which can boost the advancement of devices with built-in MR units. In specific, ideal MR materials/devices contribute to improving the storage capacity and decreasing the production cost of magnetic storage devices (such as HDDs and MRAMs). More details can be provided in position sensing, current sensing, and non-destructive monitoring since the sensitivity and cost-efficiency are enhanced for MR sensors. The LOD relies on the performance of MR sensors in magnetic biomedical sensing platforms/systems (especially for ultra-low detections). The improvements of MR sensors can lower the LOD of MR biomedical sensing platforms. Meanwhile, the decrease in production costs can help to improve the accessibility of MR sensor-based point-of-care (POC) testing devices.

Currently, GMR and TMR multilayer systems have been widely applied in commercial MR sensors [159-161]. However, the drawbacks of multilayer systems can't be ignored including inadequate MR at room temperature and low magnetic fields, limited working range, and complicated preparation process. Various MR materials have been studied to enhance the performance of MR sensors. Many attempts have been made to develop nanoconstructed MR materials such as granular MR materials, layered graphene, graphene foam, and hybrid graphene nanocomposites [33, 41, 67, 85]. However, current MR materials experience difficulties in enhancing the MR at low magnetic fields/room temperature and reducing the complicity of the preparation process. Breakthroughs are expected to improve the performance and reduce the manufacturing cost of devices with built-in MR units, which overcome existing challenges and benefit the future application of MR sensors/devices.

2.4 References

[1] G. Binasch, P. Grünberg, F. Saurenbach, W. Zinn, Enhanced magnetoresistance in layered magnetic structures with antiferromagnetic interlayer exchange. *Phys. Rev. B* **1989**, *39* (7), 4828-4830.

[2] M.N. Baibich, J.M. Broto, A. Fert, F.N. Van Dau, F. Petroff, P. Etienne*, et al.*, Giant Magnetoresistance of (001)Fe/(001)Cr Magnetic Superlattices. *Phys. Rev. Lett.* **1988**, *61* (21), 2472-2475.

[3] M. Julliere, Tunneling between ferromagnetic films. *Phys. Lett. A* **1975**, *54* (3), 225-226.

[4] C. Chappert, A. Fert, F.N. Van Dau, The emergence of spin electronics in data storage. *Nat. Mater.* **2007**, *6*, 813.

[5] T. Valet, A. Fert, Theory of the perpendicular magnetoresistance in magnetic multilayers. *Phys. Rev. B* **1993**, *48* (10), 7099-7113.

[6] J. Bass, W.P. Pratt, Current-perpendicular (CPP) magnetoresistance in magnetic metallic multilayers. *J. Magn. Magn. Mater.* **1999**, *200* (1), 274-289.

[7] E.Y. Tsymbal, D.G. Pettifor, Perspectives of giant magnetoresistance, in: H. Ehrenreich, F. Spaepen (Eds.) Solid State Phys., Academic Press, 2001, pp. 113-237.

[8] M. Kąc, J. Morgiel, A. Polit, Y. Zabila, M. Marszałek, Atomic scale structure investigations of epitaxial Fe/Cr multilayers. *Appl. Surf. Sci.* **2014**, *305*, 154-159.

[9] M. Kąc, A. Polit, A. Dobrowolska, Y. Zabila, M. Krupiński, M. Marszałek, Surfactant influence on interface roughness and magnetoresistance value in Fe/Cr multilayers. *Thin Solid Films* **2013**, *542*, 199-203.

[10] C.-L. Chang, T.-H. Chiou, P.-H. Chen, W.-C. Chen, C.-T. Ho, W.-Y. Wu, Characteristics of TiN/W_2N multilayers prepared using magnetron sputter deposition with dc and pulsed dc powers. *Surf. Coat. Technol.* **2016**, *303*, 25-31.

[11] N. Saoula, S. Djerourou, K. Yahiaoui, K. Henda, R. Kesri, R.M. Erasmus*, et al.*, Study of the deposition of Ti/TiN multilayers by magnetron sputtering. *Surf. Interface Anal.* **2010**, *42* (6‐7), 1176-1179.

[12] E. Schubert, F. Frost, B. Ziberi, G. Wagner, H. Neumann, B. Rauschenbach, Ion beam sputter deposition of soft x-ray Mo∕Si multilayer mirrors. *J. Vac. Sci. Technol., B: Microelectron. Nanometer Struct.--Process., Meas., Phenom.* **2005**, *23* (3), 959-965.

[13] P.-K. Chiu, C.-T. Lee, D. Chiang, W.-H. Cho, C.-N. Hsiao, Y.-Y. Chen*, et al.*, Conductive and transparent multilayer films for low-temperature $TiO_2/Ag/SiO_2$ electrodes by E-beam evaporation with IAD. *Nanoscale Res. Lett.* **2014**, *9* (1), 35.

[14] M. Kąc, J. Żukrowski, M. Toulemonde, R. Kruk, V. Tokman, A. Polit, *et al.*, Swift iodine ion modification of the structural and magnetotransport properties of Fe/Cr systems. *Nucl. Instrum. Methods Phys. Res. B* **2009**, *267* (6), 925-930.

[15] A. Sáenz-Trevizo, A.M. Hodge, Nanomaterials by design: a review of nanoscale metallic multilayers. *Nanotechnology* **2020**, *31* (29), 292002.

[16] I. Bakonyi, L. Péter, Electrodeposited multilayer films with giant magnetoresistance (GMR): Progress and problems. *Prog. Mater Sci.* **2010**, *55* (3), 107-245.

[17] L. Liu, Q. Zhan, H. Yang, H. Li, S. Zhang, Y. Liu, *et al.*, Magnetostrictive GMR spin valves with composite FeGa/FeCo free layers. *AIP Adv.* **2016**, *6* (3), 035206.

[18] X.G. Zhang, W.H. Butler, Large magnetoresistance in bcc Co/MgO/Co and FeCo/MgO/FeCo tunnel junctions. *Phys. Rev. B* **2004**, *70* (17), 172407.

[19] R.S. Sundar, S.C. Deevi, Soft magnetic FeCo alloys: alloy development, processing, and properties. *Int. Mater. Rev.* **2005**, *50* (3), 157-192.

[20] C. Reig, M.-D. Cubells-Beltrán, Giant Magnetoresistance (GMR) Magnetometers, in: A. Grosz, M.J. Haji-Sheikh, S.C. Mukhopadhyay (Eds.) High Sensitivity Magnetometers, Springer International Publishing, Cham, 2017, pp. 225-252.

[21] Z. Jin, M.A.I. Mohd Noor Sam, M. Oogane, Y. Ando, Serial MTJ-Based TMR Sensors in Bridge Configuration for Detection of Fractured Steel Bar in Magnetic Flux Leakage Testing. *Sensors* **2021**, *21* (2), 668.

[22] B.H. Zhou, J.D. Rinehart, A Size Threshold for Enhanced Magnetoresistance in Colloidally Prepared $CoFe_2O_4$ Nanoparticle Solids. *ACS Cent. Sci.* **2018**, *4* (9), 1222-1227.

[23] A.E. Berkowitz, J.R. Mitchell, M.J. Carey, A.P. Young, S. Zhang, F.E. Spada, *et al.*, Giant magnetoresistance in heterogeneous Cu-Co alloys. *Phys. Rev. Lett.* **1992**, *68* (25), 3745-3748.

[24] J.Q. Xiao, J.S. Jiang, C.L. Chien, Giant magnetoresistance in nonmultilayer magnetic systems. *Phys. Rev. Lett.* **1992**, *68* (25), 3749-3752.

[25] J.M.D. Coey, A.E. Berkowitz, L. Balcells, F.F. Putris, F.T. Parker, Magnetoresistance of magnetite. *Appl. Phys. Lett.* **1998**, *72* (6), 734-736.

[26] D. Zhang, Z. Liu, S. Han, C. Li, B. Lei, M.P. Stewart, *et al.*, Magnetite (Fe_3O_4) Core−Shell Nanowires: Synthesis and Magnetoresistance. *Nano Lett.* **2004**, *4* (11), 2151-2155.

[27] S. Mi, Y. Xie, Y. Li, R. Liu, X. Liu, I.I. Smalyukh, *et al.*, The Effect of Thickness-Tunable ZrO_2 Shell on Enhancing the Tunneling Magnetoresistance of Fe_3O_4 Supraparticles. *Adv. Mater. Interfaces* **2018**, *5* (12), 1800236.

[28] E. Liu, H. Yuan, Z. Kou, X. Wu, Q. Xu, Y. Zhai, *et al.*, Investigation on Spin Dependent Transport Properties of Core-Shell Structural Fe_3O_4/ZnS Nanocomposites for Spintronic Application. *Sci. Rep.* **2015**, *5* (1), 11164.

[29] Z.W. Fan, P. Li, E.Y. Jiang, H.L. Bai, Evolution of magnetoresistance mechanisms in granular Co/C films with different conduction regimes. *J. Phys. D: Appl. Phys.* **2013**, *46* (6), 065002.

[30] Z. Quan, X. Zhang, W. Liu, X. Li, K. Addison, G.A. Gehring, *et al.*, Enhanced Room Temperature Magnetoresistance and Spin Injection from Metallic Cobalt in Co/ZnO and Co/ZnAlO Films. *ACS Appl. Mater. Interfaces* **2013**, *5* (9), 3607-3613.

[31] A. Gerber, A. Milner, B. Groisman, M. Karpovsky, A. Gladkikh, A. Sulpice, Magnetoresistance of granular ferromagnets. *Phys. Rev. B* **1997**, *55* (10), 6446-6452.

[32] J. Leveneur, J. Kennedy, G.V.M. Williams, J. Metson, A. Markwitz, Large room temperature magnetoresistance in ion beam synthesized surface Fe nanoclusters on SiO_2. *Appl. Phys. Lett.* **2011**, *98* (5), 053111.

[33] Y.P. Zeng, Z.W. Liu, H.Y. Yu, Z.G. Zheng, D.C. Zeng, X.S. Gao, Large positive room temperature magnetoresistance in nanogranular FeCo–Si–N thin films. *Mater. Lett.* **2013**, *110*, 27-30.

[34] H. Fukuzawa, H. Yuasa, H. Iwasaki, CPP-GMR films with a current-confined-path nano-oxide layer (CCP-NOL). *J. Phys. D: Appl. Phys.* **2007**, *40* (5), 1213-1220.

[35] G.S. Chaubey, C. Barcena, N. Poudyal, C. Rong, J. Gao, S. Sun, *et al.*, Synthesis and Stabilization of FeCo Nanoparticles. *J. Am. Chem. Soc.* **2007**, *129* (23), 7214-7215.

[36] Y.P. Zeng, Z.W. Liu, E. Mikmeková, Magnetoresistance effects associated with various electric conduction mechanisms in nanostructured $[C/FeCo]_n$ multilayers. *J. Magn. Magn. Mater.* **2017**, *421*, 39-43.

[37] C. Wang, X. Xiao, Y. Rong, T.Y. Hsu, The effect of substrate temperature on the microstructure and tunnelling magnetoresistance of $FeCo–Al_2O_3$ nanogranular films. *J. Mater. Sci.* **2006**, *41* (12), 3873-3879.

[38] S.-h. Ge, Z.-z. Zhang, Y.-y. Lu, C.-x. Li, G. Run-jin, Influence of annealing condition on giant magnetoresistance of FeCo–Cu granular films. *Thin Solid Films* **1997**, *311* (1), 33-37.

[39] C. Wang, X. Xiao, Y. Rong, H.Y. Hsu, Nanoparticle morphology in $FeCo–SiO_2$ granular films with tunneling giant magnetoresistance. *Mater. Sci. Eng., B* **2007**, *141* (3), 126-131.

[40] K.S. Novoselov, A.K. Geim, S.V. Morozov, D. Jiang, Y. Zhang, S.V. Dubonos, *et al.*, Electric Field Effect in Atomically Thin Carbon Films. *Science* **2004**, *306* (5696), 666-669.

[41] H.-C. Wu, A.N. Chaika, M.-C. Hsu, T.-W. Huang, M. Abid, M. Abid, *et al.*, Large positive in-plane magnetoresistance induced by localized states at nanodomain boundaries in graphene. *Nat. Commun.* **2017**, *8* (1), 14453.

[42] A.H. Castro Neto, F. Guinea, N.M.R. Peres, K.S. Novoselov, A.K. Geim, The electronic properties of graphene. *Rev. Mod. Phys.* **2009**, *81* (1), 109-162.

[43] M.I. Katsnelson, Graphene: carbon in two dimensions. *Mater. Today* **2007**, *10* (1), 20-27.

[44] A.L. Friedman, J.L. Tedesco, P.M. Campbell, J.C. Culbertson, E. Aifer, F.K. Perkins, *et al.*, Quantum Linear Magnetoresistance in Multilayer Epitaxial Graphene. *Nano Lett.* **2010**, *10* (10), 3962-3965.

[45] K. Gopinadhan, Y.J. Shin, I. Yudhistira, J. Niu, H. Yang, Giant magnetoresistance in single-layer graphene flakes with a gate-voltage-tunable weak antilocalization. *Phys. Rev. B* **2013**, *88* (19), 195429.

[46] F. Kisslinger, C. Ott, C. Heide, E. Kampert, B. Butz, E. Spiecker, *et al.*, Linear magnetoresistance in mosaic-like bilayer graphene. *Nat. Phys.* **2015**, *11* (8), 650-653.

[47] M. Rein, N. Richter, K. Parvez, X. Feng, H. Sachdev, M. Kläui, *et al.*, Magnetoresistance and Charge Transport in Graphene Governed by Nitrogen Dopants. *ACS Nano* **2015**, *9* (2), 1360-1366.

[48] Y.-B. Zhou, B.-H. Han, Z.-M. Liao, H.-C. Wu, D.-P. Yu, From positive to negative magnetoresistance in graphene with increasing disorder. *Appl. Phys. Lett.* **2011**, *98* (22), 222502.

[49] K. Gopinadhan, Y.J. Shin, R. Jalil, T. Venkatesan, A.K. Geim, A.H.C. Neto, *et al.*, Extremely large magnetoresistance in few-layer graphene/boron–nitride heterostructures. *Nat. Commun.* **2015**, *6* (1), 8337.

[50] P.U. Asshoff, J.L. Sambricio, A.P. Rooney, S. Slizovskiy, A. Mishchenko, A.M. Rakowski, *et al.*, Magnetoresistance of vertical Co-graphene-NiFe junctions controlled by charge transfer and proximity-induced spin splitting in graphene. *2D Mater.* **2017**, *4* (3), 031004.

[51] H. Huang, H. Guan, M. Su, X. Zhang, Y. Liu, C. Liu, *et al.*, Gate-tunable linear magnetoresistance in molybdenum disulfide field-effect transistors with graphene insertion layer. *Nano Res.* **2020**, *14* (7), 1814–1818.

[52] E.D. Cobas, O.M.J. van 't Erve, S.-F. Cheng, J.C. Culbertson, G.G. Jernigan, K. Bussman, *et al.*, Room-Temperature Spin Filtering in Metallic Ferromagnet–Multilayer Graphene–Ferromagnet Junctions. *ACS Nano* **2016**, *10* (11), 10357-10365.

[53] R.U.R. Sagar, N. Mahmood, F.J. Stadler, T. Anwar, S.T. Navale, K. Shehzad, *et al.*, High Capacity Retention Anode Material for Lithium Ion Battery. *Electrochim. Acta* **2016**, *211*, 156-163.

[54] Z. Chen, W. Ren, L. Gao, B. Liu, S. Pei, H.-M. Cheng, Three-dimensional flexible and conductive interconnected graphene networks grown by chemical vapour deposition. *Nat. Mater.* **2011**, *10* (6), 424-428.

[55] Y. Ma, Y. Chen, Three-dimensional graphene networks: synthesis, properties and applications. *Natl. Sci. Rev.* **2015**, *2* (1), 40-53.

[56] E. Krueger, A.N. Chang, D. Brown, J. Eixenberger, R. Brown, S. Rastegar, *et al.*, Graphene Foam as a Three-Dimensional Platform for Myotube Growth. *ACS Biomater. Sci. Eng.* **2016**, *2* (8), 1234-1241.

[57] K. Shehzad, Y. Xu, C. Gao, X. Duan, Three-dimensional macro-structures of two-dimensional nanomaterials. *Chem. Soc. Rev.* **2016**, *45* (20), 5541-5588.

[58] S. Jayanthi, A. Mukherjee, K. Chatterjee, A.K. Sood, A. Misra, Tailored nitrogen dioxide sensing response of three-dimensional graphene foam. *Sens. Actuators, B* **2016**, *222*, 21-27.

[59] R.U.R. Sagar, M. Galluzzi, C. Wan, K. Shehzad, S.T. Navale, T. Anwar, *et al.*, Large, Linear, and Tunable Positive Magnetoresistance of Mechanically Stable Graphene Foam–Toward High-Performance Magnetic Field Sensors. *ACS Appl. Mater. Interfaces* **2017**, *9* (2), 1891-1898.

[60] Y. Zhang, T.-T. Tang, C. Girit, Z. Hao, M.C. Martin, A. Zettl, *et al.*, Direct observation of a widely tunable bandgap in bilayer graphene. *Nature* **2009**, *459* (7248), 820-823.

[61] C.H. Lui, Z. Li, K.F. Mak, E. Cappelluti, T.F. Heinz, Observation of an electrically tunable band gap in trilayer graphene. *Nat. Phys.* **2011**, *7* (12), 944-947.

[62] G. Xu, C.M. Torres, J. Tang, J. Bai, E.B. Song, Y. Huang, *et al.*, Edge Effect on Resistance Scaling Rules in Graphene Nanostructures. *Nano Lett.* **2011**, *11* (3), 1082-1086.

[63] A.T. Murdock, A. Koos, T.B. Britton, L. Houben, T. Batten, T. Zhang, *et al.*, Controlling the Orientation, Edge Geometry, and Thickness of Chemical Vapor Deposition Graphene. *ACS Nano* **2013**, *7* (2), 1351-1359.

[64] R.R. Sagar, X. Zhang, C. Xiong, Growth of graphene on copper and nickel foils via chemical vapour deposition using ethylene. *Mater. Res. Innovations* **2014**, *18* (sup4), S4-706-S704-710.

[65] P. Li, Q. Zhang, X. He, W. Ren, H.-M. Cheng, X.-x. Zhang, Spatial mobility fluctuation induced giant linear magnetoresistance in multilayered graphene foam. *Phys. Rev. B* **2016**, *94* (4), 045402.

[66] R.U.R. Sagar, M. Galluzzi, A. García-Peñas, M.A. Bhat, M. Zhang, F.J. Stadler, Large unsaturated room temperature negative magnetoresistance in graphene foam composite for wearable and flexible magnetoelectronics. *Nano Res.* **2019**, *12* (1), 101-107.

[67] M.H. Zeb, B. Shabbir, R.U.R. Sagar, N. Mahmood, K. Chen, I. Qasim*, et al.*, Superior Magnetoresistance Performance of Hybrid Graphene Foam/Metal Sulfide Nanocrystal Devices. *ACS Appl. Mater. Interfaces* **2019**, *11* (21), 19397-19403.

[68] R.U. Rehman Sagar, K. Shehzad, A. Ali, F.J. Stadler, Q. Khan, J. Zhao*, et al.*, Defect-induced, temperature-independent, tunable magnetoresistance of partially fluorinated graphene foam. *Carbon* **2019**, *143*, 179-188.

[69] Y. Liu, X. Dong, P. Chen, Biological and chemical sensors based on graphene materials. *Chem. Soc. Rev.* **2012**, *41* (6), 2283-2307.

[70] M. Zhang, Y. Li, Z. Su, G. Wei, Recent advances in the synthesis and applications of graphene–polymer nanocomposites. *Polym. Chem.* **2015**, *6* (34), 6107-6124.

[71] Y. Lu, B.R. Goldsmith, N.J. Kybert, A.T.C. Johnson, DNA-decorated graphene chemical sensors. *Appl. Phys. Lett.* **2010**, *97* (8), 083107.

[72] S.K. Krishnan, E. Singh, P. Singh, M. Meyyappan, H.S. Nalwa, A review on graphene-based nanocomposites for electrochemical and fluorescent biosensors. *RSC Adv.* **2019**, *9* (16), 8778-8881.

[73] W.J. Stark, Nanoparticles in Biological Systems. *Angew. Chem. Int. Ed.* **2011**, *50* (6), 1242-1258.

[74] H.-L. Xu, H. Bi, R.-B. Yang, Enhanced microwave absorption property of bowl-like Fe_3O_4 hollow spheres/reduced graphene oxide composites. *J. Appl. Phys.* **2012**, *111* (7), 07A522.

[75] M. Pumera, Graphene in biosensing. *Mater. Today* **2011**, *14* (7), 308-315.

[76] W. Guo, B. Zhao, Q. Zhou, Y. He, Z. Wang, N. Radacsi, Fe-Doped ZnO/Reduced Graphene Oxide Nanocomposite with Synergic Enhanced Gas Sensing Performance for the Effective Detection of Formaldehyde. *ACS Omega* **2019**, *4* (6), 10252-10262.

[77] D. Wang, R. Kou, D. Choi, Z. Yang, Z. Nie, J. Li*, et al.*, Ternary Self-Assembly of Ordered Metal Oxide−Graphene Nanocomposites for Electrochemical Energy Storage. *ACS Nano* **2010**, *4* (3), 1587-1595.

[78] Y. Zhang, H. Shu, G. Chang, K. Ji, M. Oyama, X. Liu, *et al.*, Facile synthesis of palladium–graphene nanocomposites and their catalysis for electro-oxidation of methanol and ethanol. *Electrochim. Acta* **2013**, *109*, 570-576.

[79] C.-Y. Cai, J.-H. Chen, Electronic transport properties of Co cluster-decorated graphene. *Chin. Phys. B* **2018**, *27* (6), 067304.

[80] U. Chandni, E.A. Henriksen, J.P. Eisenstein, Transport in indium-decorated graphene. *Phys. Rev. B* **2015**, *91* (24), 245402.

[81] J.A. Elias, E.A. Henriksen, Electronic transport and scattering times in tungsten-decorated graphene. *Phys. Rev. B* **2017**, *95* (7), 075405.

[82] Z. Jia, R. Zhang, Q. Han, Q. Yan, R. Zhu, D. Yu, *et al.*, Large tunable linear magnetoresistance in gold nanoparticle decorated graphene. *Appl. Phys. Lett.* **2014**, *105* (14), 143103.

[83] Y. Wang, M. Jaiswal, M. Lin, S. Saha, B. Özyilmaz, K.P. Loh, Electronic Properties of Nanodiamond Decorated Graphene. *ACS Nano* **2012**, *6* (2), 1018-1025.

[84] J.I. Paredes, S. Villar-Rodil, M.J. Fernández-Merino, L. Guardia, A. Martínez-Alonso, J.M.D. Tascón, Environmentally friendly approaches toward the mass production of processable graphene from graphite oxide. *J. Mater. Chem.* **2011**, *21* (2), 298-306.

[85] G. Abellán, H. Prima-García, E. Coronado, Graphene enhances the magnetoresistance of FeNi$_3$ nanoparticles in hierarchical FeNi$_3$–graphene nanocomposites. *J. Mater. Chem. C* **2016**, *4* (11), 2252-2258.

[86] C. Majumder, S. Bhattacharya, S.K. Saha, Anomalous large negative magnetoresistance in transition-metal decorated graphene: Evidence for electron-hole puddles. *Phys. Rev. B* **2019**, *99* (4), 045408.

[87] Z. Sheykhifard, S.M. Mohseni, B. Tork, M.R. Hajiali, L. Jamilpanah, B. Rahmati, *et al.*, Magnetic graphene/Ni-nano-crystal hybrid for small field magnetoresistive effect synthesized via electrochemical exfoliation/deposition technique. *J. Mater. Sci.: Mater. Electron.* **2018**, *29* (5), 4171-4178.

[88] J. Zhu, Z. Luo, S. Wu, N. Haldolaarachchige, D.P. Young, S. Wei, *et al.*, Magnetic graphene nanocomposites: electron conduction, giant magnetoresistance and tunable negative permittivity. *J. Mater. Chem.* **2012**, *22* (3), 835-844.

[89] E.E. Fullerton, J.R. Childress, Spintronics, Magnetoresistive Heads, and the Emergence of the Digital World. *Proc. IEEE* **2016**, *104* (10), 1787-1795.

[90] A.S. Hoagland, History of magnetic disk storage based on perpendicular magnetic recording. *IEEE Trans. Magn.* **2003**, *39* (4), 1871-1875.

[91] C. Tsang, M. Chen, T. Yogi, K. Ju, Gigabit density recording using dual-element MR/inductive heads on thin-film disks. *IEEE Trans. Magn.* **1990**, *26* (5), 1689-1693.

[92] D.E. Heim, R.E. Fontana, C. Tsang, V.S. Speriosu, B.A. Gurney, M.L. Williams, Design and operation of spin valve sensors. *IEEE Trans. Magn.* **1994**, *30* (2), 316-321.

[93] S. Maat, A.C. Marley, Physics and Design of Hard Disk Drive Magnetic Recording Read Heads, in: Y. Xu, D.D. Awschalom, J. Nitta (Eds.) Handbook of Spintronics, Springer Netherlands, Dordrecht, 2013, pp. 1-45.

[94] S.S.P. Parkin, K.P. Roche, M.G. Samant, P.M. Rice, R.B. Beyers, R.E. Scheuerlein*, et al.*, Exchange-biased magnetic tunnel junctions and application to nonvolatile magnetic random access memory (invited). *J. Appl. Phys.* **1999**, *85* (8), 5828-5833.

[95] S. Parkin, J. Xin, C. Kaiser, A. Panchula, K. Roche, M. Samant, Magnetically engineered spintronic sensors and memory. *Proc. IEEE* **2003**, *91* (5), 661-680.

[96] S. Tehrani, Status and Outlook of MRAM Memory Technology (Invited), in: 2006 International Electron Devices Meeting, 2006, pp. 1-4.

[97] S. Salehi, D. Fan, R.F. Demara, Survey of STT-MRAM Cell Design Strategies: Taxonomy and Sense Amplifier Tradeoffs for Resiliency. *J. Emerg. Technol. Comput. Syst.* **2017**, *13* (3), Article 48.

[98] R. Sbiaa, S.N. Piramanayagam, Recent Developments in Spin Transfer Torque MRAM. *Phys. Status Solidi RRL* **2017**, *11* (12), 1700163.

[99] K. Tsukada, M. Hayashi, Y. Nakamura, K. Sakai, T. Kiwa, Small Eddy Current Testing Sensor Probe Using a Tunneling Magnetoresistance Sensor to Detect Cracks in Steel Structures. *IEEE Trans. Magn.* **2018**, *54* (11), 1-5.

[100] S. Wang, Z. Wu, D. Peng, W. Li, Y. Zheng, Embedded position estimation using tunnel magnetoresistance sensors for permanent magnet linear synchronous motor systems. *Measurement* **2019**, *147*, 106860.

[101] C. Reig, M.-D. Cubells-Beltrán, D. Ramírez Muñoz, Magnetic Field Sensors Based on Giant Magnetoresistance (GMR) Technology: Applications in Electrical Current Sensing. *Sensors* **2009**, *9* (10), 7919-7942.

[102] J. Lenz, S. Edelstein, Magnetic sensors and their applications. *IEEE Sens. J.* **2006**, *6* (3), 631-649.

[103] R. Slatter, A6. 1-Highly integrated magnetoresistive sensors in aerospace applications. *Proceedings SENSOR 2013* **2013**, 126-131.

[104] P. Ripka, M. Janosek, Advances in Magnetic Field Sensors. *IEEE Sens. J.* **2010**, *10* (6), 1108-1116.

[105] S. Arana, N. Arana, F.J. Gracia, E. Castaño, High sensitivity linear position sensor developed using granular Ag–Co giant magnetoresistances. *Sens. Actuators, A* **2005**, *123-124*, 116-121.

[106] B. Stritzke, C. Brode, M. Danowski, A6. 2-Highly flexible absolute integrated encoder system on GMR-basis. *Proceedings SENSOR 2013* **2013**, 132-137.

[107] TMR3002-Biaxial TMR Angle Sensor http://www.dowaytech.com/en/1717.html (accessed Mar. 17, 2021).

[108] AAT001-10E TMR Angle Sensor. https://www.nve.com/Downloads/AAT001.pdf (accessed Mar. 17, 2021).

[109] C. Albon, A. Weddemann, A. Auge, K. Rott, A. Hütten, Tunneling magnetoresistance sensors for high resolutive particle detection. *Appl. Phys. Lett.* **2009**, *95* (2), 023101.

[110] V. Luong, J. Jeng, B. Lai, J. Hsu, C. Chang, C. Lu, Design of 3-D Magnetic Field Sensor With Single Bridge of Spin-Valve Giant Magnetoresistance Films. *IEEE Trans. Magn.* **2015**, *51* (11), 1-4.

[111] Y. Ouyang, J. He, J. Hu, S.X. Wang, A Current Sensor Based on the Giant Magnetoresistance Effect: Design and Potential Smart Grid Applications. *Sensors* **2012**, *12* (11), 15520-15541.

[112] D. Rifai, A.N. Abdalla, K. Ali, R. Razali, Giant Magnetoresistance Sensors: A Review on Structures and Non-Destructive Eddy Current Testing Applications. *Sensors* **2016**, *16* (3), 298.

[113] M. Pelkner, A. Neubauer, V. Reimund, M. Kreutzbruck, A. Schütze, Routes for GMR-Sensor Design in Non-Destructive Testing. *Sensors* **2012**, *12* (9), 12169-12183.

[114] A. Bernieri, L. Ferrigno, M. Laracca, A. Rasile, Eddy Current Testing Probe Based on Double-Coil Excitation and GMR Sensor. *IEEE Trans. Instrum. Meas.* **2019**, *68* (5), 1533-1542.

[115] J. Schotter, P.B. Kamp, A. Becker, A. Pühler, G. Reiss, H. Brückl, Comparison of a prototype magnetoresistive biosensor to standard fluorescent DNA detection. *Biosens. Bioelectron.* **2004**, *19* (10), 1149-1156.

[116] K. Wu, R. Saha, D. Su, V.D. Krishna, J. Liu, M.C.J. Cheeran*, et al.*, Magnetic-Nanosensor-Based Virus and Pathogen Detection Strategies before and during COVID-19. *ACS Appl. Nano Mater.* **2020**, *3* (10), 9560-9580.

[117] D.A. Hall, R.S. Gaster, K.A.A. Makinwa, S.X. Wang, B. Murmann, A 256 Pixel Magnetoresistive Biosensor Microarray in 0.18 μm CMOS. *IEEE J. Solid-State Circuits* **2013**, *48* (5), 1290-1301.

[118] J. Chou, C. Wu, P. Kuo, C. Lai, Y. Nien, Y. Wu*, et al.*, The Flexible Urea Biosensor Using Magnetic Nanoparticles. *IEEE Trans. Nanotechnol.* **2019**, *18*, 484-490.

[119] D.R. Baselt, G.U. Lee, M. Natesan, S.W. Metzger, P.E. Sheehan, R.J. Colton, A biosensor based on magnetoresistance technology. *Biosens. Bioelectron.* **1998**, *13* (7), 731-739.

[120] P.P. Freitas, F.A. Cardoso, V.C. Martins, S.A.M. Martins, J. Loureiro, J. Amaral*, et al.*, Spintronic platforms for biomedical applications. *Lab Chip* **2012**, *12* (3), 546-557.

[121] J.M. Lagaron, L. Cabedo, D. Cava, J.L. Feijoo, R. Gavara, E. Gimenez, Improving packaged food quality and safety. Part 2: Nanocomposites. *Food Addit. Contam.* **2005**, *22* (10), 994-998.

[122] D.A. Hall, R.S. Gaster, T. Lin, S.J. Osterfeld, S. Han, B. Murmann*, et al.*, GMR biosensor arrays: A system perspective. *Biosens. Bioelectron.* **2010**, *25* (9), 2051-2057.

[123] C. Ren, Q. Bayin, S. Feng, Y. Fu, X. Ma, J. Guo, Biomarkers detection with magnetoresistance-based sensors. *Biosens. Bioelectron.* **2020**, *165*, 112340.

[124] S.P. Mulvaney, C.L. Cole, M.D. Kniller, M. Malito, C.R. Tamanaha, J.C. Rife*, et al.*, Rapid, femtomolar bioassays in complex matrices combining microfluidics and magnetoelectronics. *Biosens. Bioelectron.* **2007**, *23* (2), 191-200.

[125] D.L. Graham, H.A. Ferreira, P.P. Freitas, J.M.S. Cabral, High sensitivity detection of molecular recognition using magnetically labelled biomolecules and magnetoresistive sensors. *Biosens. Bioelectron.* **2003**, *18* (4), 483-488.

[126] B. Srinivasan, Y. Li, Y. Jing, C. Xing, J. Slaton, J.-P. Wang, A Three-Layer Competition-Based Giant Magnetoresistive Assay for Direct Quantification of Endoglin from Human Urine. *Anal. Chem.* **2011**, *83* (8), 2996-3002.

[127] Y. Wang, W. Wang, L. Yu, L. Tu, Y. Feng, T. Klein*, et al.*, Giant magnetoresistive-based biosensing probe station system for multiplex protein assays. *Biosens. Bioelectron.* **2015**, *70*, 61-68.

[128] T. Klein, W. Wang, L. Yu, K. Wu, K.L.M. Boylan, R.I. Vogel*, et al.*, Development of a multiplexed giant magnetoresistive biosensor array prototype to quantify ovarian cancer biomarkers. *Biosens. Bioelectron.* **2019**, *126*, 301-307.

[129] Y. Gao, W. Huo, L. Zhang, J. Lian, W. Tao, C. Song*, et al.*, Multiplex measurement of twelve tumor markers using a GMR multi-biomarker immunoassay biosensor. *Biosens. Bioelectron.* **2019**, *123*, 204-210.

[130] G. Kolifarhood, M. Aghaali, H. Mozafar Saadati, N. Taherpour, S. Rahimi, N. Izadi*, et al.*, Epidemiological and Clinical Aspects of COVID-19; a Narrative Review. *Arch Acad Emerg Med* **2020**, *8* (1), e41-e41.

[131] N. Chen, M. Zhou, X. Dong, J. Qu, F. Gong, Y. Han, *et al.*, Epidemiological and clinical characteristics of 99 cases of 2019 novel coronavirus pneumonia in Wuhan, China: a descriptive study. *Lancet* **2020**, *395* (10223), 507-513.

[132] V.D. Krishna, K. Wu, A.M. Perez, J.-P. Wang, Giant Magnetoresistance-based Biosensor for Detection of Influenza A Virus. *Front. Microbiol.* **2016**, *7*, 400.

[133] K. Wu, T. Klein, V.D. Krishna, D. Su, A.M. Perez, J.-P. Wang, Portable GMR Handheld Platform for the Detection of Influenza A Virus. *ACS Sens.* **2017**, *2* (11), 1594-1601.

[134] J. Choi, A.W. Gani, D.J.B. Bechstein, J.-R. Lee, P.J. Utz, S.X. Wang, Portable, one-step, and rapid GMR biosensor platform with smartphone interface. *Biosens. Bioelectron.* **2016**, *85*, 1-7.

[135] X. Zhi, Q. Liu, X. Zhang, Y. Zhang, J. Feng, D. Cui, Quick genotyping detection of HBV by giant magnetoresistive biochip combined with PCR and line probe assay. *Lab Chip* **2012**, *12* (4), 741-745.

[136] P.P. Sharma, E. Albisetti, M. Massetti, M. Scolari, C. La Torre, M. Monticelli, *et al.*, Integrated platform for detecting pathogenic DNA via magnetic tunneling junction-based biosensors. *Sens. Actuators, B* **2017**, *242*, 280-287.

[137] L. Li, K.-Y. Mak, Y. Zhou, Detection of HIV-1 antigen based on magnetic tunnel junction sensors. *Chin. Phys. B* **2020**, *29* (8), 088701.

[138] Y. Wu, Y. Liu, Q. Zhan, J.P. Liu, R.-W. Li, Rapid detection of Escherichia coli O157:H7 using tunneling magnetoresistance biosensor. *AIP Adv.* **2017**, *7* (5), 056658.

[139] G. Kokkinis, S.F. Cardoso, F.A. Cardoso, I. Giouroudi, Microfluidics for the Rapid Detection of Pathogens Using Giant Magnetoresistance Sensors. *IEEE Trans. Magn.* **2014**, *50* (11), 1-4.

[140] M. Koets, T. van der Wijk, J.T.W.M. van Eemeren, A. van Amerongen, M.W.J. Prins, Rapid DNA multi-analyte immunoassay on a magneto-resistance biosensor. *Biosens. Bioelectron.* **2009**, *24* (7), 1893-1898.

[141] A.C. Mak, S.J. Osterfeld, H. Yu, S.X. Wang, R.W. Davis, O.A. Jejelowo, *et al.*, Sensitive giant magnetoresistive-based immunoassay for multiplex mycotoxin detection. *Biosens. Bioelectron.* **2010**, *25* (7), 1635-1639.

[142] E. Ng, K.C. Nadeau, S.X. Wang, Giant magnetoresistive sensor array for sensitive and specific multiplexed food allergen detection. *Biosens. Bioelectron.* **2016**, *80*, 359-365.

[143] W. Wang, Y. Wang, L. Tu, T. Klein, Y. Feng, Q. Li, *et al.*, Magnetic Detection of Mercuric Ion Using Giant Magnetoresistance-Based Biosensing System. *Anal. Chem.* **2014**, *86* (8), 3712-3716.

[144] X.-H. Mu, H.-F. Liu, Z.-Y. Tong, B. Du, S. Liu, B. Liu*, et al.*, A new rapid detection method for ricin based on tunneling magnetoresistance biosensor. *Sens. Actuators, B* **2019**, *284*, 638-649.

[145] S.S.P. Parkin, M. Hayashi, L. Thomas, Magnetic Domain-Wall Racetrack Memory. *Science* **2008**, *320* (5873), 190-194.

[146] U. Ausserlechner, The Optimum Layout for Giant Magneto-Resistive Angle Sensors. *IEEE Sens. J.* **2010**, *10* (10), 1571-1582.

[147] S. Wu, J. Chen, S. Wu, A Rotary Encoder With an Eccentrically Mounted Ring Magnet. *IEEE Trans. Instrum. Meas.* **2014**, *63* (8), 1907-1915.

[148] R. Hahn, T. Schmidt, R. Slatter, B. Olberts, F. Romera, Magnetoresistive angular sensors for space applications: Results of breadboard and EQM testing and lessons learned. *Proc. ESMATS* **2017**, 1-6.

[149] R. Rempt, Scanning with magnetoresistive sensors for subsurface corrosion. *AIP Conf. Proc.* **2002**, *615* (1), 1771-1778.

[150] B. Wincheski, J. Simpson, M. Namkung, D. Perey, E. Scales, R. Louie, Development of Giant Magnetoresistive inspection system for detection of deep fatigue cracks under airframe fasteners. *AIP Conf. Proc.* **2002**, *615* (1), 1007-1014.

[151] R.S. Gaster, D.A. Hall, C.H. Nielsen, S.J. Osterfeld, H. Yu, K.E. Mach*, et al.*, Matrix-insensitive protein assays push the limits of biosensors in medicine. *Nat. Med.* **2009**, *15* (11), 1327-1332.

[152] C. Giebeler, D.J. Adelerhof, A.E.T. Kuiper, J.B.A. van Zon, D. Oelgeschläger, G. Schulz, Robust GMR sensors for angle detection and rotation speed sensing. *Sens. Actuators, A* **2001**, *91* (1), 16-20.

[153] G. Rieger, K. Ludwig, J. Hauch, W. Clemens, GMR sensors for contactless position detection. *Sens. Actuators, A* **2001**, *91* (1), 7-11.

[154] T.M. Hermann, W.C. Black, S. Hui, Magnetically coupled linear isolator. *IEEE Trans. Magn.* **1997**, *33* (5), 4029-4031.

[155] J.C. Rife, M.M. Miller, P.E. Sheehan, C.R. Tamanaha, M. Tondra, L.J. Whitman, Design and performance of GMR sensors for the detection of magnetic microbeads in biosensors. *Sens. Actuators, A* **2003**, *107* (3), 209-218.

[156] M. Pannetier-Lecoeur, L. Parkkonen, N. Sergeeva-Chollet, H. Polovy, C. Fermon, C. Fowley, Magnetocardiography with sensors based on giant magnetoresistance. *Appl. Phys. Lett.* **2011**, *98* (15), 153705.

[157] Y. Shirai, K. Hirao, T. Shibuya, S. Okawa, Y. Hasegawa, Y. Adachi*, et al.*, Magnetocardiography Using a Magnetoresistive Sensor Array. *Int. Heart J.* **2019**, *60* (1), 50-54.

[158] R. Dixon Magnetic Sensors Report. https://cdn.ihs.com/www/pdf/1118/ABSTRACT-Magnetic-Sensors%20Report-2017.pdf (accessed Aug. 27, 2020).

[159] Y. Ouyang, Z. Wang, G. Zhao, J. Hu, S. Ji, J. He*, et al.*, Current sensors based on GMR effect for smart grid applications. *Sens. Actuators, A* **2019**, *294*, 8-16.

[160] L. Schnitzspan, J. Cramer, J. Kubik, M. Tarequzzaman, G. Jakob, M. Kläui, Impact of Annealing Temperature on Tunneling Magnetoresistance Multilayer Stacks. *IEEE Magn. Lett.* **2020**, *11*, 1-5.

[161] S. Tumanski, Thin film magnetoresistive sensors, CRC Press, 2001.

Chapter 3

3 Developing FeCo/Reduced Graphene Oxide (rGO) Hybrid Nanosheets with Special Magnetoresistance Used for Wireless Magnetic Field Sensor

In this chapter, we applied a facile polyol method to synthesis the FeCo/rGO hybrid nanosheets with large special positive magnetoresistance (MR) at room temperature and low magnetic field (10 kOe). MR sensors/devices have been studied extensively since the discovery of MR in 1856. The developments of MR sensors/devices surged after the observation of giant magnetoresistance (GMR) in the 1980s. The MR devices/sensors have been applied in magnetic storage, position sensing, non-destructive monitoring, and biomedical testing [1-4]. Most of these devices/sensors are based on multilayer systems with GMR or tunneling magnetoresistance (TMR), which require special equipment and prolong/complex fabrication process since it is challenging to precisely control the layer thickness [5]. The recent advancements of nanotechnology have introduced nanoconstructed materials to the development of cost-effective and highly-sensitive MR devices/sensors. However, most of the current nanoconstructed MR materials/structures suffer the problems such as requiring extreme conditions (~ 10 K), limited sensing range, and inadequate MR at low magnetic fields ($\leq$ 10 kOe) [6-8].

We successfully synthesized the FeCo/rGO hybrid nanosheets with a facile polyol process. The FeCo nanoparticles (NPs) were *in situ* modified on the surface of chemically synthesized reduced graphene oxide (rGO). A large MR up to $21 \pm 6\%$ was observed on FeCo/rGO hybrid nanosheets at room temperature and low magnetic fields (10 kOe). In the meantime, the tunable MR was achieved by adjusting the mass ratio of adding rGO in the reaction (M_{rGO}). The A. A. Abrikosov's quantum magnetoresistance (QMR) model was applied to investigate the possible origin of the large special MR of FeCo/rGO hybrid nanosheets at the low magnetic field, which exhibits good agreements with the resistance change curves of FeCo/rGO hybrid nanosheets with different M_{rGO}. In addition, a wireless magnetic field sensing system based on FeCo/rGO hybrid nanosheets

was developed to detect the electromagnetic radiation caused by a working mobile phone in real-time. With large MR at room temperature and low magnetic fields, flexible/adjustable MR performance, and facile fabrication process, the FeCo/rGO hybrid nanosheets can be considered as the appropriate candidate for various applications that demand highly-sensitive and cost-effective MR materials. In addition, we believe that the wireless field sensing system based on the integrated FeCo/rGO hybrid nanosheets magnetic field sensor can benefit the developments of the future connected society and internet-of-things (IoT).

3.1   Introduction

Since the discovery of giant magnetoresistance (GMR), magnetoresistance (MR) sensors have been widely applied for various applications. MR refers to the resistance change of the material under the presence of the external magnetic field. However, the ordinary magnetoresistance (OMR) exhibits less than 1% of MR at the large magnetic field for several Tesla [9]. The discoveries of GMR and tunneling magnetoresistance (TMR) have significantly improved the performance of MR sensors/devices. In magnetic storage, IBM has introduced both GMR and TMR reading heads based on multilayer systems to increase the storage capacity of the hard disk drive (HDD) [10]. The GMR/TMR multilayer systems have brought dramatic improvements in the data density of magnetic storage devices.

Non-destructive monitoring and position sensing are two major applications of MR sensors/devices [11, 12]. By detecting the magnetic field generated by the target probe or the current, MR sensors can transfer the resistance change into various other output signals including voltage or current variations. As the magnetic nanoparticles (MNPs) can generate the stray magnetic fields for biological labelling, the MR sensors were extensively investigated for developing novel biomedical testing platforms [13]. MR biosensors with MNPs testing probes were employed in detecting various biological targets such as bacteria, proteins, viruses, and biomolecules [14-17].

In recent years, magnetic field sensors have been widely applied in industrial applications for precise measurement and control purposes. The demands on highly-sensitive and cost-effective magnetic field sensors became essential. For the previous applications, the highly-sensitive and cost-effective MR sensors significantly reduced the potential cost of mass production and dramatically increased the measurement accuracy of the magnetic field sensors. Moreover, the performance of MR sensors at the low magnetic field is crucial for detections of the limited quantity of magnetic targets, weak electric currents, and low-level electromagnetic fields. Due to the developments of communication technology and personal electronic devices, concerns regarding the negative effects of low-level electromagnetic fields (EMF) on children's brains and organs have been raised [18-20]. Whereas the lack of a sensitive sensing device for quickly detecting low-level EMF leads to difficulties in information collection and decision-making to prevent the adverse effects of EMF generated by personal electronic devices on the environment and health. Compared with traditional Hall effect magnetic field sensors, MR magnetic field sensors offer lower energy consumption and higher sensitivity [21, 22].

Currently, although targets with low magnetic fields are detectable for conventional MR magnetic field sensors, the prolonged fabrication process and strict limitations on the layer thickness of GMR and TMR multilayer systems lead to less cost-efficiency and requirements on specific equipment. Moreover, the TMR multilayer system exhibits a limited working range as the MR rapidly reaches the plateau at a small magnetic field intensity variation. The fast advancements of nanotechnology in recent years have given a rise to nanoconstructured MR materials. The granular/nanogranular MR material is one of the alternative configurations that were developed to reduce the complexity of the multilayer systems. However, most nanostructured granular MR systems display inadequate MR at low magnetic fields (< 10 kOe) and room temperature [6, 8, 23].

The investigations have revealed the unusual phenomena of transport in graphene due to the unusual energy dispersion relation at the Fermi energy [24, 25]. MR is one of the most interesting transport phenomena in graphene, which allows graphene-based materials to contribute to the miniaturized spintronic devices [24, 25]. Multilayered graphene, graphene foams, and hybrid nanocomposites based on graphene (or reduced

75

graphene oxide (rGO)) are potential candidates for fabricating cost-effective and highly-sensitive MR devices/sensors. The layered graphene MR systems require complicated fabrication processes such as chemical vapor deposition (CVD) to control the layer number and position, and extremely low temperature/high magnetic fields are needed for layered graphene MR systems to achieve large MR [26, 27]. To achieve satisfactory MR performance, the graphene foam MR systems require the presence of high external magnetic fields and extreme temperatures [7, 28].

The hybrid graphene (or rGO) nanocomposites are considered as the solution to the current obstacles. The one type of hybrid graphene nanocomposites involves complex processes to introduce disorder or inhomogeneity on monolayer and bilayer graphene, which leads to the unsolved issues of cost and complicated fabrication process [29, 30]. It is more appropriate and accessible to design the hybrid nanocomposites based on rGO due to its facile and low-cost chemical synthesis process and residual function groups for chemical modification. In addition, studies indicate that rGO could show abnormal electrical and magnetic properties because of the alter of conducting π-π^* states in a weakly disordered graphene sheet [31, 32]. However, few investigations were performed, and the current attempts can achieve < 8% of MR at the low magnetic field ($\leq$ 10 kOe) and room temperature, which are not suitable for quickly sensing low-level EMF [33, 34]. Thus, new manufacturing processes and suitable theory of the magneto-transport in hybrid graphene (or rGO) nanocomposites are in high demand to overcome the barriers for the development of graphene-based materials with large MR at low magnetic fields and room temperature.

In this study, we developed the FeCo/rGO hybrid nanosheets with large MR at low magnetic fields and room temperature. The nanoconstructed hybrid material was designed by integrating FeCo nanoparticles (NPs) with rGO as A. A. Abrikosov proposed that large MR could occur in inhomogeneous materials consisting of layered materials with relatively small electron concentration and clusters of metallic atoms [35, 36]. In addition, incorporating inorganic elements or NPs with graphene nanosheets can alter the charge carriers and scatters in graphene, which leads to the change of magnetotransport properties [37, 38].

In this work, we demonstrated the FeCo/rGO hybrid nanosheets that exhibited large MR up to 21 ± 6% at the low magnetic field (10 kOe) and room temperature. FeCo NPs were *in situ* modified onto the surface of rGO as the residual functional groups on the rGO surface provide the nucleation sites [39, 40]. The tunable MR was achieved by simply adjusting the particle density of FeCo NPs on rGO with varying the mass ratio of adding rGO (M_{rGO}). Meanwhile, the quantum magnetoresistance (QMR) model proposed by Abrikosov was applied to understand the possible origin of the large positive MR of FeCo/rGO hybrid nanosheets. In addition, the MR sensor based on FeCo/rGO hybrid nanosheets was seamlessly integrated with a wireless system to achieve real-time detection of the EMF generated by a mobile phone.

3.2   Experimental

3.2.1   Preparation of Reduced Graphene Oxide (rGO)

rGO was obtained by reduction of graphene oxide (GO) with hydrazine, which can introduce defects and amine groups on the rGO surface (**Figure 3.1**) [40]. In specific, 1 g of graphite flake (Graphite flake, natural, -325 mesh, 99.8% (metals basis), Alfa Aesar) was added to 50 mL concentrated sulfuric acid (98%, Caledon Laboratory Chemicals). 3 g of potassium permanganate (≥ 99.0%, ACS, Millipore Sigma) was gradually added while maintaining the temperature of the solution below 10 °C. After proper stirring for 20 mins, the suspension was kept stirring for 22 mins, followed by 8 mins of sonication. The stirring-sonication cycle was repeated 12 times (6 hours in total). The reaction was quenched by adding 200 mL of Milli-Q water into the mixture. The mixture was further sonicated for 2 hours before adjusting the pH to 7 by sodium hydroxide solution (1 M). Before the reduction process, the mixture was sonicated for another hour. The reduction process was carried out by adding 50 mL of hydrazine hydrate (50 - 60%, Sigma-Aldrich) solution into the mixture, and the temperature of the mixture was increased to 90 °C for 3 hours. The black rGO precipitates were simply collected by high-speed centrifugation and washed with 1 M hydrochloric acid (Caledon Laboratory Chemicals).
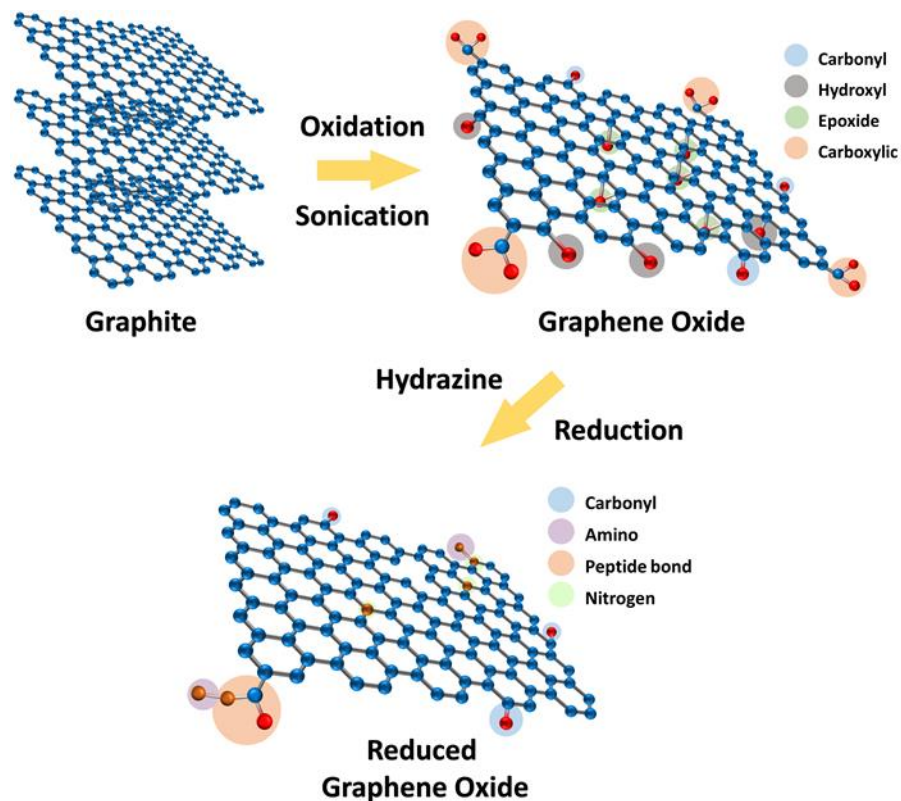
Figure 3.1 Schematic illustration of the reduced graphene oxide (rGO) preparation process.

3.2.2   Preparation of FeCo/rGO Hybrid Nanosheets

FeCo NPs were *in situ* grown on the surface of rGO *via* a modified polyol process (**Figure 3.2**) [41]. Briefly, 2.5 mmol of ferrous chloride tetrahydrate (FeCl$_2\cdot$4H$_2$O, puriss. p.a., $\geq$ 99.0%, Sigma-Aldrich), 2.5 mmol of cobaltous acetate tetrahydrate (Co(OAc)$_2$ 4H$_2$O, ACS reagent, $\geq$ 98.0%, Sigma-Aldrich), 200 mmol of sodium hydroxide (ACS reagent, $\geq$ 97.0%, pellets, Sigma-Aldrich), and varied mass of as-prepared rGO were added into 100 mL of ethylene glycol (EG, Fisher chemical). Samples were prepared with different mass ratios of rGO (M$_{rGO}$) added to the reaction. The samples (M$_{rGO}$ increasing from 10 wt.% to 50 wt.% with an interval of 10 wt.%) are denoted to Sample 1 to 5. After proper mixing for 20 minutes, the suspension was further sonicated to allow the rGO to disperse uniformly in ethylene glycol. The mixture was heated to 130 °C for 1 hour under nitrogen gas protection. The black precipitate was washed by ethanol,

centrifuged, and freeze-dried. FeCo NPs were synthesized with the same polyol process without adding rGO into the reaction.
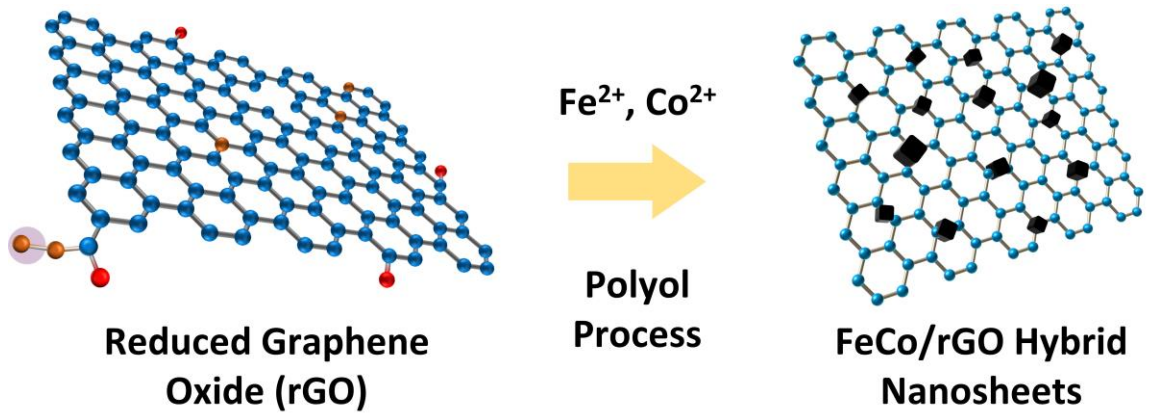
Figure 3.2 Schematic illustration of the FeCo/rGO hybrid nanosheets preparation process.

3.2.3   Magnetoresistance Measurement

Each sample with 10 mg was pressed with a dimension of 1 cm × 1 cm, and the thickness was kept at 150 µm. The MR measurement was performed by the Model 74046 MR probe attached to the vibrating sample magnetometer (VSM, LakeShore 7407). In the MR measurement and mathematical calculation part, the MR (%) is defined by the following equation:

$$MR(\%) = \frac{R - R_0}{R_0} \times 100\% \qquad (3.1)$$

The resistance change (ΔR, Ω) is defined by the equation below

$$\Delta R = R - R_0 \qquad (3.2)$$

where R is the total resistance (Ω) of the sample under the presence of an external magnetic field and R_0 the sample resistance (Ω) at zero magnetic field.

3.2.4   Materials Characterization

Transmission electron microscope (TEM) micrographs and electron diffraction patterns were taken by Philips CM-10 (TEM) operating at 80 kV. A Hitachi S-3400N scanning electron microscope (SEM) attached with the INCA PentaFET-x3 system (Oxford Instruments) was used to obtain SEM micrographs and energy-dispersive X-ray spectra (SEM-EDX) of FeCo/rGO hybrid nanosheets. The magnetic property and MR measurements were performed by the vibrating sample magnetometer (VSM, LakeShore 7407, moment measure range: 10^{-7} to 10^3 emu; field accuracy: "± 0.05%" full scale). The PHI Quantera scanning X-ray microprobe (X-ray source: Al Kα, sputter rate: 2.7 nm min-1, take-off angle: 45°) was utilized to measure the X-ray photoelectron spectra (XPS) and depth profile of FeCo/rGO hybrid nanosheets. X-ray diffraction spectra (XRD) of the samples were measured by Rigaku rotating-anode X-ray diffractometer (XRD, Co-Kα radiation).

3.2.5   Mathematical Calculation

The mathematical calculation for the quantum magnetoresistance (QMR) model was performed by MATLAB (The MathWorks), Python(x,y) (https://python-xy.github.io/), and 1stOpt (7D-Soft High Technology Inc.), which gave us similar results.

3.2.6   Constructing Wireless Magnetic Field Sensing System

The ZigBee radio module unit (XBee®/XBee-PRO® ZigBee RF Modules) was produced by Digi International (Digi International, Inc.) (**Figure 3.3**). All electronic devices involved were purchased from Digi-Key Electronics (https://www.digikey.com/). The magnetic field sensor chip was connected to a resistor with appropriate resistance to perform in the physical pins' function range of the ZigBee module.

Figure 3.3 Picture of the XBee® ZigBee radio module unit (Digi International).

3.3 Results and Discussion

3.3.1 Developing FeCo/rGO Hybrid Nanosheets for Magnetic Field Sensing

rGO was obtained by reduction of graphene oxide (GO) with hydrazine, which can introduce defects and amine groups on the rGO surface [42]. In a modified one-pot process, the mixture of iron (Fe^{2+}) salt and cobalt (Co^{2+}) salt can be reduced to Fe^0 and Co^0. FeCo NPs deposited on the surface of rGO through reacting with sodium hydroxide in ethylene glycol (EG) at 130 °C with an inert (N_2) atmosphere [41]. In the reaction, the metal hydroxides were reduced to obtain FeCo NPs. The synthesis process includes dehydration (1) and oxidation (2) reactions in ethylene glycol [41].

$$2CH_2OH-CH_2OH \rightarrow 2CH_3CHO + 2H_2O \qquad (1)$$

$$2CH_3CHO + M(OH)_2 \rightarrow CH_3COCOCH_3 + 2H_2O + M^0 \qquad (2)$$

Different amounts of rGO were introduced in the one-pot reaction. The as-prepared FeCo/rGO hybrid nanosheets were denoted as Sample 1 to Sample 5 based on the increasing mass ratio of rGO (M_{rGO}) from 10 wt.% to 50 wt.% with an interval of 10 wt.%.

FeCo/rGO hybrid nanosheets were studied with the transmission electron microscope (TEM). As M_{rGO} increases from 10 wt.% to 50 wt.%, the average particle size of the FeCo NPs growing on the rGO decreases from 220 ± 50 nm to 89 ± 20 nm correspondingly (**Figure 3.4**). The cubic structure of NPs is observed in all 5 samples. The size distribution of FeCo NPs is narrower when M_{rGO} increases to 50 wt.%. The decrease in particle size of FeCo NPs with increasing M_{rGO} can be related to the increase of nucleation sites on rGO as the *in situ* deposition occurs on the defects and residual functional groups of rGO.

The selected area electron diffraction (SAED) patterns of Sample 1 and Sample 5 are shown in the inset images of **Figure 3.4**. The diffraction ring patterns indicate the body-centered cubic (BCC) structure of the FeCo NPs with (110), (200), and (211) crystal planes. The result is similar to the reported FeCo nanostructures [43, 44]. **Figure 3.4e** shows the HRTEM micrograph of Sample 5 that displays the BCC FeCo NPs *in situ* deposited on rGO with an interplanar distance (*d*) of 0.20 nm.

To further investigate the crystal structures, FeCo/rGO hybrid nanosheets were measured by X-ray powder diffraction (XRD). In **Figure 3.5**, the XRD profile of rGO shows two broad diffraction peaks around 23.5° and 43.3° representing (002) and (100) planes of rGO, respectively. The typical peak of GO at $2\theta = 11°$ in the XRD profile disappears after the hydrazine reduction, which indicates the successful reduction of the rGO [45]. The XRD profile of FeCo NPs displays two peaks at 44.8° and 65.3° referring to (110) and (200) crystal planes of the BCC FeCo (CoFe PDF# 49-1568) [46]. Furthermore, no single Co phase is observed in the pattern, which confirms that the BCC FeCo is successfully produced by the polyol process [46, 47]. Meanwhile, since all the products are stored in the ambient environment, the possibility of the presence of the Fe metal can be eliminated [46].
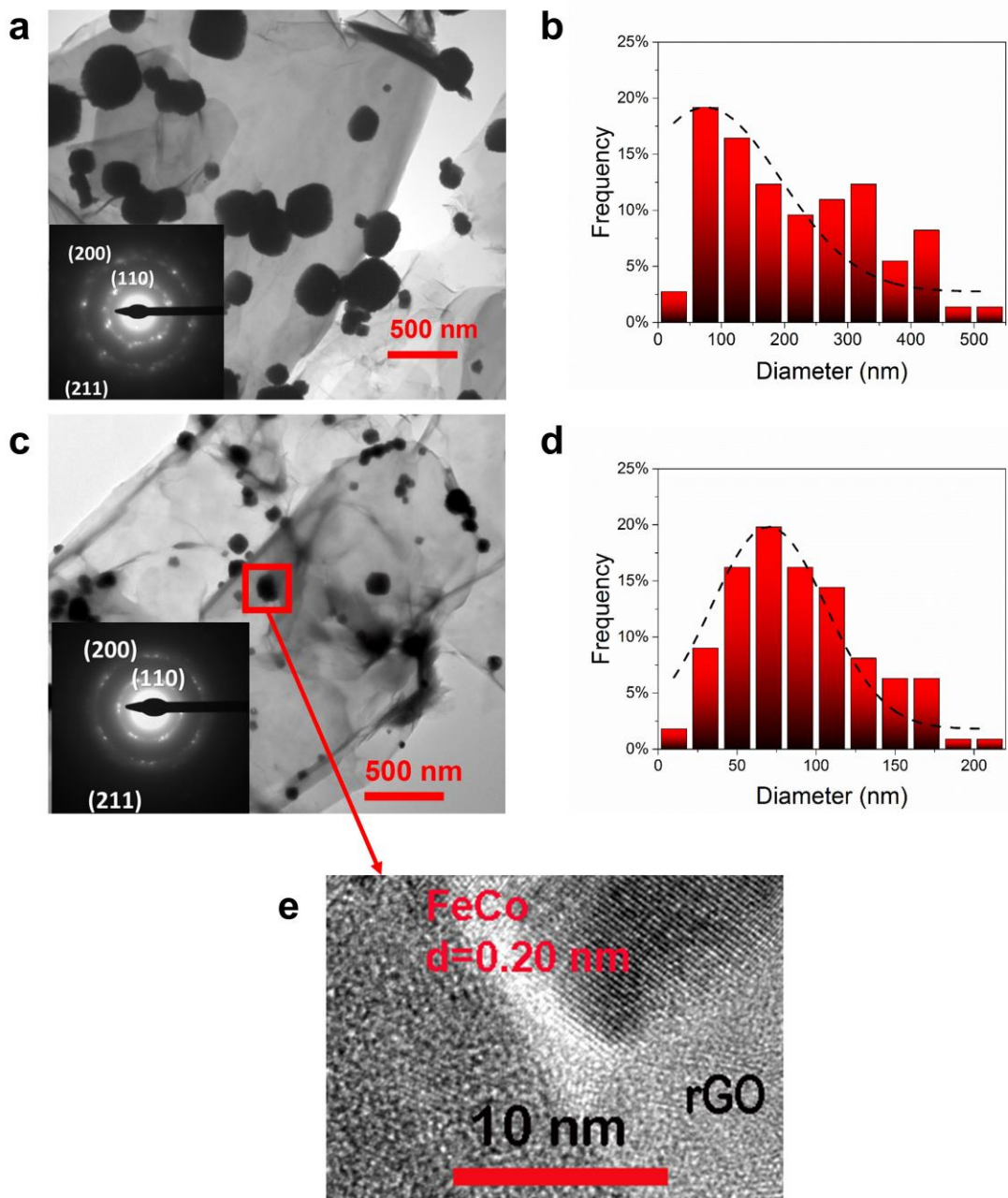
Figure 3.4 TEM micrographs of FeCo/rGO hybrid nanosheets. (a) TEM micrograph of Sample 1 (M_{rGO} = 10 wt.%), and the small inset is the SAED pattern of Sample 1; (b) Size distribution of Sample 1; (c) TEM micrograph of Sample 5 (M_{rGO} = 50 wt.%), and the small inset is the SAED pattern of Sample 5; (d) Size distribution of Sample 5; (e) HRTEM micrograph of Sample 5.

In the XRD data of FeCo/rGO hybrid nanosheets (i.e., Sample 2 (M_{rGO} = 20 wt.%)), two diffraction peaks of (110) and (200) crystal planes of the BCC FeCo are observed at similar positions with FeCo NPs. The presence of the diffraction peak at 23.5° indicates that (002) plane of rGO remains in the FeCo/rGO hybrid nanosheets, and part of the peak at 43.3° referring to (100) plane of rGO overlaps with the (200) crystal plane of BCC FeCo at 44.8°. Thus, the FeCo NPs on FeCo/rGO hybrid nanosheets maintain the BCC FeCo structure. In addition, we notice that the crystal structure and the chemical composition of NPs on rGO may change as M_{rGO} increases beyond 50% due to the interference of imported ions/impurities in a large amount of rGO, which will be discussed in another paper of our group.
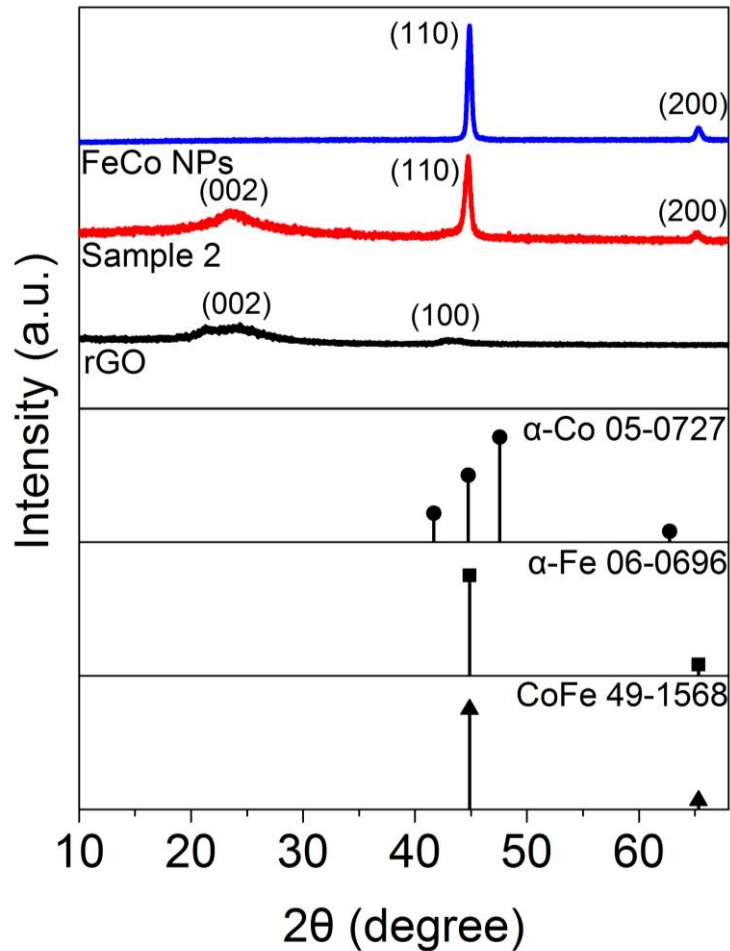
Figure 3.5 X-ray powder diffraction (XRD) profile of FeCo NPs, FeCo/rGO hybrid nanosheets (i.e., Sample 2, M_{rGO} = 20 wt.%), and rGO.

The scanning electron microscope (SEM) micrographs and energy-dispersive X-ray spectra (SEM-EDX) are shown in **Figure 3.6**. The SEM micrographs indicate the presence of the rGO with FeCo NPs grafted on the surface, which is consistent with the results of TEM characterization. To investigate the chemical composition of the FeCo/rGO hybrid nanosheets with various M_{rGO} amounts, the SEM-EDX was applied. Four major elements (i.e., C, O, Fe, and Co) are detected in the FeCo/rGO hybrid nanosheets with different M_{rGO} (10 wt.% and 50 wt.%). A significant increase in carbon content is observed due to the rise of rGO in the sample. Meanwhile, the decline of the signals of iron and cobalt elements is noticed as the result of the increase of M_{rGO}.
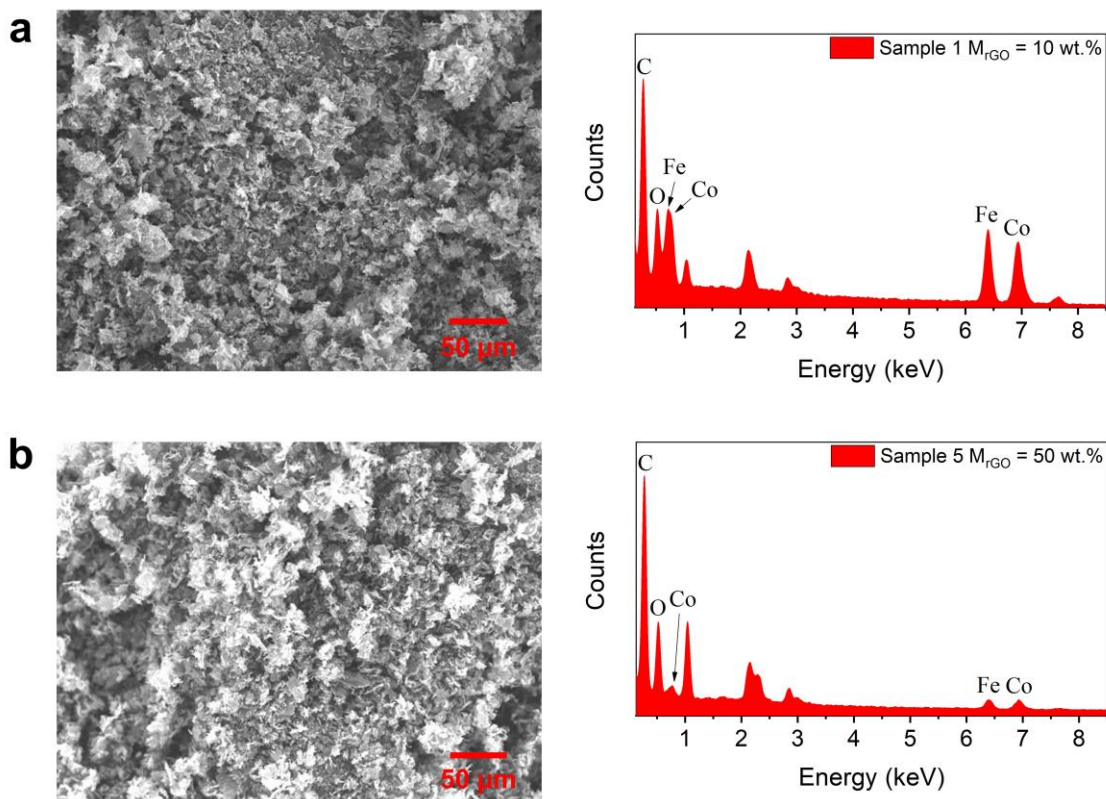
Figure 3.6 SEM micrographs and corresponding SEM-EDX of (a) sample 1 (M_{rGO} = 10 wt.%) and (b) sample 5 (M_{rGO} = 50 wt.%).

The atomic ratio of FeCo NPs in FeCo/rGO hybrid nanosheets decreases from 9.6 ± 0.4 at.% to 1.3 ± 0.1 at.% as M_{rGO} increases from 10 wt.% to 50 wt.%. In addition, as shown in **Figure 3.7**, the atomic ratio of Fe:Co is approximately 1:1 to all samples as the M_{rGO}

increases from 10 wt.% to 50 wt.%, which is consistent with the XRD data. The weight percentage (wt.%) of FeCo NPs in samples is estimated as shown in **Figure S3.1**. Sample 1 (M_{rGO} = 10 wt.%) shows 39 ± 2 wt.% of FeCo NPs, and Sample 5 (M_{rGO} = 50 wt.%) shows 9 ± 1 wt.% of FeCo NPs. The exponential fitting curve ($y = 7.9 + 31.9e^{((x-32.1)/67.1)}$, $R^2 = 0.965$) depicts the relationship between the weight percentage of FeCo NPs and M_{rGO}.
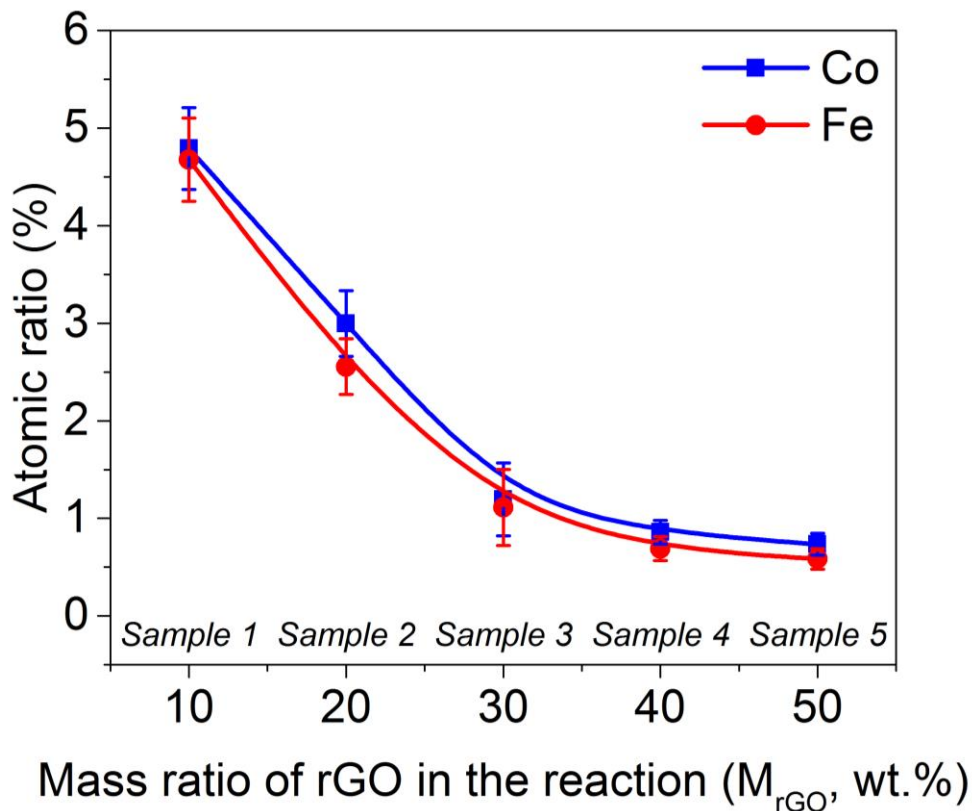
Figure 3.7 The atomic ratio of Fe and Co in FeCo/rGO hybrid nanosheets with different M_{rGO}.

X-ray photoelectron spectroscopy (XPS) survey and in-depth XPS were performed to analyze the chemical status of the major elements in FeCo/rGO hybrid nanosheets. The peaks of O 1s, C 1s, N 1s, Co 2p, and Fe 2p are observed in the XPS survey scan spectra (**Figure 3.8**) of Sample 2, 4, and 5 (M_{rGO} = 20 wt.%, 40 wt.%, and 50 wt.%). The O 1s peak indicates the presence of the remaining oxygen function groups that work as 'anchor spot' of FeCo NPs together with the nitrogen residues [48, 49]. Meanwhile, the presence of the N 1s peak is due to the hydrazine reduction process of the rGO [50].
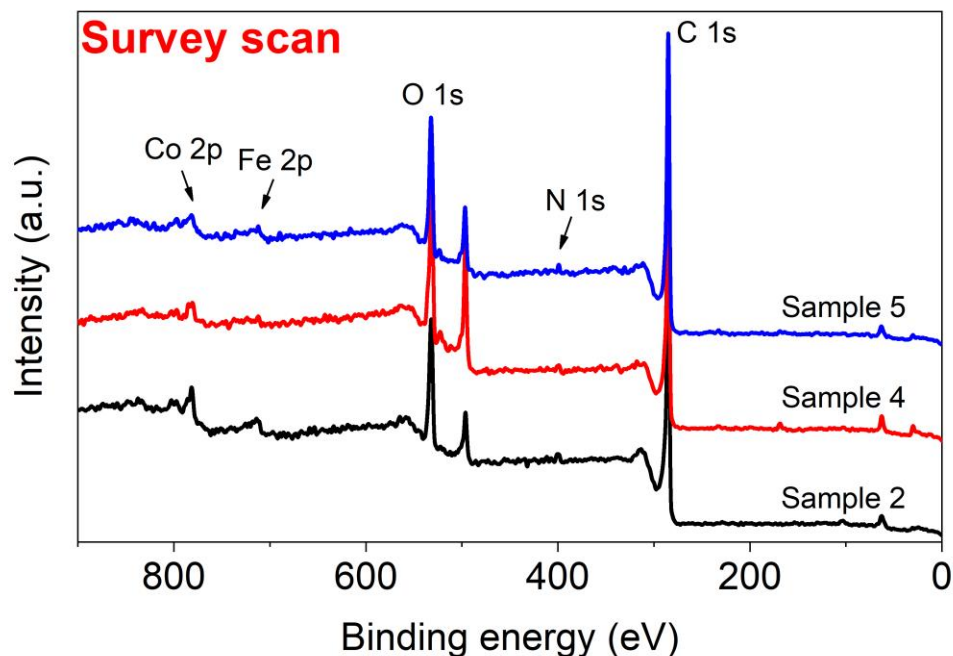
Figure 3.8 The XPS survey spectra of FeCo/rGO hybrid nanosheets with different M_{rGO} (20 wt.%, 40 wt.%, and 50 wt.%).

High resolution XPS spectra of C 1s and N 1s are shown in **Figure 3.9**. All samples exhibit comparable deconvoluted peaks of C 1s spectra. The C sp^2 and C sp^3 peaks are observed at 284.6 eV and 285.6 eV [50-54]. The epoxy groups are not observed in the samples, which indicates the successful reduction of GO.

The high resolution N 1s XPS spectra of Sample 2, 4, and 5 indicate the existence of pyridinic N (Sample 2: 398.6 eV, Sample 4: 398.5 eV, Sample 5: 398.4 eV) and amine groups (Sample 2: 400.1 eV, Sample 4: 400.0 eV, Sample 5: 399.9 eV). The pyrrolic N peaks are observed in the spectra of Sample 4 (399.5 eV) and Sample 5 (399.4 eV) [55-57]. As shown in **Figure 3.9**, the proportion of pyrrolic N raises as the M_{rGO} increases to 50 wt.%. Meanwhile, the peak that is attributed to pyrrolic N is not observed in Sample 2 (M_{rGO} = 20 wt.%), which is possibly due to the formation of FeCo NPs on the rGO surface since the pyrrolic N exhibits a strong chelation effect with ions of Fe and Co [49]. Less M_{rGO} provides limited pyrrolic N spots, and most of the spots are taken by FeCo NPs during the *in situ* deposition. On the other hand, the increase of rGO in the reaction

introduces a large quantity of pyrrolic N sites, which are not completely occupied by the FeCo NPs.
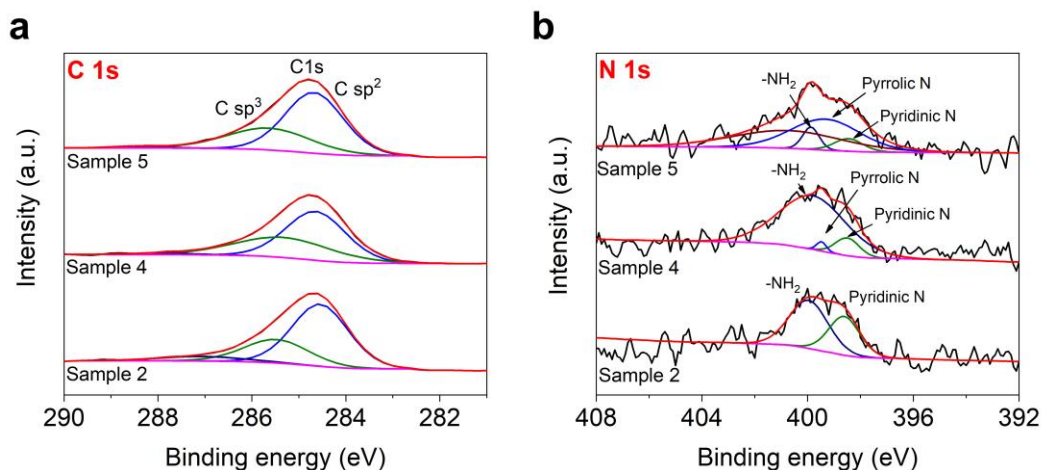
Figure 3.9 High resolution XPS spectra of FeCo/rGO hybrid nanosheets: (a) C 1s and (b) N 1s.

The high resolution Co 2p XPS spectra of samples are shown in **Figure 3.10**. Peaks at 778.8 eV, 782.8 eV, and 793.5 eV (Sample 2, 4, and 5) are attributed to Co $2p_{3/2}$, Co $2p_{3/2}$ (satellite), and Co $2p_{1/2}$, respectively. The spin-orbit splitting peaks of Co indicate the presence of the zerovalent metallic states Co elements [58, 59]. The peaks at 707.4 eV, 713.4 eV, and 721.4 eV in the high resolution Fe 2p spectra of Sample 2, 4, and 5 correspond to Fe $2p_{3/2}$, Fe (III) $2p_{3/2}$, and Fe $2p_{1/2}$ [48, 60]. The peaks at 707.3 ~ 707.4 eV are attributed to the presence of metal Fe [61, 62].

To further study the oxidation of Fe in samples, XPS depth profiling characterization was performed on FeCo/rGO hybrid nanosheets (**Table S3.1-S3.4**). The atomic ratio of the Fe element increases with increasing sputter time as the characterization depth increases from 0 nm to 81 nm. Meanwhile, the atomic ratio of the oxygen element decreases simultaneously. The ratio of Fe (0) over oxidized Fe (II/III) increases with increasing sputter time (**Figure S3.2**). Therefore, the oxidized iron remains on the surface as all samples are stored in the ambient environment.

It is noticed that XRD provides the characterization with a larger penetration depth (micrometer level) compared with XPS (surface characterization). Thus, the results of XPS do not conflict with the results of XRD that indicate the formation of the BCC phase of FeCo NPs on rGO. Furthermore, the ratio of Fe (III) $2p_{3/2}$ peak over Fe $2p_{3/2}$ peak increases with increasing M_{rGO}. The decrease of particle size and the increase of particle density of FeCo NPs with increasing M_{rGO} can enlarge the surface area of NPs, which leads to more oxidation on the surface of NPs detected by XPS.
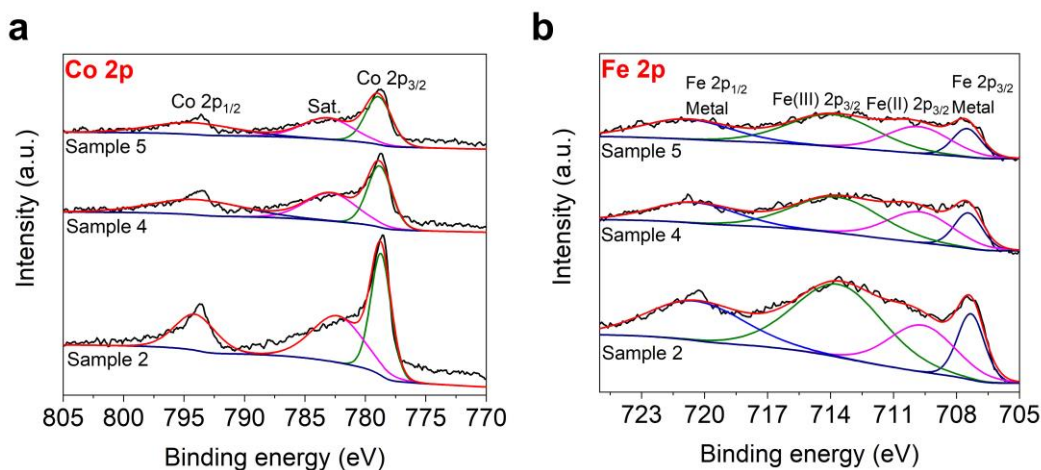
Figure 3.10 High resolution XPS spectra of FeCo/rGO hybrid nanosheets: (a) Co 2p and (b) Fe 2p.

3.3.2 Special Magnetoresistance of FeCo/rGO Hybrid Nanosheets

The magnetic hysteresis loops were measured by vibrating sample magnetometer (VSM) at ambient temperature (**Figure 3.11,** the VSM result of rGO is shown in **Figure S3.3**). The FeCo/rGO hybrid nanosheets exhibit ferromagnetic behaviours. The coercivities of all samples are less than 250 Oe. The saturation magnetizations (M_S) at 10 kOe for FeCo/rGO hybrid nanosheets (M_{rGO} = 10 wt.% - 50 wt.%) are 74 emu/g, 36 emu/g, 28 emu/g, 14 emu/g, and 12 emu/g, respectively (**Table S3.5**). The M_S (emu/g) of the FeCo/rGO hybrid nanosheets decreases with increasing M_{rGO}. All samples of FeCo/rGO hybrid nanosheets display very small M_r/M_S ratios, which stems from the thin thickness. Moreover, to characterize the magnetic anisotropy of as-prepared FeCo/rGO hybrid nanosheets, the samples were measured with parallel and perpendicular configurations.

The magnetic anisotropy of FeCo/rGO hybrid nanosheets is not significant (**Figure 3.11b**).
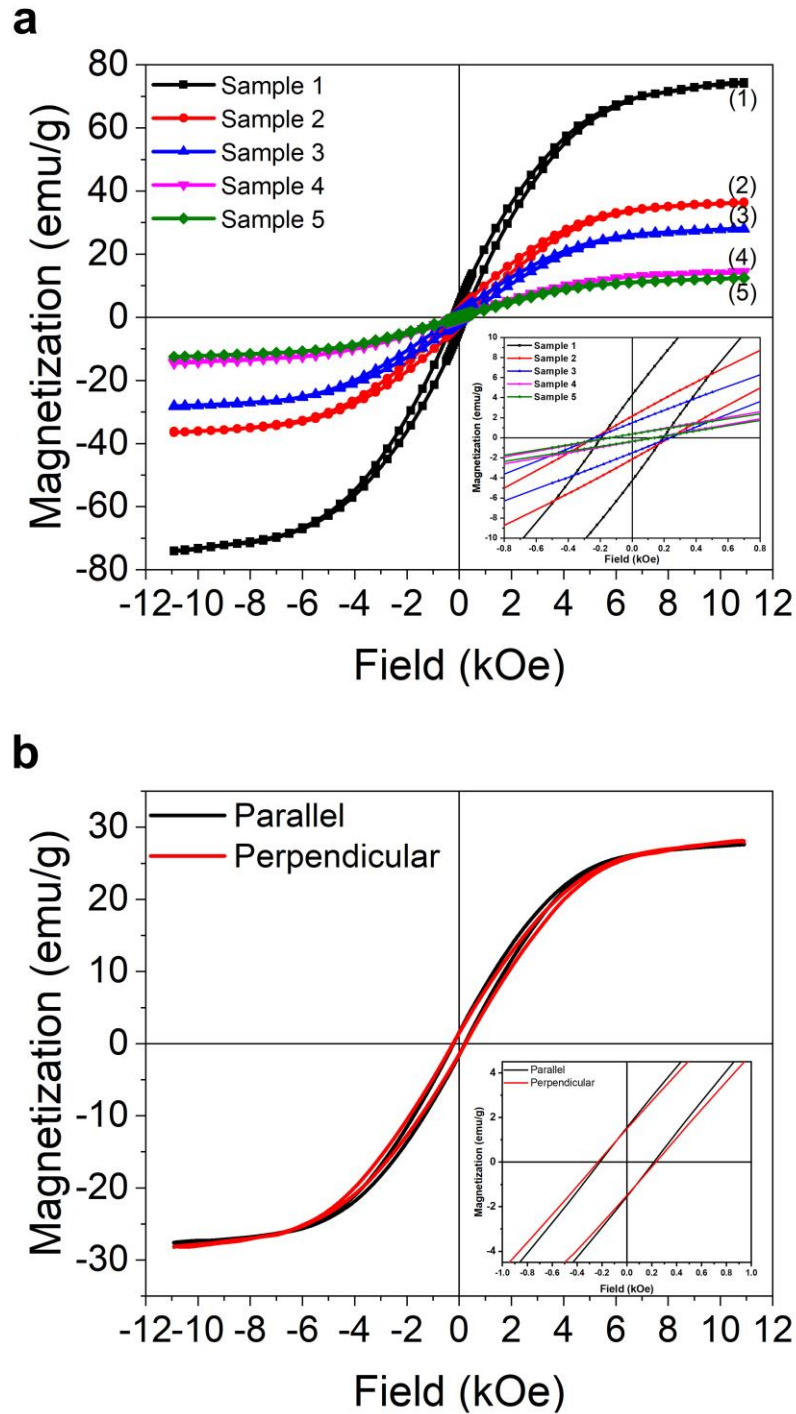
Figure 3.11 Magnetic hysteresis loops of FeCo/rGO hybrid nanosheets. (a) Magnetic hysteresis loops of samples with different M_{rGO} (M_{rGO} = 10 wt.%, 20 wt.%, 30 wt.%,

40 wt.%, and 50 wt.%). (b) Magnetic hysteresis loops of Sample 3 (M$_{rGO}$ = 30 wt.%) at parallel and perpendicular magnetic fields.

The magnetoresistance (MR, %) curves of FeCo/rGO hybrid nanosheets were measured by the 4-pin probe of LakeShore 7407. To investigate the MR (MR (%), $\Delta R/R_0$) and further understand the relationship between MR of FeCo/rGO hybrid nanosheets and the mass ratio of adding rGO (M$_{rGO}$), the MR curves of Sample 1-5 were obtained as the magnetic field increased from 0 to 10 kOe at room temperature. As shown in **Figure 3.12**, the FeCo/rGO hybrid nanosheets with different M$_{rGO}$ exhibit positive magnetoresistance (PMR) as the magnetic field increases from 0 to 10 kOe. The average increasing rates of MR (%) per kOe of FeCo/rGO hybrid nanosheets increase from $0.45 \pm 0.10\%$ (M$_{rGO}$ = 10 wt.%) to $2.50 \pm 0.07\%$ (M$_{rGO}$ = 50 wt.%).
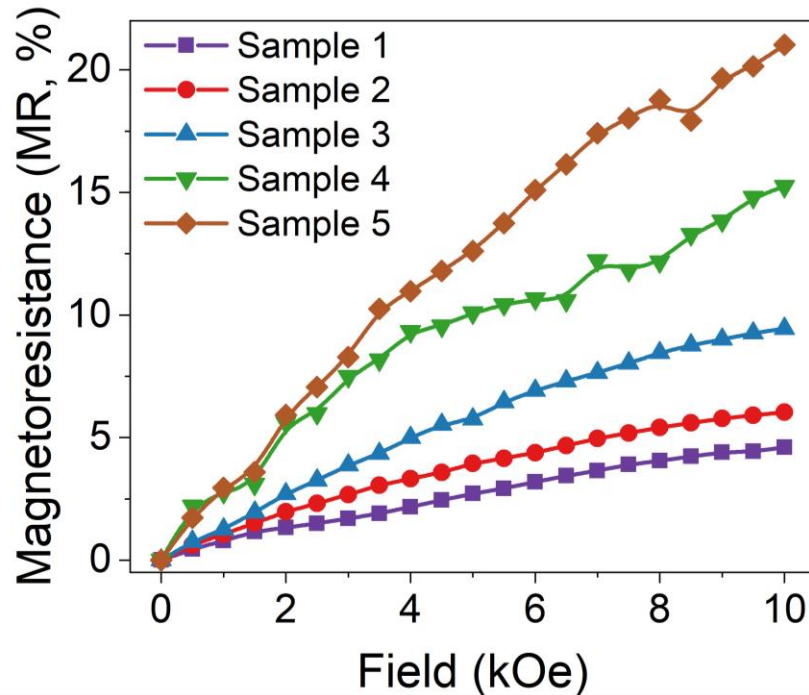
Figure 3.12 Magnetoresistance (MR, %) of FeCo/rGO hybrid nanosheets (Sample 1 - Sample 5, M$_{rGO}$ = 10 wt.% - 50 wt.%) at room temperature (magnetic field increases from 0 to 10 kOe).

Figure 3.13 shows that the MR at 10 kOe increases as M$_{rGO}$ increases from 10 wt.% to 50 wt.%. The average MR at 10 kOe of FeCo/rGO hybrid nanosheets with various M$_{rGO}$

(Sample 1 - 5, M_{rGO} = 10 wt.% - 50 wt.%) are 5 ± 1%, 6 ± 1%, 9 ± 4%, 15 ± 5%, and 21 ± 6%, respectively. A very high MR (21 ± 6%) is achieved by FeCo/rGO hybrid nanosheets with 50 wt.% of M_{rGO} at room temperature and low magnetic field. Thus, the tunable MR is achieved by simply adjusting the mass ratio of adding rGO (M_{rGO}) in the synthesis of FeCo/rGO hybrid nanosheets.
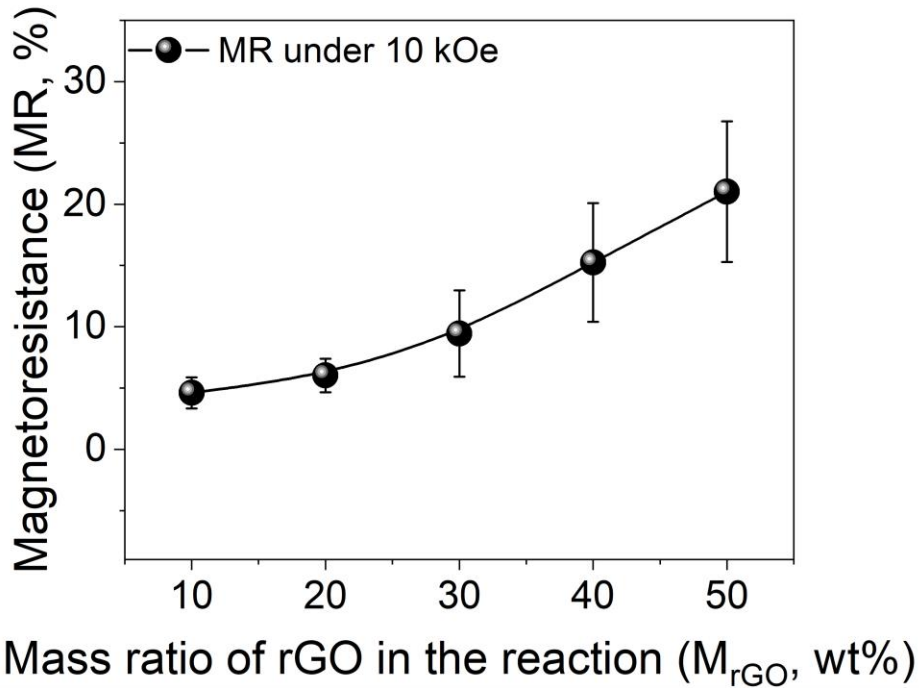
Figure 3.13 Magnetoresistance (MR, %) of FeCo/rGO hybrid nanosheets (Sample 1 - Sample 5, M_{rGO} = 10 wt.% - 50 wt.%) at 10 kOe (room temperature).

The quantum magnetoresistance (QMR) model proposed by A. A. Abrikosov is applied to understand the MR of the FeCo/rGO hybrid nanosheets. As Abrikosov proposed, QMR can happen in complex materials with 'charge reservoirs' (atom/layer with higher electron density) embedding into the layered materials possessing relatively lower electron density [35, 36]. The electron density of FeCo is 1.1×10^{25} cm^{-3}, and the electron density of graphene is 2.5×10^{16} cm^{-3} (300 K), which meets the condition calculated by Abrikosov (n < 10^{18} cm^{-3}) [35, 63, 64]. In our assumption, FeCo NPs play the role of charge reservoirs, and FeCo NPs hinder the transportation of electron carriers on FeCo/rGO hybrid nanosheets [65]. As per Abrikosov's QMR model, the total resistance

(in resistivity) of complex material (ρ_{xx}) can be expressed by Equation 3.3 (the size differences of the testing samples are neglectable in our study) [35]

$$\rho_{xx} = \frac{HN_i}{\pi e c n_0^2} \cdot \frac{\sinh(^1/_\theta)}{\cosh(^m/_\theta) + \cosh(^m/_\theta)} \qquad (3.3)$$

where n_0 is the excess electron density, H the magnetic field intensity, N_i the concentration of scattering centers, e the elementary electron charge, c the invariant speed, $\theta = T/t$ ($2t$ is the bandwidth), $m = \mu/t$, $h = H/H_0$, and $H_0 = (\pi \cdot n_0 \cdot c \cdot d)/e$ (d is the interlayer distance). Abrikosov's QMR model indicates that $m = sin(\pi/h)$ as $T = 0$, which is applied to simplify the modified equation. Meanwhile, the theoretical factor ρ_{xx} is more close to resistance change (ΔR) instead of actual total resistance since it equals zero when $H = 0$ [35]. Therefore, the relationship between magnetic field intensity ($x = H$) and resistance change ($y = \Delta R$) in our case can be expressed by Equation (3.4).

$$y = b \cdot a \cdot x \cdot \left\{ \frac{\sinh(\frac{1}{c})}{\cosh\left[\frac{\sin(^\pi/_{ax})}{c}\right] + \cosh\left[\frac{\sin(^\pi/_{ax})}{c}\right]} \right\} \qquad (3.4)$$

Three different parameters (a, b, and c) are introduced based on Equation 3.3, where $a = 1/H_0$, $b = (N_i \cdot d)/(n_0 \cdot e^2)$, and $c = \theta$.

In our case, c is set at 1.5 for fitting optimization since the QMR model has been used to study the MR at different temperatures (including room temperature) [27, 35, 36]. The resistances (Ω) of FeCo/rGO hybrid nanosheets increase when the magnetic field increases from 0 to 10 kOe. As M_{rGO} increases from 10 wt.% (Sample 1) to 50 wt.% (Sample 5), the average increasing rate of resistance (in resistance per kOe) rises from 0.0837 Ω/kOe to 0.9282 Ω/kOe (**Table S3.6**). **Figure 3.14** shows that the QMR model exhibits good agreements with the MR of FeCo/rGO hybrid nanosheets. The fitting results are displayed in **Figure 3.14a-e**; for Sample 1: $a \approx 0.0002238$, $b \approx 1.36584$, and for Sample 5: $a \approx 0.0002243$, $b \approx 15.18023$. Factor b is related to $(N_i \cdot d)/(n_0 \cdot e^2)$, and the difference between Sample 1 and Sample 5 in terms of factor a ($a = e/(\pi \cdot n_0 \cdot c \cdot d)$) is

negligible. Therefore, the concentration of scattering centers (N_i) is the dominating parameter for the increase of MR.
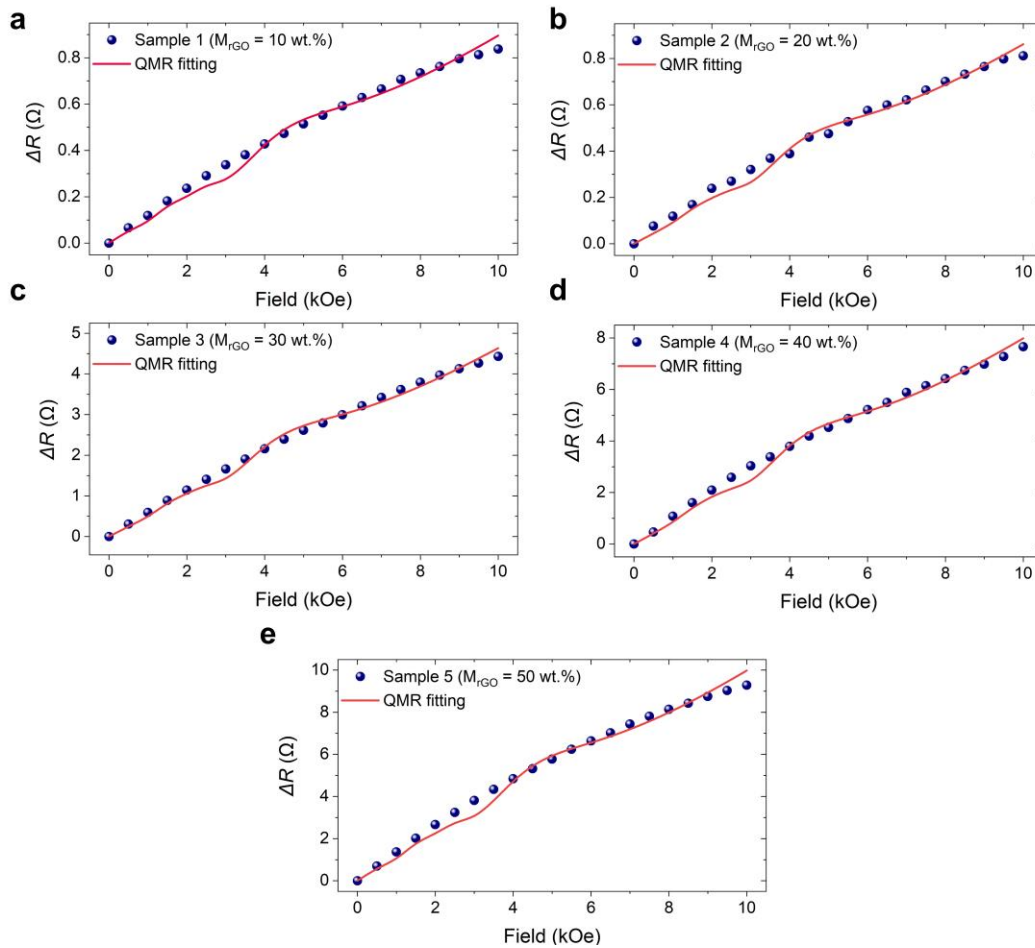
Figure 3.14 Fitting results of QMR model on FeCo/rGO hybrid nanosheets with different M$_{rGO}$: (a) Sample 1 ($R^2 \approx 0.996$), (b) Sample 2 ($R^2 \approx 0.996$), (c) Sample 3 ($R^2 \approx 0.997$), (d) Sample 4 ($R^2 \approx 0.997$), and (e) Sample 5 ($R^2 \approx 0.991$).

In our study, the increase of N_i is directly related to the particle density of metallic nanoparticles (FeCo NPs) on rGO (**Figure 3.15**). It is noted that the particle density of FeCo NPs rises as the nucleation sites of rGO increase with increasing M$_{rGO}$, which also leads to the decrease of particle size of FeCo NPs [65, 66]. The phenomenon is observed in the results of TEM and scanning electron microscope (SEM). **Figure 3.15c, d** show the SEM micrographs of Sample 1 (M$_{rGO}$ = 10 wt.%) and Sample 5 (M$_{rGO}$ = 50 wt.%). Thus, the results suggest that improving the particle density of FeCo NPs on rGO can enhance the scattering effect. Meanwhile, tunable MR is achieved by adjusting the

particle density of FeCo NPs on the rGO surface, which can be controlled by varying the quantity of the nucleation site.
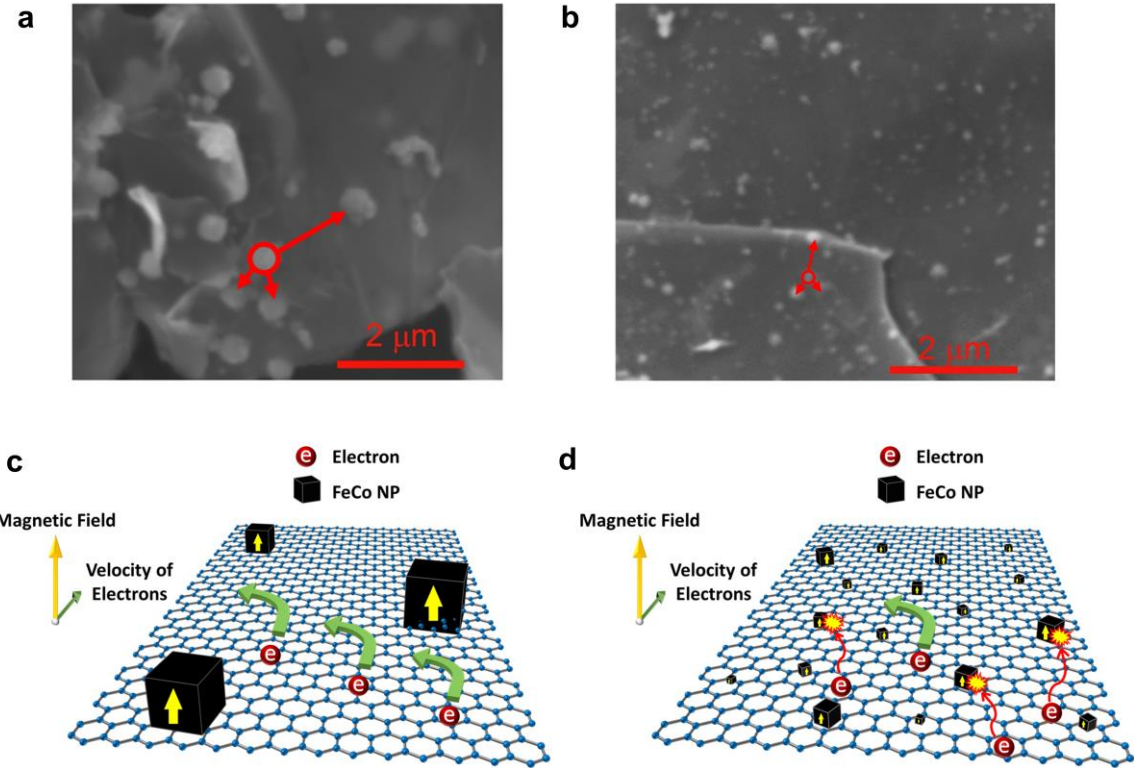
Figure 3.15 SEM micrographs of, (a) Sample 1 and (b) Sample 5 (Average distance between random FeCo NPs (red circle) and three closest NPs: Sample 1 ≈ 790.21 nm and Sample 5 ≈ 410.21 nm). Schematic illustration of the conduction process based on Abrikosov's model: (c) Sample 1 with fewer scattering centers and (d) Sample 5 with more scattering centers (FeCo NPs on rGO acting as the scattering centers).

3.3.3 Fabricating the Magnetoresistance Wireless Field Sensor System with FeCo/rGO Hybrid Nanosheets

To harness the FeCo/rGO hybrid nanosheets with special MR in the real-time detection of the low-level EMF, we integrated the magnetic field sensor based on FeCo/rGO hybrid nanosheets into a wireless communication system. As shown in **Figure 3.16,** three components of the wireless magnetic field sensing system are (i) a data center, (ii) a wireless FeCo/rGO hybrid nanosheets-based magnetic field sensor, and (iii) a wireless

signal indicator. ZigBee protocol is adopted, and three ZigBee radio modules (i.e., XBee-Pro® ZigBee RF module, products of Digi International) are used for wireless communications.
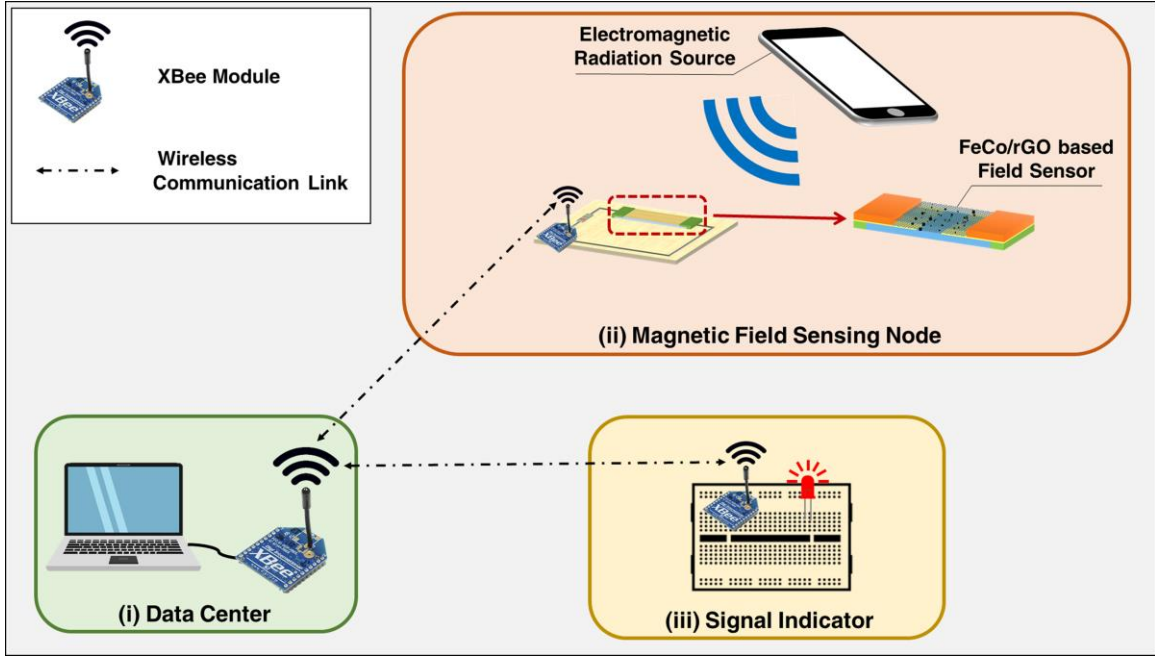
Figure 3.16 Schematic diagram of the wireless magnetic field sensing system based on FeCo/rGO hybrid nanosheets.

The data center (i) is formed up for data collection and visualization by linking an XBee module to the computer. The wireless magnetic field sensing node (ii) is made by combining an XBee module and the FeCo/rGO hybrid nanosheets-based magnetic field sensor on a motherboard. As shown in **Figure 3.17a**, the FeCo/rGO hybrid nanosheets-based magnetic field sensor is kept on a glass slide to easily connect with the XBee module through a motherboard. The wireless signal indicator (iii) is built by connecting a light-emitting diode (LED) with an XBee module (**Figure 3.17b**).
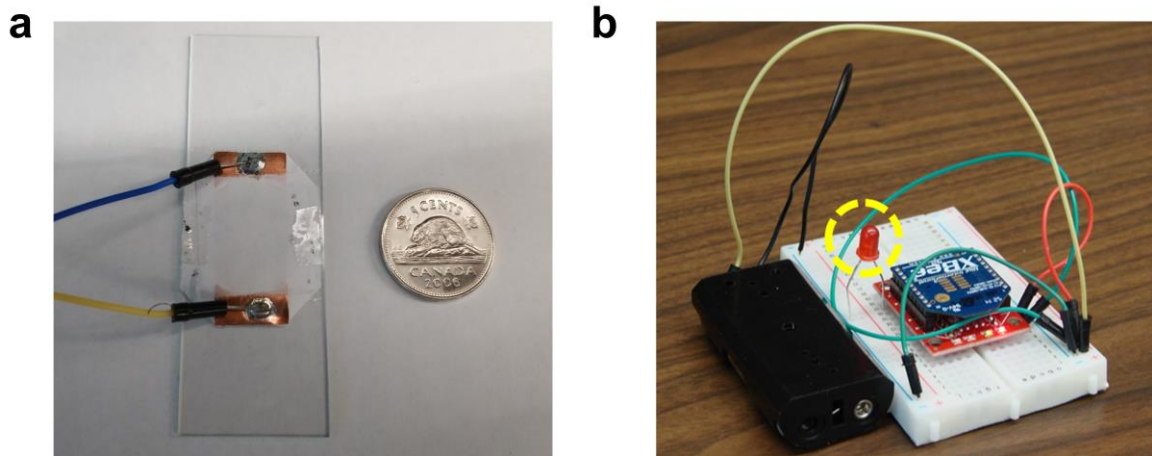
Figure 3.17 (a) Picture of the magnetic field sensor based on FeCo/rGO hybrid nanosheets (ii). (b) Picture of the signal indicator (iii) in the sensing system (LED marked with yellow circle).

As the resistance of the magnetic field sensor is affected by the external electromagnetic radiation source, the data center (i) receives the disturbing of voltage sent from the wireless magnetic field sensing node (ii) and sends a remote command to the wireless signal indicator (iii) to turn on the LED as an alert (**Figure 3.18**).

It is noted that the average maximum power density of a working mobile phone is in a range of 0.01 - 0.1 mW/cm^2, ~100 nT [67]. Previous studies have shown that long-term exposure under low-level (1.0 - 2.5 mW/cm^2, 1 mT) electromagnetic radiation could lead to potential health risks. In contrast with the conventional magnetic field sensing devices, our wireless magnetic field sensing system based on FeCo/rGO hybrid nanosheets shows superiorities in portability, real-time detection, and flexible data collection/communication [68, 69].
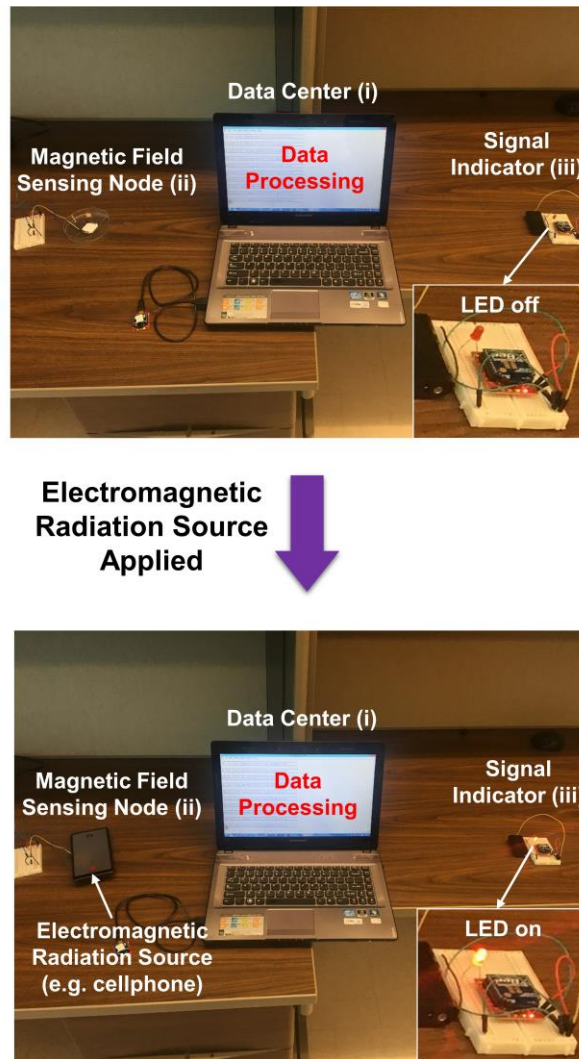
Figure 3.18 The wireless magnetic field sensing process. As the resistance of the magnetic field sensor is affected by the external electromagnetic radiation source, the data center (i) receives the disturbing of voltage sent from the wireless magnetic field sensing node (ii) and sends a remote command to the wireless signal indicator (iii) to turn on the LED (small inset figure) as an alert.

3.4 Conclusions

In this study, we demonstrated a wireless magnetic field sensing system based on FeCo/rGO hybrid nanosheets with special MR. This wireless magnetic field sensing system can quickly detect signals/collect data, and it can provide a real-time alert for the presence of a low-level EMF generated by a working mobile phone. FeCo/rGO hybrid

nanosheets were fabricated *via* a facile and cost-effective process, and a large MR up to $21 \pm 6\%$ was achieved at room temperature and low magnetic field (10 kOe), which is significantly higher than the MR of other reported graphene-based materials at the magnetic field of 10 kOe and room temperature [24, 25, 27, 33, 70, 71]. As the amount of adding rGO in the reaction (M_{rGO}) increased, the particle size of FeCo NPs declined. The particle density of FeCo NPs on rGO increased due to the increase of nucleation sites. The MR curves of FeCo/rGO hybrid nanosheets displayed good agreement with A. A. Abrikosov's quantum magnetoresistance (QMR) model. Moreover, the MR of FeCo/rGO hybrid nanosheets can be adjusted by controlling the particle density of FeCo NPs on the rGO.

The wireless magnetic field sensing system was built by combining FeCo/rGO hybrid nanosheets-based magnetic field sensor with a wireless communication system. The results indicate that the wireless magnetic field sensing system can successfully detect the low-level EMF generated by a working mobile phone. Therefore, the *in situ* modification of FeCo NPs on rGO by the facile process can pave the path for developing materials/structures exhibiting large MR with a cost-effective process. In addition, the sensitive FeCo/rGO hybrid nanosheets-based magnetic field sensor can be easily integrated with a wireless system for real-time detection, data collection, and signalling, which will certainly benefit the future connected society.

3.5 Supplementary Materials
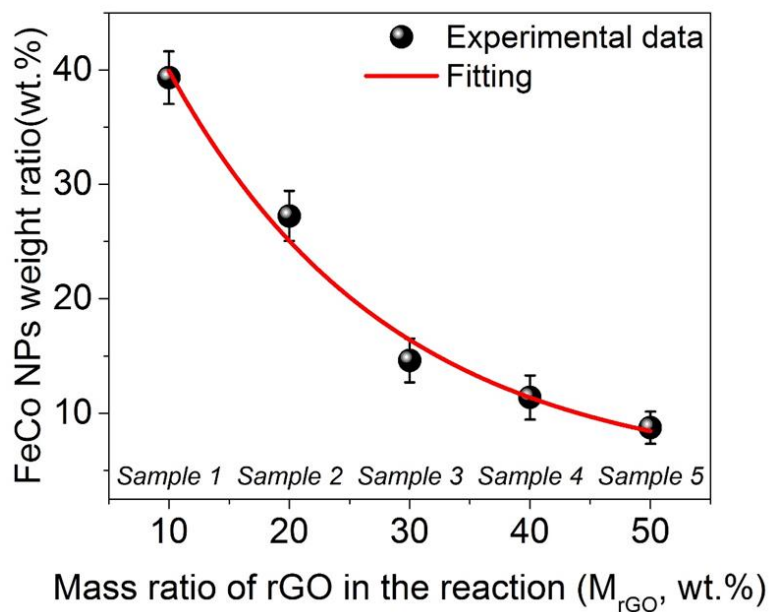
Figure S3.1 Weight ratio (wt.%) of FeCo NPs in FeCo/rGO hybrid nanosheets (Sample 1 - 5 with M_{rGO} = 10 wt.% - 50 wt.%).
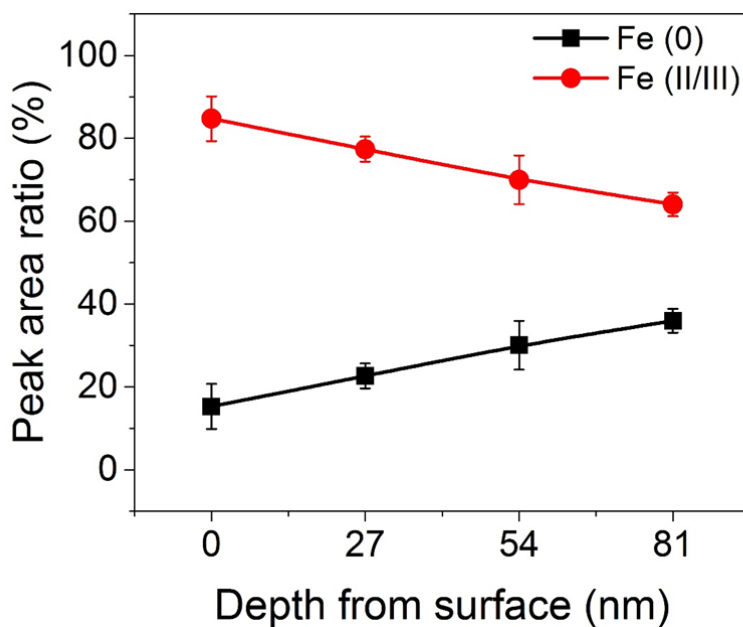
Figure S3.2 XPS peak area ratios of Fe (0) and Fe (II/III) with increasing characterization depth.
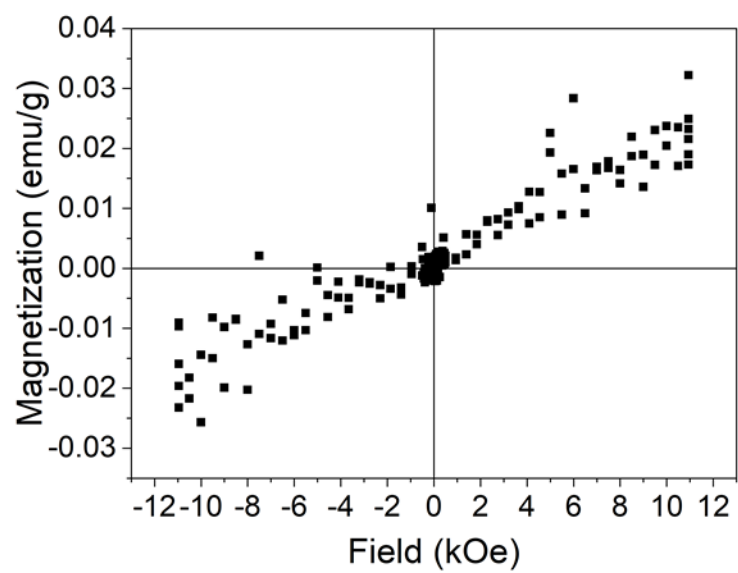
Figure S3.3 The magnetic hysteresis loop of rGO measured by VSM.

Table S3.1 XPS depth profiling results (in atomic ratio) of major elements of Sample 2.

Sputter time (min)	Depth (nm)	C 1s	O 1s	Fe 2p	Co 2p
0	0	80.5	16.5	1.2	1.9
10	27	82.3	9.3	4.5	3.9
20	54	81.3	8.0	6.3	4.5
30	81	80.3	7.7	7.3	4.7

Table S3.2 XPS depth profiling results (in atomic ratio) of major elements of Sample 4.

Sputter time (min)	Depth (nm)	C 1s	O 1s	Fe 2p	Co 2p
0	0	76.9	21.5	0.7	0.9
10	27	79.4	15.0	2.7	2.9
20	54	78.4	14.9	3.1	3.7
30	81	78.3	14.6	3.7	3.4

Table S3.3 XPS depth profiling results (in atomic ratio) of major elements of Sample 5.

Sputter time (min)	Depth (nm)	C 1s	O 1s	Fe 2p	Co 2p
0	0	80.8	17.4	0.9	0.9
10	27	83.8	12.0	1.8	2.4
20	54	84.5	10.4	2.5	2.5
30	81	84.4	10.3	2.7	2.7

Table S3.4 Ratios of iron/carbon in different samples with increasing sputter time.

Sputter time (min)	Depth (nm)	Sample 2	Sample 4	Sample 5
0	0	0.014	0.009	0.011
10	27	0.055	0.034	0.021
20	54	0.078	0.039	0.030
30	81	0.091	0.047	0.031

Table S3.5 Magnetic properties of FeCo/rGO hybrid nanosheets at room temperature.

Sample No.	M_S (emu/g)	M_r (emu/g)	H_C (Oe)
Sample 1 (M_{rGO} 10 wt.%)	74.1	4.28	192.4
Sample 2 (M_{rGO} 20 wt.%)	36.4	2.15	235.2
Sample 3 (M_{rGO} 30 wt.%)	27.9	1.50	233.9
Sample 4 (M_{rGO} 40 wt.%)	14.2	0.38	136.6
Sample 5 (M_{rGO} 50 wt.%)	12.5	0.37	138.4

Table S3.6 The sensitivity of magnetic field sensors based on FeCo/rGO hybrid nanosheets to the low magnetic field (< 10 kOe) at room temperature.

Sample No.	Sample 1	Sample 2	Sample 3	Sample 4	Sample 5
Ω/kOe	0.0837	0.0857	0.4431	0.7660	0.9282

3.6 References

[1] S.S.P. Parkin, M. Hayashi, L. Thomas, Magnetic Domain-Wall Racetrack Memory. *Science* **2008**, *320* (5873), 190-194.

[2] U. Ausserlechner, The Optimum Layout for Giant Magneto-Resistive Angle Sensors. *IEEE Sens. J.* **2010**, *10* (10), 1571-1582.

[3] R. Rempt, Scanning with magnetoresistive sensors for subsurface corrosion. *AIP Conf. Proc.* **2002**, *615* (1), 1771-1778.

[4] R.S. Gaster, D.A. Hall, C.H. Nielsen, S.J. Osterfeld, H. Yu, K.E. Mach, *et al.*, Matrix-insensitive protein assays push the limits of biosensors in medicine. *Nat. Med.* **2009**, *15* (11), 1327-1332.

[5] C.B. Ene, G. Schmitz, R. Kirchheim, A. Hütten, Stability and thermal reaction of GMR NiFe/Cu thin films. *Acta Mater.* **2005**, *53* (12), 3383-3393.

[6] Y.K. Wakabayashi, R. Akiyama, Y. Takeda, M. Horio, G. Shibata, S. Sakamoto, *et al.*, Origin of the large positive magnetoresistance of $Ge_{1-x}Mn_x$ granular thin films. *Phys. Rev. B* **2017**, *95* (1), 014417.

[7] R.U.R. Sagar, H.I.A. Qazi, M.H. Zeb, F.J. Stadler, B. Shabbir, X. Wang, *et al.*, Tunable sign of magnetoresistance in graphene foam – Ecoflex® composite for wearable magnetoelectronic devices. *Mater. Lett.* **2019**, *253*, 166-170.

[8] Y.P. Zeng, Z.W. Liu, E. Mikmeková, Magnetoresistance effects associated with various electric conduction mechanisms in nanostructured $[C/FeCo]_n$ multilayers. *J. Magn. Magn. Mater.* **2017**, *421*, 39-43.

[9] A.B. Pippard, Magnetoresistance in metals, Cambridge university press, 1989.

[10] C. Rizal, B. Moa, B.B. Niraula, Ferromagnetic Multilayers: Magnetoresistance, Magnetic Anisotropy, and Beyond. *Magnetochemistry* **2016**, *2* (2), 22.

[11] L. Liu, Y. Yang, B. Yang, Non-contact and high-precision displacement measurement based on tunnel magnetoresistance. *Meas. Sci. Technol.* **2020**, *31* (6), 065102.

[12] D. Rifai, A.N. Abdalla, K. Ali, R. Razali, Giant Magnetoresistance Sensors: A Review on Structures and Non-Destructive Eddy Current Testing Applications. *Sensors* **2016**, *16* (3), 298.

[13] D. Issadore, Y.I. Park, H. Shao, C. Min, K. Lee, M. Liong, *et al.*, Magnetic sensing technology for molecular analyses. *Lab Chip* **2014**, *14* (14), 2385-2397.

[14] Y. Wu, Y. Liu, Q. Zhan, J.P. Liu, R.-W. Li, Rapid detection of Escherichia coli O157:H7 using tunneling magnetoresistance biosensor. *AIP Adv.* **2017**, *7* (5), 056658.

[15] J. Choi, A.W. Gani, D.J.B. Bechstein, J.-R. Lee, P.J. Utz, S.X. Wang, Portable, one-step, and rapid GMR biosensor platform with smartphone interface. *Biosens. Bioelectron.* **2016**, *85*, 1-7.

[16] V.D. Krishna, K. Wu, A.M. Perez, J.-P. Wang, Giant Magnetoresistance-based Biosensor for Detection of Influenza A Virus. *Front. Microbiol.* **2016**, *7* (400).

[17] K. Wu, T. Klein, V.D. Krishna, D. Su, A.M. Perez, J.-P. Wang, Portable GMR Handheld Platform for the Detection of Influenza A Virus. *ACS Sens.* **2017**, *2* (11), 1594-1601.

[18] R. Baan, Y. Grosse, B. Lauby-Secretan, F. El Ghissassi, V. Bouvard, L. Benbrahim-Tallaa*, et al.*, Carcinogenicity of radiofrequency electromagnetic fields. *Lancet Oncol.* **2011**, *12* (7), 624-626.

[19] E. van Deventer, E. van Rongen, R. Saunders, WHO research agenda for radiofrequency fields. *Bioelectromagnetics* **2011**, *32* (5), 417-421.

[20] M. Markov, Y. Grigoriev, Protect children from EMF. *Electromagn. Biol. Med.* **2015**, *34* (3), 251-256.

[21] S. Parkin, J. Xin, C. Kaiser, A. Panchula, K. Roche, M. Samant, Magnetically engineered spintronic sensors and memory. *Proc. IEEE* **2003**, *91* (5), 661-680.

[22] J.S. Moodera, L.R. Kinder, T.M. Wong, R. Meservey, Large Magnetoresistance at Room Temperature in Ferromagnetic Thin Film Tunnel Junctions. *Phys. Rev. Lett.* **1995**, *74* (16), 3273-3276.

[23] Y.P. Zeng, Z.W. Liu, H.Y. Yu, Z.G. Zheng, D.C. Zeng, X.S. Gao, Large positive room temperature magnetoresistance in nanogranular FeCo–Si–N thin films. *Mater. Lett.* **2013**, *110*, 27-30.

[24] B. Song, K. Moon, C. Wong, Recent Developments in Design and Fabrication of Graphene-Based Interdigital Micro-Supercapacitors for Miniaturized Energy Storage Devices. *IEEE Trans. Compon., Packag., Manuf. Technol.* **2016**, *6* (12), 1752-1765.

[25] M.S. Purewal, Y. Zhang, P. Kim, Unusual transport properties in carbon based nanoscaled materials: nanotubes and graphene. *Phys. Status Solidi B* **2006**, *243* (13), 3418-3422.

[26] J.-J. Chen, J. Meng, Y.-B. Zhou, H.-C. Wu, Y.-Q. Bie, Z.-M. Liao*, et al.*, Layer-by-layer assembly of vertically conducting graphene devices. *Nat. Commun.* **2013**, *4* (1), 1921.

[27] A.L. Friedman, J.L. Tedesco, P.M. Campbell, J.C. Culbertson, E. Aifer, F.K. Perkins*, et al.*, Quantum Linear Magnetoresistance in Multilayer Epitaxial Graphene. *Nano Lett.* **2010**, *10* (10), 3962-3965.

[28] R.U. Rehman Sagar, K. Shehzad, A. Ali, F.J. Stadler, Q. Khan, J. Zhao*, et al.*, Defect-induced, temperature-independent, tunable magnetoresistance of partially fluorinated graphene foam. *Carbon* **2019**, *143*, 179-188.

[29] Z. Jia, R. Zhang, Q. Han, Q. Yan, R. Zhu, D. Yu*, et al.*, Large tunable linear magnetoresistance in gold nanoparticle decorated graphene. *Appl. Phys. Lett.* **2014**, *105* (14), 143103.

[30] R. Lukose, N. Zurauskiene, S. Balevicius, V. Stankevic, S. Keršulis, V. Plausinaitiene*, et al.*, Hybrid graphene-manganite thin film structure for magnetoresistive sensor application. *Nanotechnology* **2019**, *30* (35), 355503.

[31] V.B. Mohan, R. Brown, K. Jayaraman, D. Bhattacharyya, Characterisation of reduced graphene oxide: Effects of reduction variables on electrical conductivity. *Mater. Sci. Eng., B* **2015**, *193*, 49-60.

[32] F. Ortmann, A. Cresti, G. Montambaux, S. Roche, Magnetoresistance in disordered graphene: The role of pseudospin and dimensionality effects unraveled. *EPL (Europhysics Letters)* **2011**, *94* (4), 47006.

[33] G. Abellán, H. Prima-García, E. Coronado, Graphene enhances the magnetoresistance of $FeNi_3$ nanoparticles in hierarchical $FeNi_3$–graphene nanocomposites. *J. Mater. Chem. C* **2016**, *4* (11), 2252-2258.

[34] J. Zhu, Z. Luo, S. Wu, N. Haldolaarachchige, D.P. Young, S. Wei*, et al.*, Magnetic graphene nanocomposites: electron conduction, giant magnetoresistance and tunable negative permittivity. *J. Mater. Chem.* **2012**, *22* (3), 835-844.

[35] A.A. Abrikosov, Quantum magnetoresistance of layered semimetals. *Phys. Rev. B* **1999**, *60* (6), 4231-4234.

[36] A.A. Abrikosov, Quantum linear magnetoresistance. *EPL* **2000**, *49* (6), 789-793.

[37] G. Lu, K. Yu, Z. Wen, J. Chen, Semiconducting graphene: converting graphene from semimetal to semiconductor. *Nanoscale* **2013**, *5* (4), 1353-1368.

[38] A.H. Castro Neto, F. Guinea, N.M.R. Peres, K.S. Novoselov, A.K. Geim, The electronic properties of graphene. *Rev. Mod. Phys.* **2009**, *81* (1), 109-162.

[39] G. Goncalves, P.A.A.P. Marques, C.M. Granadeiro, H.I.S. Nogueira, M.K. Singh, J. Grácio, Surface Modification of Graphene Nanosheets with Gold Nanoparticles: The Role of Oxygen Moieties at Graphene Surface on Gold Nucleation and Growth. *Chem. Mater.* **2009**, *21* (20), 4796-4802.

[40] X. Huang, Z. Yin, S. Wu, X. Qi, Q. He, Q. Zhang*, et al.*, Graphene-Based Materials: Synthesis, Characterization, Properties, and Applications. *Small* **2011**, *7* (14), 1876-1902.

[41] B. Jeyadevan, K. Shinoda, R.J. Justin, T. Matsumoto, K. Sato, H. Takahashi*, et al.*, Polyol Process for Fe-Based Hard(fct-FePt) and Soft(FeCo) Magnetic Nanoparticles. *IEEE Trans. Magn.* **2006**, *42* (10), 3030-3035.

[42] R. Wang, Y. Wang, C. Xu, J. Sun, L. Gao, Facile one-step hydrazine-assisted solvothermal synthesis of nitrogen-doped reduced graphene oxide: reduction effect and mechanisms. *RSC Adv.* **2013**, *3* (4), 1194-1200.

[43] X. Li, J. Feng, Y. Du, J. Bai, H. Fan, H. Zhang*, et al.*, One-pot synthesis of $CoFe_2O_4$/graphene oxide hybrids and their conversion into FeCo/graphene hybrids for lightweight and highly efficient microwave absorber. *J. Mater. Chem. A* **2015**, *3* (10), 5535-5546.

[44] X.-W. Wei, G.-X. Zhu, Y.-J. Liu, Y.-H. Ni, Y. Song, Z. Xu, Large-Scale Controlled Synthesis of FeCo Nanocubes and Microcages by Wet Chemistry. *Chem. Mater.* **2008**, *20* (19), 6248-6253.

[45] K. Zhang, Y. Zhang, S. Wang, Enhancing thermoelectric properties of organic composites through hierarchical nanostructures. *Sci. Rep.* **2013**, *3* (1), 3448.

[46] D. Kodama, K. Shinoda, K. Sato, Y. Sato, B. Jeyadevan, K. Tohji, Synthesis of Fe-Co Alloy Particles by Modified Polyol Process. *IEEE Trans. Magn.* **2006**, *42* (10), 2796-2798.

[47] G.S. Chaubey, C. Barcena, N. Poudyal, C. Rong, J. Gao, S. Sun*, et al.*, Synthesis and Stabilization of FeCo Nanoparticles. *J. Am. Chem. Soc.* **2007**, *129* (23), 7214-7215.

[48] I. Arief, S. Biswas, S. Bose, FeCo-Anchored Reduced Graphene Oxide Framework-Based Soft Composites Containing Carbon Nanotubes as Highly Efficient Microwave Absorbers with Excellent Heat Dissipation Ability. *ACS Appl. Mater. Interfaces* **2017**, *9* (22), 19202-19214.

[49] X.-W. Gao, J. Yang, K. Song, W.-B. Luo, S.-X. Dou, Y.-M. Kang, Robust FeCo nanoparticles embedded in a N-doped porous carbon framework for high oxygen conversion catalytic activity in alkaline and acidic media. *J. Mater. Chem. A* **2018**, *6* (46), 23445-23456.

[50] W. Gao, L.B. Alemany, L. Ci, P.M. Ajayan, New insights into the structure and reduction of graphite oxide. *Nat. Chem.* **2009**, *1* (5), 403-408.

[51] D.V. Kosynkin, A.L. Higginbotham, A. Sinitskii, J.R. Lomeda, A. Dimiev, B.K. Price*, et al.*, Longitudinal unzipping of carbon nanotubes to form graphene nanoribbons. *Nature* **2009**, *458* (7240), 872-876.

[52] S.-K. Jerng, D. Seong Yu, J. Hong Lee, C. Kim, S. Yoon, S.-H. Chun, Graphitic carbon growth on crystalline and amorphous oxide substrates using molecular beam epitaxy. *Nanoscale Res. Lett.* **2011**, *6* (1), 565.

[53] J. Jo, S. Lee, J. Gim, J. Song, S. Kim, V. Mathew*, et al.*, Facile synthesis of reduced graphene oxide by modified Hummer's method as anode material for Li-, Na- and K-ion secondary batteries. *R. Soc. Open Sci.* **2019**, *6* (4), 181978.

[54] B. Lesiak, L. Kövér, J. Tóth, J. Zemek, P. Jiricek, A. Kromka*, et al.*, C sp^2/sp^3 hybridisations in carbon nanomaterials – XPS and (X)AES study. *Appl. Surf. Sci.* **2018**, *452*, 223-231.

[55] B.K. Mutuma, C.I. Garcia-Martinez, R.C. Dias, B.J. Matsoso, N.J. Coville, I.A. Hümmelgen, Nitrogen-doped hollow carbon spheres as chemical vapour sensors. *New J. Chem.* **2019**, *43* (22), 8418-8427.

[56] B.J. Matsoso, K. Ranganathan, B.K. Mutuma, T. Lerotholi, G. Jones, N.J. Coville, Time-dependent evolution of the nitrogen configurations in N-doped graphene films. *RSC Adv.* **2016**, *6* (108), 106914-106920.

[57] M.K. Rabchinskii, S.A. Ryzhkov, D.A. Kirilenko, N.V. Ulin, M.V. Baidakova, V.V. Shnitov*, et al.*, From graphene oxide towards aminated graphene: facile synthesis, its structure and electronic properties. *Sci. Rep.* **2020**, *10* (1), 6902.

[58] S. Bai, X. Shen, G. Zhu, M. Li, H. Xi, K. Chen, In situ Growth of Ni_xCo_{100-x} Nanoparticles on Reduced Graphene Oxide Nanosheets and Their Magnetic and Catalytic Properties. *ACS Appl. Mater. Interfaces* **2012**, *4* (5), 2378-2386.

[59] L. Chen, Y. Zhang, H. Wang, Y. Wang, D. Li, C. Duan, Cobalt layered double hydroxides derived CoP/Co_2P hybrids for electrocatalytic overall water splitting. *Nanoscale* **2018**, *10* (45), 21019-21024.

[60] H. Zhang, J. Zheng, Y. Chao, K. Zhang, Z. Zhu, Surface engineering of FeCo-based electrocatalysts supported on carbon paper by incorporating non-noble metals for water oxidation. *New J. Chem.* **2018**, *42* (9), 7254-7261.

[61] L. An, N. Jiang, B. Li, S. Hua, Y. Fu, J. Liu*, et al.*, A highly active and durable iron/cobalt alloy catalyst encapsulated in N-doped graphitic carbon nanotubes for oxygen reduction reaction by a nanofibrous dicyandiamide template. *J. Mater. Chem. A* **2018**, *6* (14), 5962-5970.

[62] H. Lv, H. Zhao, T. Cao, L. Qian, Y. Wang, G. Zhao, Efficient degradation of high concentration azo-dye wastewater by heterogeneous Fenton process with iron-based metal-organic framework. *J. Mol. Catal. A: Chem.* **2015**, *400*, 81-89.

[63] K. Schwarz, P. Mohn, P. Blaha, J. Kubler, Electronic and magnetic structure of BCC Fe-Co alloys from band theory. *J. Phys. F: Met. Phys.* **1984**, *14* (11), 2659-2671.

[64] T. Fang, A. Konar, H. Xing, D. Jena, Carrier statistics and quantum capacitance of graphene sheets and ribbons. *Appl. Phys. Lett.* **2007**, *91* (9), 092109.

[65] M.I. Katsnelson, F. Guinea, A.K. Geim, Scattering of electrons in graphene by clusters of impurities. *Phys. Rev. B* **2009**, *79* (19), 195426.

[66] K. Spilarewicz-Stanek, A. Kisielewska, J. Ginter, K. Bałuszyńska, I. Piwoński, Elucidation of the function of oxygen moieties on graphene oxide and reduced graphene oxide in the nucleation and growth of silver nanoparticles. *RSC Adv.* **2016**, *6* (65), 60056-60067.

[67] S. Wall, Z.-M. Wang, T. Kendig, D. Dobraca, M. Lipsett, Real-world cell phone radiofrequency electromagnetic field exposures. *Environ. Res.* **2019**, *171*, 581-592.

[68] B.B. Levitt, H. Lai, Biological effects from exposure to electromagnetic radiation emitted by cell tower base stations and other antenna arrays. *Environ. Rev.* **2010**, *18* (NA), 369-395.

[69] H. Jonai, M.B.G. Villanueva, A. Yasuda, Cytokine profile of human peripheral blood mononuclear cells exposed to 50Hz EMF. *Ind. Health* **1996**, *34* (4), 359-368.

[70] Z.-M. Liao, H.-C. Wu, S. Kumar, G.S. Duesberg, Y.-B. Zhou, G.L.W. Cross*, et al.*, Large Magnetoresistance in Few Layer Graphene Stacks with Current Perpendicular to Plane Geometry. *Adv. Mater.* **2012**, *24* (14), 1862-1866.

[71] K. Gopinadhan, Y.J. Shin, I. Yudhistira, J. Niu, H. Yang, Giant magnetoresistance in single-layer graphene flakes with a gate-voltage-tunable weak antilocalization. *Phys. Rev. B* **2013**, *88* (19), 195429.

Chapter 4

4 Investigation of the Effect of Increasing the Mass Ratio of rGO Adding in the Reaction and the Formation of Co-Mn Oxides

In this chapter, the influences of imported ions due to the increase of reduced graphene oxide (rGO) mass ratio on the synthesis process of FeCo/rGO hybrid nanosheets were investigated. Although various studies were performed to investigate the fabrication of composite materials based on FeCo and graphene (rGO), most of these studies focused on discussing and investigating the microwave absorption properties, electrochemical applications, and catalysis applications (such as oxygen reduction reaction (ORR)) [1-3]. Few studies were carried out to characterize the magnetoresistance (MR) properties and the influences of varying the ratio of FeCo and rGO precursors on the performance and microstructure of the FeCo/graphene (rGO) composite materials.

In our previous work, we successfully developed FeCo/rGO hybrid nanosheets with large MR at the low magnetic field (10 kOe) and room temperature [4]. The tunable MR was achieved by adjusting the ratio of the FeCo and rGO precursors, which leads to the variation of FeCo/rGO hybrid nanosheets' microstructure (particle size and particle density of FeCo nanoparticles (NPs) on rGO). As we increased the mass ratio of rGO added in the reaction (M_{rGO}) over 50 wt.% to 60 wt.% and 70 wt.%, the formation of the Co-Mn oxides spherical NPs was observed. Few studies were performed to investigate Co-Mn oxides NPs produced with the hydrothermal/solvothermal processes [5, 6]. Moreover, most of these investigations focused on catalysis or electrochemical applications.

By increasing M_{rGO} over 60 wt.%, the formation of Co-Mn oxides NPs was observed due to the involvement of imported ions. Surprisingly, the rGO with Co-Mn oxides exhibited positive MR at the level of 3.5% ~ 4.5% at the low magnetic field (10 kOe) and room temperature. Therefore, this study proposed a route to produce nanocomposite with Co-

Mn oxides and rGO with positive MR *via* the chemical synthesis process. The microstructure of Co-Mn oxides NPs on rGO is adjustable by shifting the M_{rGO}. The results of this study could contribute to potential applications on electrocatalysis and help to investigate the applications of nanocomposites based on Co-Mn oxides and rGO in the fabrication of MR devices/sensors.

4.1 Introduction

In recent years, the non-noble transition metal oxides have drawn the attention of researchers due to their applications in electrocatalysis and energy storage. Among these metal oxides, MnO_2 is one of the well-known non-noble transition metal oxides applied in different electrochemical processes due to their special physical and chemical properties [7]. Moreover, cobalt oxide (Co_3O_4) and manganese oxide (Mn_2O_3) have been extensively studied for the applications such as ceramic pigments, energy storage, rechargeable Li-ion batteries, gas sensors, and heterogeneous catalysts [8-12]. However, the limitations on the conductivity of metal oxides such as MnO_2 obstruct the development of MnO_2 based materials in electrochemical catalysis and energy-storage applications [13].

To overcome these obstacles and achieve superior properties in terms of electrocatalysis and energy storage, metal dopants are involved in the fabrication of complex metal oxides. In general, complex oxides combine transition metal oxide/post-transition metal oxide or two transition metal oxides ($ZnCo_2O_4$, $ZnMn_2O_4$, $CoMn_2O_4$, $MnCo_2O_4$, etc.) [14-16]. These complex metal oxides were developed to achieve higher electronic conductivity and greater reversible storage capacity in energy-related applications [17, 18]. Especially for the binary system of cobalt and manganese, manganese transports extra electrons compared with cobalt. Meanwhile, cobalt exhibits greater oxidation potential than manganese. With the synergetic effect of Co and Mn, $CoMn_2O_4$ and $MnCo_2O_4$ become suitable materials for the fabrication of anode in rechargeable Li-ion batteries [19, 20].

For the applications in catalysis, complex metal oxides with the combination of Co, Mn, Zn, Fe, Cu, etc. were extensively investigated due to their high activity and robust thermal stability in contrast with single metal oxide catalysts, which include $Co_{3-x}Fe_xO_4$, $Mn_xCo_{3-x}O_4$, $Co_{3-x}Cu_xO_4$, and $Zn_xCo_{1-x}Co_2O_4$ [21-24]. Among these catalysts, $Mn_xCo_{3-x}O_4$ received increasing attention since $Mn_xCo_{3-x}O_4$ is cost-effective and environmental-friendly. The high performance of $Mn_xCo_{3-x}O_4$ in the combustion of volatile organic compounds (such as *n*-hexane, methane, 1,2-dichlorobenzene, and formaldehyde) due to the synergetic effect between manganese and cobalt oxides was noticed by researchers [22, 25-27]. Meanwhile, $CoMn_2O_4$ was applied in the oxygen reduction reaction (ORR) and oxygen evolution reaction (OER) [28]. Other complex metal oxides based on Mn and Co such as $CoMnO_3$ and $CoMn_3O_4$ were used in the detection of toxic 4-nitrophenol and reduction of H_2O_2 [5, 29].

With attractive electrical/mechanical properties and high surface area, graphene becomes a suitable substrate for constructing various hybrid nanomaterials [30]. Reduced graphene oxide (rGO) is more accessible with fewer requirements on the equipment in contrast with multilayer graphene produced with chemical vapor deposition (CVD). Moreover, the defects and residual functional groups on rGO offer nucleation sites for nanoparticles (NPs) [31]. Previous studies indicated that the hybrid materials fabricated by grafting $MnCo_2O_4$ or Co_3O_4 on rGO achieved superior stability and durability for ORR and OER catalysis [32, 33]. For catalysis-related applications, these hybrid materials enlarge the specific surface areas and prevent agglomerations of the metal oxide nanostructures [34]. Meanwhile, in energy-related applications, $MnCo_2O_4$ hybrid materials increase the cycle lives and decrease the overpotentials of $Li-O_2$ cells [35].

Currently, the preparation processes of complex metal oxides (such as $CoMn_2O_4$) include the combustion method and solvothermal method [16, 27]. The combustion method has advantages regarding fewer requirements on fabrication equipment and facile procedure [36]. However, the temperature requirements of the combustion are strict, which requires calcination at 500 to 700 °C for more than 2 hours. This leads to extra energy consumptions and challenges. The solvothermal or hydrothermal methods are facile and easy to obtain. With accessible materials and wet-chemistry equipment, the preparation

of complex metal oxides can be finish at a lower temperature (150 °C)/less time, and temperature requirements for calcination are reduced. In addition, most of the hybrid materials based on the combination of complex metal oxides (such as $CoMn_2O_4$) and rGO were produced with solvothermal/hydrothermal processes in order to achieve the uniform dispersion of complex metal oxides NPs on rGO [34, 37]. For some metal oxides such as $CoMnO_3$, few fabrication processes were developed based on facile solvothermal/hydrothermal methods, and few investigations were carried out to combine their NPs with rGO [5, 6].

In our previous study, we successfully synthesized FeCo/rGO hybrid nanosheets with large magnetoresistance (MR) at low magnetic fields (10 kOe) and room temperature [4]. Meanwhile, the investigation on the influences of adjusting the ratio of FeCo and rGO precursors on the microstructure and magnetic properties (including MR) were performed since few studies were carried out for this purpose. The tunable MR of FeCo/rGO hybrid nanosheets and adjustable density/size of FeCo NPs were achieved as the mass ratio of rGO added in the reaction (M_{rGO}) is in the range of 10 wt.% - 50 wt.%. As we further increased the M_{rGO} to 60 wt.% and 70 wt.%, the presence of NPs with the uniformly spherical shape different from FeCo NPs was observed on the surface of rGO. Further characterizations indicate that the formation of these Co-Mn oxides NPs on the rGO surface can be triggered by imported ions due to the increase of M_{rGO}.

In this study, we confirmed that the imported ions (especially manganese ions) interfered with the fabrication of FeCo/rGO hybrid nanosheets as the FeCo NPs were replaced by the *in situ* grown spherical Co-Mn oxides NPs. The characterizations of Co-Mn oxides NPs suggested that the size of the NPs is adjustable by varying M_{rGO}. The characterizations of crystal structure and chemical composition indicated the possible existence of $CoMnO_3$. Although extensive investigations were performed to study the electrochemical properties of Co-Mn oxide and rGO hybrid structure, few studies were completed to characterize the possible MR responses of the nanocomposites with Co-Mn oxides and rGO. Surprisingly, the MR of rGO with Co-Mn oxides reached 3.5 ~ 4.5% at the low magnetic field (10 kOe) and room temperature, which is significantly larger than multilayer or composite structures containing Co and Mn under equivalent conditions [38,

39]. Meanwhile, the possible origin of the MR was studied with the quantum magnetoresistance (QMR) model [40]. Therefore, the formation of Co-Mn oxides on rGO confirmed the possible adverse effects of imported ions on the fabrication of the FeCo/rGO hybrid nanosheets. Meanwhile, this study purposed a possible route to produce nanocomposites based on Co-Mn oxides and rGO with large MR at the low magnetic field and room temperature, which can benefit the fabrication of MR devices/sensors and energy or catalysis-related materials/devices.

4.2 Experimental

4.2.1 Synthesis of Graphene Oxide (GO)

Graphene oxide (GO) was produced by oxidation of the graphite powers based on the modified Hummers method described in our previous study, which has been discussed in Chapter 3 [4].

4.2.2 Synthesis of Reduced Graphene Oxide (rGO)

Reduced graphene oxide (rGO) was prepared by the reduction of GO, which has been discussed in Chapter 3.

4.2.3 Preparation of rGO with Co-Mn oxides

The preparation process was described in our previous work, which has been discussed in Chapter 3 [4]. Two different mass ratios of rGO (M_{rGO}) were applied, which were 60 wt.% and 70 wt.%. The samples were denoted as Sample 6 (60 wt.%) and Sample 7 (70 wt.%). Due to the large amount of rGO added, the mixture was further sonicated for 20 minutes to achieve a proper dispersion of rGO.

4.2.4 Materials Characterization

Micrographs of the transmission electron microscope (TEM) were obtained by Philips CM-10. Micrographs of the scanning electron microscope (SEM) were obtained Hitachi S-3400N. The energy-dispersive X-ray spectra (SEM-EDX) were characterized by the

INCA PentaFET-x3 system (Oxford Instruments) attached to Hitachi S-3400N. The X-ray photoelectron spectra (XPS) and XPS depth profiling were measured by the PHI Quantera scanning X-ray microprobe (Al Kα). The Rigaku rotating-anode X-ray diffractometer (XRD, Co-Kα radiation) was applied to collect the X-ray diffraction data. The magnetic hysteresis loop was measured by the vibrating sample magnetometer (VSM, LakeShore 7407, moment measure range: 10^{-7} to 10^3 emu; field accuracy: "± 0.05%" full scale).

4.2.5   Magnetoresistance Characterization

The characterization of magnetoresistance (MR, %) was performed by vibrating sample magnetometer (VSM, LakeShore 7407).

The MR of the testing sample is defined by equation (4.1).

$$MR(\%) = \frac{R - R_0}{R_0} \times 100\% \qquad (4.1)$$

The resistance change ($\varDelta R$, Ω) is defined by equation (4.2)

$$\Delta R = R - R_0 \qquad (4.2)$$

where R is the total resistance (Ω) of the sample under the presence of an external magnetic field and R_0 the sample resistance (Ω) at zero magnetic field.

4.2.6   Data Simulation

The mathematical calculations for the quantum magnetoresistance (QMR) model were carried out by MATLAB (The MathWorks), Python(x,y) (https://python-xy.github.io/), and 1stOpt (7D-Soft High Technology Inc.).

4.3 Results and Discussion

4.3.1 Characterization of rGO with Co-Mn Oxides

As shown in **Figure 4.1**, the formation of Co-Mn oxides on rGO was observed as rGO adding in the reaction (M_{rGO}) surpassed the threshold (60 wt.%).
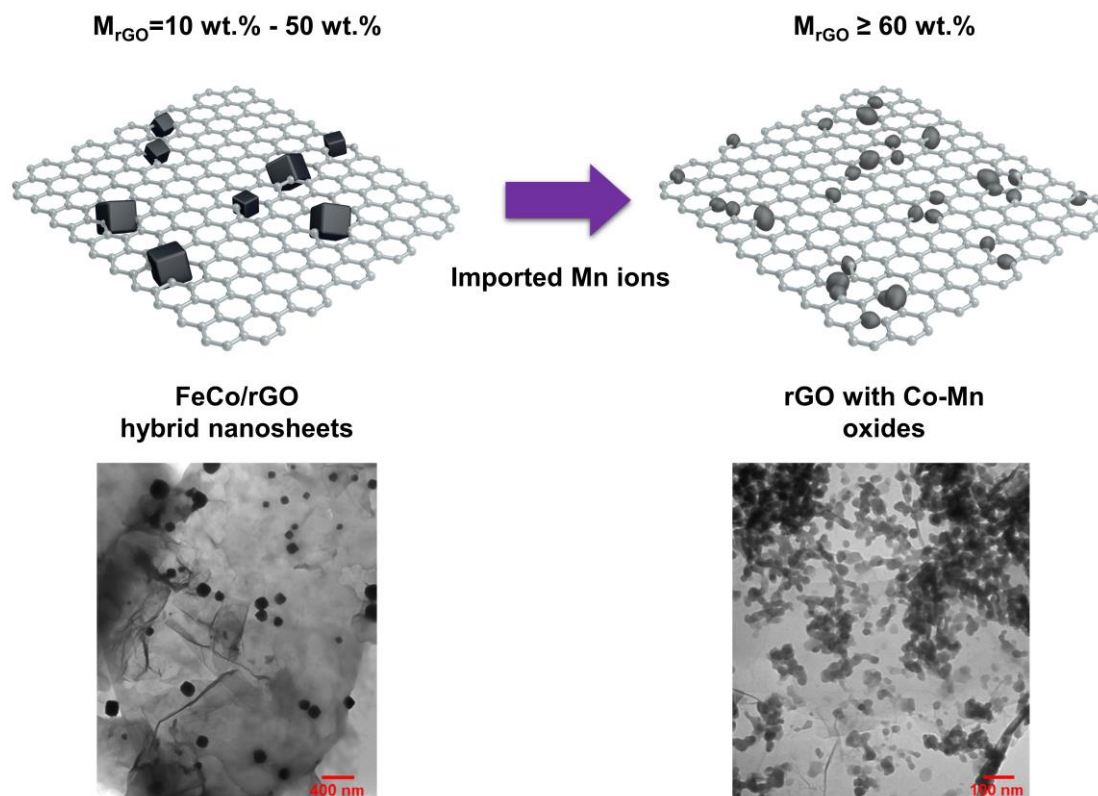
Figure 4.1 Schematic illustration of the formation of Co-Mn oxides on rGO.

The morphology and structure of Co-Mn oxides NPs on rGO were studied with the transmission electron microscope (TEM) (**Figure 4.2**). The Co-Mn oxides NPs were observed on the surface of rGO in Sample 6 (M_{rGO} = 60 wt.%) and Sample 7 (M_{rGO} = 70 wt.%). It is noticed that the rGO displays some wrinkles and folds due to its large aspect ratio. TEM micrographs indicate that the cubic shape FeCo NPs on the rGO surface are replaced by the spherical shape Co-Mn oxides NPs due to the introduced ions. The average diameters of Co-Mn oxides NPs for Sample 6 and Sample 7 are 31 ± 8 nm and 28 ± 7 nm. As shown in **Figure 4.2**, the size distribution analysis suggests that the

117

diameter of the Co-Mn oxides NPs shifts to a smaller size. Meanwhile, the diameter of NPs becomes more centred as the quantity of rGO added to the reaction (M_{rGO}) increases. In our previous study, FeCo NPs on FeCo/rGO hybrid nanosheets exhibit a similar size shift, which can be attributed to the rise of nucleation sites due to the increase of the M_{rGO} [4, 31]. Therefore, the results indicate the size adjustable feature of Co-Mn oxides NPs on rGO.
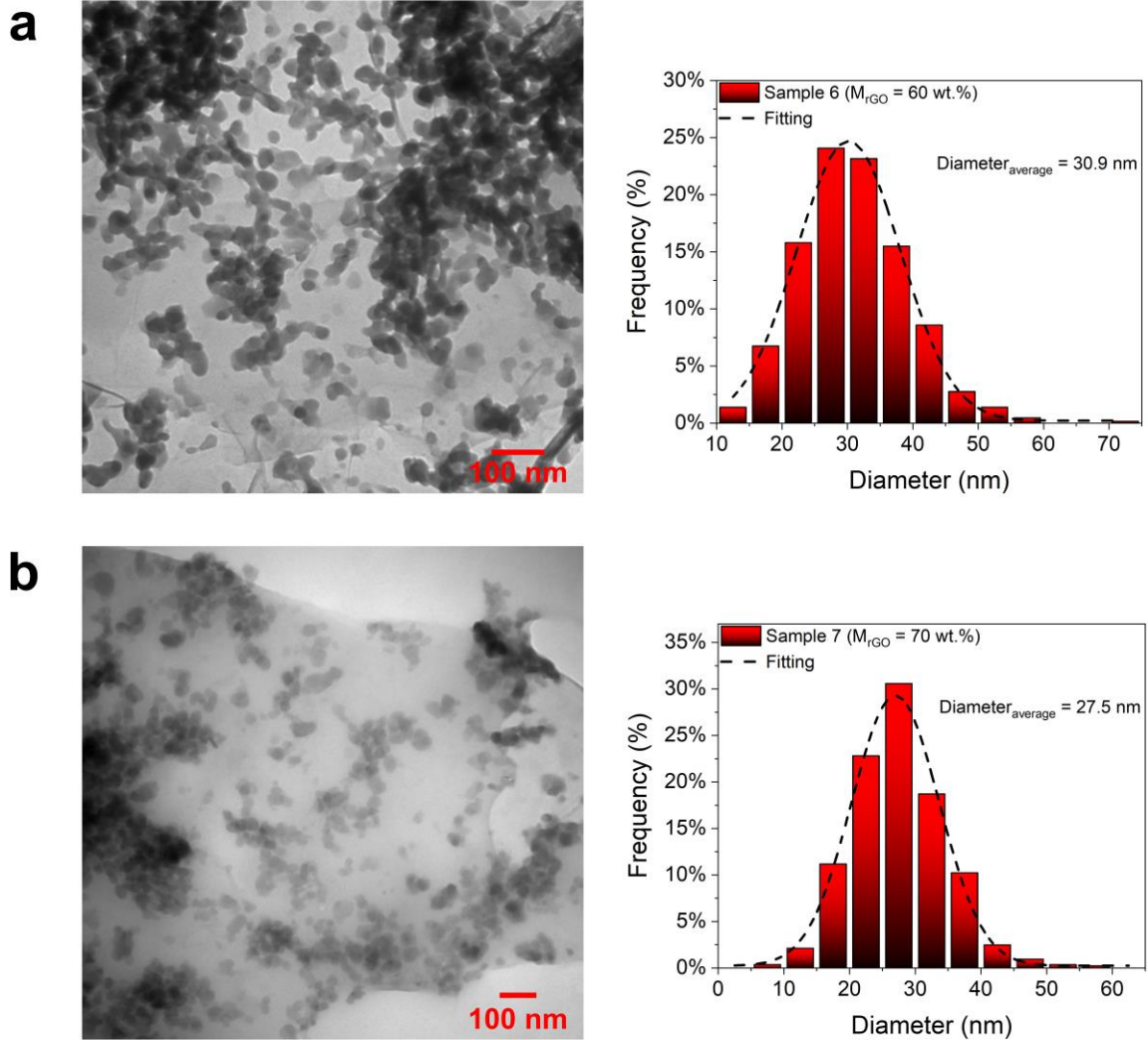
Figure 4.2 TEM micrographs and size distributions of Co-Mn oxides NPs on rGO with different M_{rGO}: (a) Sample 6 (M_{rGO} = 60 wt.%) and (b) Sample 7 (M_{rGO} = 70 wt.%).

Figure 4.3 shows the scanning electron microscope (SEM) micrographs and energy-dispersive X-ray spectra (SEM-EDX) of rGO with Co-Mn oxides. The presence of Co-Mn oxides NPs is observed on rGO, which is consistent with the characterization of TEM. The SEM-EDX was applied to study the chemical composition of the rGO with Co-Mn oxides. As shown in **Figure 4.3**, the presence of the Co, Mn, C, and O peaks is observed in the EDX spectra of both Sample 6 and Sample 7. Meanwhile, peaks of residual iron are indicated in both two spectra. The amount of carbon content increases significantly due to the increase of M_{rGO}. Meanwhile, the increase of M_{rGO} leads to the rise of manganese content compared with the cobalt content and iron content. The poor signal of the Fe peak indicates that less iron content remains in the sample compared with the cobalt content.
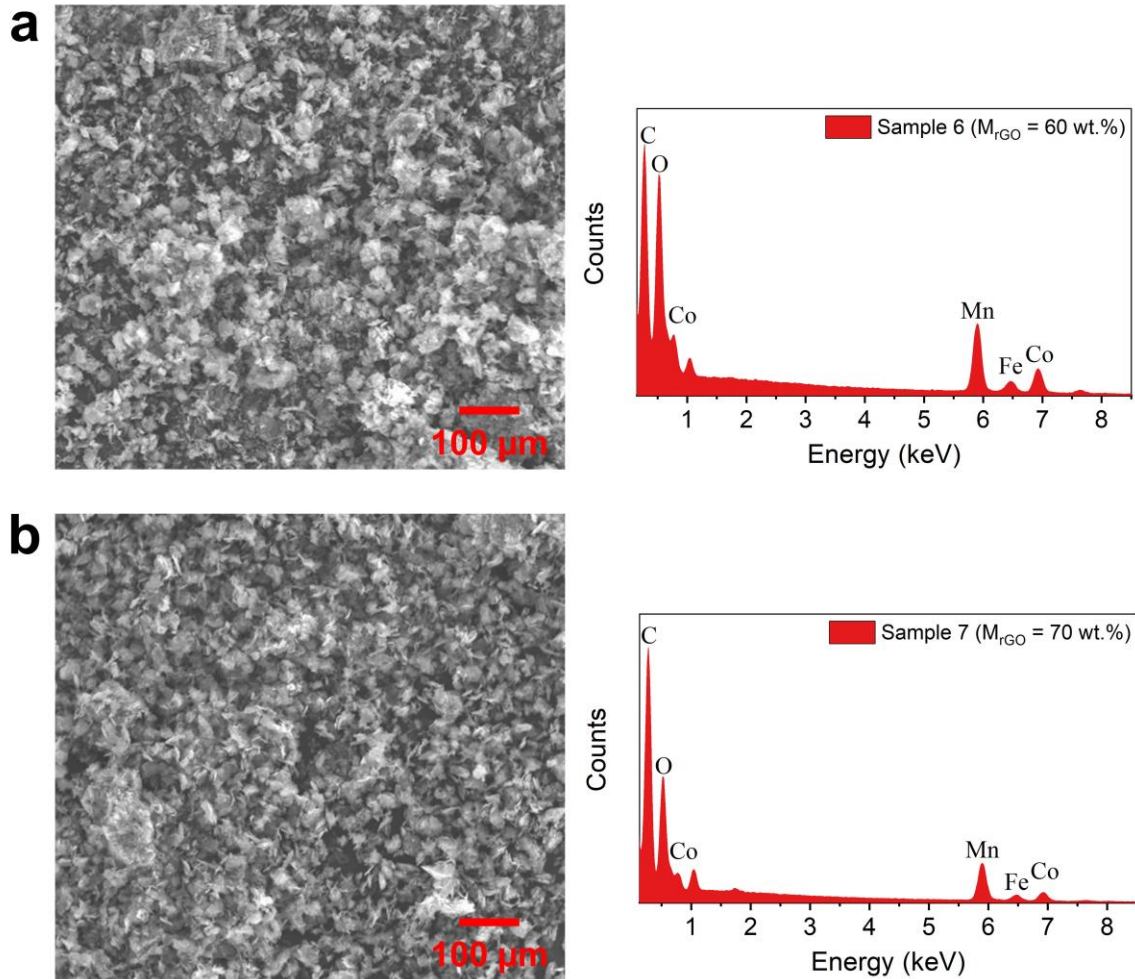
Figure 4.3 SEM micrographs and SEM-EDX of (a) Sample 6 and (b) Sample 7.

To further study the chemical composition, the average atomic ratios (at.%) of Mn, Co, and Fe of Sample 6 and 7 (together with sample 1-5 from the previous work) were investigated by SEM-EDX (**Figure 4.4**). Specifically, the average atomic ratios of Mn, Co, and Fe in Sample 6 are 3.15 ± 0.24 at.%, 1.86 ± 0.19 at.%, and 0.23 ± 0.05 at.%, respectively. In Sample 7, they are 1.79 ± 0.35 at.%, 0.61 ± 0.18 at.%, and 0.07 ± 0.02 at.%. The ratio between Mn:Co are around 2:1 for Sample 6 and 3:1 for Sample 7. The significant decrease of the atomic ratio of Fe is due to the formation of Co-Mn oxides NPs. Therefore, the presence of Co-Mn oxides NPs is confirmed by the results of SEM-EDX as the M_{rGO} reaches the threshold at 60 wt.%.
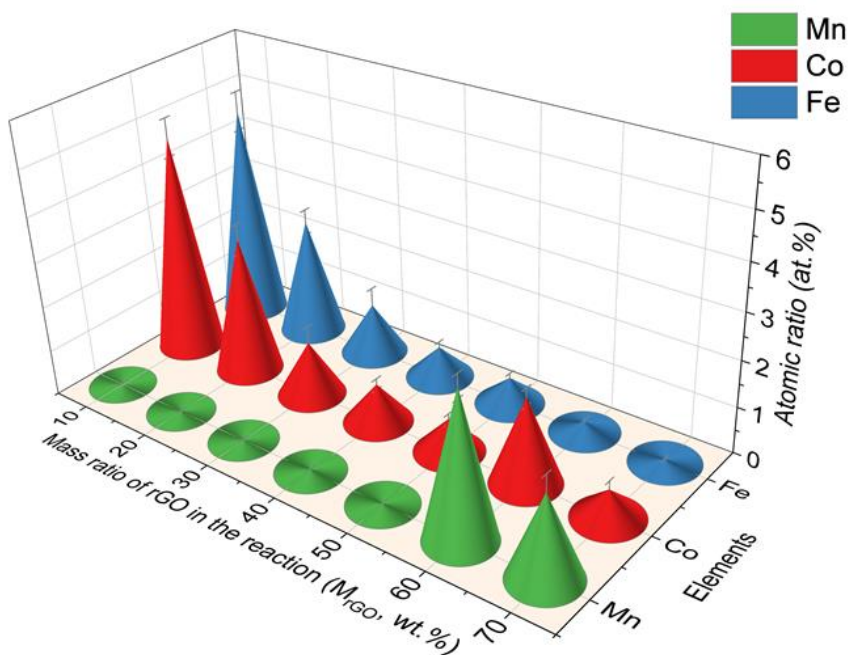
Figure 4.4 The average atomic ratio of Co, Fe, and Mn of samples with the M_{rGO} increase from 10 wt.% to 70 wt.% (with 10 wt.% interval).

To further characterize the crystal structure of rGO and Co-Mn oxides NPs, X-ray powder diffraction (XRD) profiles were obtained. As shown in **Figure 4.5**, the XRD profile suggests the successful reduction of rGO as the peak at $2\theta = 11°$ is not observed [41]. The diffraction peaks at 23.5° and 43.3° indicate (002) and (100) crystal planes of rGO, which are also observed in the XRD profiles of Sample 6 and Sample 7. In the XRD profiles of Sample 6 and 7, the peaks at 24.4°, 32.6°, and 36.4° can be attributed to

the (012), (104), and (110) crystal planes of $CoMnO_3$ (PDF# 12-0476). The peak at 58.0° can be attributed to the presence of Mn_2O_3 (PDF# 78-0390) in the system. In addition, the presence of the peak at 44.4° is observed in the XRD profile of Sample 6, which refers to the (110) crystal plane of FeCo (PDF# 49-1568). This indicates that the formation of FeCo NPs may not be completely replaced as M_{rGO} reaches 60 wt.%. However, this peak disappears in the XRD profile of Sample 7, which indicates that most of the rGO surface is occupied by Co-Mn oxides NPs as M_{rGO} increases to 70 wt.%. Therefore, the results of XRD are consistent with the results of SEM-EDX.
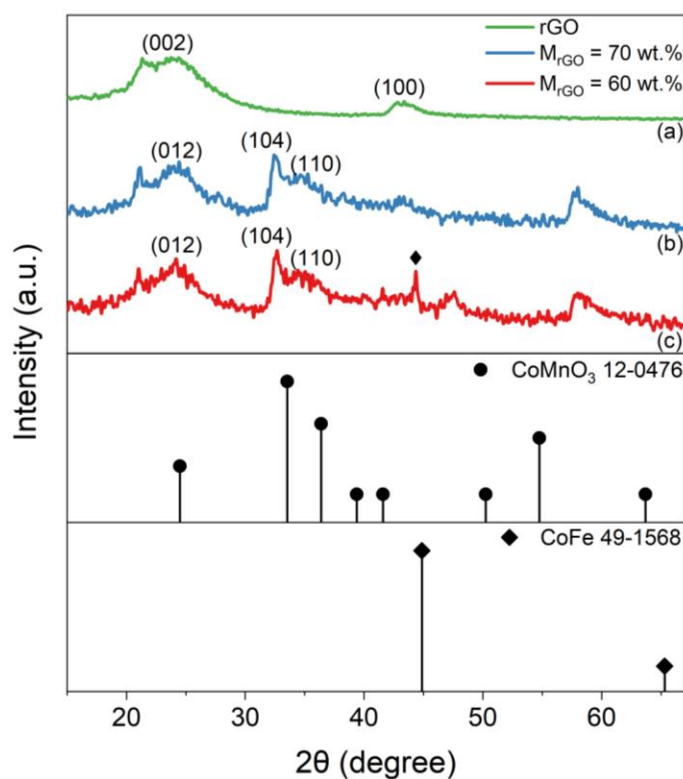
Figure 4.5 XRD profile of (a) rGO, (b) Sample 6 (M_{rGO} = 60 wt.%), and (c) Sample 7 (M_{rGO} = 70 wt.%).

X-ray photoelectron spectroscopy (XPS) was applied to further investigate the chemical composition and surface electronic state of the elements of rGO with Co-Mn oxides. The presence of O, C, N, Mn, Co, and Fe peaks in Sample 6 (M_{rGO} = 60 wt.%) and Sample 7 (M_{rGO} = 70 wt.%) is confirmed by the XPS survey scan (**Figure 4.6**). The O 1s peak can

be attributed to the oxygen content of Co-Mn oxides NPs and oxygen functional groups of rGO, and the N 1s peak is related to the hydrazine reduction of rGO [4].
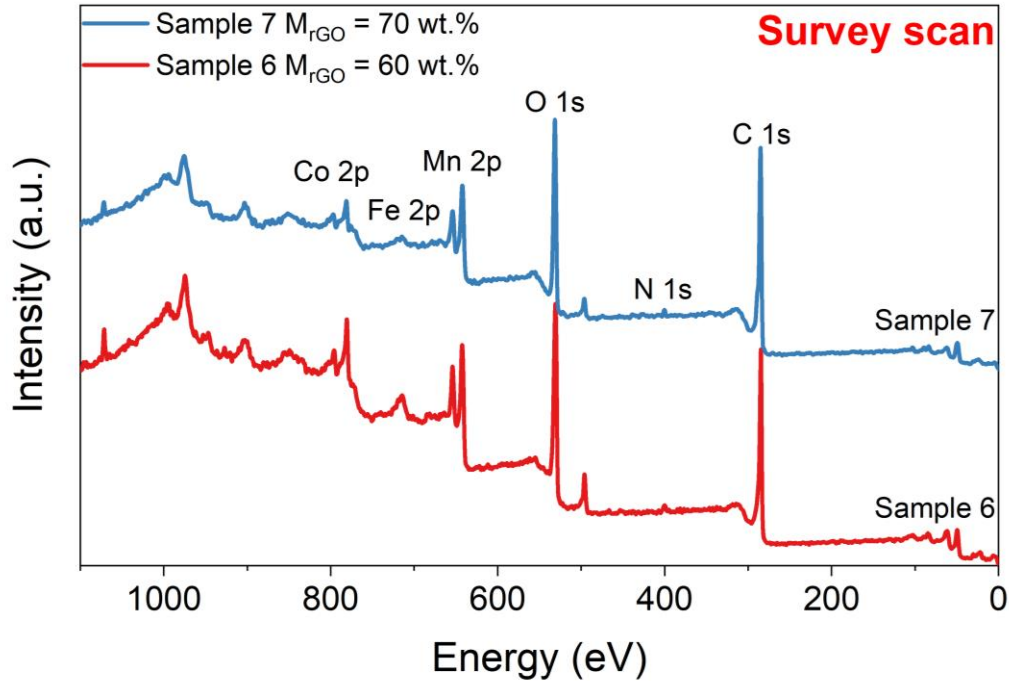
Figure 4.6 The XPS survey spectra of rGO with Co-Mn oxides.

Figure 4.7 shows the high-resolution XPS spectra of C 1s, O 1s, and N 1s. In the high-resolution XPS spectra of C 1s (**Figure 4.7a**), the peaks corresponding to C sp^2, C sp^3, and C-O bonds are observed at the binding energy of 284.6 eV, 285.5 eV, and 286.2 eV for Sample 6 and Sample 7 [42-44].

In the high-resolution XPS spectra of O 1s (**Figure 4.7b**), the peaks that appear at the binding energy of 530.2 eV (Sample 6) and 530.0 eV (Sample 7) are attributed to metal-oxygen bonds. The peaks that relate to the non-lattice oxygen (oxygen vacancies) are observed at 532.0 eV (Sample 6) and 531.7 eV (Sample 7). Meanwhile, the peaks at the binding energy of 533.7 eV (Sample 6) and 532.1 eV (Sample 7) are attributed to the absorbed oxygen [34, 45]. The results indicate that the variation of the ratio between metal-oxygen bonds and non-lattice oxygen can be triggered by the increase of M_{rGO} [46].

In the high-resolution XPS spectra of N 1s (**Figure 4.7c**), the peaks at the binding energy of 398.1 eV (Sample 6) and 398.5 eV (Sample 7) indicate the existence of pyridinic N. The peaks at 399.2 eV (Sample 6) and 399.6 eV (Sample 7) are attributed to the pyrrolic N [47-49]. The peaks of the amine group appear at 400.5 eV for both Sample 6 and Sample 7 [50].
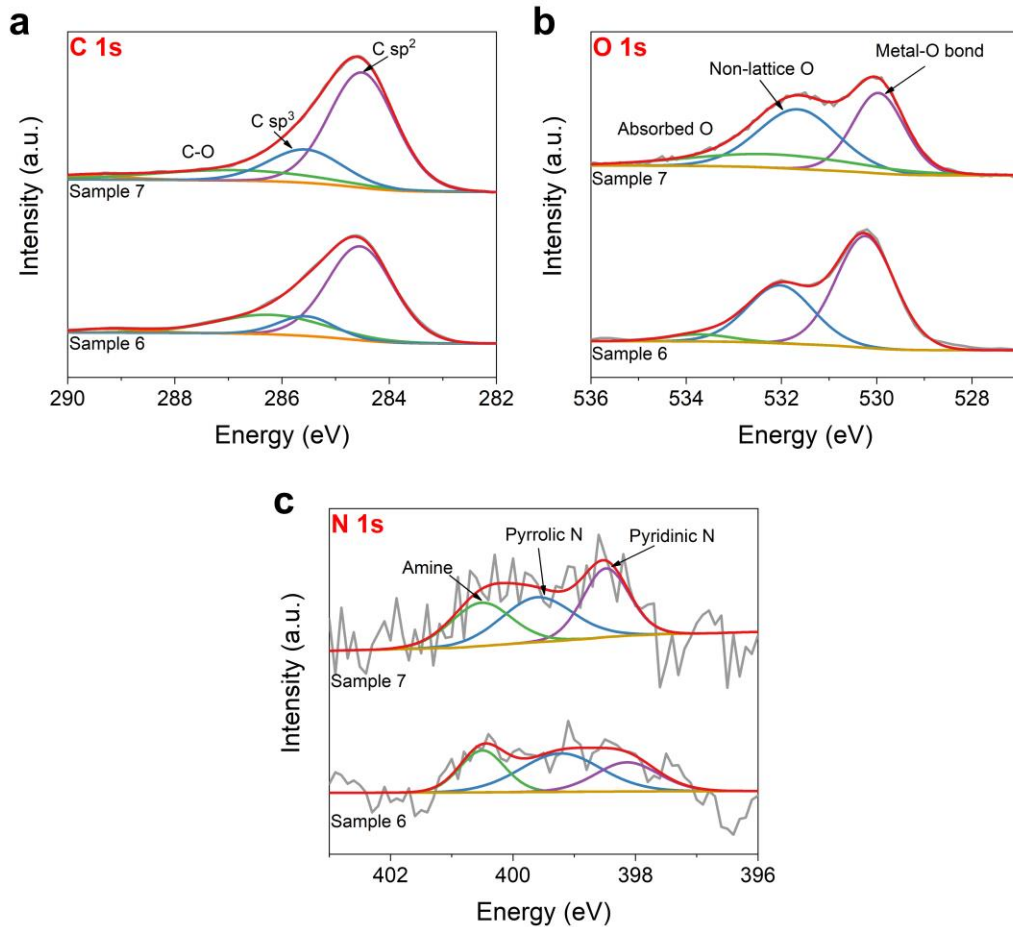
Figure 4.7 High-resolution XPS spectra of rGO with Co-Mn oxides: (a) C 1s, (b) O 1s, and (c) N 1s.

The high-resolution XPS spectra of Co 2p, Mn 2p, and Fe 2p are shown in **Figure 4.8**. In the high-resolution XPS spectra of Co 2p (**Figure 4.8a**), the Co $2p_{3/2}$ and Co $2p_{1/2}$ peaks are observed in the spectra of Sample 6 and Sample 7. The peaks of Co (II) appear at the binding energy of 780.4/796.0 eV and 779.3/794.3 eV for Sample 6 and Sample 7. The peaks of Co (III) are observed at 782.6/798.1 eV and 781.5/797.3 eV for Sample 6 and

Sample 7 [6, 51]. The two shake-up type satellite peaks are observed at the binding energy of 786.8/803.2 eV for Sample 6 and 786.6/803.4 eV for Sample 7 [52]. The peaks at 778.7 eV and 793.7 eV are attributed to the metal Co, which indicates the possible presence of the limited amount of FeCo NPs in Sample 6. The peak of metal Co disappears in the spectrum of Sample 7, which indicates that the reaction completely transfers to the formation of Co-Mn oxides on rGO. The results of XPS are consistent with the XRD and EDX results [53].

As shown in **Figure 4.8b**, the Mn $2p_{3/2}$ and Mn $2p_{1/2}$ peaks are observed in the high-resolution XPS spectra of Mn 2p (Sample 6 and 7). The peaks that appear at the binding energy of 641.3/653.0 eV and 640.3/651.8 eV for Sample 6 and Sample 7 correspond to Mn (II). Meanwhile, the peaks that appear at 642.4/654.0 eV and 641.5/653.0 eV for Sample 6 and Sample 7 are ascribed to Mn (III). In addition, the peaks at the binding energy of 643.8/655.3 eV and 643.9/654.3 eV of Sample 6 and Sample 7 are attributed to Mn (IV) [27, 51]. Therefore, three different oxidation states of Mn are observed in the Mn 2p spectra, which can be due to the formation of other phases.

The weak signals of Fe 2p are observed in the XPS survey scan (**Figure 4.6**) and high-resolution XPS spectra of Fe $2p_{3/2}$ (**Figure 4.8c**) for Sample 6 and Sample 7 due to the limited amounts of Fe contents. The peaks that appear at the binding energy of 710.6 eV, 713.0 eV, and 715.9 eV for the Sample 6 and 710.5 eV, 712.5 eV, and 714.2 eV for Sample 7 correspond to the Fe (II) and Fe (III) for oxidized Fe [54, 55]. The peak at the binding energy of 707.4 eV of Sample 6 indicates the existence of metallic Fe, which is not observed in the spectra of Sample 7 [56, 57]. This result suggests the formation of the small amount of FeCo NPs in Sample 6, and most of them are replaced by Co-Mn oxides NPs as the mass ratio of added rGO in the reaction (M_{rGO}) increases. In addition, the XPS depth profiling (**Table 4.1**) indicates that the atomic ratio of Mn and Co is at the level of 4:1, which is close to the estimation of EDX results. Therefore, the results of XPS spectra suggest the possible formation of the limited amount of FeCo NPs as M_{rGO} equals 60 wt.%. The reaction is mostly transferred to the production of Co-Mn oxides NPs on rGO surface as the M_{rGO} increases, which is consistent with the results of XRD and EDX.

Table 4.1 XPS depth profiling results of atomic ratio of major elements of Sample 7.

Sputter time (min)	Depth (nm)	C 1s	O 1s	Mn 2p	Co 2p
0	0	64.7	26.3	5.2	1.5
10.4	28.1	67.5	16.6	10.2	2.6
27.2	73.4	71.9	14.1	8.8	2.2
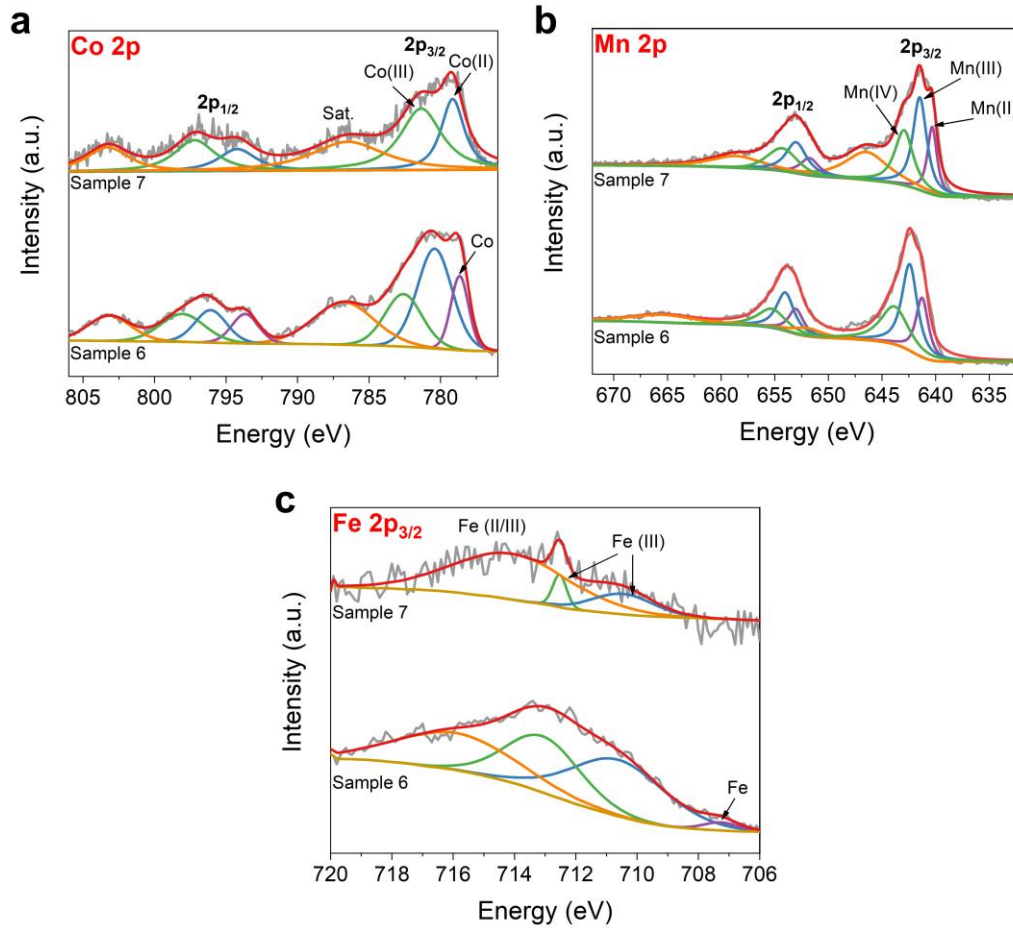
Figure 4.8 High-resolution XPS spectra of rGO with Co-Mn oxides: (a) Co 2p, (b) Mn 2p, and (c) Fe 2p$_{3/2}$.

4.3.2　Magnetic Properties of rGO with Co-Mn Oxides

The magnetic hysteresis loops of rGO with Co-Mn oxides were measured with the vibrating sample magnetometer (VSM) at ambient temperature. As shown in **Figure 4.9**, the magnetic hysteresis loop of Sample 6 exhibits a weak ferromagnetic behaviour (mixed with paramagnetic phase), and the saturation is not reached at 10 kOe [58]. The coercivity (H_c) of Sample 6 (M_{rGO} = 60 wt.%) is at 108.5 Oe with the remanence (M_r) at 0.16 emu/g. As the added rGO ratio (M_{rGO}) increases to 70 wt.% (**Figure 4.10**), the magnetism of Sample 7 increases linearly with no significant hysteresis loop presence, which is consistent with the previous work of Co-Mn oxides [6]. The results suggest that the rise of M_{rGO} (70 wt.%) has completely shifted the reaction to the formation of Co-Mn oxides NPs. Moreover, a small amount of FeCo NPs exists in Sample 6 when M_{rGO} = 60 wt.%, which has been confirmed by the results of XRD, EDX, and XPS. Thus, it can be proved that the threshold of reaction transformation is at M_{rGO} = 60 wt.%, and the formation of Co-Mn oxides NPs becomes dominant as the M_{rGO} increases to 70 wt.%.
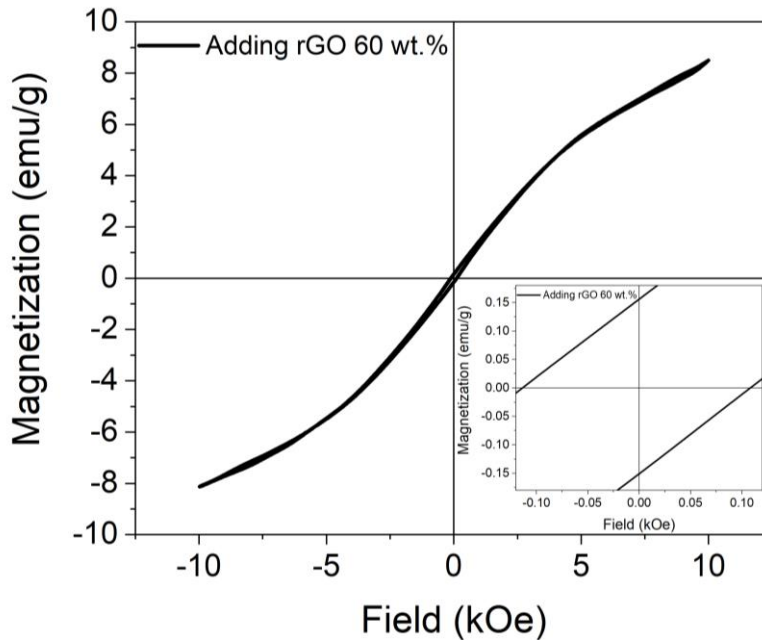
Figure 4.9 The magnetic hysteresis loop of Sample 6 (M_{rGO} = 60 wt.%) at room temperature.
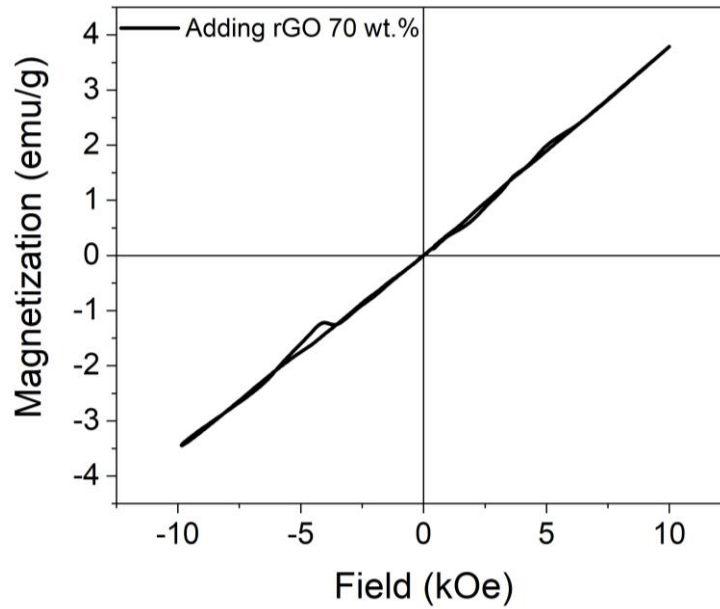
Figure 4.10 The magnetic hysteresis loop of Sample 7 (M_{rGO} = 70 wt.%) at room temperature.

4.3.3 The Magnetoresistance of rGO with Co-Mn Oxides

To investigate the magnetoresistance (MR (%), $\Delta R/R_0$) of the rGO with Co-Mn oxides, the as-prepared samples were pressed to pellets and tested with the 4-pin probe. As shown in **Figure 4.11**, the MR (%) of Sample 6 reaches 4.2 ± 0.4% at the room temperature and low magnetic field (10 kOe). The MR of Sample 7 reaches 3.50 ± 0.04% at equivalent conditions as M_{rGO} increases to 70 wt.%. The rGO with Co-Mn oxides (Sample 7) achieves an average MR at 3.5% at room temperature and low magnetic field (10 kOe), considering the possible effects from FeCo NPs in Sample 6. The MR of rGO with Co-Mn oxides is significantly higher than the MR of other materials/structures with Co and Mn content at ambient temperature and low magnetic field, and most of these materials/structures require extremely low temperature (4 ~ 20 K) to reach the comparable MR value (~ 3%) [38, 39]. Although the tunneling magnetoresistance (TMR) multilayer systems contained Co and Mn can obtain a huge MR, the drawbacks such as limited response range and requiring specific equipment in the fabrication hinder their applications in the preparation of MR sensors/devices. Therefore, the nanocomposites

with Co-Mn oxides and rGO could be developed for constructing MR sensors/devices in the future.
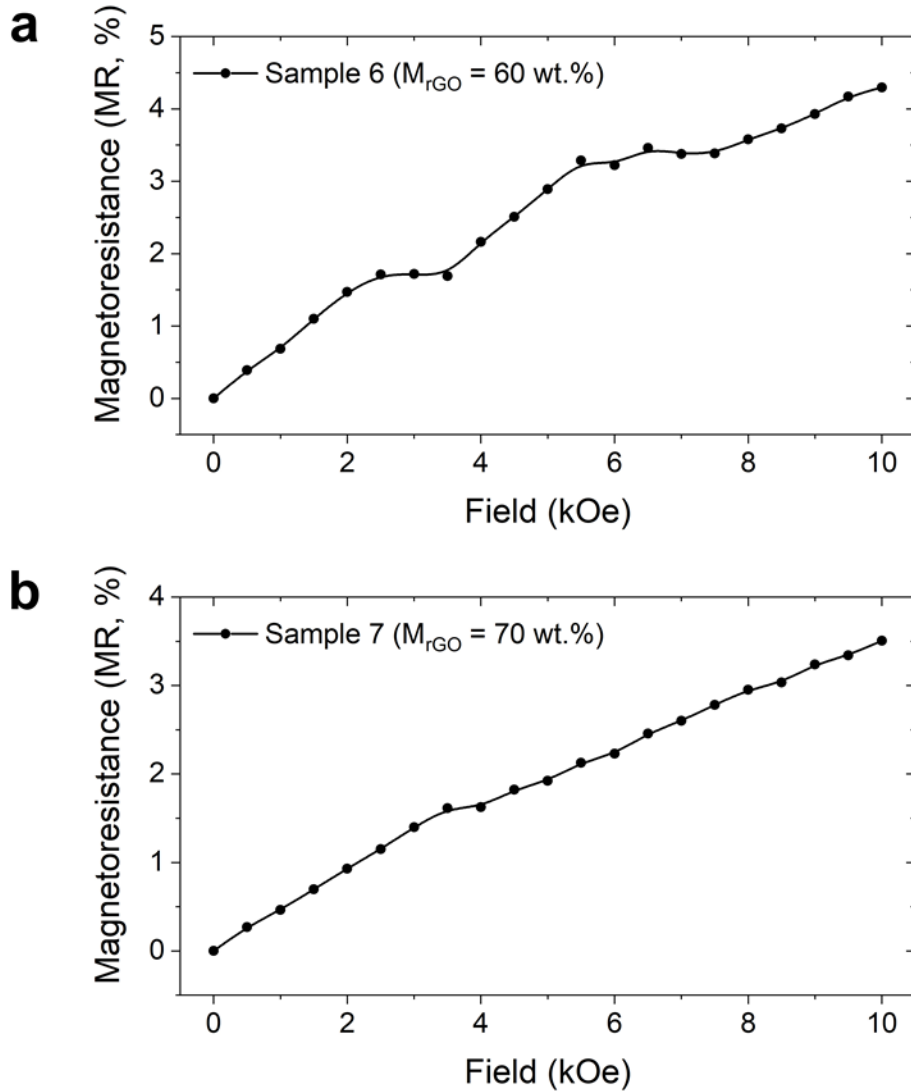
Figure 4.11 Magnetoresistance (MR, %) of rGO with Co-Mn oxides: (a) Sample 6 (M_{rGO} = 60 wt.%) and (b) Sample 7 (M_{rGO} = 70 wt.%).

To study the possible origin of the positive MR of rGO with Co-Mn oxides, the quantum magnetoresistance (QMR) model was applied [40]. A. A. Abrikosov introduces the QMR model to explain the origin of the MR in the complex materials/compounds with 'charge reservoirs' (atom/layer with higher electron density) embedding into the layered materials with relatively lower electron density. In our previous work, the FeCo NPs play the role

of the charge reservoirs and scattering centers on rGO [4]. In the case of rGO with Co-Mn oxides, the Co-Mn NPs can serve as scattering centers to alter the trajectory of carriers and reduce the length of the mean free path of carriers [59]. Therefore, the following equation is introduced

$$\rho_{xx} = \frac{HN_i}{\pi e c n_0^2} \cdot \frac{\sinh(1/\theta)}{\cosh(m/\theta) + \cosh(m/\theta)} \qquad (4.3)$$

where ρ_{xx} is the total resistance (in resistivity), H the magnetic field intensity, n_0 the excess electron density, $H_0 = (\pi \cdot n_0 \cdot c \cdot d)/e$ (d is the interlayer distance), $h = H/H_0$, and N_i the concentration of scattering centers. Abrikosov points out that $m = sin(\pi/h)$ as $T = 0$, and this relation is applied in developing the modified equation as the QMR model has been used to study different materials at different temperatures [60]. Therefore, a modified equation is developed to describe the correlation between the intensity of the external magnetic field (H) and resistance change (ΔR) of the target material

$$y = b \cdot a \cdot x \cdot \left\{ \frac{\sinh(\frac{1}{c})}{\cosh\left[\frac{\sin(\pi/ax)}{c}\right] + \cosh\left[\frac{\sin(\pi/ax)}{c}\right]} \right\} \qquad (4.4)$$

where $y = \Delta R$, $x = H$, $a = 1/H_0$, $b = (N_i \cdot d)/(n_0 \cdot e^2)$, and $c = \theta$.

The fitting results of rGO with Co-Mn oxides are shown in **Figure 4.12**. Good fitting agreements with the original data of the positive MR are observed for both Sample 6 ($R^2 = 0.985$) and Sample 7 ($R^2 = 0.991$). We propose that the Co-Mn oxides NPs perform as scattering centers on the rGO matrix in the QMR system. Although the QMR model exhibits a good agreement with the resistance change, further investigations are required to understand the origin of the MR and other possible roles that Co-Mn oxides NPs play in generating large MR at low magnetic fields.
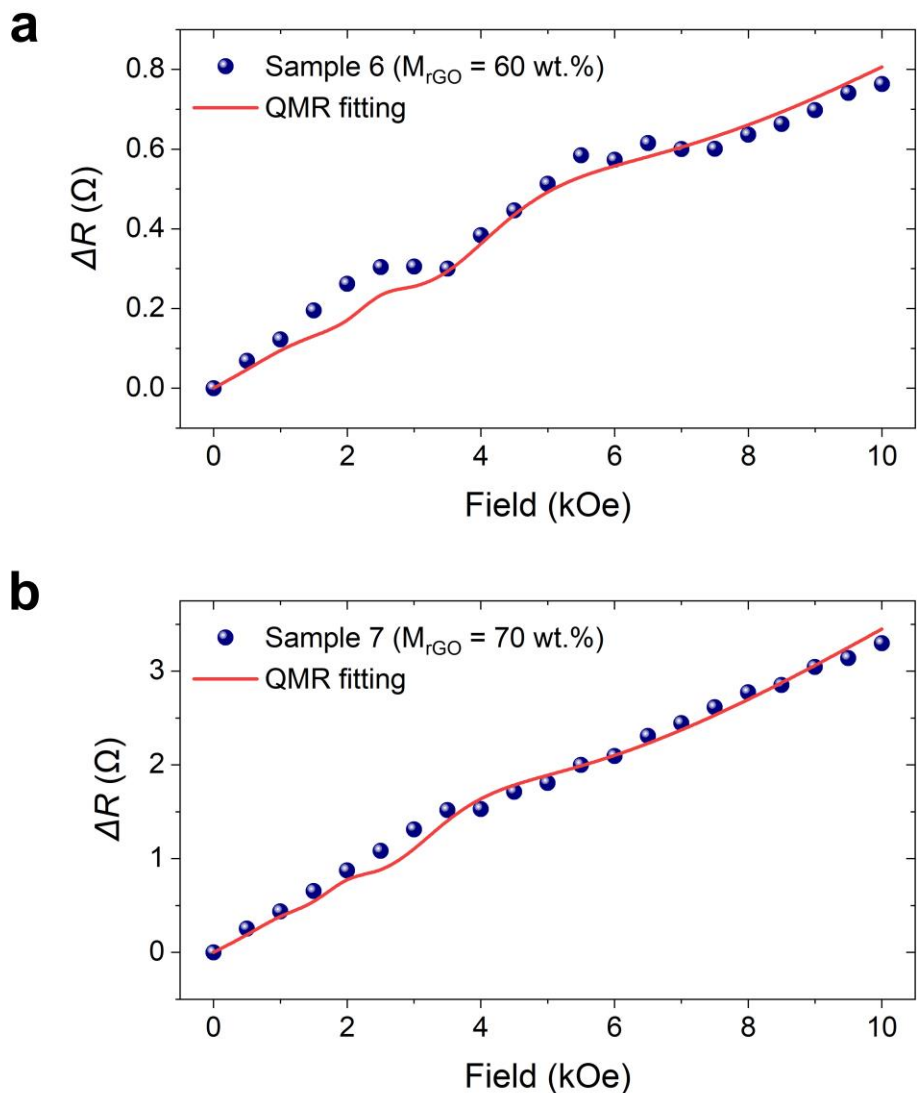
Figure 4.12 Fitting results of QMR model on resistance change (ΔR) of rGO with Co-Mn oxides: (a) Sample 6 (M_{rGO} = 60 wt.%) and (b) Sample 7 (M_{rGO} = 70 wt.%).

4.4   Conclusions

In this study, we investigated the influences of the imported ions introduced by increasing the mass ratio of rGO added in the reaction (M_{rGO}). The formation of Co-Mn oxides NPs was observed on rGO. The spherical Co-Mn oxides NPs exhibited a size-adjustable feature, which can be related to the increase of nucleation sites due to the increase of M_{rGO}. The characterization results revealed that the ratio between Co and Mn is at 1:3 to 1:4 along with the possible presence of the $CoMnO_3$ phase. Moreover, characterization

results confirmed that most of the rGO surface was occupied by Co-Mn oxides NPs as M_{rGO} increased to 70 wt.%. Therefore, $M_{rGO} = 60$ wt.% can be determined as the threshold for the reaction to shift to the synthesis of Co-Mn hybrid nanosheets. Meanwhile, as the forming of Co-Mn oxides NPs on the rGO surface becomes dominating ($M_{rGO} = 70$ wt.%) the effects of the residual Fe contents can be ignored.

Moreover, the rGO with Co-Mn oxides displayed MR at the level of 3.5% ~ 4.5% at the low magnetic field (10 kOe) and ambient temperature. Considering the possible influences of the FeCo contents, the MR of rGO with Co-Mn oxides is 3.5% at the low magnetic field (10 kOe) and room temperature, which is significantly larger in contrast with the MR of materials/structures based on Co/Mn under the same conditions [38, 39]. Meanwhile, though TMR multilayer systems with Co/Mn contents can accomplish relatively large MR, the shortcomings such as prerequisites of specific fabrication equipment and the limited sensing range can not be ignored. Therefore, this study proposes a possible route to produce MR materials with Co-Mn oxides and rGO, which can contribute to the development of MR sensors and energy/catalysis-related applications.

4.5 References

[1] M. Sarno, C. Cirillo, C. Scudieri, M. Polichetti, P. Ciambelli, Electrochemical Applications of Magnetic Core–Shell Graphene-Coated FeCo Nanoparticles. *Ind. Eng. Chem. Res.* **2016**, *55* (11), 3157-3166.

[2] X. Fu, Y. Liu, X. Cao, J. Jin, Q. Liu, J. Zhang, FeCo–N_x embedded graphene as high performance catalysts for oxygen reduction reaction. *Appl. Catal.* **2013**, *130-131*, 143-151.

[3] X. Li, J. Feng, Y. Du, J. Bai, H. Fan, H. Zhang*, et al.*, One-pot synthesis of $CoFe_2O_4$/graphene oxide hybrids and their conversion into FeCo/graphene hybrids for lightweight and highly efficient microwave absorber. *J. Mater. Chem. A* **2015**, *3* (10), 5535-5546.

[4] S. Yang, M. Tan, T. Yu, X. Li, X. Wang, J. Zhang, Hybrid Reduced Graphene Oxide with Special Magnetoresistance for Wireless Magnetic Field Sensor. *Nano-Micro Lett.* **2020**, *12* (1), 69.

[5] P. Balasubramanian, T.S.T. Balamurugan, S.-M. Chen, T.-W. Chen, Simplistic synthesis of ultrafine $CoMnO_3$ nanosheets: An excellent electrocatalyst for highly sensitive detection of toxic 4-nitrophenol in environmental water samples. *J. Hazard. Mater.* **2019**, *361*, 123-133.

[6] J.-Y. Wang, P.-Y. Kuang, N. Li, Z.-Q. Liu, Y.-Z. Su, S. Chen, Facile hydrothermal synthesis of cobalt manganese oxides spindles and their magnetic properties. *Ceram. Int.* **2015**, *41* (7), 8670-8679.

[7] C. Yuan, H.B. Wu, Y. Xie, X.W. Lou, Mixed Transition-Metal Oxides: Design, Synthesis, and Energy-Related Applications. *Angew. Chem. Int. Ed.* **2014**, *53* (6), 1488-1504.

[8] M.V. Reddy, G. Prithvi, K.P. Loh, B.V.R. Chowdari, Li Storage and Impedance Spectroscopy Studies on Co_3O_4, CoO, and CoN for Li-Ion Batteries. *ACS Appl. Mater. Interfaces* **2014**, *6* (1), 680-690.

[9] D. Banerjee, R.V. Jagadeesh, K. Junge, M.M. Pohl, J. Radnik, A. Brückner, *et al.*, Convenient and mild epoxidation of alkenes using heterogeneous cobalt oxide catalysts. *Angew. Chem.* **2014**, *126* (17), 4448-4452.

[10] L. Li, M. Liu, S. He, W. Chen, Freestanding 3D Mesoporous Co_3O_4@Carbon Foam Nanostructures for Ethanol Gas Sensing. *Anal. Chem.* **2014**, *86* (15), 7996-8002.

[11] T.I. Dimitrov, Synthesis and structure of zircon-based ceramic pigments containing Mn, Co, and Ni AS chromophoric elements. *Glass Ceram.* **2011**, *67* (11-12), 383-385.

[12] D. Kong, J. Luo, Y. Wang, W. Ren, T. Yu, Y. Luo, *et al.*, Three‐dimensional Co_3O_4@MnO_2 hierarchical nanoneedle arrays: morphology control and electrochemical energy storage. *Adv. Funct. Mater.* **2014**, *24* (24), 3815-3826.

[13] R. Peng, N. Wu, Y. Zheng, Y. Huang, Y. Luo, P. Yu, *et al.*, Large-Scale Synthesis of Metal-Ion-Doped Manganese Dioxide for Enhanced Electrochemical Performance. *ACS Appl. Mater. Interfaces* **2016**, *8* (13), 8474-8480.

[14] Y. Qiu, S. Yang, H. Deng, L. Jin, W. Li, A novel nanostructured spinel $ZnCo_2O_4$ electrode material: morphology conserved transformation from a hexagonal shaped nanodisk precursor and application in lithium ion batteries. *J. Mater. Chem.* **2010**, *20* (21), 4439-4444.

[15] L. Zhou, H.B. Wu, T. Zhu, X.W. Lou, Facile preparation of $ZnMn_2O_4$ hollow microspheres as high-capacity anodes for lithium-ion batteries. *J. Mater. Chem.* **2012**, *22* (3), 827-829.

[16] J. Li, S. Xiong, X. Li, Y. Qian, A facile route to synthesize multiporous $MnCo_2O_4$ and $CoMn_2O_4$ spinel quasi-hollow spheres with improved lithium storage properties. *Nanoscale* **2013**, *5* (5), 2045-2054.

[17] L. Zhou, D. Zhao, X.W. Lou, Double‑shelled $CoMn_2O_4$ hollow microcubes as high‑capacity anodes for lithium‑ion batteries. *Adv. Mater.* **2012**, *24* (6), 745-748.

[18] M.M.S. Sanad, A.K. Yousef, M.M. Rashad, A.H. Naggar, A.Y. El-Sayed, Robust and facile strategy for tailoring $CoMn_2O_4$ and $MnCo_2O_4$ structures as high capacity anodes for Li-ions batteries. *Physica B Condens. Matter* **2020**, *579*, 411889.

[19] G. Yang, X. Xu, W. Yan, H. Yang, S. Ding, Single-spinneret electrospinning fabrication of $CoMn_2O_4$ hollow nanofibers with excellent performance in lithium-ion batteries. *Electrochim. Acta* **2014**, *137*, 462-469.

[20] J. Li, J. Wang, X. Liang, Z. Zhang, H. Liu, Y. Qian, *et al.*, Hollow $MnCo_2O_4$ Submicrospheres with Multilevel Interiors: From Mesoporous Spheres to Yolk-in-Double-Shell Structures. *ACS Appl. Mater. Interfaces* **2014**, *6* (1), 24-30.

[21] N. Bahlawane, P.H.T. Ngamou, V. Vannier, T. Kottke, J. Heberle, K. Kohse-Höinghaus, Tailoring the properties and the reactivity of the spinel cobalt oxide. *Phys. Chem. Chem. Phys.* **2009**, *11* (40), 9224-9232.

[22] C. Shi, Y. Wang, A. Zhu, B. Chen, C. Au, $Mn_xCo_{3-x}O_4$ solid solution as high-efficient catalysts for low-temperature oxidation of formaldehyde. *Catal. Commun.* **2012**, *28*, 18-22.

[23] Y. Feng, X. Zheng, Copper Ion Enhanced Synthesis of Nanostructured Cobalt Oxide Catalyst for Oxidation of Methane. *ChemCatChem* **2012**, *4* (10), 1551-1554.

[24] F. Rubio‑Marcos, V. Calvino‑Casilda, M.A. Bañares, J.F. Fernandez, Control of the interphases formation degree in Co_3O_4/ZnO catalysts. *ChemCatChem* **2013**, *5* (6), 1431-1440.

[25] S. Todorova, A. Naydenov, H. Kolev, J.P. Holgado, G. Ivanov, G. Kadinov, *et al.*, Mechanism of complete n-hexane oxidation on silica supported cobalt and manganese catalysts. *Appl. Catal., A* **2012**, *413-414*, 43-51.

[26] J. Li, X. Liang, S. Xu, J. Hao, Catalytic performance of manganese cobalt oxides on methane combustion at low temperature. *Appl. Catal.* **2009**, *90* (1), 307-312.

[27] T. Cai, H. Huang, W. Deng, Q. Dai, W. Liu, X. Wang, Catalytic combustion of 1,2-dichlorobenzene at low temperature over Mn-modified Co_3O_4 catalysts. *Appl. Catal.* **2015**, *166-167*, 393-405.

[28] P.W. Menezes, A. Indra, N.R. Sahraie, A. Bergmann, P. Strasser, M. Driess, Cobalt–Manganese-Based Spinels as Multifunctional Materials that Unify Catalytic Water Oxidation and Oxygen Reduction Reactions. *ChemSusChem* **2015**, *8* (1), 164-171.

[29] K. Cheng, F. Yang, G. Wang, J. Yin, D. Cao, Facile synthesis of porous (Co, Mn)$_3$O$_4$ nanowires free-standing on a Ni foam and their catalytic performance for H$_2$O$_2$ electroreduction. *J. Mater. Chem. A* **2013**, *1* (5), 1669-1676.

[30] H. Wang, J.T. Robinson, G. Diankov, H. Dai, Nanocrystal Growth on Graphene with Various Degrees of Oxidation. *J. Am. Chem. Soc.* **2010**, *132* (10), 3270-3271.

[31] K. Spilarewicz-Stanek, A. Kisielewska, J. Ginter, K. Bałuszyńska, I. Piwoński, Elucidation of the function of oxygen moieties on graphene oxide and reduced graphene oxide in the nucleation and growth of silver nanoparticles. *RSC Adv.* **2016**, *6* (65), 60056-60067.

[32] Y. Liang, H. Wang, J. Zhou, Y. Li, J. Wang, T. Regier*, et al.*, Covalent Hybrid of Spinel Manganese–Cobalt Oxide and Graphene as Advanced Oxygen Reduction Electrocatalysts. *J. Am. Chem. Soc.* **2012**, *134* (7), 3517-3523.

[33] X. Ge, Y. Liu, F.W.T. Goh, T.S.A. Hor, Y. Zong, P. Xiao*, et al.*, Dual-Phase Spinel MnCo$_2$O$_4$ and Spinel MnCo$_2$O$_4$/Nanocarbon Hybrids for Electrocatalytic Oxygen Reduction and Evolution. *ACS Appl. Mater. Interfaces* **2014**, *6* (15), 12684-12691.

[34] Z. Zheng, W. Zhang, L. Chen, W. Xiong, G. Zeng, J. Liu*, et al.*, In-situ synthesis of MnCo$_2$O$_{4.5}$ nanosheets on reduced graphene oxide for a great promotion in the thermal decomposition of ammonium perchlorate. *Appl. Surf. Sci.* **2019**, *483*, 496-505.

[35] H. Wang, Y. Yang, Y. Liang, G. Zheng, Y. Li, Y. Cui*, et al.*, Rechargeable Li–O$_2$ batteries with a covalently coupled MnCo$_2$O$_4$–graphene hybrid as an oxygen cathode catalyst. *Energy Environ. Sci.* **2012**, *5* (7), 7931-7935.

[36] R.K.N. Kutty, P.R. Kasturi, J. Jaganath, S. Padmanapan, Y.S. Lee, D. Meyrick*, et al.*, Structural and magnetic properties of CoMn$_2$O$_4$ synthesized by auto combustion method. *J. Mater. Sci.: Mater. Electron.* **2019**, *30* (2), 975-981.

[37] S.G. Krishnan, M. Harilal, A. Yar, B.L. Vijayan, J.O. Dennis, M.M. Yusoff*, et al.*, Critical influence of reduced graphene oxide mediated binding of M (M=Mg, Mn) with Co ions, chemical stability and charge storability enhancements of spinal-type hierarchical MCo$_2$O$_4$ nanostructures. *Electrochim. Acta* **2017**, *243*, 119-128.

[38] L.Z. Kong, H. Wang, S.Q. Xiao, J.J. Lu, Y.X. Xia, G.J. Hu*, et al.*, Integrated properties of large lateral photovoltage and positive magnetoresistance in Co/Mn/Co/c-Si structures. *J. Phys. D: Appl. Phys.* **2008**, *41* (5), 052003.

[39] Z.-B. Gu, C.-S. Yuan, M.-H. Lu, J. Wang, D. Wu, S.-T. Zhang*, et al.*, Magnetic and transport properties of (Mn, Co)-codoped ZnO films prepared by radio-frequency magnetron cosputtering. *J. Appl. Phys.* **2005**, *98* (5), 053908.

[40] A.A. Abrikosov, Quantum magnetoresistance of layered semimetals. *Phys. Rev. B* **1999**, *60* (6), 4231-4234.

[41] K. Zhang, Y. Zhang, S. Wang, Enhancing thermoelectric properties of organic composites through hierarchical nanostructures. *Sci. Rep.* **2013**, *3* (1), 3448.

[42] S.-K. Jerng, D. Seong Yu, J. Hong Lee, C. Kim, S. Yoon, S.-H. Chun, Graphitic carbon growth on crystalline and amorphous oxide substrates using molecular beam epitaxy. *Nanoscale Res. Lett.* **2011**, *6* (1), 565.

[43] J. Jo, S. Lee, J. Gim, J. Song, S. Kim, V. Mathew*, et al.*, Facile synthesis of reduced graphene oxide by modified Hummer's method as anode material for Li-, Na- and K-ion secondary batteries. *R. Soc. Open Sci.* **2019**, *6* (4), 181978.

[44] B. Lesiak, L. Kövér, J. Tóth, J. Zemek, P. Jiricek, A. Kromka*, et al.*, C sp^2/sp^3 hybridisations in carbon nanomaterials – XPS and (X)AES study. *Appl. Surf. Sci.* **2018**, *452*, 223-231.

[45] B. Pattanayak, F.M. Simanjuntak, D. Panda, C.C. Yang, A. Kumar, P.A. Le*, et al.*, Role of precursors mixing sequence on the properties of $CoMn_2O_4$ cathode materials and their application in pseudocapacitor. *Sci. Rep.* **2019**, *9* (1), 16852.

[46] Y.-H. Zhang, X.-L. Cai, D.-Y. Guo, H.-J. Zhang, N. Zhou, S.-M. Fang*, et al.*, Oxygen vacancies in concave cubes Cu_2O-reduced graphene oxide heterojunction with enhanced photocatalytic H_2 production. *J. Mater. Sci.: Mater. Electron.* **2019**, *30* (7), 7182-7193.

[47] B.J. Matsoso, K. Ranganathan, B.K. Mutuma, T. Lerotholi, G. Jones, N.J. Coville, Time-dependent evolution of the nitrogen configurations in N-doped graphene films. *RSC Adv.* **2016**, *6* (108), 106914-106920.

[48] T. Kondo, D. Guo, T. Shikano, T. Suzuki, M. Sakurai, S. Okada*, et al.*, Observation of Landau levels on nitrogen-doped flat graphite surfaces without external magnetic fields. *Sci. Rep.* **2015**, *5* (1), 16412.

[49] B.K. Mutuma, C.I. Garcia-Martinez, R.C. Dias, B.J. Matsoso, N.J. Coville, I.A. Hümmelgen, Nitrogen-doped hollow carbon spheres as chemical vapour sensors. *New J. Chem.* **2019**, *43* (22), 8418-8427.

[50] M.K. Rabchinskii, S.A. Ryzhkov, D.A. Kirilenko, N.V. Ulin, M.V. Baidakova, V.V. Shnitov*, et al.*, From graphene oxide towards aminated graphene: facile synthesis, its structure and electronic properties. *Sci. Rep.* **2020**, *10* (1), 6902.

[51] M.C. Biesinger, B.P. Payne, A.P. Grosvenor, L.W.M. Lau, A.R. Gerson, R.S.C. Smart, Resolving surface chemical states in XPS analysis of first row transition metals, oxides and hydroxides: Cr, Mn, Fe, Co and Ni. *Appl. Surf. Sci.* **2011**, *257* (7), 2717-2730.

[52] W. Yan, Z. Yang, W. Bian, R. Yang, $FeCo_2O_4$/hollow graphene spheres hybrid with enhanced electrocatalytic activities for oxygen reduction and oxygen evolution reaction. *Carbon* **2015**, *92*, 74-83.

[53] L. Chen, Y. Zhang, H. Wang, Y. Wang, D. Li, C. Duan, Cobalt layered double hydroxides derived CoP/Co$_2$P hybrids for electrocatalytic overall water splitting. *Nanoscale* **2018**, *10* (45), 21019-21024.

[54] L. Li, P. Ma, S. Hussain, L. Jia, D. Lin, X. Yin, *et al.*, FeS$_2$/carbon hybrids on carbon cloth: a highly efficient and stable counter electrode for dye-sensitized solar cells. *Sustainable Energy Fuels* **2019**, *3* (7), 1749-1756.

[55] H. Lv, H. Zhao, T. Cao, L. Qian, Y. Wang, G. Zhao, Efficient degradation of high concentration azo-dye wastewater by heterogeneous Fenton process with iron-based metal-organic framework. *J. Mol. Catal. A: Chem.* **2015**, *400*, 81-89.

[56] L. An, N. Jiang, B. Li, S. Hua, Y. Fu, J. Liu, *et al.*, A highly active and durable iron/cobalt alloy catalyst encapsulated in N-doped graphitic carbon nanotubes for oxygen reduction reaction by a nanofibrous dicyandiamide template. *J. Mater. Chem. A* **2018**, *6* (14), 5962-5970.

[57] F. Aftab, H. Duran, K. Kirchhoff, M. Zaheer, B. Iqbal, M. Saleem, *et al.*, A Facile Synthesis of FeCo Nanoparticles Encapsulated in Hierarchical N-Doped Carbon Nanotube/Nanofiber Hybrids for Overall Water Splitting. *ChemCatChem* **2020**, *12* (3), 932-943.

[58] B.J. Sarkar, A. Bandyopadhyay, J. Mandal, A.K. Deb, P.K. Chakrabarti, Paramagnetic to ferromagnetic phase transition of Co doped Gd$_2$O$_3$ prepared by chemical route. *J. Alloys Compd.* **2016**, *656*, 339-346.

[59] M.I. Katsnelson, F. Guinea, A.K. Geim, Scattering of electrons in graphene by clusters of impurities. *Phys. Rev. B* **2009**, *79* (19), 195426.

[60] A.L. Friedman, J.L. Tedesco, P.M. Campbell, J.C. Culbertson, E. Aifer, F.K. Perkins, *et al.*, Quantum Linear Magnetoresistance in Multilayer Epitaxial Graphene. *Nano Lett.* **2010**, *10* (10), 3962-3965.

Chapter 5

5 Fabrication of FeCo/rGO Hybrid Nanosheets with the Physical Deposition Process

In this chapter, we applied the matrix-assisted pulsed laser evaporation (MAPLE) technique in the construction of FeCo/rGO hybrid nanosheets. The physical deposition of magnetic nanoparticles draws the increasing attention of researchers due to the fast developments and potential applications. Most of the studies were carried out to investigate the biomedical applications of modified iron oxide (Fe_3O_4) nanoparticles transferred by the MAPLE technique. However, few studies were performed for understanding magnetic properties especially magnetoresistance (MR) of the products.

Here, we successfully developed the FeCo/rGO hybrid nanosheets with the MAPLE technique. The results of TEM and EDX indicate that it is feasible to transfer FeCo nanoparticles (NPs) onto the rGO in a stoichiometrical manner by the MAPLE technique. The increase of FeCo NPs' density on rGO was observed as the deposition time shifted from 0.5 hours to 2 hours, which was confirmed by SEM-EDX. The MAPLE-prepared FeCo/rGO hybrid nanosheets exhibited ferromagnetic properties. Moreover, with a limited FeCo ratio (0.4 at.%) compared with previous studies, MAPLE-prepared FeCo/rGO hybrid nanosheets displayed relatively large positive magnetoresistance (0.7%, MR) at the low magnetic field (10 kOe) and room temperature. Therefore, the results indicate that the MAPLE technique can be applied in preparing FeCo/rGO hybrid nanosheets with large MR, which benefits the potential applications of producing MR sensors/devices with requirements on thicknesses.

5.1 Introduction

Magnetic nanoparticles (MNPs) have become an important topic of nanotechnology in the recent two decades. Various methods were developed to produce MNPs with high magnetic saturation, stability, and biocompatibility. Multifunctional MNPs were applied in various fields including contaminants/pollution removing [1, 2], *in vitro* cell separation

[3, 4], drug delivery [5], hyperthermia treatment [6], and contrast agent for magnetic resonance imaging (MRI) [7, 8]. Fe_3O_4 MNPs are preferred in biological applications due to the fast magnetization at specific magnetic fields. Meanwhile, Fe_3O_4 MNPs exhibit low remanence magnetizations, which reduces the risk for aggregation [9].

Magnetoresistance (MR) is another interesting property, which refers to the change in electrical resistance of materials under the presence of magnetic fields. Since the discovery of giant magnetoresistance (GMR) in the 1980s, researches on MR devices and sensors surged [10]. In addition, MR sensors were widely applied in magnetic field detection due to the advantages including low energy consumption, physical size, sensitivity, and temperature stability in contrast with traditional Hall effect field sensors [11, 12]. Nanoconstructed MR materials showed benefits in both reducing the size and enhancing the performance of MR. However, current results indicate that most physically produced granular MR systems based on MNPs require low temperatures or large magnetic fields to achieve large MR, which is not suitable for applications at room temperature and low magnetic fields [13, 14].

FeCo possesses unusual magnetic properties such as large permeability and high magnetic saturation (~ 200 emu/g) [15, 16]. Both bulk FeCo layer and FeCo granular system were applied in constructing MR materials/structures because of the strong spin-dependent scattering effects [17-19]. Previous research indicated that it is possible to achieve large MR by producing a uniform distribution of FeCo magnetic granules in the non-magnetic material matrix due to the influence on the mean free path of electrons [19]. However, current results exhibited inadequate MR at low magnetic fields and room temperature. A. A. Abrikosov proposed that large MR can be achieved by inhomogeneous materials consisting of layered materials with relatively small electron concentration and clusters of metallic atoms embedded [20, 21]. Therefore, incorporating FeCo NPs with graphene can be considered as a possible pathway for producing materials/structures with large MR responses.

Graphene exhibits high carrier mobility at room temperature and unique electrical properties [22, 23]. In contrast with monolayer/bilayer graphene, chemically synthesized

reduced graphene oxide (rGO) is preferred since rGO shows minimum requirements on high-quality SiO_2 substrates and specific fabrication techniques [24, 25]. Our previous study successfully developed FeCo/rGO hybrid nanosheets with enhanced MR properties *via* the chemical synthesis process [26]. Although constructing FeCo/rGO hybrid nanosheets with chemical synthesis can reduce the cost and demands on equipment, it is difficult for the chemical route to produce ultra-thin layers/films. Therefore, the feasibility to construct FeCo/rGO hybrid nanosheets *via* physical routes such as the physical vapor deposition (PVD) technique needs to be investigated. However, it is important to preserve the chemical composition and crystal structure of FeCo NPs in this process, which is challenging for some conventional PVD techniques such as pulsed laser deposition (PLD).

Matrix-assisted pulsed laser evaporation (MAPLE) technique was developed to overcome the drawbacks of conventional PLD by introducing the highly volatile matrix solvent (frozen by liquid nitrogen) to absorb most of the laser beam energy (**Figure 5.1**) [27]. As a physical deposition process for transferring delicate materials onto the preferred substrate, MAPLE was applied in producing thin films consist of polymers, proteins, and nanoparticles [28-32]. However, current studies on transferring functionalized MNPs with the MAPLE technique focus on biomedical applications [33-35]. Few investigations were performed to explore the feasibility of constructing MR materials/structures with MAPLE.

In this study, we successfully constructed FeCo/rGO hybrid nanosheets with matrix-assisted pulsed laser evaporation (MAPLE). FeCo NPs were stoichiometrically transferred on the rGO substrate, which was confirmed by TEM-EDX. The influences of deposition duration on morphology and structure of physically prepared FeCo/rGO hybrid nanosheets were studied by varying deposition time from 0.5 hour to 2 hours. A positive correlation between deposition duration and FeCo NPs' particle density on the rGO surface was observed. The hysteresis loop of as-prepared FeCo/rGO hybrid nanosheets indicated that FeCo NPs retained ferromagnetic behaviour after transferring to the rGO surface by MAPLE. In addition, the FeCo/rGO hybrid nanosheets exhibited MR (~ 0.7%) at room temperature and low magnetic field (10 kOe), which is larger than or

139

close to the MR of granular FeCo materials/structures prepared by other physical processes (i.e., magnetron sputtering) under equivalent conditions [19, 36].
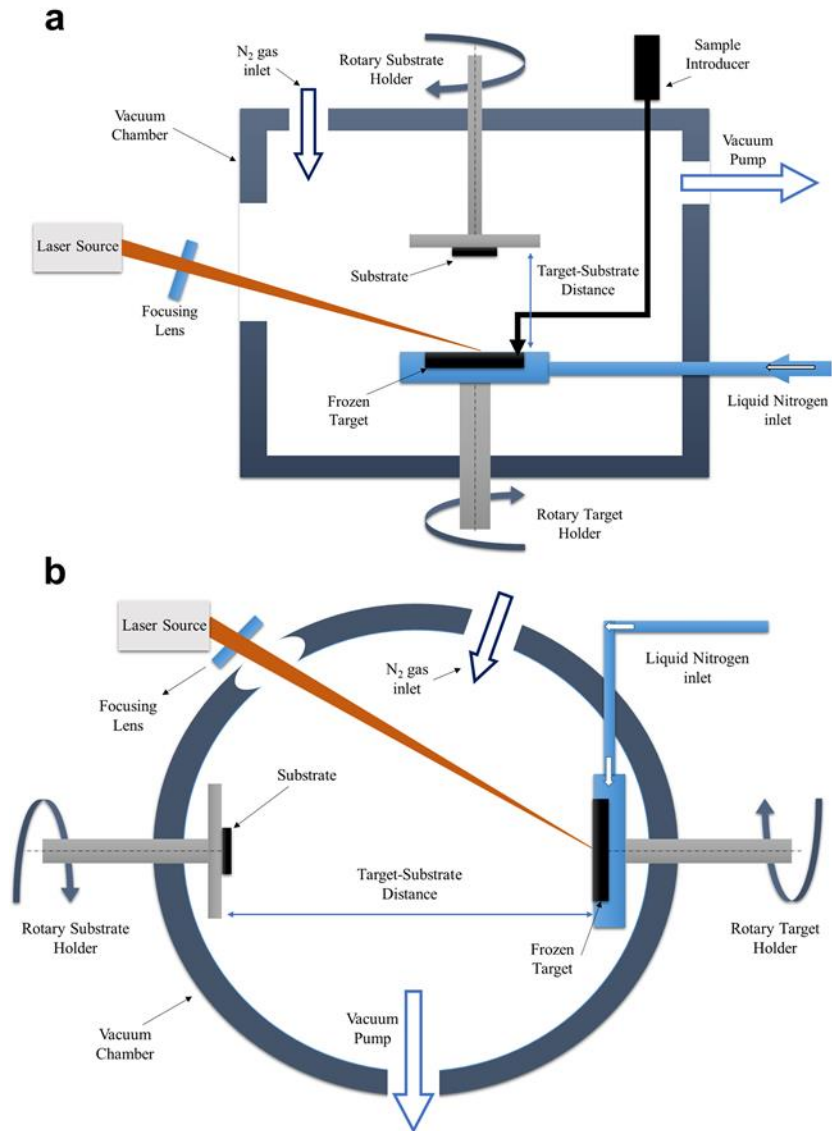
Figure 5.1 Schematic diagram of two major configurations of MAPLE technique. (a) Vertical configuration. (b) Horizontal configuration.

5.2 Experimental

5.2.1 Preparation of Reduced Graphene Oxide (rGO)

rGO was obtained by reduction of graphene oxide (GO) with hydrazine, which has been discussed in Chapter 3 [26].

5.2.2 Preparation of FeCo Nanoparticles (NPs)

The preparation of FeCo NPs was described in our previous work, which has been discussed in Chapter 3 [26]. The FeCo nanoparticles (NPs) were prepared with the modified polyol process with no rGO added to the reaction.

5.2.3 Preparation of FeCo/rGO Hybrid Nanosheets with MAPLE

The preparation of FeCo/rGO hybrid nanosheets was performed by matrix-assisted pulsed laser evaporation (MAPLE, PVD Products, Inc., USA). FeCo NPs were suspended in the 2-propanol (isopropanol, Caledon laboratory chemicals) with a concentration of 1 wt%. Further sonication was applied to achieve the uniform dispersion of FeCo NPs. The solution was injected into the target holder and frozen by liquid nitrogen. Thus, the preparation of the irradiation target was finished. A Nd:YAG laser (secondary harmonic, wavelength 532 nm) was applied as the laser source of the MAPLE system (**Figure 5.2**). Laser frequency was 10 Hz with pulse duration at 320 µs, $\tau_{fwhm} \cong 200$ µs, and 0.63 cm^2 laser spot area size. The laser fluence was set to 300 mJ/cm^2. rGO was immobilized on the surface of 5 mm $\times$ 5 mm glass slips. The substrates were fixed on the substrate holder as shown in **Figure 5.3**. The background pressure was set to 0.01 Pa. The substrate-to-target distance was 4.5 cm.

Figure 5.2 Picture of MAPLE system.
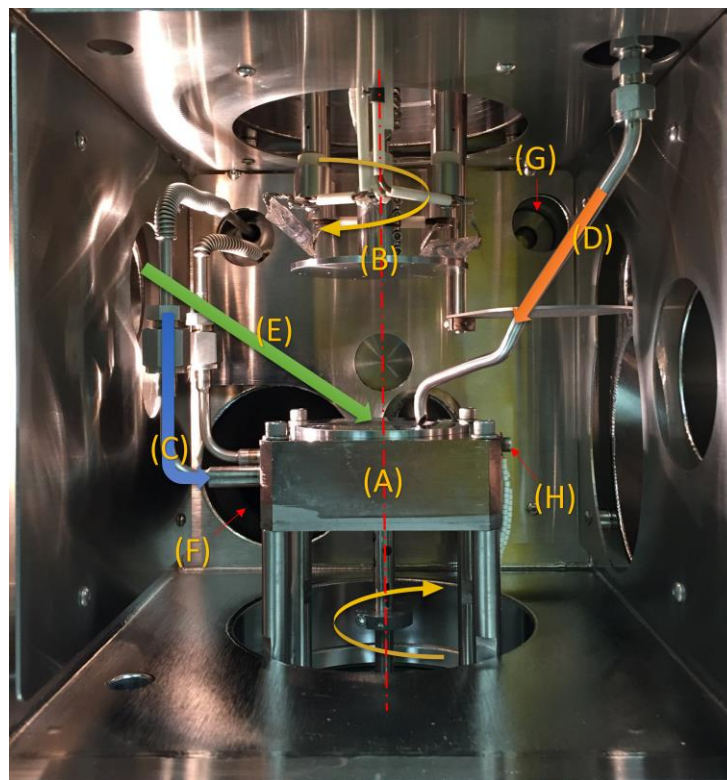
Figure 5.3 Picture of vacuum chamber: (a) Target holder, (b) substrate holder, (c) liquid nitrogen purge tube, (d) loading tube, (e) laser beam, (g) nitrogen inlet, and (h) thermocouple.

5.2.4   Magnetoresistance Measurement

The magnetoresistance measurement of the samples was performed by the Model 74046 magnetoresistance (MR) probe attached to the vibrating sample magnetometer (VSM, LakeShore 7407). The MR (%) is defined by the following equation.

$$MR(\%) = \frac{R - R_0}{R_0} \times 100\% \qquad (5.1)$$

The resistance change (ΔR, Ω) is defined by the equation below

$$\Delta R = R - R_0 \qquad (5.2)$$

where R is the total resistance (Ω) of the sample under the presence of an external magnetic field and R_0 the sample resistance (Ω) at zero magnetic field.

5.2.5   Materials Characterization

Transmission electron microscope (TEM) micrographs and energy-dispersive X-ray spectra (TEM-EDX) were obtained by Philips CM-10. A Hitachi S-3400N scanning electron microscope (SEM) attached with the INCA PentaFET-x3 system (Oxford Instruments) was used to obtain SEM micrographs and energy-dispersive X-ray spectra (SEM-EDX). The ultraviolet-visible (UV-Vis) spectra were obtained by Cary 60 UV-Vis spectrophotometer (Agilent Technologies). The magnetic hysteresis loop and MR were obtained by the vibrating sample magnetometer (VSM, LakeShore 7407, moment measure range: 10^{-7} to 10^3 emu; field accuracy: "± 0.05%" full scale).

5.2.6   Software for Data Simulation

The mathematical calculation for the quantum magnetoresistance (QMR) model was performed by MATLAB (The MathWorks), Python(x,y) (https://python-xy.github.io/), and 1stOpt (7D-Soft High Technology Inc.), which gave us similar results.

5.3 Results and Discussion

5.3.1 Characterization of rGO and FeCo NPs

As shown in **Figure 5.4**, the as-prepared FeCo NPs were transferred from the frozen target onto the surface of the rGO substrate to construct FeCo/rGO hybrid nanosheets *via* the physical deposition process. The influences of deposition time (*t*) on the morphology and structure of physically produced FeCo/rGO hybrid nanosheets were studied by varying the deposition time from 0.5 hours to 2 hours (time interval 0.5 hours). The transmission electron microscope (TEM) micrograph and the UV-Vis spectrum of rGO were obtained (**Figure 5.5**). The redshift of the rGO absorbance peak (271 nm) compared with the peak of graphene oxide (GO, 230 nm) indicates the successful preparation of rGO substrates [37].
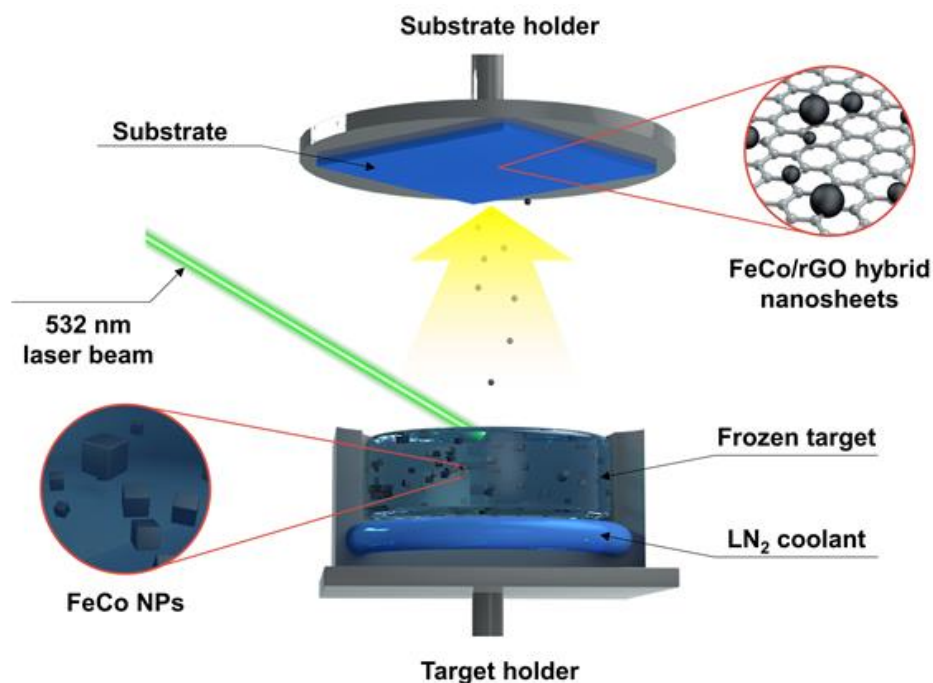
Figure 5.4 Schematic illustration of physical preparation process of FeCo/rGO hybrid nanosheets by MAPLE.

144
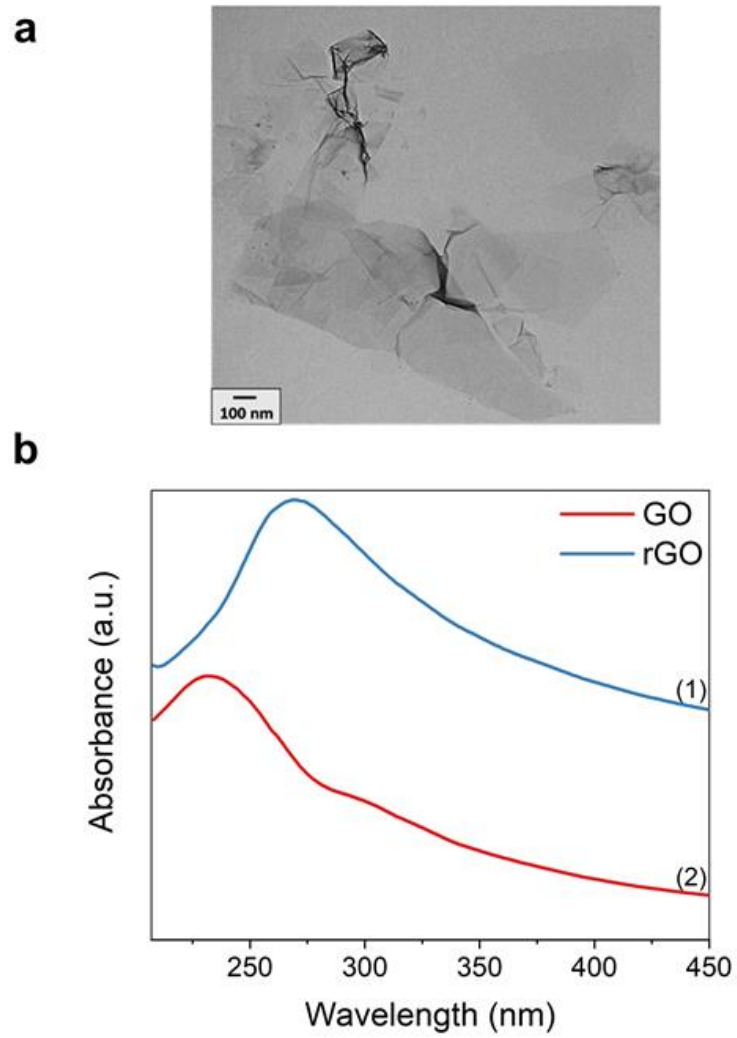
Figure 5.5 (a) TEM micrograph of rGO. (b) UV-Vis spectrum of (1) rGO and (2) graphene oxide (GO).

FeCo NPs were produced with a facile one-pot polyol process. The layered cubic structure FeCo NPs were observed in the TEM micrograph (**Figure 5.6a**). The average diameter of chemically synthesized FeCo NPs is 350 ± 50 nm. The energy-dispersive X-ray spectroscopy (TEM-EDX) was applied. **Figure S5.1** suggests that the ratio between Fe and Co is close to 1:1 for chemically synthesized FeCo NPs. The magnetic properties were measured by the vibrating sample magnetometer (VSM). **Figure 5.6b** shows the magnetic hysteresis loop that indicates the high saturation magnetizations (M_S, 181.21 ± 0.83 emu/g at 10 kOe) of FeCo NPs. Moreover, the coercivity (H_C) of FeCo NPs is 0.13 ± 0.01 kOe.
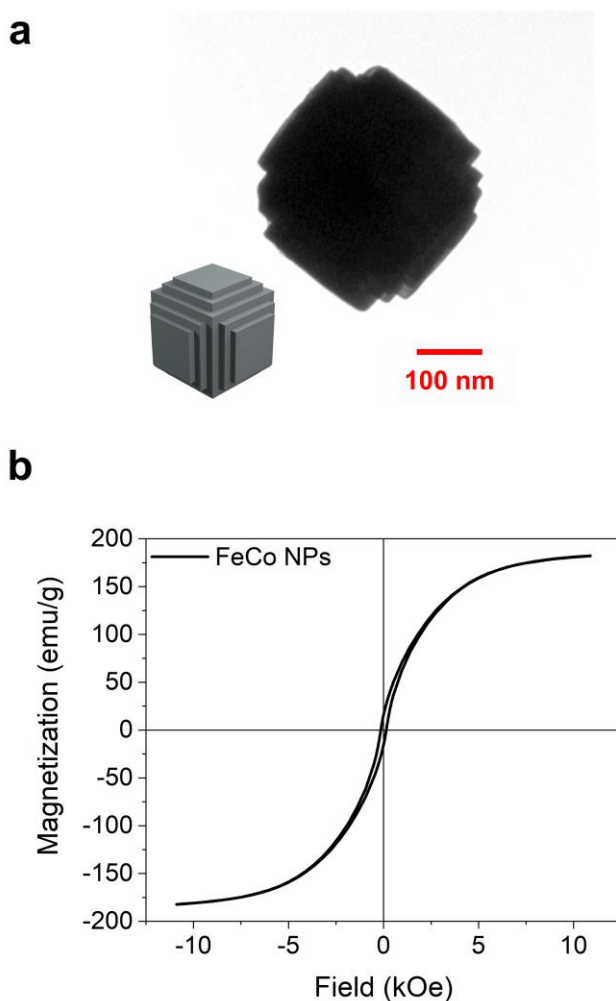
Figure 5.6 (a) TEM micrograph of FeCo NPs with layered cubic structure. (b) Magnetic hysteresis loop of FeCo NPs.

5.3.2 Developing FeCo/rGO Hybrid Nanosheets with MAPLE Technique

The morphology and structure of physically prepared FeCo/rGO hybrid nanosheets were characterized by transmission electron microscopy (TEM). As shown in **Figure 5.7**, the presence of FeCo NPs on the surface of rGO is observed in the TEM micrographs. The average size of FeCo NPs transferred by MAPLE is at 10 nm level, which decreases significantly compared with the average size of the chemically synthesized FeCo NPs (350 ± 50 nm). Meanwhile, the shape of FeCo NPs on physically prepared FeCo/rGO hybrid nanosheets transforms to the sphere shape in contrast with the layered cubic shape of FeCo NPs before being transferred by MAPLE. Laser-introduced coalescence could be the driving force of this transformation based on the investigations of previous works [38].

The effects of deposition time (t) on the structure and morphology were studied by varying the deposition time from 0.5 hours to 2 hours with the 0.5 hours interval. As shown in **Figure 5.7**, the particle density of FeCo NPs on FeCo/rGO hybrid nanosheets increases significantly as the deposition time increases from 0.5 hours to 1 hour and 1 hour to 1.5 hours. Therefore, the quantity of FeCo NPs transferred by MAPLE onto the surface of rGO substrates increases substantially as deposition time raises from 0.5 hours to 2 hours.

The average size of the FeCo NPs on physically prepared FeCo/rGO nanosheets was measured and analyzed. **Figure 5.8** indicates that the average sizes of the FeCo NPs for different deposition times are 10 ± 5 nm, 10 ± 7 nm, 8 ± 6 nm, and 4 ± 3 nm for samples of 0.5 hours, 1 hour, 1.5 hours, and 2 hours. Though the average sizes are close for 0.5 hours sample and 1 hour sample, a significant drop in the average sizes of FeCo NPs is observed between the samples with the deposition time of 1 hour and 2 hours. As shown in **Figure 5.9**, the box chart indicates the shift of the size distribution as the deposition time increases from 0.5 hours to 2 hours (ignored the outliners). Therefore, the results suggest that it is possible to adjust the particle density and size distribution of FeCo NPs

on physically prepared FeCo/rGO hybrid nanosheets by simply varying the deposition time (t) of MAPLE process.
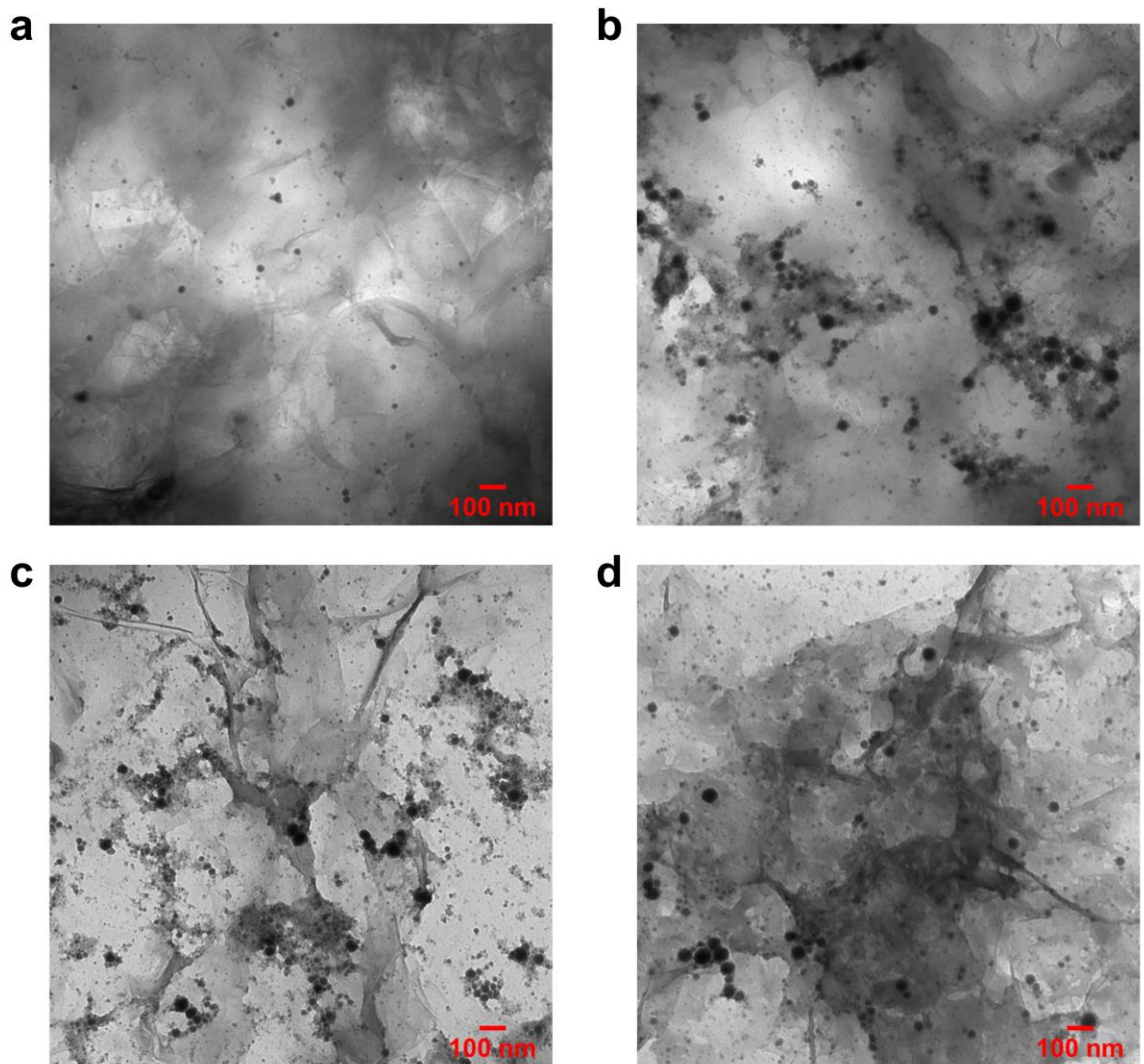
Figure 5.7 TEM micrographs of FeCo/rGO hybrid nanosheets prepared with physical process: (a) deposition time = 0.5 hour, (b) deposition time = 1 hour, (c) deposition = 1.5 hours, and (d) deposition time =2 hours.
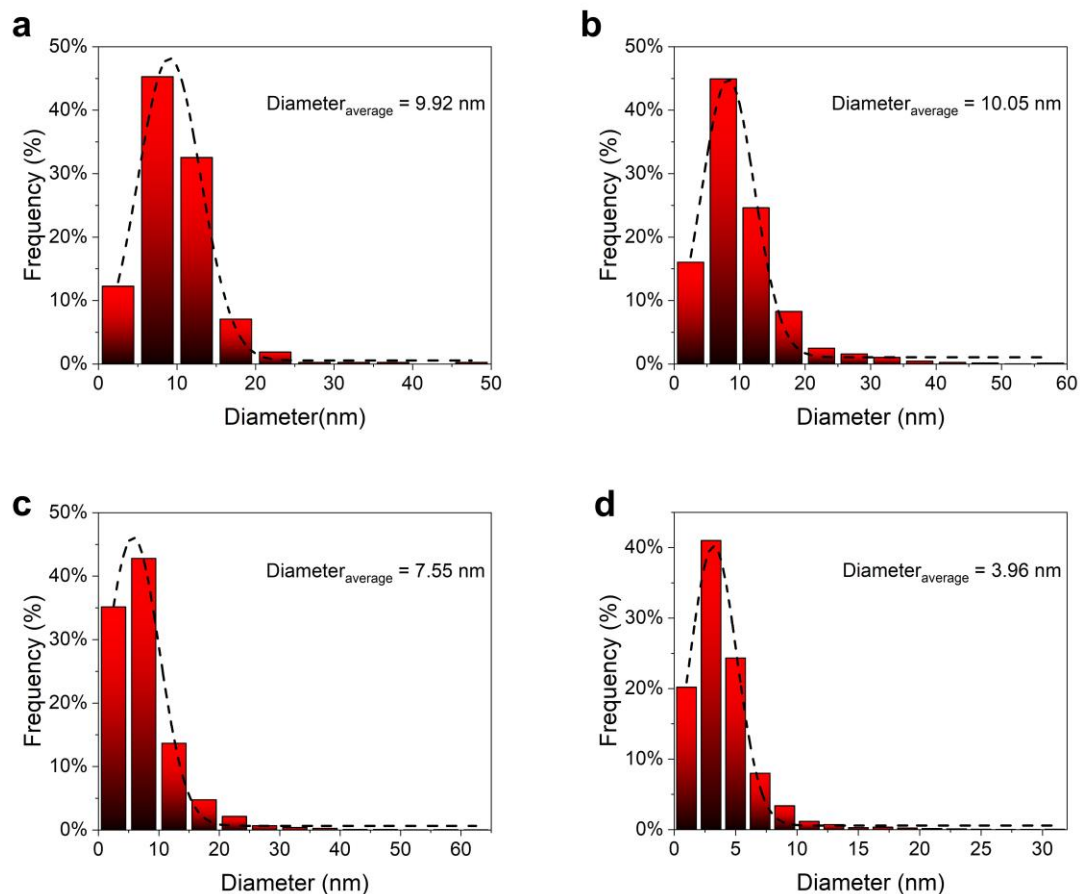
Figure 5.8 Size distributions and its fitting lines for FeCo NPs on MAPLE-fabricated FeCo/rGO hybrid nanosheets with different deposition time. (a) 0.5 hour, (b) 1 hour, (c) 1.5 hours, and (d) 2 hours.
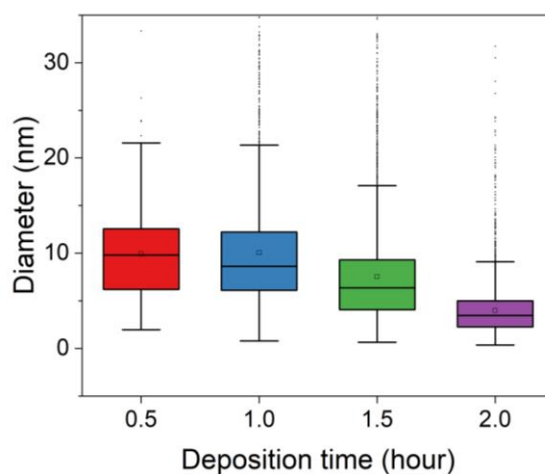
Figure 5.9 Box chart of size distributions of FeCo NPs on rGO with different deposition time.

The TEM-EDX was applied to investigate the chemical composition and element ratio of physically prepared FeCo/rGO hybrid nanosheets. As shown in **Figure 5.10**, the results of the EDX spectrum suggest that the atomic ratio of Fe and Co were 1.79 at.% and 1.92 at.%. The carbon peak is attributed to the integration of rGO. The ratio between iron and cobalt of MAPLE-transferred FeCo NPs is around 1:1, which is close to the ratio of FeCo NPs before being transferred by MAPLE. Thus, the stoichiometric transfer of FeCo NPs is achieved by MAPLE to construct FeCo/rGO hybrid nanosheets *via* the physical route.

Element	Weight ratio (%)	Atomic ratio (%)
Iron	7.13	1.79
Cobalt	8.07	1.92
Carbon	81.32	95.60
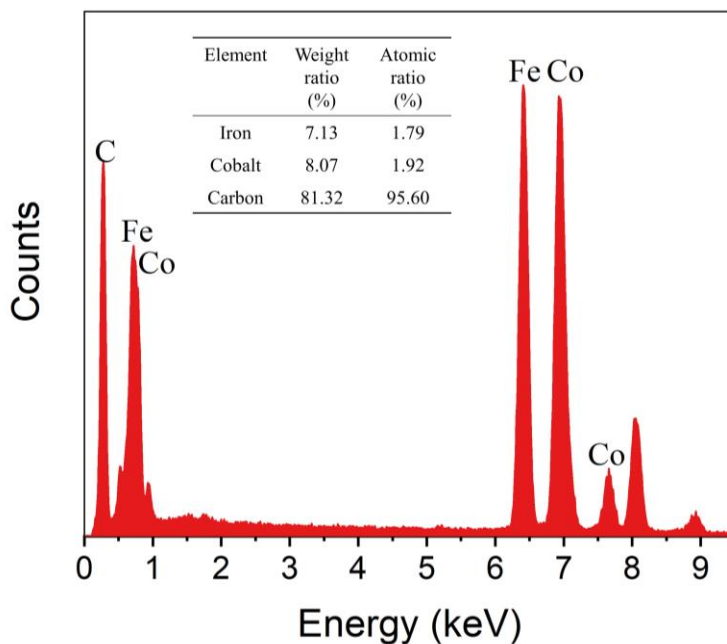
Figure 5.10 TEM-EDX spectrum of physically prepared FeCo/rGO hybrid nanosheets.

The scanning electron microscope (SEM) was applied for further characterizations. As shown in **Figure 5.11**, the FeCo/rGO hybrid nanosheets are observed in the SEM micrographs along with the FeCo NPs with the spherical shape. The quantity of FeCo NPs on physically prepared FeCo/rGO hybrid nanosheets increases significantly as the deposition time raises from 0.5 hours to 2 hours. Meanwhile, more FeCo NPs with smaller sizes appear as the deposition time increases. In addition, the SEM-EDX was applied to study the influence of the deposition time on the ratio of FeCo NPs on the FeCo/rGO hybrid nanosheets prepared by MAPLE. **Figure 5.11e** displays a stepped

increase for the atomic ratio of FeCo NPs as the deposition time varies from 0.5 hours to 2 hours, which is consistent with the observations of TEM and SEM.
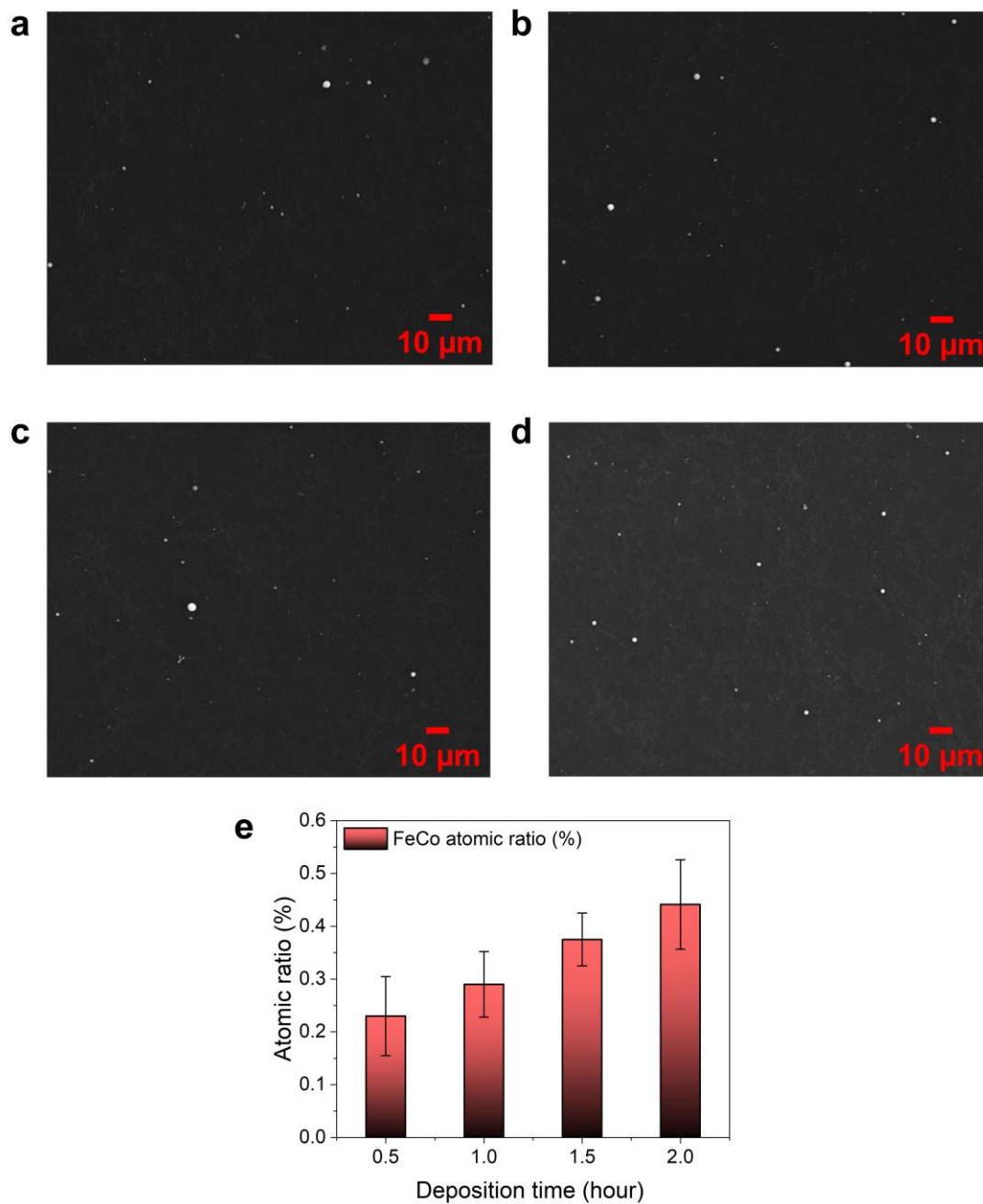
Figure 5.11 SEM micrographs and SEM-EDX of FeCo/rGO hybrid nanosheets produced with physical process: (a) deposition time = 0.5 hour, (b) deposition time = 1 hour, (c) deposition = 1.5 hours, and (d) deposition time =2 hours. (e) SEM-EDX results of FeCo NPs on FeCo/rGO hybrid nanosheets.

5.3.3 Magnetic Properties and Magnetoresistance of MAPLE Developed FeCo/rGO Hybrid Nanosheets

The magnetic hysteresis loop of physically prepared FeCo/rGO hybrid nanosheets was measured by vibrating sample magnetometer (VSM) at room temperature. As shown in **Figure 5.12**, the saturation magnetization (M_S) of FeCo/rGO hybrid nanosheets is 0.4 emu/g (deposition time = 0.5 hour). The coercivity (H_C) of the FeCo/rGO hybrid nanosheets is 28 Oe with the remanence at 0.02 emu/g. The FeCo/rGO hybrid nanosheets prepared by MAPLE exhibit ferromagnetic behaviour. The dramatic decrease of the saturation magnetization relates to the limited FeCo faction of FeCo/rGO hybrid nanosheets prepared by MAPLE and the small particle size of FeCo NPs [39]. Meanwhile, a significant decrease regarding the coercivity of physically prepared FeCo/rGO hybrid nanosheets (28 Oe) compared with the coercivity of chemically synthesized FeCo NPs (130 Oe) is observed. The room temperature coercivity of FeCo NPs on physically prepared FeCo/rGO hybrid nanosheets is at the same level as the coercivity of FeCo NPs in previous work with similar sizes [40]. In addition, the decrease of coercivity indicates that the sizes of some FeCo NPs on FeCo/rGO hybrid nanosheets prepared by MAPLE are close to the critical diameter (d_c), which could fall in the single-domain or pseudo-single domain regions [39, 41].
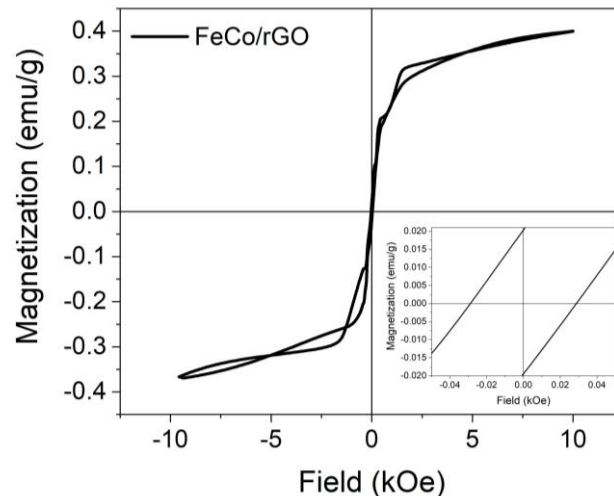
Figure 5.12 The room temperature magnetic hysteresis loop of FeCo/rGO hybrid nanosheets prepared by MAPLE.

To study the magnetoresistance (MR (%), $\Delta R/R_0$) of MAPLE prepared FeCo/rGO hybrid nanosheets, the as-prepared FeCo/rGO hybrid nanosheets were transferred to the 4-pin probe for MR measurement. As shown in **Figure 5.13**, the MR of MAPLE prepared FeCo/rGO hybrid nanosheets (deposition time = 2 hours) reaches $0.67 \pm 0.03\%$ at 10 kOe at room temperature. Although physically prepared FeCo granules embedded in non-magnetic matrix exhibit large MR in previous studies, high magnetic field (> 40 kOe), extreme temperatures (i.e., 50 K), specific substrates, or high FeCo fraction are prerequisites, which is not suitable for the applications in sensing low magnetic fields at room temperature and requiring low FeCo fraction [19, 36, 42]. The FeCo/rGO hybrid nanosheets prepared by MAPLE, with lesser FeCo NPs required (0.4 at.%), achieve MR that is close or larger than MR of FeCo-based nanomaterials produced by other physical processes (e.g., magnetron sputtering) at the low magnetic field and room temperature [19, 36, 42]. Therefore, it is feasible to construct FeCo/rGO hybrid nanosheets with low FeCo fraction and relatively large MR at the low magnetic field and room temperature by the MAPLE technique.
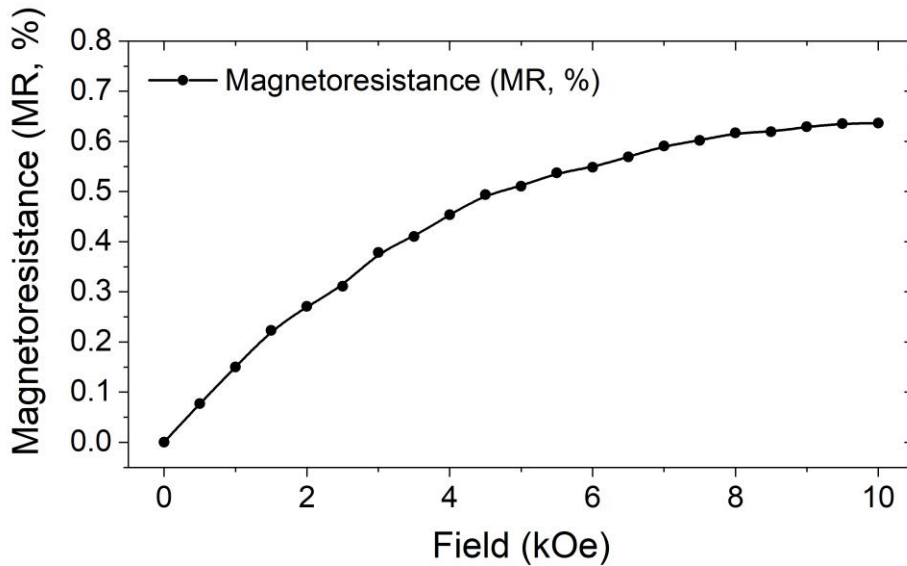
Figure 5.13 Magnetoresistance (MR, %) of the FeCo/rGO hybrid nanosheets prepared by MAPLE at room temperature.

To investigate the origin of the positive MR, the quantum magnetoresistance (QMR) model proposed by A. A. Abrikosov was introduced [21]. The QMR model is appliable

153

in complex materials with 'charge reservoirs' (atom/layer with higher electron density) embedding into the layered materials possessing relatively lower electron density. The FeCo NPs are considered as the charge reservoirs since the electron density of FeCo is higher [21, 43, 44]. Meanwhile, FeCo NPs on physically prepared FeCo/rGO hybrid nanosheets provide the scattering centers that change the trajectory and decrease the mean free path of carriers [45]. Based on the QMR model, the total resistance (in resistivity) of complex material (ρ_{xx}) with an excess density of carriers is expressed by the following equation

$$\rho_{xx} = \frac{HN_i}{\pi e c n_0^2} \cdot \frac{\sinh(^1/_\theta)}{\cosh(^m/_\theta) + \cosh(^m/_\theta)} \qquad (5.3)$$

where N_i is the concentration of scattering centers, H the magnetic field intensity, n_0 the excess electron density, $H_0 = (\pi \cdot n_0 \cdot c \cdot d)/e$ (d is the interlayer distance), $h = H/H_0$, and $m = \mu/t$. In Abrikosov's assumption, $m = sin(\pi/h)$ when $T = 0$. This relation is employed to simplify the equation since the QMR model has been used to study the MR behaviour at different temperatures [20, 21, 46]. Since the theoretical total resistance (in resistivity) of complex materials ρ_{xx} starts from zero, the resistance change (ΔR) is applied in the equation instead of the total resistance (R) of the material. Therefore, a new equation is developed to describe the relationship between the intensity of the external magnetic field (H) and resistance change (ΔR) of the material

$$y = b \cdot a \cdot x \cdot \left\{ \frac{\sinh(\frac{1}{c})}{\cosh\left[\frac{\sin(^\pi/_{ax})}{c}\right] + \cosh\left[\frac{\sin(^\pi/_{ax})}{c}\right]} \right\} \qquad (5.4)$$

where $y = \Delta R$, $x = H$, $a = 1/H_0$, $b = (N_i \cdot d)/(n_0 \cdot e^2)$, and $c = \theta$.

Figure 5.14 indicates that the QMR model exhibits a good fitting agreement with the positive MR of physically prepared FeCo/rGO hybrid nanosheets ($R^2 = 0.96$). The fitting results become less agreed with the experimental data as the magnetic field exceeds 8 kOe, which indicates that the performance of physically prepared FeCo/rGO hybrid

nanosheets is distinct from their chemically synthesized counterparts [26]. Therefore, the QMR model is appliable to explain and understand the origin of the MR of the physically prepared FeCo/rGO hybrid nanosheets as the FeCo NPs transferred by the MAPLE technique serve as scattering centers and rGOs play the role of the nonmagnetic matrix/layered materials.
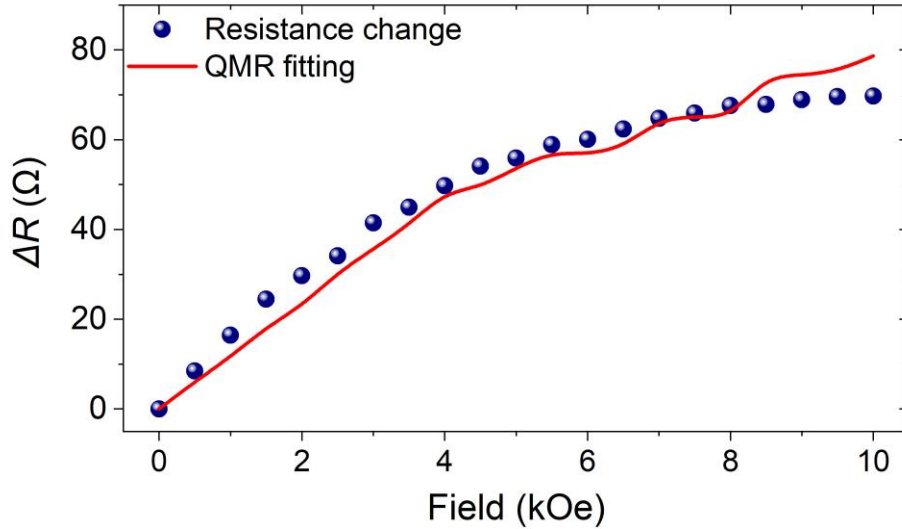
Figure 5.14 Fitting results of QMR model on resistance change (ΔR) of FeCo/rGO hybrid nanosheets prepared by MAPLE.

5.4 Conclusions

Although increasing attention was drawn to producing hybrid materials with the MAPLE process, few studies were carried out to investigate the fabrication of materials with specific magnetic properties such as magnetoresistance (MR). In this study, we successfully developed FeCo/rGO hybrid nanosheets with the MAPLE technique. The stoichiometric transfer of chemically synthesized FeCo NPs was achieved by the MAPLE technique, which was confirmed by EDX results. The presence of spherical shape FeCo NPs on the physically prepared FeCo/rGO hybrid nanosheets was observed. The deposition time (t) was adjusted from 0.5 hours to 2 hours to study the consequence of varying the duration of MAPLE process on the morphology and structure of physically prepared FeCo/rGO hybrid nanosheets. The increase of particle density and the decrease

of average size were discovered in this process, which indicates that particle size and quantity of FeCo NPs on rGO are tunable by adjusting the deposition time (*t*).

Moreover, the physically prepared FeCo/rGO hybrid nanosheets displayed ferromagnetic properties and a large positive MR at room temperature and low magnetic field. With less FeCo fraction and minimum requirements on specific substrates, the MR of FeCo/rGO hybrid nanosheets prepared by MAPLE is up to 0.7% at 10 kOe and room temperature, which is close to or larger than the MR of physically prepared FeCo-based granular systems in previous works under same conditions [19, 36, 42]. In addition, the QMR model is appliable to understand the origin of the positive MR of FeCo/rGO hybrid nanosheets prepared by MAPLE. Therefore, we demonstrated that it is feasible to apply MAPLE as an alternate method to develop FeCo/rGO hybrid nanosheets with special MR *via* physical routes. We believe that this study can benefit the mass production of MR sensors/devices functioning at room temperature and low magnetic fields with demands on lower FeCo fraction and thickness.

5.5   Supplementary Materials
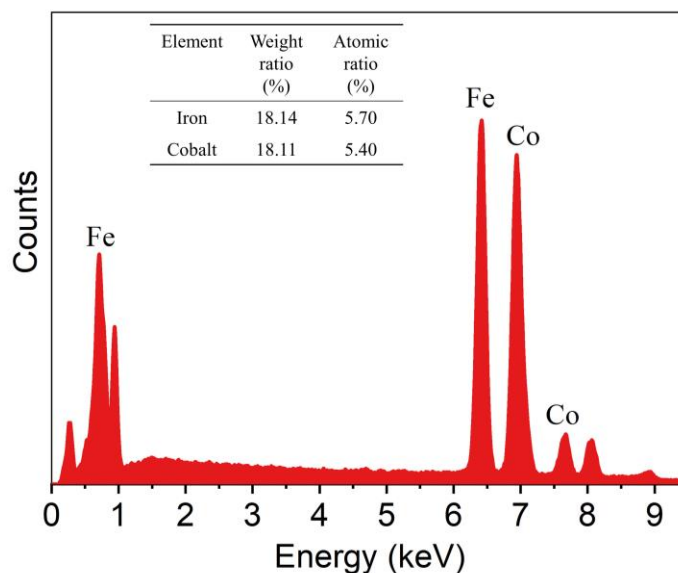
Figure S5.1 TEM-EDX spectrum of FeCo NPs.

5.6 References

[1] M. Takafuji, S. Ide, H. Ihara, Z. Xu, Preparation of Poly(1-vinylimidazole)-Grafted Magnetic Nanoparticles and Their Application for Removal of Metal Ions. *Chem. Mater.* **2004**, *16* (10), 1977-1983.

[2] D.W. Elliott, W.-x. Zhang, Field Assessment of Nanoscale Bimetallic Particles for Groundwater Treatment. *Environ. Sci. Technol.* **2001**, *35* (24), 4922-4926.

[3] J.P. Dailey, J.P. Phillips, C. Li, J.S. Riffle, Synthesis of silicone magnetic fluid for use in eye surgery. *J. Magn. Magn. Mater.* **1999**, *194* (1), 140-148.

[4] A. Jordan, R. Scholz, P. Wust, H. Schirra, S. Thomas, H. Schmidt, *et al.*, Endocytosis of dextran and silan-coated magnetite nanoparticles and the effect of intracellular hyperthermia on human mammary carcinoma cells in vitro. *J. Magn. Magn. Mater.* **1999**, *194* (1), 185-196.

[5] S. Kayal, R.V. Ramanujan, Doxorubicin loaded PVA coated iron oxide nanoparticles for targeted drug delivery. *Mater. Sci. Eng., C* **2010**, *30* (3), 484-490.

[6] S. Laurent, S. Dutz, U.O. Häfeli, M. Mahmoudi, Magnetic fluid hyperthermia: Focus on superparamagnetic iron oxide nanoparticles. *Adv. Colloid Interface Sci.* **2011**, *166* (1), 8-23.

[7] S. Mornet, S. Vasseur, F. Grasset, E. Duguet, Magnetic nanoparticle design for medical diagnosis and therapy. *J. Mater. Chem.* **2004**, *14* (14), 2161-2175.

[8] Y.-X.J. Wang, Superparamagnetic iron oxide based MRI contrast agents: Current status of clinical application. *Quant Imaging Med Surg* **2011**, *1* (1), 35-40.

[9] J. Chomoucka, J. Drbohlavova, D. Huska, V. Adam, R. Kizek, J. Hubalek, Magnetic nanoparticles and targeted drug delivering. *Pharmacol. Res.* **2010**, *62* (2), 144-149.

[10] M.N. Baibich, J.M. Broto, A. Fert, F.N. Van Dau, F. Petroff, P. Etienne, *et al.*, Giant Magnetoresistance of (001)Fe/(001)Cr Magnetic Superlattices. *Phys. Rev. Lett.* **1988**, *61* (21), 2472-2475.

[11] J.S. Moodera, L.R. Kinder, T.M. Wong, R. Meservey, Large Magnetoresistance at Room Temperature in Ferromagnetic Thin Film Tunnel Junctions. *Phys. Rev. Lett.* **1995**, *74* (16), 3273-3276.

[12] S. Parkin, J. Xin, C. Kaiser, A. Panchula, K. Roche, M. Samant, Magnetically engineered spintronic sensors and memory. *Proc. IEEE* **2003**, *91* (5), 661-680.

[13] E. Liu, H. Yuan, Z. Kou, X. Wu, Q. Xu, Y. Zhai, *et al.*, Investigation on Spin Dependent Transport Properties of Core-Shell Structural Fe_3O_4/ZnS Nanocomposites for Spintronic Application. *Sci. Rep.* **2015**, *5* (1), 11164.

[14] I.C. Lekshmi, R. Buonsanti, C. Nobile, R. Rinaldi, P.D. Cozzoli, G. Maruccio, Tunneling Magnetoresistance with Sign Inversion in Junctions Based on Iron Oxide Nanocrystal Superlattices. *ACS Nano* **2011**, *5* (3), 1731-1738.

[15] B. Srinivasan, Y. Li, Y. Jing, Y. Xu, X. Yao, C. Xing*, et al.*, A detection system based on giant magnetoresistive sensors and high‐moment magnetic nanoparticles demonstrates zeptomole sensitivity: potential for personalized medicine. *Angew. Chem.* **2009**, *121* (15), 2802-2805.

[16] R.S. Sundar, S.C. Deevi, Soft magnetic FeCo alloys: alloy development, processing, and properties. *Int. Mater. Rev.* **2005**, *50* (3), 157-192.

[17] S. Maekawa, T. Shinjo, Spin dependent transport in magnetic nanostructures, CRC press, 2002.

[18] H.N. Fuke, S. Hashimoto, M. Takagishi, H. Iwasaki, S. Kawasaki, K. Miyake*, et al.*, Magnetoresistance of FeCo Nanocontacts With Current-Perpendicular-to-Plane Spin-Valve Structure. *IEEE Trans. Magn.* **2007**, *43* (6), 2848-2850.

[19] Y.P. Zeng, Z.W. Liu, H.Y. Yu, Z.G. Zheng, D.C. Zeng, X.S. Gao, Large positive room temperature magnetoresistance in nanogranular FeCo–Si–N thin films. *Mater. Lett.* **2013**, *110*, 27-30.

[20] A.A. Abrikosov, Quantum linear magnetoresistance. *EPL* **2000**, *49* (6), 789-793.

[21] A.A. Abrikosov, Quantum magnetoresistance of layered semimetals. *Phys. Rev. B* **1999**, *60* (6), 4231-4234.

[22] A.H. Castro Neto, F. Guinea, N.M.R. Peres, K.S. Novoselov, A.K. Geim, The electronic properties of graphene. *Rev. Mod. Phys.* **2009**, *81* (1), 109-162.

[23] K.S. Novoselov, A.K. Geim, S.V. Morozov, D. Jiang, M.I. Katsnelson, I.V. Grigorieva*, et al.*, Two-dimensional gas of massless Dirac fermions in graphene. *Nature* **2005**, *438* (7065), 197-200.

[24] Y. Liu, I. Yudhistira, M. Yang, E. Laksono, Y.Z. Luo, J. Chen*, et al.*, Phonon-Mediated Colossal Magnetoresistance in Graphene/Black Phosphorus Heterostructures. *Nano Lett.* **2018**, *18* (6), 3377-3383.

[25] J.-J. Chen, J. Meng, Y.-B. Zhou, H.-C. Wu, Y.-Q. Bie, Z.-M. Liao*, et al.*, Layer-by-layer assembly of vertically conducting graphene devices. *Nat. Commun.* **2013**, *4* (1), 1921.

[26] S. Yang, M. Tan, T. Yu, X. Li, X. Wang, J. Zhang, Hybrid Reduced Graphene Oxide with Special Magnetoresistance for Wireless Magnetic Field Sensor. *Nano-Micro Lett.* **2020**, *12* (1), 69.

[27] A. Caricato, S. Capone, M. Epifani, M. Lomascolo, A. Luches, M. Martino, *et al.*, Nanoparticle thin films deposited by MAPLE for sensor applications, SPIE, 2008.

[28] A.L. Mercado, C.E. Allmond, J.G. Hoekstra, J.M. Fitz-Gerald, Pulsed laser deposition vs. matrix assisted pulsed laser evaporation for growth of biodegradable polymer thin films. *Appl. Phys. A* **2005**, *81* (3), 591-599.

[29] D.M. Bubb, P.K. Wu, J.S. Horwitz, J.H. Callahan, M. Galicia, A. Vertes, *et al.*, The effect of the matrix on film properties in matrix-assisted pulsed laser evaporation. *J. Appl. Phys.* **2002**, *91* (4), 2055-2058.

[30] R. Cristescu, C. Popescu, G. Socol, I. Iordache, I.N. Mihailescu, D.E. Mihaiescu, *et al.*, Magnetic core/shell nanoparticle thin films deposited by MAPLE: Investigation by chemical, morphological and in vitro biological assays. *Appl. Surf. Sci.* **2012**, *258* (23), 9250-9255.

[31] S. Yang, W.H. Tse, J. Zhang, Deposition of Antibody Modified Upconversion Nanoparticles on Glass by a Laser-Assisted Method to Improve the Performance of Cell Culture. *Nanoscale Res. Lett.* **2019**, *14* (1), 101.

[32] C. Popescu, J. Roqueta, A. Pérez del Pino, M. Moussaoui, M.V. Nogués, E. György, Processing and immobilization of enzyme Ribonuclease A through laser irradiation. *J. Mater. Res.* **2011**, *26* (6), 815-821.

[33] C.S. Ciobanu, S.L. Iconaru, E. Gyorgy, M. Radu, M. Costache, A. Dinischiotu, *et al.*, Biomedical properties and preparation of iron oxide-dextran nanostructures by MAPLE technique. *Chem. Cent. J.* **2012**, *6* (1), 17.

[34] I. Negut, V. Grumezescu, A. Ficai, A.M. Grumezescu, A.M. Holban, R.C. Popescu, *et al.*, MAPLE deposition of *Nigella sativa* functionalized Fe_3O_4 nanoparticles for antimicrobial coatings. *Appl. Surf. Sci.* **2018**, *455*, 513-521.

[35] V. Grumezescu, E. Andronescu, A.M. Holban, L. Mogoantă, G.D. Mogoşanu, A.M. Grumezescu, *et al.*, MAPLE fabrication of thin films based on kanamycin functionalized magnetite nanoparticles with anti-pathogenic properties. *Appl. Surf. Sci.* **2015**, *336*, 188-195.

[36] C. Wang, X. Xiao, Y. Rong, H.Y. Hsu, Nanoparticle morphology in $FeCo$–SiO_2 granular films with tunneling giant magnetoresistance. *Mater. Sci. Eng., B* **2007**, *141* (3), 126-131.

[37] B. Haghighi, M.A. Tabrizi, Green-synthesis of reduced graphene oxide nanosheets using rose water and a survey on their characteristics and applications. *RSC Adv.* **2013**, *3* (32), 13365-13371.

[38] A.P. Caricato, V. Arima, M. Catalano, M. Cesaria, P.D. Cozzoli, M. Martino, *et al.*, MAPLE deposition of nanomaterials. *Appl. Surf. Sci.* **2014**, *302*, 92-98.

[39] S. Chakraverty, M. Bandyopadhyay, Coercivity of magnetic nanoparticles: a stochastic model. *J. Phys.: Condens. Matter* **2007**, *19* (21), 216201.

[40] J. Liu, K. Wu, J.-P. Wang, Magnetic properties of cubic FeCo nanoparticles with anisotropic long chain structure. *AIP Adv.* **2016**, *6* (5), 056126.

[41] L. Tauxe, H.N. Bertram, C. Seberino, Physical interpretation of hysteresis loops: Micromagnetic modeling of fine particle magnetite. *Geochem. Geophys. Geosyst.* **2002**, *3* (10), 1-22.

[42] Y.P. Zeng, Z.W. Liu, E. Mikmeková, Magnetoresistance effects associated with various electric conduction mechanisms in nanostructured $[C/FeCo]_n$ multilayers. *J. Magn. Magn. Mater.* **2017**, *421*, 39-43.

[43] K. Schwarz, P. Mohn, P. Blaha, J. Kubler, Electronic and magnetic structure of BCC Fe-Co alloys from band theory. *J. Phys. F: Met. Phys.* **1984**, *14* (11), 2659-2671.

[44] T. Fang, A. Konar, H. Xing, D. Jena, Carrier statistics and quantum capacitance of graphene sheets and ribbons. *Appl. Phys. Lett.* **2007**, *91* (9), 092109.

[45] M.I. Katsnelson, F. Guinea, A.K. Geim, Scattering of electrons in graphene by clusters of impurities. *Phys. Rev. B* **2009**, *79* (19), 195426.

[46] A.L. Friedman, J.L. Tedesco, P.M. Campbell, J.C. Culbertson, E. Aifer, F.K. Perkins*, et al.*, Quantum Linear Magnetoresistance in Multilayer Epitaxial Graphene. *Nano Lett.* **2010**, *10* (10), 3962-3965.

Chapter 6

6   Developing FeCo/rGO Hybrid Nanosheets Reinforced p(HEMA-co-AEMA) Nanocomposite Hydrogel with Enhanced Mechanical Properties and Magnetoresistances

In this chapter, we developed a new nanocomposite hydrogel by introducing FeCo/rGO hybrid nanosheets to the copolymer of 2-hydroxyethyl methacrylate and 2-aminoethyl methacrylate (p(HEMA-co-AEMA)). Poly (2-Hydroxyethyl methacrylate) (pHEMA) has been broadly applied in the biomedical field including drug delivery, surgical prostheses, wound dressing, and contact lens [1-4]. The advantages of pHEMA hydrogel include biocompatibility, transparency, and high water content [5, 6]. However, the poor mechanical property of pHEMA hydrogel is a drawback that strongly hinders the applications with load-bearing requirements [7]. Although many attempts were made to strengthen the mechanical properties, these modifications may bring disadvantages in some crucial aspects such as biocompatibility and productivity [8, 9].

In this study, with the direct integration of FeCo/rGO hybrid nanosheets and the photopolymerization process of p(HEMA-co-AEMA), a simple and facile preparation process was achieved. The nanocomposite hydrogel (G-p(HEMA-co-AEMA)) fabricated with this process offers outstanding mechanical properties without deterioration of swelling properties. For the mechanical properties, the toughness of the nanocomposite hydrogel is up to 0.11 MPa, which is around 2.0x higher than plain p(HEMA-co-AEMA). The Young's modulus of the nanocomposite hydrogel is up to 0.48 MPa, which is 1.5x higher than p(HEMA-co-AEMA). In addition, the maximal tensile stress of the nanocomposite hydrogel reaches 0.22 MPa, which is 1.7x higher than p(HEMA-co-AEMA). Meanwhile, the integration of FeCo/rGO hybrid nanosheets introduces magnetoresistance (MR) to the nanocomposite hydrogel. The combination of FeCo/rGO

hybrid nanosheets with p(HEMA-co-AEMA) offers a new nanocomposite hydrogel (G-p(HEMA-co-AEMA)) with a facile fabrication process for potential applications in tissue engineering and flexible electronics.

6.1 Introduction

Hydrogels are described as polymer chains with the three-dimensional structure of special cross-linked networks, which leads to the ability to maintain high water content due to the interstitial spaces in hydrogel [10]. In 1949, the first commercialized hydrogel product based on poly(vinyl alcohol) was launched with the trading name Ivalon, which was used for biomedical implant applications [11]. The preparation of the poly(2-hydroxyethyl methacrylate, pHEMA) in 1960 is a great leap for the commercialization of hydrogel, the production of contact lenses, and the development of the hydrogel market [11, 12]. Nowadays, hydrogels have been applied in various applications of biomedical fields such as drug delivery, wound dressing, tissue engineering, hydrogel fillers, and contact lens [5, 13-15].

For the past six decades, pHEMA is viewed as a very promising hydrogel in various applications of the biomedical field. pHEMA that consists of the 2-hydroxyethyl methacrylate (HEMA) monomer is characterized as the hydrogel with a less fouling problem since it exhibits limited adsorption of proteins, platelets, and cells [16]. With superb biocompatibility, the Food and Drug Administration (FDA) has approved pHEMA in the commercial productions and applications of contact lenses and keratoprosthesis [16, 17]. The pHEMA hydrogel is applied in various biomedical applications including contact lens fabrication and tissue engineering due to the biocompatibility and flexibility.

The pHEMA has been applied in the production of contact lens due to its good transparency, robust stability, and cost-effective feature. Meanwhile, the high water content feature of pHEMA is not significantly influenced by the temperature and pH value of the external environment [18]. To achieve satisfactory stability and meet the demands of contact lens applications, except 2-hydroxyethyl methacrylate (HEMA),

crosslinkers such as ethylene glycol dimethylacrylate (EGDMA) were added to the formation of 3-D networks of overlapping polymer chains (**Scheme 6.1**). The crosslinkers prevent the pHEMA hydrophilic contact lens from dissolving in the environmental liquid matrix such as tears [19].
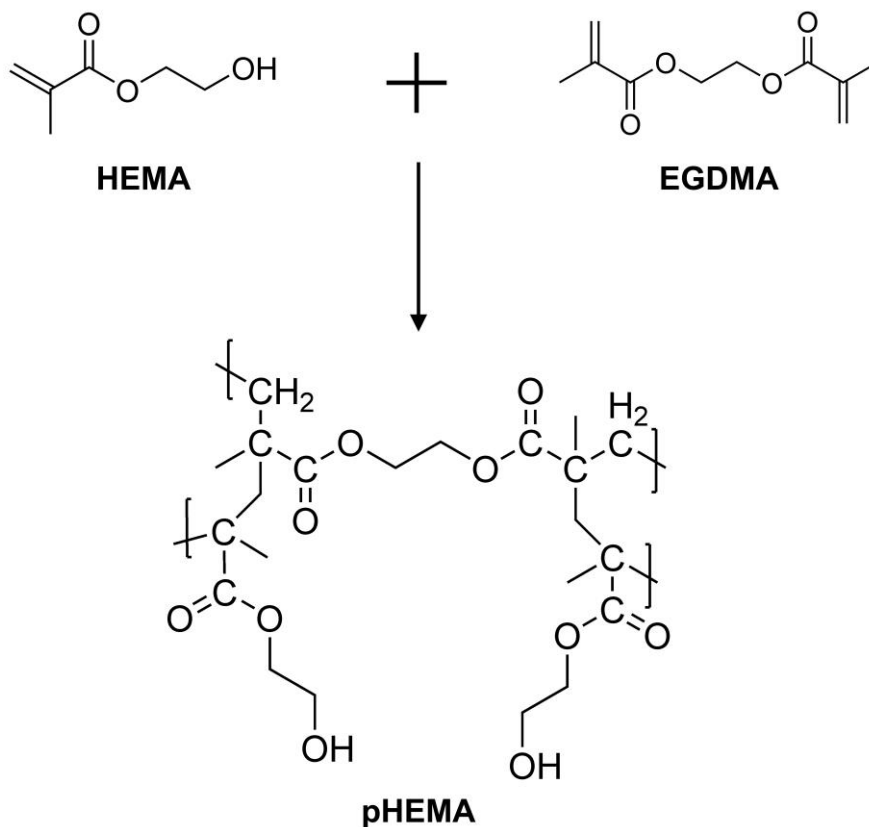
Scheme 6.1 Chemical schematic illustration of the fabrication of pHEMA contact lens.

One major shortcoming of the pHEMA-based contact lens is the limited oxygen permeability, and this can trigger the reduced mitosis and epithelial microcysts as the consequence of hypoxic treatment [20]. Numerous efforts were made to enhance the oxygen permeability of the pHEMA hydrogel. One of the methods is introducing strong hydrophilic monomers with better water absorption properties to increase the water content, which leads to enhanced oxygen transport in the pHEMA. N-vinylpyrolidinone (NVP) and methacrylic acid (MAA) were applied in the fabrication of the pHEMA-based contact lens, which significantly increases the oxygen transport in the pHEMA hydrogel

[21]. Although pHEMA experiences fewer fouling problems in contrast with other materials, some modifications are needed since the requirements of contact lens are strict due to the external environment in its application process (i.e., tears). The complex tear film ingredients can prompt lipid/protein fouling, which leads to inflammatory problems and unsatisfactory wearing experiences.

Meanwhile, pHEMA was broadly applied in the field of tissue engineering. The high swelling capacity of the hydrogel in water offers similar features to soft tissues in the human body. The superb biocompatibility of pHEMA leads to the fast mass transfer in cells/surroundings and little immunogenicity, which is important to the applications of tissue engineering. As the biomimetic matrix is crucial in tissue engineering together with cell and biology growth factors in the restoration of the tissue functions, hydrogels are considered as an appropriate candidate to serve as tissue engineering scaffold due to the comparable constructions and functions between the hydrogel and extracellular matrix (ECM). The prerequisites for hydrogels to be applied in tissue engineering include biocompatibility, permeability (gas, nutrients, and metabolite), the capacity to maintain proper mechanical support for a long time [22, 23]. In addition to these requirements, the pHEMA hydrogel has been developed for the applications of tissue engineering since pHEMA is nonbiodegradable, facile to fabricate, and hydrophilic [6, 24].

However, hydrogels including pHEMA suffer from poor mechanical properties especially in applications that demand solid support for prolonged times such as polymer scaffolds [7, 25]. The methods such as increasing the loading of crosslinkers in the hydrogel and introducing interpenetrating networks (double-networks) were adopted to enhance the mechanical properties of hydrogel [26-28]. Although these methods increase the mechanical properties, some of the crucial qualities of hydrogel would deteriorate such as swelling capacity, biocompatibility, and non-fouling property. Meanwhile, most of these processes lead to the increase of the complexity of fabrication [8, 29].

Nanocomposite hydrogel is one of the potential solutions for current obstacles. The nanocomposite hydrogel systems combined with nanoparticles possess unique physical and chemical properties such as multifunctionality. To enhance the mechanical properties

and add other functions to the hydrogel system, nanocomposite hydrogel is developed by combining the nanoparticles with the conventional hydrogel matrix. The key properties such as porosity, stiffness, and swelling ability have been reinforced in this process [30-32]. Various nanomaterials were incorporated with polymeric networks to develop nanocomposite hydrogel systems including metal-based nanoparticles, inorganic/ceramic nanoparticles, polymeric nanoparticles, and carbon nanomaterials [33, 34]. Currently, nanocomposite hydrogels were broadly applied in biomedical fields such as drug delivery, biosensor, regenerative medicine, bioactuator, and tissue engineering [35, 36].

Among the nanomaterials with the potential to combine with hydrogels, carbon-based materials such as graphene, graphene oxide, and carbon nanotube have drawn increasing attention in recent years due to their special physical and chemical properties. In the past decades, graphene-based materials have been employed in the fabrication of various polymers to enhance different features [37]. Graphene-enhanced polyacrylamide, cellulose, alginate, polyvinyl alcohol, and graphene-based hydrogel were developed for improving electrical conductivity, thermal resistance, absorption capacity, and elasticity [38-40]. In contrast with layered graphene grown with the physical or chemical methods (such as chemical vapor deposition (CVD)), the chemically synthesized reduced graphene oxide (rGO) is the appropriate candidate for the nanofillers of the hydrogels since the facile fabrication process allows the mass production of rGO. Meanwhile, the large specific surface area and functional groups of rGO provide the suitable substrate and nucleation sites for modifications [41, 42].

In this study, we successfully developed a new nanocomposite hydrogel based on the reinforced copolymer of 2-hydroxyethyl methacrylate and 2-aminoethyl methacrylate (p(HEMA-co-AEMA)) with FeCo/rGO hybrid nanosheets. The nanocomposite hydrogel was obtained by facile direct incorporation of FeCo/rGO hybrid nanosheets with the p(HEMA-co-AEMA). Significant enhancements were observed in terms of the mechanical properties of the newly developed nanocomposite hydrogel. The toughness of the nanocomposite hydrogel is up to 0.11 MPa, which is around 2.0x higher than plain p(HEMA-co-AEMA). The Young's modulus of the nanocomposite hydrogel is up to 0.48 MPa, which is 1.5x higher than p(HEMA-co-AEMA). The maximal tensile stress of the

nanocomposite hydrogel reaches 0.22 MPa, which is 1.7x higher than p(HEMA-co-AEMA). Meanwhile, the nanocomposite hydrogel displayed comparable swelling capacity in contrast with p(HEMA-co-AEMA) hydrogel. Moreover, the negative magnetoresistance (MR) was observed on the nanocomposite hydrogel with a level of - $1.4 \pm 0.3\%$ at the low magnetic field (10 kOe) and room temperature. With the improved mechanical properties and MR responses, the FeCo/rGO hybrid nanosheets enhanced p(HEMA-co-AEMA) can benefit the biomedical applications with load-bearing requirements such as scaffolds in tissue engineering and contribute to the applications on developing flexible electronics and sensors.

6.2 Experimental

6.2.1   Materials

$Co(OAc)_2 \cdot 4H_2O$ (cobaltous acetate tetrahydrate, ACS reagent, $\geq 98.0\%$), $FeCl_2 \cdot 4H_2O$ (ferrous chloride tetrahydrate, puriss. p.a., $\geq 99.0\%$), NaOH (sodium hydroxide, ACS reagent, $\geqslant 97.0\%$, pellets), $KMnO_4$ (potassium permanganate, $\geq 99.0\%$, ACS), N_2H_4 (hydrazine hydrate, reagent grade, 50-60%), HEMA(2-hydroxyethyl methacrylate, 97%), AEMA (2-aminoethyl methacrylate hydrochloride, 90%), DMPA (2,2-dimethoxy-2-phenylacetophenone, 99%), EGDMA (Ethylene glycol dimethacrylate, 98%), and dimethyl sulfoxide (DMSO, $\geq 99.9\%$) were purchased from Sigma-Aldrich. Ethylene glycol (EG) was purchased from Fisher Chemical. Sulfuric acid (98%) and hydrochloric acid (37%) were purchased from Caledon Laboratory Chemicals. Graphite flake, natural, -325 mesh, 99.8% (metals basis) was purchased from Alfa Aesar.

6.2.2   Preparation of Reduced Graphene Oxide (rGO)

The reduced graphene oxide (rGO) was obtained by the reduction of the graphene oxide (GO) that was fabricated with the modified Hummers method, which has been discussed in Chapter 3 [41].

6.2.3   Synthesis of FeCo/rGO Hybrid Nanosheets

The synthesis of FeCo/rGO hybrid nanosheets was based on the modified process of our previous study, which has been discussed in Chapter 3 [41].

6.2.4   Preparation of FeCo/rGO Hybrid Nanosheets Reinforced p(HEMA-co-AEMA) (G-p(HEMA-co-AEMA))

The FeCo/rGO hybrid nanosheets reinforced p(HEMA-co-AEMA) was prepared with the modified process of the previous work of our group [5]. As shown in **Scheme 6.2**, the copolymer p(HEMA-co-AEMA) was produced with the photo-initiated polymerization and crosslinking reaction. The reaction was triggered by deep UV radiation. DMPA, as the photoinitiator, generated free radicals under UV radiation and initiated the chain reaction of AEMA, HEMA, and EGDMA.
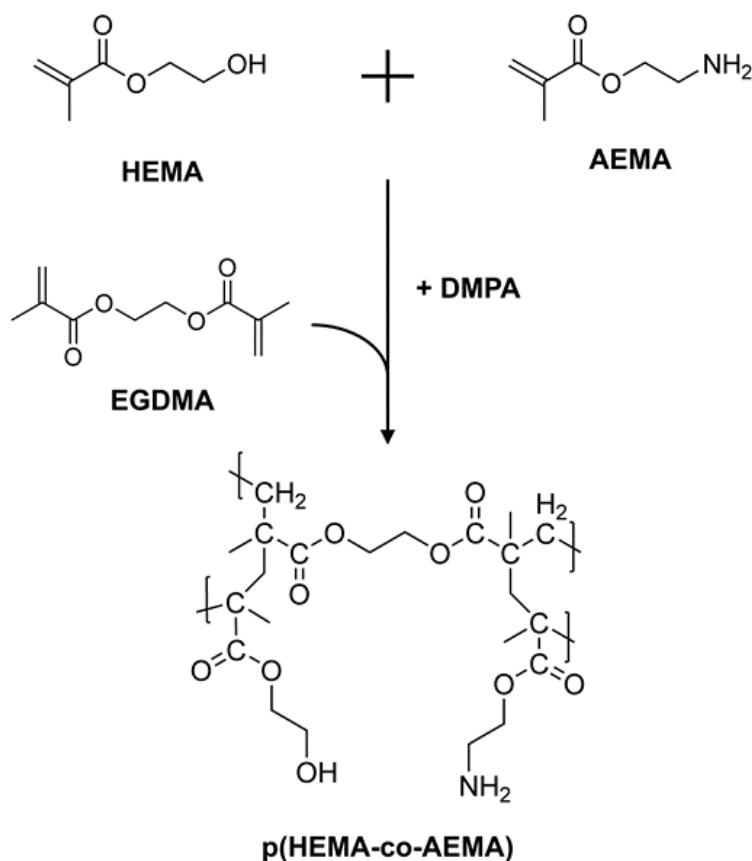
Scheme 6.2 Chemical schematic illustration of the synthesis of p(HEMA-co-AEMA).

In specific, 100 µL of the AEMA solution in the DMSO (300 mg/mL) was mixed with 3 mL HEMA. Subsequently, 100 µL of the DMPA solution in the DMSO was added to the mixture. The mixture was further mixed with 1 mL of DMSO and 6 µL EGDMA (crosslinker). Finally, 0.2% (w/v) of FeCo/rGO hybrid nanosheets was added to the mixture (the ratio was set to achieve appropriate dispersion of FeCo/rGO hybrid nanosheets without interrupting the polymerization of p(HEMA-co-AEMA)). The mixture was purged with nitrogen for 5 minutes. Subsequently, the mixture was injected into the mould and exposed to UV radiation for 15 minutes. The obtained nanocomposite hydrogel (G-p(HEMA-co-AEMA)) was stored in Milli-Q water at 4 °C overnight to remove the chemical residues. The p(HEMA-co-AEMA) hydrogel was fabricated following the same procedure without adding FeCo/rGO hybrid nanosheets.

6.2.5　Materials Characterization

Philips CM-10 transmission electron microscope (TEM) was applied to obtain the TEM micrograph and selected area electron diffraction (SAED) pattern. The mechanical test was performed by Bio-Tester 5000 test system (CellScale Biomaterials Testing, Waterloo, Ontario). The Fourier-transform infrared spectroscopy (FT-IR) spectra were obtained by Thermo Scientific Nicolet 6700 FT-IR spectrometer. The magnetic hysteresis loop was characterized by the vibrating sample magnetometer (VSM, LakeShore 7407, moment measure range: 10^{-7} to 10^{3} emu; field accuracy: "$\pm$ 0.05%" full scale). The magnetoresistance (MR) was measured by the Model 74046 probe attached to the VSM.

6.2.6　Swelling Behaviors of Hydrogels

Gravimetric analysis was applied to characterize the swelling behaviors of p(HEMA-co-AEMA) hydrogel and G-p(HEMA-co-AEMA) nanocomposite hydrogel. The hydrogel discs were freeze-dried to dehydrate. Then the pre-weighed hydrogels were immersed in Milli-Q water for 22 hours in total. The hydrogel pellets were taken out and wiped with filter paper to remove the absorbed water before weighing. The hydrogels were weighed at different time points at ambient temperature. The swelling ratio was calculated with the following equation

$$Swelling\ ratio = \frac{W_s - W_d}{W_d} \times 100\% \qquad (6.1)$$

where W_d is the weight of the dry hydrogel and W_s the weight of the swollen hydrogel. Each sample was prepared with three repetitions. The time points of measurements included 2, 8, and 10 minutes as the hydrogel was immersed in water for less than 0.5 hours. As the time of hydrogels immersed in water surpassed 0.5 hours, the time points to weigh hydrogels were 0.5, 1, 3, 6, 15, 20, and 22 hours.

6.2.7   Mechanical Test

The mechanical tests of both G-p(HEMA-co-AEMA) and p(HEMA-co-AEMA) were performed with the BioTester 5000 testing system (CellScale Biomaterials Testing, Waterloo, Ontario). The tensile properties were determined at room temperature with a stretching speed of 15 mm/min. The 1×1 cm specimens of both p(HEMA-co-AEMA) hydrogels and G-p(HEMA-co-AEMA) nanocomposite hydrogels were prepared for the mechanical test. The specimens were tested uniaxially and biaxially. The Young's modulus (E) was calculated with the following equation

$$E = \frac{stress}{strain} = \frac{\sigma}{\varepsilon} = \frac{F}{A} \bigg/ \frac{\delta L}{L_0} \qquad (6.2)$$

where F is the applied force (N), A the cross-sectional area of the specimen (m^2), δL the displacement of testing material (m), L_0 the original length of testing material (m), and E the Young's modulus (Pa).

For the biaxial mechanical test, the specimens were stretched evenly in two directions. The deformation for the specimens was tracked by the pictures captured by a 1280×960 pixel CCD (charge-coupled device) camera. The internal strains were recorded with the image-tracking software provided by the CellScale Biomaterals Testing. The tracking data was used to generate maps of the biaxial strain field.

6.2.8　Magnetoresistance Characterization

The vibrating sample magnetometer (VSM, LakeShore 7407) with Model 74046 magnetoresistance (MR) probe was applied to measure the MR of the nanocomposite hydrogel. The MR of the testing sample was calculated by the following equation.

$$MR(\%) = \frac{R - R_0}{R_0} \times 100\% \qquad (6.3)$$

The resistance change (ΔR, Ω) was calculated by the following equation

$$\Delta R = R - R_0 \qquad (6.4)$$

where R is the total resistance (Ω) of the sample under the presence of an external magnetic field and R_0 the sample resistance (Ω) at zero magnetic field.

6.3　Results and Discussion

6.3.1　Developing FeCo/rGO Hybrid Nanosheets Reinforced p(HEMA-co-AEMA) Nanocomposite Hydrogel

The FeCo/rGO hybrid nanosheets reinforced nanocomposite hydrogel (G-p(HEMA-co-AEMA)) was developed by direct incorporation of FeCo/rGO hybrid nanosheets and p(HEMA-co-AEMA) hydrogel (**Figure 6.1**). The FeCo/rGO hybrid nanosheets were prepared based on the previous work of our group [41].

As shown in **Figure 6.2**, the cubic FeCo nanoparticles (NPs) on the rGO surface are observed in the transmission electron microscope (TEM) micrographs of the FeCo/rGO hybrid nanosheets. The average size of the FeCo NPs is 89 ± 20 nm as the mass ratio of rGO added into the reaction (M_{rGO}) reaches 50 wt.%. Meanwhile, the structure and morphology of rGO are revealed by the TEM micrograph. The folds and wrinkles of rGO are noticed, which suggests the successful preparation of rGO with the chemical process. Three diffraction rings that correspond to the (110), (200), and (211) crystal planes are

displayed in the selected area electron diffraction (SAED) pattern of FeCo/rGO hybrid nanosheets (**Figure 6.2a**) [43]. Meanwhile, the magnetic hysteresis loop suggests that the saturation magnetization (M_s) of FeCo/rGO hybrid nanosheets is 12 emu/g, which decreases significantly in contrast with FeCo NPs (~ 200 emu/g). The coercivity (H_C) of FeCo/rGO hybrid nanosheets is 138 Oe, which is at the same level as the coercivity of FeCo NPs (~ 130 Oe). The decrease of saturation magnetization (M_s) is triggered by the introduced rGO as the M_{rGO} reaches 50 wt.%.
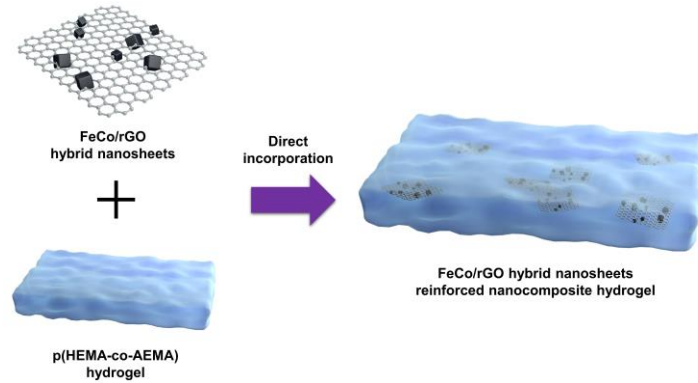
Figure 6.1 Schematic illustration of the preparation of G-p(HEMA-co-AEMA).
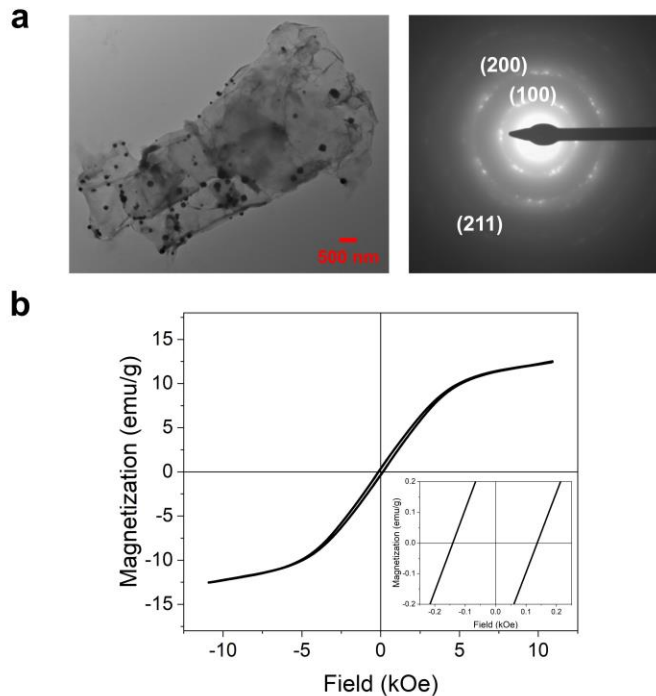
Figure 6.2 (a) The TEM micrograph and SAED pattern of FeCo/rGO hybrid nanosheets. (b) The magnetic hysteresis loop of the FeCo/rGO hybrid nanosheets.

The picture of p(HEMA-co-AEMA) and FeCo/rGO hybrid nanosheets reinforced G-p(HEMA-co-AEMA) is shown in **Figure 6.3**. In contrast with the plain p(HEMA-co-AEMA), the G-p(HEMA-co-AEMA) exhibits dark color and less transparency due to the combination of rGO. The uniform dispersion of FeCo/rGO hybrid nanosheets in the p(HEMA-co-AEMA) matrix is observed.
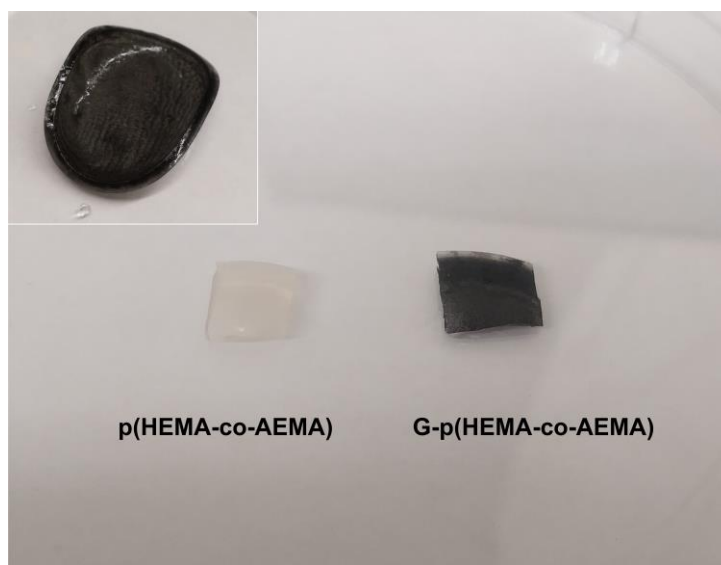
Figure 6.3 The picture of p(HEMA-co-AEMA) and G-p(HEMA-co-AEMA) (Small inset: the as-prepared G-p(HEMA-co-AEMA)).

The Fourier-transform infrared spectroscopy (FT-IR) spectra of FeCo/rGO hybrid nanosheets, p(HEMA-co-AEMA) hydrogel, and FeCo/rGO hybrid nanosheets reinforced G-p(HEMA-co-AEMA) nanocomposite hydrogel are shown in **Figure 6.4**. For the spectrum of FeCo/rGO hybrid nanosheets, the stretching peak of C=C in graphitic rings of rGO appears at 1592 cm^{-1}, and the stretching of the C-O epoxide group is observed at 1211 cm^{-1} [44, 45]. The C-H stretching of rGO appears at 2915 cm^{-1}. The p(HEMA-co-AEMA) and G-p(HEMA-co-AEMA) exhibit similar FT-IR spectra. The broad peaks at 3386 cm^{-1} are ascribed to the -OH vibration and -NH stretching. Similar to the FeCo/rGO hybrid nanosheets' spectrum, the C-H stretching peaks are observed at 2940 cm^{-1}. The strong C=O stretching peaks appear at 1711 cm^{-1}. The peaks at 1637 cm^{-1} correspond to the -NH stretching of the hydrogel matrix [5]. Moreover, the peaks of -C-O-H and -C-O-C- are observed at 1455 cm^{-1} and 1154 cm^{-1} [46]. The differences between the FT-IR

spectra of p(HEMA-co-AEMA) hydrogel and G-p(HEMA-co-AEMA) nanocomposite hydrogel are not significant due to the limited quantity of FeCo/rGO hybrid nanosheets [47].
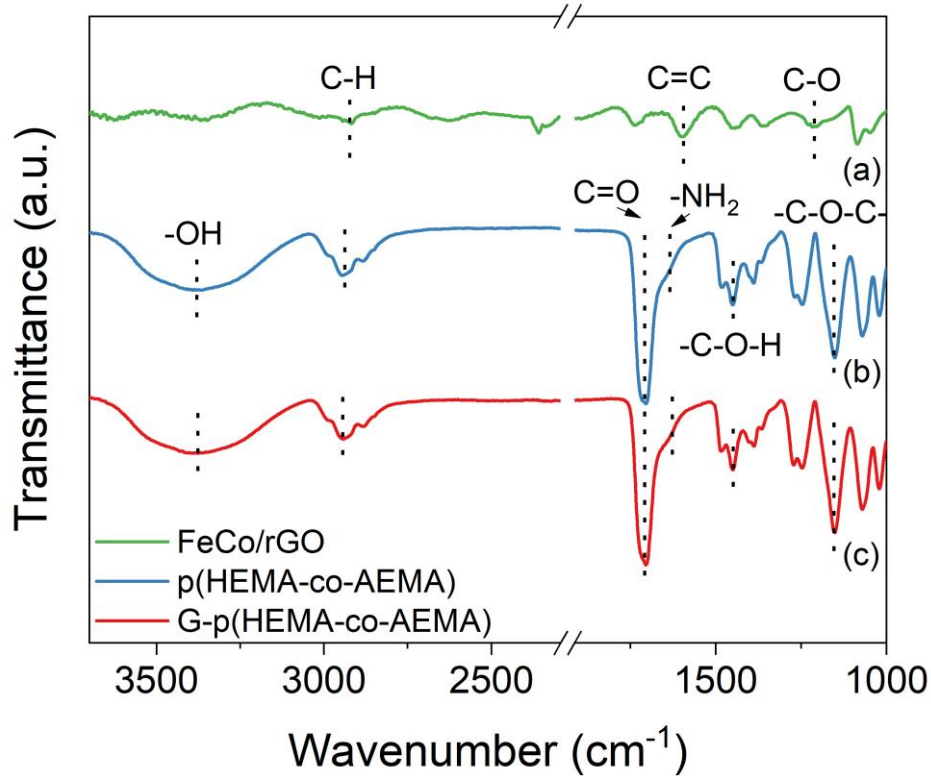
Figure 6.4 FT-IR spectra of (a) FeCo/rGO hybrid nanosheets, (b) p(HEMA-co-AEMA), and (c) G-p(HEMA-co-AEMA).

The swelling behavior of p(HEMA-co-AEMA) hydrogel and G-p(HEMA-co-AEMA) nanocomposite hydrogel are shown in **Figure 6.5**. The characterization of swelling behavior was performed with Milli-Q water at ambient temperature. p(HEMA-co-AEMA) hydrogel and G-p(HEMA-co-AEMA) nanocomposite hydrogel exhibit comparable ratios (64.2 ± 1.9% vs. 62.5 ± 0.9%) of absorbed water after 22 hours, which is close to previous studies [5, 47, 48]. Meanwhile, **Figure 6.5** shows that the swelling ratios of both p(HEMA-co-AEMA) hydrogel and G-p(HEMA-co-AEMA) nanocomposite hydrogel reach the plateau after 6 hours. In addition, no significant decrease is observed in the swelling rate of G-p(HEMA-co-AEMA) nanocomposite hydrogel in contrast with

p(HEMA-co-AEMA) hydrogel. The results indicate that the negative effects introduced by the incorporation of FeCo/rGO hybrid nanosheets with p(HEMA-co-AEMA) hydrogel matrix on swelling capacity are ignorable. Therefore, the high water absorption capacity of p(HEMA-co-AEMA) hydrogel is maintained in the newly developed nanocomposite hydrogel, which is crucial in the applications such as dye absorption and drug delivery [49].
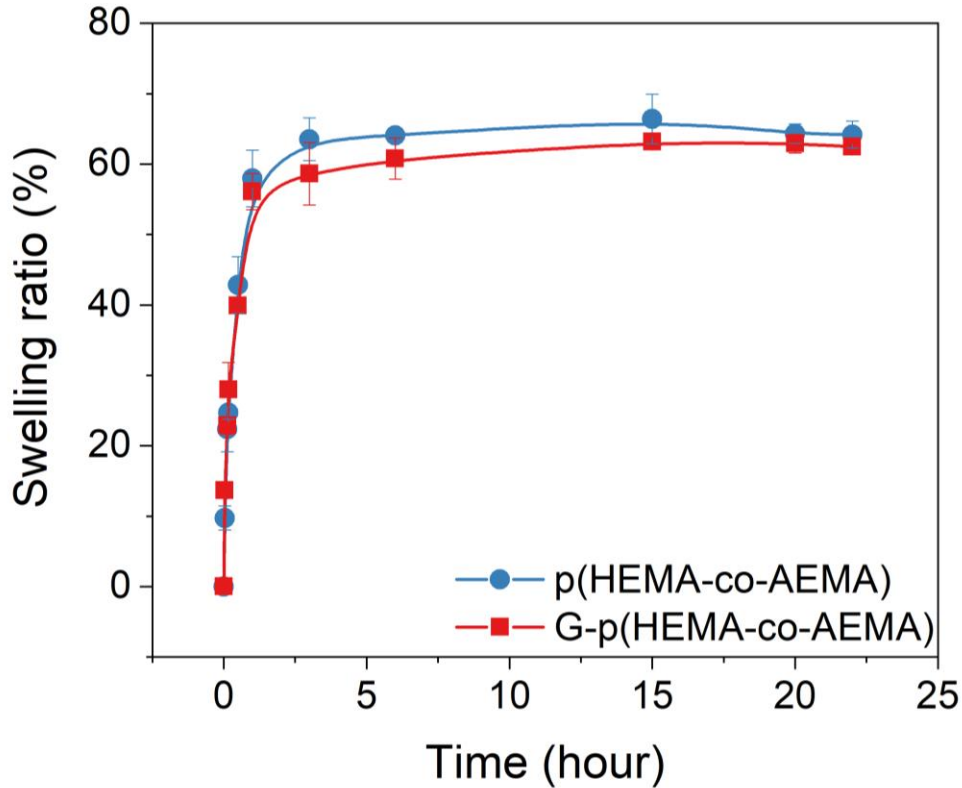
Figure 6.5 Swelling behavior of the p(HEMA-co-AEMA) hydrogel and the G-p(HEMA-co-AEMA) nanocomposite hydrogel.

6.3.2 The Mechanical Properties of FeCo/rGO Hybrid Nanosheets Reinforced p(HEMA-co-AEMA) Nanocomposite Hydrogel

The mechanical properties of p(HEMA-co-AEMA) hydrogel and G-p(HEMA-co-AEMA) nanocomposite hydrogel were characterized uniaxially and biaxially by the BioTester 5000 testing system (CellScale Biomaterials Testing, Waterloo, Ontario). The tensile strain-stress curves of p(HEMA-co-AEMA) hydrogel and G-p(HEMA-co-AEMA)

nanocomposite hydrogel are shown in **Figure 6.6**. Meanwhile, **Table 6.1** depicts the summary of Young's modulus, maximal tensile strength, toughness, and elongation at break of p(HEMA-co-AEMA) hydrogel and G-p(HEMA-co-AEMA) nanocomposite hydrogel. With the incorporation of FeCo/rGO hybrid nanosheets, the Young' modulus is improved from 0.32 ± 0.02 MPa to 0.48 ± 0.03 MPa, and the toughness is increased from 0.06 ± 0.01 MJ/m^3 to 0.11 ± 0.02 MJ/m^3. Meanwhile, the maximal tensile strength and elongation at break are significantly increased from 0.13 ± 0.02 MPa to 0.22 ± 0.03 MPa and from 0.82 ± 0.05 to 0.94 ± 0.05. The significant enhancements of mechanical properties can be attributed to the strong attractive interactions between the p(HEMA-co-AEMA) matrix and well-dispersed FeCo/rGO hybrid nanosheets, which lead to better load transfers [47, 50].
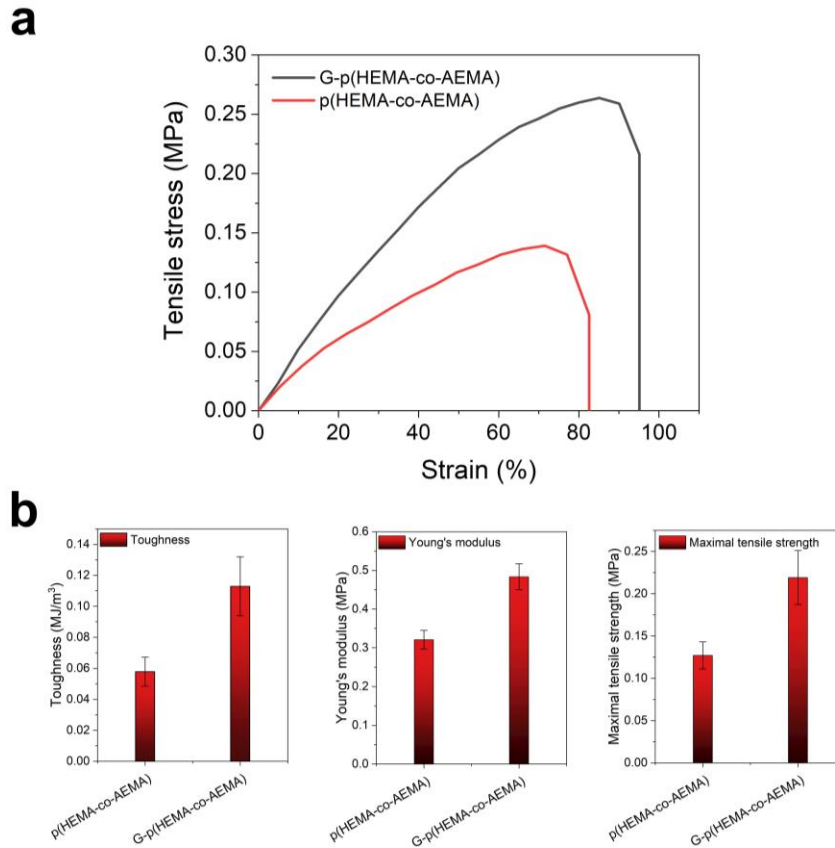
Figure 6.6 The tensile properties of p(HEMA-co-AEMA) hydrogel and G-p(HEMA-co-AEMA) nanocomposite hydrogel. (a) The tensile strain-stress curves; (b) the bar diagrams of toughness (MJ/m^3), Young's modulus (MPa), and maximal tensile strength (MPa).

Table 6.1 Summary of tensile properties of p(HEMA-co-AEMA) hydrogel and G-p(HEMA-co-AEMA) nanocomposite hydrogel.

Sample	Young's modulus (MPa)	Toughness (MJ/m^3)	Maximal tensile strength (MPa)	Elongation at break ($\mu m/\mu m$)
p(HEMA-co-AEMA)	0.32 ± 0.02	0.06 ± 0.01	0.13 ± 0.02	0.82 ± 0.05
G-p(HEMA-co-AEMA)	0.48 ± 0.03	0.11 ± 0.02	0.22 ± 0.03	0.94 ± 0.05

To further characterize the mechanical properties of p(HEMA-co-AEMA) hydrogel and G-p(HEMA-co-AEMA) nanocomposite hydrogel, the tensile loading-unloading tests were performed (**Figure 6.7**). The tensile loading-unloading tests were carried out to verify the energy dissipation of G-p(HEMA-co-AEMA) nanocomposite hydrogel in contrast with p(HEMA-co-AEMA) hydrogel. As shown in **Figure 6.7a**, the clear hysteresis loops are noticed for both p(HEMA-co-AEMA) hydrogel and G-p(HEMA-co-AEMA) nanocomposite hydrogel under the same strain (70%). The toughness increases significantly from 0.047 MJ/m^3 for p(HEMA-co-AEMA) to 0.063 MJ/m^3 for G-p(HEMA-co-AEMA).

Hysteresis loops of G-p(HEMA-co-AEMA) nanocomposite hydrogel are observed at different strains (from 40% to 90%) as shown in **Figure 6.7b**. The dissipated energy of G-p(HEMA-co-AEMA) nanocomposite hydrogel is 0.034 MJ/m^3 as the strain reaches 90% (**Figure 6.7c**). However, in contrast with p(HEMA-co-AEMA) hydrogel, the value of dissipated energy of G-p(HEMA-co-AEMA) is not largely increased, which indicates that the energy efficiency is not strongly enhanced by FeCo/rGO hybrid nanosheets. In addition, the six successive loading-unloading cycles are applied on G-p(HEMA-co-AEMA) nanocomposite hydrogel at 70% strain, and the stress-strain curves are shown in **Figure 6.7d**. The hysteresis loop is observed in each cycle with an overlapping shape, which indicates a good recovery at 70% strain for 6 cycles. In addition, the slight change of the hysteresis loop and dissipated energy between the first cycle and the other five

successive cycles suggests that some damages occur in the G-p(HEMA-co-AEMA) nanocomposite hydrogel [51].
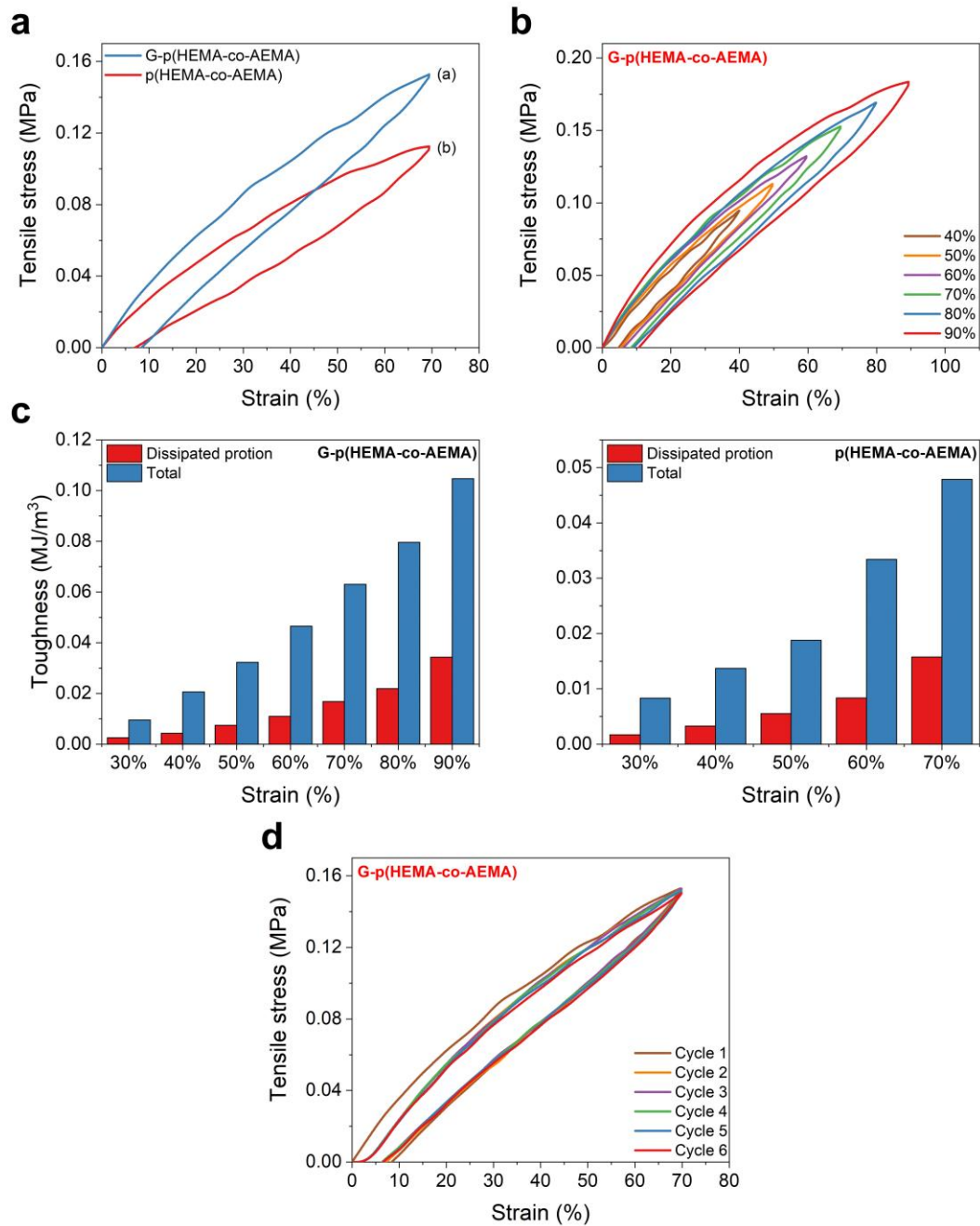
Figure 6.7 Tensile loading-unloading tests of p(HEMA-co-AEMA) and G-p(HEMA-co-AEMA): (a) loading-unloading tests at 70% strain; (b) loading-unloading tests at different strain (40% - 70%); (c) calculated total toughness and dissipated toughness; (d) six cyclic loading-unloading tests (70% strain).

The biaxial tensile tests were performed with the BioTester 5000 for both p(HEMA-co-AEMA) hydrogel and G-p(HEMA-co-AEMA) nanocomposite hydrogel. The results of the image tracking of p(HEMA-co-AEMA) and G-p(HEMA-co-AEMA) under 30% strain are displayed in **Figure 6.8**. The G-p(HEMA-co-AEMA) nanocomposite hydrogel exhibits homogeneous displacements and uniform interior strains in contrast with p(HEMA-co-AEMA) hydrogel as the shapes of tracking grids and displacement vectors (yellow dots with white tails) are more irregular (two directions) for p(HEMA-co-AEMA) specimen. Therefore, the results indicate that FeCo/rGO hybrid nanosheets help to unify the internal strains of the nanocomposite hydrogel.
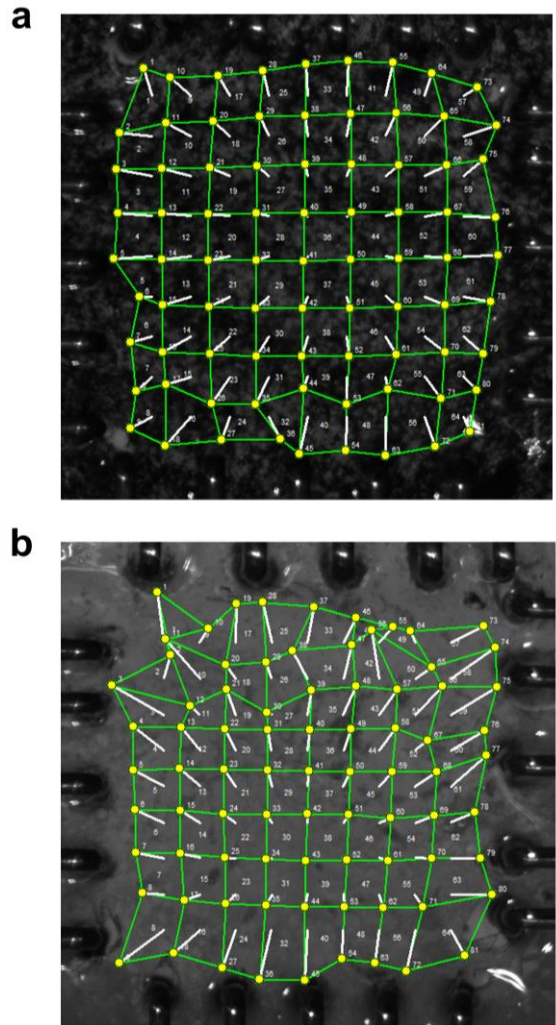
Figure 6.8 Image tracking of the biaxial test (30% strain): (a) G-p(HEMA-co-AEMA) nanocomposite hydrogel and (b) p(HEMA-co-AEMA) hydrogel.

6.3.3 Magnetic Properties of G-p(HEMA-co-AEMA) Nanocomposite Hydrogel

The magnetic hysteresis loop of G-p(HEMA-co-AEMA) nanocomposite hydrogel was obtained by the vibrating sample magnetometer (VSM) at room temperature. As shown in **Figure 6.9**, the magnetic hysteresis loop of G-p(HEMA-co-AEMA) nanocomposite hydrogel indicates a paramagnetic behavior. The magnetism of G-p(HEMA-co-AEMA) nanocomposite hydrogel displays a positive relationship with the magnetic field and increases almost linearly as the magnetic field increasing. Meanwhile, a slight curvature is observed in **Figure 6.9**, which suggests the presence of ferromagnetic behavior due to the introduced FeCo/rGO hybrid nanosheets in the nanocomposite hydrogel. However, because of the limited quantity of FeCo/rGO hybrid nanosheets incorporated with the p(HEMA-co-AEMA) hydrogel, the influences of FeCo/rGO hybrid nanosheets are not significant compared with the paramagnetic behavior of the p(HEMA-co-AEMA) hydrogel matrix, which is consistent with the result of FT-IR characterization.
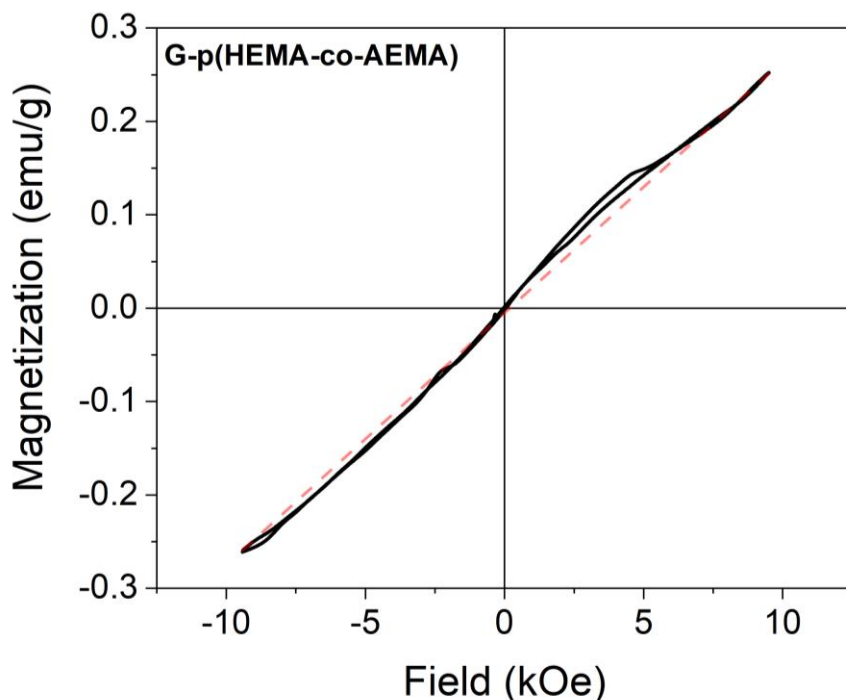
Figure 6.9 The magnetic hysteresis loop of G-p(HEMA-co-AEMA) nanocomposite hydrogel at room temperature.

The magnetoresistance (MR (%), $\Delta R/R_0$) of the G-p(HEMA-co-AEMA) nanocomposite hydrogel was measured by the 4-pin probe attached to the VSM. The MR values of G-p(HEMA-co-AEMA) were measured at room temperature and low magnetic fields ($\leq$ 10 kOe). As shown in **Figure 6.10**, a negative magnetoresistance (NMR) is observed as the magnetic field increases from 0 kOe to 10 kOe. The MR of the G-p(HEMA-co-AEMA) nanocomposite hydrogel reaches -1.29% at 10 kOe. Moreover, the G-p(HEMA-co-AEMA) nanocomposite hydrogel achieves an average MR of -1.4 $\pm$ 0.3% at 10 kOe and room temperature. Previous studies suggest that it is possible to achieve a large MR at a low magnetic field by the gel-like matrix with magnetic nanoparticles embedded [52]. Although NMR has been reported in various carbon-based materials, the origin of the NMR in G-p(HEMA-co-AEMA) nanocomposite hydrogel requires further investigation as the hydrogel matrix is involved [53-55]. Meanwhile, the G-p(HEMA-co-AEMA) nanocomposite hydrogel with MR responses can benefit the development of cost-effective and flexible MR devices/sensors for different applications.
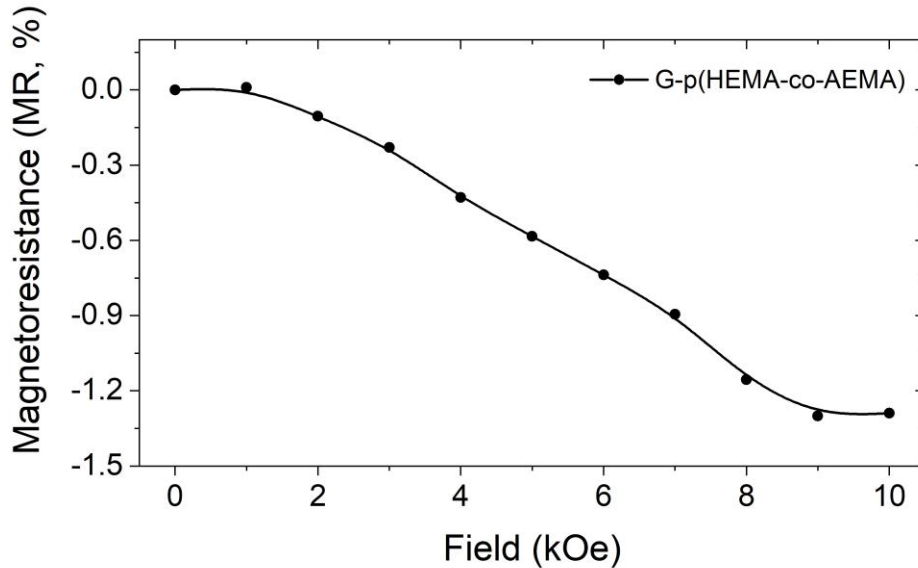
Figure 6.10 Magnetoresistance (MR, %) of G-p(HEMA-co-AEMA) nanocomposite hydrogel at room temperature.

6.4 Conclusions

In this study, we directly incorporated FeCo/rGO hybrid nanosheets with the p(HEMA-co-AEMA) hydrogel matrix to develop the nanocomposite hydrogel with enhanced mechanical properties. The facile polymerization process was applied, which can benefit the future mass production of the nanocomposite hydrogel. The incorporation of FeCo/rGO hybrid nanosheets significantly increases the mechanical properties. The Young's modulus, toughness, and maximal tensile strength of G-p(HEMA-co-AEMA) nanocomposite hydrogel are 1.5x, 2.0x, and 1.7x higher than the p(HEMA-co-AEMA) hydrogel. The results of the biaxial mechanic tensile test indicate uniform interior strains of G-p(HEMA-co-AEMA) nanocomposite hydrogel under the two-direction stretching. Moreover, the G-p(HEMA-co-AEMA) nanocomposite hydrogel exhibits comparable swelling capacity in contrast with p(HEMA-co-AEMA) hydrogel after introducing FeCo/rGO hybrid nanosheets into the p(HEMA-co-AEMA) matrix.

In addition, the G-p(HEMA-co-AEMA) nanocomposite hydrogel displays a negative MR at $-1.4 \pm 0.3\%$ at the low magnetic field (10 kOe) and room temperature. With the significantly improved mechanical properties and negative MR, we believe that the FeCo/rGO hybrid nanosheets reinforced G-p(HEMA-co-AEMA) nanocomposite hydrogel can boost the development of biomaterials demanding robust mechanical properties and flexible MR sensors/devices.

6.5 References

[1] F.P. Carney, C.A. Morris, B. Milthorpe, J.L. Flanagan, M.D.P. Willcox, *In Vitro* Adsorption of Tear Proteins to Hydroxyethyl Methacrylate-Based Contact Lens Materials. *Eye Contact Lens* **2009**, *35* (6).

[2] B. Balakrishnan, M. Mohanty, P.R. Umashankar, A. Jayakrishnan, Evaluation of an in situ forming hydrogel wound dressing based on oxidized alginate and gelatin. *Biomaterials* **2005**, *26* (32), 6335-6342.

[3] P. Gupta, K. Vermani, S. Garg, Hydrogels: from controlled release to pH-responsive drug delivery. *Drug Discov. Today* **2002**, *7* (10), 569-579.

[4] D.-H. Kim, M. Abidian, D.C. Martin, Conducting polymers grown in hydrogel scaffolds coated on neural prosthetic devices. *J. Biomed. Mater. Res., Part A* **2004**, *71A* (4), 577-585.

[5] J. Zhang, R. Bi, W. Hodge, P. Yin, W.H. Tse, A nanocomposite contact lens for the delivery of hydrophilic protein drugs. *J. Mater. Chem. B* **2013**, *1* (35), 4388-4395.

[6] D.-M. Dragusin, S. Van Vlierberghe, P. Dubruel, M. Dierick, L. Van Hoorebeke, H.A. Declercq*, et al.*, Novel gelatin–PHEMA porous scaffolds for tissue engineering applications. *Soft Matter* **2012**, *8* (37), 9589-9602.

[7] M.L. Oyen, Mechanical characterisation of hydrogel materials. *Int. Mater. Rev.* **2014**, *59* (1), 44-59.

[8] A.M.S. Costa, J.F. Mano, Extremely strong and tough hydrogels as prospective candidates for tissue repair – A review. *Eur. Polym. J.* **2015**, *72*, 344-364.

[9] A. Vedadghavami, F. Minooei, M.H. Mohammadi, S. Khetani, A. Rezaei Kolahchi, S. Mashayekhan*, et al.*, Manufacturing of hydrogel biomaterials with controlled mechanical properties for tissue engineering applications. *Acta Biomater.* **2017**, *62*, 42-63.

[10] E.M. Ahmed, F.S. Aggor, A.M. Awad, A.T. El-Aref, An innovative method for preparation of nanometal hydroxide superabsorbent hydrogel. *Carbohydr. Polym.* **2013**, *91* (2), 693-698.

[11] S. Cascone, G. Lamberti, Hydrogel-based commercial products for biomedical applications: A review. *Int. J. Pharm.* **2020**, *573*, 118803.

[12] O. Wichterle, D. LÍM, Hydrophilic Gels for Biological Use. *Nature* **1960**, *185* (4706), 117-118.

[13] H. Liu, C. Wang, C. Li, Y. Qin, Z. Wang, F. Yang*, et al.*, A functional chitosan-based hydrogel as a wound dressing and drug delivery system in the treatment of wound healing. *RSC Adv.* **2018**, *8* (14), 7533-7549.

[14] K.F. Bruggeman, R.J. Williams, D.R. Nisbet, Dynamic and Responsive Growth Factor Delivery from Electrospun and Hydrogel Tissue Engineering Materials. *Adv. Healthcare Mater.* **2018**, *7* (1), 1700836.

[15] W.I. Choi, Y. Hwang, A. Sahu, K. Min, D. Sung, G. Tae*, et al.*, An injectable and physical levan-based hydrogel as a dermal filler for soft tissue augmentation. *Biomater. Sci.* **2018**, *6* (10), 2627-2638.

[16] J.-P. Montheard, M. Chatzopoulos, D. Chappard, 2-Hydroxyethyl Methacrylate (HEMA): Chemical Properties and Applications in Biomedical Fields. *J. Macromol. Sci., Polym. Rev.* **1992**, *32* (1), 1-34.

[17] L. Indolfi, F. Causa, P.A. Netti, Coating process and early stage adhesion evaluation of poly(2-hydroxy-ethyl-methacrylate) hydrogel coating of 316L steel surface for stent applications. *J. Mater. Sci.: Mater. Med.* **2009**, *20* (7), 1541.

[18] L. Jones, K. Dumbleton, Contact lenses. *Optometry: Science, Techniques and Clinical Management (Rosenfield M & Logan N, editors), Butterworth-Heinemann Elsevier: Edinburgh* **2009**, 335-355.

[19] N. Nogueira, O. Conde, M. Miñones, J.M. Trillo, J. Miñones, Characterization of poly(2-hydroxyethyl methacrylate) (PHEMA) contact lens using the Langmuir monolayer technique. *J. Colloid Interface Sci.* **2012**, *385* (1), 202-210.

[20] D.F. Sweeney, Clinical signs of hypoxia with high-Dk soft lens extended wear: is the cornea convinced? *Eye Contact Lens* **2003**, *29* (1), S22-S25.

[21] P.C. Nicolson, J. Vogt, Soft contact lens polymers: an evolution. *Biomaterials* **2001**, *22* (24), 3273-3283.

[22] R. Langer, D.A. Tirrell, Designing materials for biology and medicine. *Nature* **2004**, *428* (6982), 487-492.

[23] M.P. Lutolf, P.M. Gilbert, H.M. Blau, Designing materials to direct stem-cell fate. *Nature* **2009**, *462* (7272), 433-441.

[24] M.F. Passos, N.M.S. Carvalho, A.A. Rodrigues, V.P. Bavaresco, A.L. Jardini, M.R.W. Maciel*, et al.*, PHEMA Hydrogels Obtained by Infrared Radiation for Cartilage Tissue Engineering. *Int. J. Chem. Eng.* **2019**, *2019*, 4249581.

[25] H. Geckil, F. Xu, X. Zhang, S. Moon, U. Demirci, Engineering hydrogels as extracellular matrix mimics. *Nanomed.* **2010**, *5* (3), 469-484.

[26] F. Li, G. Zhang, Y. Xia, Z. Wang, H. Jiang, X. Feng*, et al.*, Hierarchically crosslinked ionic nanocomposite hydrogels with ultrahigh mechanical properties for underwater bioinspired capturing device. *Compos. Sci. Technol.* **2018**, *165*, 339-346.

[27] J.-Y. Sun, X. Zhao, W.R.K. Illeperuma, O. Chaudhuri, K.H. Oh, D.J. Mooney*, et al.*, Highly stretchable and tough hydrogels. *Nature* **2012**, *489* (7414), 133-136.

[28] X. Yan, J. Yang, F. Chen, L. Zhu, Z. Tang, G. Qin*, et al.*, Mechanical properties of gelatin/polyacrylamide/graphene oxide nanocomposite double-network hydrogels. *Compos. Sci. Technol.* **2018**, *163*, 81-88.

[29] G.E. Giammanco, B. Carrion, R.M. Coleman, A.D. Ostrowski, Photoresponsive Polysaccharide-Based Hydrogels with Tunable Mechanical Properties for Cartilage Tissue Engineering. *ACS Appl. Mater. Interfaces* **2016**, *8* (23), 14423-14429.

[30] L. Toledo, B.F. Urbano, Poly(2-hydroxyethyl methacrylate)-based porous hydrogel: Influence of surfactant and SiO_2 nanoparticles on the morphology, swelling and thermal properties. *Eur. Polym. J.* **2016**, *81*, 316-326.

[31] S. Abdurrahmanoglu, V. Can, O. Okay, Equilibrium swelling behavior and elastic properties of polymer–clay nanocomposite hydrogels. *J. Appl. Polym. Sci.* **2008**, *109* (6), 3714-3724.

[32] M.K. Jaiswal, J.R. Xavier, J.K. Carrow, P. Desai, D. Alge, A.K. Gaharwar, Mechanically Stiff Nanocomposite Hydrogels at Ultralow Nanoparticle Content. *ACS Nano* **2016**, *10* (1), 246-256.

[33] S. Goenka, V. Sant, S. Sant, Graphene-based nanomaterials for drug delivery and tissue engineering. *J. Controlled Release* **2014**, *173*, 75-88.

[34] P. Schexnailder, G. Schmidt, Nanocomposite polymer hydrogels. *Colloid. Polym. Sci.* **2009**, *287* (1), 1-11.

[35] A.K. Gaharwar, N.A. Peppas, A. Khademhosseini, Nanocomposite hydrogels for biomedical applications. *Biotechnol. Bioeng.* **2014**, *111* (3), 441-453.

[36] J. Huang, Y. Liang, Z. Jia, J. Chen, L. Duan, W. Liu*, et al.*, Development of Magnetic Nanocomposite Hydrogel with Potential Cartilage Tissue Engineering. *ACS Omega* **2018**, *3* (6), 6182-6189.

[37] Y. Bai, H. Cai, X. Qiu, X. Fang, J. Zheng, Effects of graphene reduction degree on thermal oxidative stability of reduced graphene oxide/silicone rubber nanocomposites. *High Perform. Polym.* **2015**, *27* (8), 997-1006.

[38] C. Pan, L. Liu, G. Gai, Recent Progress of Graphene-Containing Polymer Hydrogels: Preparations, Properties, and Applications. *Macromol. Mater. Eng.* **2017**, *302* (10), 1700184.

[39] A. Kumar, S.M. Zo, J.H. Kim, S.-C. Kim, S.S. Han, Enhanced physical, mechanical, and cytocompatibility behavior of polyelectrolyte complex hydrogels by reinforcing halloysite nanotubes and graphene oxide. *Compos. Sci. Technol.* **2019**, *175*, 35-45.

[40] Z. Sun, L. Zhao, C. Liu, Y. Zhen, W. Zhang, J. Ma, A novel 3D adsorbent of reduced graphene oxide-β-cyclodextrin aerogel coupled hardness with softness for efficient removal of bisphenol A. *Chem. Eng. J.* **2019**, *372*, 896-904.

[41] S. Yang, M. Tan, T. Yu, X. Li, X. Wang, J. Zhang, Hybrid Reduced Graphene Oxide with Special Magnetoresistance for Wireless Magnetic Field Sensor. *Nano-Micro Lett.* **2020**, *12* (1), 69.

[42] Y. Liang, H. Wang, J. Zhou, Y. Li, J. Wang, T. Regier*, et al.*, Covalent Hybrid of Spinel Manganese–Cobalt Oxide and Graphene as Advanced Oxygen Reduction Electrocatalysts. *J. Am. Chem. Soc.* **2012**, *134* (7), 3517-3523.

[43] X. Li, J. Feng, Y. Du, J. Bai, H. Fan, H. Zhang, *et al.*, One-pot synthesis of CoFe$_2$O$_4$/graphene oxide hybrids and their conversion into FeCo/graphene hybrids for lightweight and highly efficient microwave absorber. *J. Mater. Chem. A* **2015**, *3* (10), 5535-5546.

[44] N. Sharma, V. Sharma, Y. Jain, M. Kumari, R. Gupta, S.K. Sharma, *et al.*, Synthesis and Characterization of Graphene Oxide (GO) and Reduced Graphene Oxide (rGO) for Gas Sensing Application. *Macromol. Symp.* **2017**, *376* (1), 1700006.

[45] B.A. Aragaw, Reduced graphene oxide-intercalated graphene oxide nano-hybrid for enhanced photoelectrochemical water reduction. *J. Nanostruct. Chem.* **2020**, *10* (1), 9-18.

[46] K.-i. Mimura, M. Moriya, W. Sakamoto, T. Yogo, Synthesis of BaTiO$_3$ nanoparticle/poly(2-hydroxyethyl methacrylate) hybrid nanofibers via electrospinning. *Compos. Sci. Technol.* **2010**, *70* (3), 492-497.

[47] A.T. Pereira, P.C. Henriques, P.C. Costa, M.C.L. Martins, F.D. Magalhães, I.C. Gonçalves, Graphene oxide-reinforced poly(2-hydroxyethyl methacrylate) hydrogels with extreme stiffness and high-strength. *Compos. Sci. Technol.* **2019**, *184*, 107819.

[48] P. Yin, Hydrogel-based Nanocomposites and Laser-assisted Surface Modification for Biomedical Application. **2012**.

[49] A.S. Hoffman, Hydrogels for biomedical applications. *Adv. Drug Del. Rev.* **2012**, *64*, 18-23.

[50] L. Bai, Y. Bai, J. Zheng, Improving the filler dispersion and performance of silicone rubber/multi-walled carbon nanotube composites by noncovalent functionalization of polymethylphenylsiloxane. *J. Mater. Sci.* **2017**, *52* (12), 7516-7529.

[51] X. Li, Y. Jiang, F. Wang, Z. Fan, H. Wang, C. Tao, *et al.*, Preparation of polyurethane/polyvinyl alcohol hydrogel and its performance enhancement *via* compositing with silver particles. *RSC Adv.* **2017**, *7* (73), 46480-46485.

[52] J. Meyer, T. Rempel, M. Schäfers, F. Wittbracht, C. Müller, A.V. Patel, *et al.*, Giant magnetoresistance effects in gel-like matrices. *Smart Mater. Struct.* **2013**, *22* (2), 025032.

[53] G. Abellán, H. Prima-García, E. Coronado, Graphene enhances the magnetoresistance of FeNi$_3$ nanoparticles in hierarchical FeNi$_3$–graphene nanocomposites. *J. Mater. Chem. C* **2016**, *4* (11), 2252-2258.

[54] H. Gu, H. Zhang, J. Lin, Q. Shao, D.P. Young, L. Sun, *et al.*, Large negative giant magnetoresistance at room temperature and electrical transport in cobalt ferrite-polyaniline nanocomposites. *Polymer* **2018**, *143*, 324-330.

[55] J. Cai, W. Wang, D. Pan, D.P. Young, H. Gu, Z. Guo, Electrical Transport in Polyaniline–Barium Ferrite Nanocomposites with Negative Giant Magnetoresistance. *J. Phys. Chem. C* **2020**, *124* (41), 22646-22655.

Chapter 7

7   Thesis Summary and Future Directions

7.1   Summary and Conclusions

7.1.1   Overview of Motivations and Research Questions

Magnetoresistance (MR) has profoundly shaped the development of magnetic sensors since the first observation of MR in 1857 [1]. The development of GMR and TMR sensors significantly increased the data storage capacity of hard disk drives (HDDs) [2-4]. More and more studies focused on constructing MR sensors/devices in various applications [5-7]. Currently, GMR and TMR sensors are mainstream in commercial applications of MR sensors.

In the meantime, other MR materials are developed to obtain ideal performance. Granular MR systems break the bulk layer of magnetic materials into small magnetic particles [8, 9]. The emerging nanotechnology benefits the design of granular MR systems as nanoparticles were introduced [10]. Meanwhile, graphene-based MR systems attracted the interest of researchers due to graphene's unique physical and chemical properties, which include layered graphene, graphene foams, and hybrid graphene nanocomposites [11, 12].

MR sensors have been widely applied in various fields of modern industry. The most well-known application is the MR reading head of HDD, which boosts the development of electronic devices since the 1990s [13]. Nowadays, MR sensors are mainly applied in data storage, position sensing, current sensing, non-destructive monitoring, and biomedical sensing systems [14-20]. Moreover, MR sensors are employed in the design of devices for antilock brakes, magnetocardiography, and galvanic isolators [21-27]. It is noticed that most of these sensors and devices are based on GMR/TMR multilayer systems. The production process is complicated and time-consuming for GMR/TMR multilayer systems due to the requirements of specific layer repetitions and precise layer

186

thickness control. This has hindered the commercial applications of MR sensors/devices. Meanwhile, the investment is further increased by the demands on specific preparation techniques for producing GMR/TMR multilayer systems (such as chemical vapor deposition (CVD), molecular beam epitaxy (MBE), and magnetron sputtering) [38-44].

The highly-sensitive and cost-effective MR materials can improve the data storage capacity and reduce the average retail price of magnetic storage devices. The highly-sensitive MR sensors can increase the resolution and scale down the noise for position sensing, current sensing, and non-destructive monitoring [28]. The ideal MR materials/sensors can increase the working range and benefit the sensitivity of biomedical sensing systems [29]. Meanwhile, the production cost could be reduced by introducing cost-effective MR sensors [30]. In addition, ideal MR sensors are required for detecting radiofrequency electromagnetic field (RF-EMF) radiations.

Currently, the challenge is to enhance the MR performance at low magnetic fields and room temperature. Although various nanoconstructed MR materials have been developed, the performances are inadequate at the low magnetic field and room temperature. Therefore, further investigations are required to push the limit of MR materials/structures and provide the possible solution for current challenges.

The objective of this thesis is to prepare MR materials with a simplified production process and improved performance at low magnetic fields and room temperature. rGO was adapted as the substrate of the hybrid nanocomposite. rGO exhibits abnormal chemical and physical properties, and it is facile to produce [31-33]. FeCo NPs are applied to enhance the MR performance of the hybrid nanocomposite. Various studies have indicated that FeCo is one of the promising candidates for developing ideal MR materials [34-45]. Moreover, large positive MR could be achieved by incorporating nanoparticles with layered structures such as rGO [46-49]. In this thesis, we designed and developed FeCo/rGO hybrid nanosheets with different routes and constructed appliable MR sensors and composite materials based on the hybrid nanosheets.

7.1.2 Summary and Conclusions of Current Works

This thesis employed both the chemical synthesis process and laser-assisted physical deposition process to develop FeCo/rGO hybrid nanosheets (**Figure 7.1**). FeCo/rGO hybrid nanosheets were successfully produced by chemical synthesis and physical deposition. Large and tunable MR was obtained at room temperature and low magnetic fields by adjusting the ratio of rGO in the chemical synthesis process. The investigations suggested the formation of Co-Mn oxides on rGO as the mass ratio of rGO surpassed the threshold. FeCo/rGO hybrid nanosheets were applied in constructing a wireless magnetic field sensing system with real-time detection and flexible data collection features. In addition, a nanocomposite hydrogel was developed by incorporating FeCo/rGO hybrid nanosheets with hydrogel matrix (i.e., p(HEMA-co-AEMA)). This mechanically flexible nanocomposite hydrogel displayed outstanding mechanical properties and negative MR.
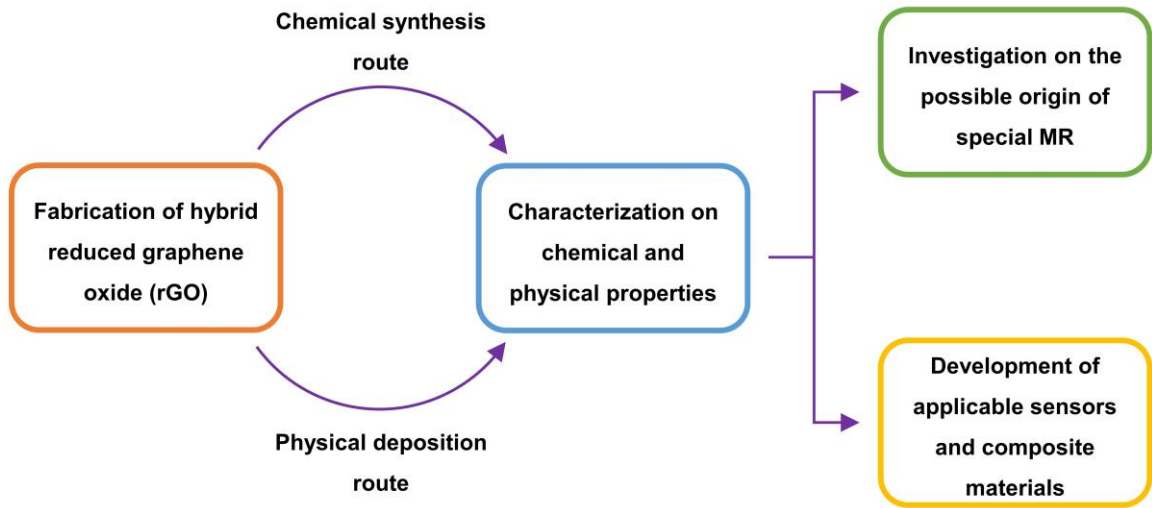
Figure 7.1 Schematic diagram of the research objectives of this thesis.

In Chapter 3, we successfully developed FeCo/rGO hybrid nanosheets with the facile chemical synthesis process. The hybrid nanosheets were produced by combing FeCo NPs and rGO. The FeCo/rGO hybrid nanosheets displayed a significant MR ($21 \pm 6\%$) at low magnetic fields (10 kOe) and room temperature, which is larger in contrast with other reported graphene-based MR materials [50-55]. The tunable MR was achieved by simply adjusting the mass ratio of rGO in reaction (10 wt.% - 50 wt.%). The possible origin of

MR was studied by applying the quantum magnetoresistance (QMR) model. The fitting results suggest that the variation of MR could be related to the increase of scattering centers (i.e., FeCo NPs) on the rGO surface. In addition, we constructed a wireless magnetic field sensing system based on FeCo/rGO hybrid nanosheets and Zigbee radio modules. This wireless magnetic field sensing system successfully achieved the real-time detection and data collection of a working mobile phone. The highlights of this study:

1. FeCo/rGO hybrid nanosheets were designed and developed with the facile chemical synthesis process.

2. Significant MR ($21 \pm 6\%$) was achieved by FeCo/rGO hybrid nanosheets at low magnetic fields (10 kOe) and room temperature.

3. Tunable MR was obtained by simply adjusting the mass ratio of rGO (10 wt.% - 50 wt.%) in the reaction.

4. The study of the origin of MR revealed the correlation between the variation of MR and the density of FeCo NPs on the rGO surface.

5. The wireless magnetic field sensing system was developed based on the integration of FeCo/rGO hybrid nanosheets and ZigBee radio modules, which achieved real-time detection and data collection.

In Chapter 4, we studied the effect of increasing the mass ratio of rGO in the preparation of FeCo/rGO hybrid nanosheets. The formation of Co-Mn oxides NPs became dominant as the mass ratio of rGO (M_{rGO}) exceed 60 wt.% in the reaction. The average size of the Co-Mn oxides NPs on rGO decreased as the M_{rGO} increased. Furthermore, the rGO with Co-Mn oxides achieved a large MR ($3.5\% \sim 4.5\%$) at ambient temperature and low magnetic fields (10 kOe) in contrast with other MR materials based on Co and Mn [56, 57]. Other structures with Co and Mn require extreme conditions ($4 \sim 20$ K) to achieve the MR at the level of 3% [56, 57]. This study also suggests a possible route to produce nanocomposites with Co-Mn oxides and rGO that display a large positive MR. The highlights of this study:

1. The forming of Co-Mn oxides on rGO was observed as the mass ratio of rGO surpassed 60 wt.% in the reaction.

2. The size of Co-Mn oxides NPs is adjustable as more rGO adding to the reaction.

3. The rGO with Co-Mn oxides exhibited large MR (3.5% ~ 4.5%) at room temperature and low magnetic fields (10 kOe) in contrast with other MR materials based on Co and Mn.

4. This study suggests a possible route to produce nanocomposites with Co-Mn oxides and rGO that exhibit relatively large positive MR.

In Chapter 5, we constructed FeCo/rGO hybrid nanosheets with the laser-assisted physical deposition process (i.e., matrix-assisted pulsed laser evaporation (MAPLE)). The results indicate that MAPLE is capable to stoichiometrically transfer FeCo NPs onto the rGO substrates. The amount of FeCo NPs on rGO has a positive correlation with deposition duration (0.5 hours ~ 2 hours). MAPLE-prepared FeCo/rGO hybrid nanosheets displayed positive MR (~0.7%) at room temperature and low magnetic fields (10 kOe). The MAPLE-prepared hybrid nanosheets achieved a similar or relatively larger MR compared with the MR of other reported FeCo-based granular systems with higher FeCo ratios [20, 37, 44]. In addition, this study confirmed the possibility to produce FeCo/rGO hybrid nanosheets with positive MR by the physical processes such as MAPLE.

1. The FeCo/rGO hybrid nanosheets were successfully prepared by the laser-assisted physical deposition process (i.e., MAPLE).

2. This study revealed the positive correlation between deposition duration and the density of FeCo NPs on the rGO surface.

3. MAPLE-prepared FeCo/rGO hybrid nanosheets exhibited a positive MR (~ 0.7%) at room temperature and low magnetic fields.

4. This positive MR is larger than or close to the MR of other reported FeCo-based granular structures with higher FeCo ratios.

5. This study confirmed the possibility to produce FeCo/rGO hybrid nanosheets with positive MR by MAPLE.

In Chapter 6, we developed a mechanically flexible nanocomposite hydrogel by integrating FeCo/rGO hybrid nanosheets with the hydrogel matrix (i.e., p(HEMA-co-AEMA)). The nanocomposite hydrogel displayed outstanding mechanical properties with significant improvements in toughness (0.11 MPa, 2.0x higher), Young's modulus (0.48 MPa, 1.5x higher), and maximal tensile stress (0.22 MPa, 1.7x higher) compared with plain p(HEMA-co-AEMA). Meanwhile, the nanocomposite hydrogel showed homogeneous displacements and uniform interior strains in the biaxial tensile tests. Furthermore, the nanocomposite hydrogel exhibited a negative MR (-1.4 ± 0.3%) at room temperature and low magnetic fields. The highlight of this study:

1. We successfully developed a mechanically flexible nanocomposite hydrogel by incorporating FeCo/rGO hybrid nanosheets with the hydrogel matrix (i.e., p(HEMA-co-AEMA)).

2. The nanocomposite hydrogel exhibited enhanced mechanical properties (toughness (0.11 MPa, 2.0x higher), Young's modulus (0.48 MPa, 1.5x higher), and maximal tensile stress (0.22 MPa, 1.7x higher)).

3. The nanocomposite hydrogel showed homogeneous displacements and uniform interior strains in the biaxial tensile test.

4. This nanocomposite hydrogel displayed a negative MR (-1.4 ± 0.3%) at room temperature and low magnetic fields.

7.2 Thesis Contributions

MR sensors and devices have been widely applied in magnetic storage (recording), position sensing, current sensing, non-destructive monitoring, biomedical sensing

systems, etc. The GMR and TMR sensors were adopted by most commercial applications of MR sensors. However, the drawbacks of multilayer systems lead to the escalation of both economic cost and time cost (i.e., complicated fabrication processes and demands on special preparation techniques). Nanoconstructed MR materials are developed to provide solutions for current obstacles. Though some nanoconstructed MR materials can simplify the production processes, most of these materials display inadequate MR at room temperature and low magnetic fields ($\leq$ 10 kOe).

The main goal of this thesis is to develop nanoconstructed materials with large MR at low magnetic fields/room temperature and facile preparation processes. We successfully developed the rGO hybrid nanosheets with FeCo NPs and rGO by chemical synthesis and physical deposition. The rGO-based MR materials in this thesis provided enhanced MR at low magnetic fields (10 kOe) and room temperature in contrast with previous studies. In addition, we successfully designed and constructed the wireless magnetic field sensing system and the mechanically flexible nanocomposite hydrogel, which demonstrate the flexibility and integrability of the FeCo/rGO hybrid nanosheets. Specifically:

- In Chapter 3, we developed FeCo/rGO hybrid nanosheets with the facile chemical synthesis process. A significant MR ($21 \pm 6\%$) was achieved at the low magnetic field/ambient temperature. Meanwhile, tunable MR was achieved by varying the mass ratio of rGO adding to the reaction. Studies on the origin of the MR revealed the correlation between the density of FeCo NPs on the rGO surface with the MR variation. In addition, we constructed a wireless magnetic field sensing system with FeCo/rGO hybrid nanosheets and ZigBee radio modules. This system achieved real-time detection and data collection of a working mobile phone, which can benefit the future connected society.

- In Chapter 4, we investigated the effect of increasing the mass ratio of rGO in the preparation of FeCo/rGO hybrid nanosheets. The formation of Co-Mn oxides NPs was observed on the rGO surface as the mass ratio of rGO (M_{rGO}) surpassed the 60 wt.% thresholds. The rGO with Co-Mn oxides displayed positive MR (3.5% ~ 4.5%) at room temperature and low magnetic fields, which is higher than the MR

of other structures based on Co and Mn. This study enhances the understanding of the effects of increasing the mass ratio of rGO in the reaction. In addition, it proposes a possible route to produce nanocomposites based on Co-Mn oxides and rGO with positive MR.

- In Chapter 5, we successfully constructed FeCo/rGO hybrid nanosheets with matrix-assisted pulsed laser evaporation (MAPLE). MAPLE-prepared FeCo/rGO hybrid nanosheets achieved a positive MR (~ 0.7%) at low magnetic fields and room temperature with a very low FeCo fraction (0.4 at.%). This MR is larger than or close to the MR of other reported FeCo-based granular MR systems with higher FeCo ratios. This study revealed the capability of MAPLE to transfer FeCo NPs and produce FeCo/rGO hybrid nanosheets with positive MR. This study benefits the development of physically produced MR sensors/devices.

- In Chapter 6, we designed and constructed a mechanically flexible nanocomposite hydrogel by incorporating FeCo/rGO hybrid nanosheets with the hydrogel matrix (i.e., p(HEMA-co-AEMA)). This nanocomposite hydrogel offers remarkable mechanical properties (toughness (0.11 MPa, 2.0x higher), Young's modulus (0.48 MPa, 1.5x higher), and maximal tensile stress (0.22 MPa, 1.7x higher)). In addition, the nanocomposite hydrogel displayed a negative MR (-1.4 ± 0.3%) at room temperature and low magnetic fields. This study provides a novel nanocomposite hydrogel with reinforced mechanical properties, which is suitable for the requirement of load-bearing biomaterials. Moreover, this study benefits the development of hydrogel matrix-based MR materials.

In summary, this thesis expands the fundamental understanding of the design and preparation strategies of nanoconstructed MR materials. Studies in this thesis suggest that nanoconstructed MR materials can be considered as the solution to the current challenges of MR sensors/devices. In addition, this thesis can benefit the future developments of MR devices by developing the wireless magnetic field sensing system and nanocomposite hydrogel.

7.3 Future Directions

This thesis aims to provide solutions to obstacles of current MR materials by strengthening the MR at room temperature and low magnetic fields. Our results in Chapters 2 to 5 demonstrate the enhanced MR and excellent integrability of the rGO hybrid nanosheets. However, it still has a long way to go for industrial applications. More details are required to be identified regarding the mechanisms and properties. Meanwhile, further studies will be performed to optimize the performance of rGO hybrid nanosheets. In specific:

For Chapter 3, we successfully developed the wireless magnetic field sensing system based on FeCo/rGO hybrid nanosheets. The optimization can be applied to the circuit design of the MR sensor system to achieve higher efficiency and sensitivity. The wireless magnetic field sensing system could be applied in real-time position detection (such as current sensing and non-destructive monitoring). The MR sensor array could be developed, which offers higher resolution and more details [58-61]. Moreover, MR biosensing platforms could be constructed based on the wireless magnetic field sensing system [30].

For Chapter 4, we studied the effect of increasing the mass ratio of rGO in the preparation of FeCo/rGO hybrid nanosheets. The formation of Co-Mn oxides was observed on rGO. Specific investigations could be applied to understand the MR of rGO with Co-Mn oxides. Further studies are required to investigate the mechanism of Co-Mn oxides' formation in this solvothermal process [62-65]. More investigations will be performed to develop applications of rGO with Co-Mn oxides in MR sensing, catalysis, and energy storage [66-68].

For Chapter 5, we successfully constructed FeCo/rGO hybrid nanosheets with MAPLE. More studies will be performed to understand the effects of other deposition parameters. Meanwhile, MAPLE-produced FeCo/rGO hybrid nanosheets could be integrated with the electronic circuits. Further studies are required to develop MR biosensing platforms with

MAPLE since the MAPLE technique is designed to transfer delicate materials including proteins and biomolecules [69-71].

For Chapter 6, we constructed a mechanically flexible nanocomposite hydrogel with remarkable mechanical properties. Further studies are required to understand the biocompatibility of this nanocomposite hydrogel. More investigations will be performed to study the origin of the negative MR. In addition, this nanocomposite hydrogel could be the key component for constructing flexible MR position sensors and biosensing platforms.

In general, there is still much to be done for developing the commercial appliable MR sensors and devices based on rGO hybrid nanosheets. The results in this thesis demonstrate that rGO hybrid nanosheets can enhance the MR and simplify the preparation process of MR materials/devices. We believe that rGO hybrid nanosheets not only benefit the development of MR materials/devices with high sensitivity and low cost but also contribute to the evolution of MR sensors in commercial applications.

7.4 References

[1] W. Thomson, XIX. On the electro-dynamic qualities of metals:—Effects of magnetization on the electric conductivity of nickel and of iron. *Proc. R. Soc. London* **1857**, (8), 546-550.

[2] G. Binasch, P. Grünberg, F. Saurenbach, W. Zinn, Enhanced magnetoresistance in layered magnetic structures with antiferromagnetic interlayer exchange. *Phys. Rev. B* **1989**, *39* (7), 4828-4830.

[3] J. Inoue, S. Maekawa, Theory of tunneling magnetoresistance in granular magnetic films. *Phys. Rev. B* **1996**, *53* (18), R11927-R11929.

[4] E.E. Fullerton, J.R. Childress, Spintronics, Magnetoresistive Heads, and the Emergence of the Digital World. *Proc. IEEE* **2016**, *104* (10), 1787-1795.

[5] Y. Ouyang, Z. Wang, G. Zhao, J. Hu, S. Ji, J. He*, et al.*, Current sensors based on GMR effect for smart grid applications. *Sens. Actuators, A* **2019**, *294*, 8-16.

[6] L. Schnitzspan, J. Cramer, J. Kubik, M. Tarequzzaman, G. Jakob, M. Kläui, Impact of Annealing Temperature on Tunneling Magnetoresistance Multilayer Stacks. *IEEE Magn. Lett.* **2020**, *11*, 1-5.

[7] S. Tumanski, Thin film magnetoresistive sensors, CRC Press, 2001.

[8] A.E. Berkowitz, J.R. Mitchell, M.J. Carey, A.P. Young, S. Zhang, F.E. Spada, *et al.*, Giant magnetoresistance in heterogeneous Cu-Co alloys. *Phys. Rev. Lett.* **1992**, *68* (25), 3745-3748.

[9] J.Q. Xiao, J.S. Jiang, C.L. Chien, Giant magnetoresistance in nonmultilayer magnetic systems. *Phys. Rev. Lett.* **1992**, *68* (25), 3749-3752.

[10] Y.P. Zeng, Z.W. Liu, H.Y. Yu, Z.G. Zheng, D.C. Zeng, X.S. Gao, Large positive room temperature magnetoresistance in nanogranular FeCo–Si–N thin films. *Mater. Lett.* **2013**, *110*, 27-30.

[11] K.S. Novoselov, A.K. Geim, S.V. Morozov, D. Jiang, Y. Zhang, S.V. Dubonos, *et al.*, Electric Field Effect in Atomically Thin Carbon Films. *Science* **2004**, *306* (5696), 666-669.

[12] H.-C. Wu, A.N. Chaika, M.-C. Hsu, T.-W. Huang, M. Abid, M. Abid, *et al.*, Large positive in-plane magnetoresistance induced by localized states at nanodomain boundaries in graphene. *Nat. Commun.* **2017**, *8* (1), 14453.

[13] S.S.P. Parkin, N. More, K.P. Roche, Oscillations in exchange coupling and magnetoresistance in metallic superlattice structures: Co/Ru, Co/Cr, and Fe/Cr. *Phys. Rev. Lett.* **1990**, *64* (19), 2304-2307.

[14] S.S.P. Parkin, M. Hayashi, L. Thomas, Magnetic Domain-Wall Racetrack Memory. *Science* **2008**, *320* (5873), 190-194.

[15] U. Ausserlechner, The Optimum Layout for Giant Magneto-Resistive Angle Sensors. *IEEE Sens. J.* **2010**, *10* (10), 1571-1582.

[16] S. Wu, J. Chen, S. Wu, A Rotary Encoder With an Eccentrically Mounted Ring Magnet. *IEEE Trans. Instrum. Meas.* **2014**, *63* (8), 1907-1915.

[17] R. Hahn, T. Schmidt, R. Slatter, B. Olberts, F. Romera, Magnetoresistive angular sensors for space applications: Results of breadboard and EQM testing and lessons learned. *Proc. ESMATS* **2017**, 1-6.

[18] R. Rempt, Scanning with magnetoresistive sensors for subsurface corrosion. *AIP Conf. Proc.* **2002**, *615* (1), 1771-1778.

[19] B. Wincheski, J. Simpson, M. Namkung, D. Perey, E. Scales, R. Louie, Development of Giant Magnetoresistive inspection system for detection of deep fatigue cracks under airframe fasteners. *AIP Conf. Proc.* **2002**, *615* (1), 1007-1014.

[20] R.S. Gaster, D.A. Hall, C.H. Nielsen, S.J. Osterfeld, H. Yu, K.E. Mach, *et al.*, Matrix-insensitive protein assays push the limits of biosensors in medicine. *Nat. Med.* **2009**, *15* (11), 1327-1332.

[21] C. Giebeler, D.J. Adelerhof, A.E.T. Kuiper, J.B.A. van Zon, D. Oelgeschläger, G. Schulz, Robust GMR sensors for angle detection and rotation speed sensing. *Sens. Actuators, A* **2001**, *91* (1), 16-20.

[22] G. Rieger, K. Ludwig, J. Hauch, W. Clemens, GMR sensors for contactless position detection. *Sens. Actuators, A* **2001**, *91* (1), 7-11.

[23] T.M. Hermann, W.C. Black, S. Hui, Magnetically coupled linear isolator. *IEEE Trans. Magn.* **1997**, *33* (5), 4029-4031.

[24] J.C. Rife, M.M. Miller, P.E. Sheehan, C.R. Tamanaha, M. Tondra, L.J. Whitman, Design and performance of GMR sensors for the detection of magnetic microbeads in biosensors. *Sens. Actuators, A* **2003**, *107* (3), 209-218.

[25] D.A. Hall, R.S. Gaster, T. Lin, S.J. Osterfeld, S. Han, B. Murmann*, et al.*, GMR biosensor arrays: A system perspective. *Biosens. Bioelectron.* **2010**, *25* (9), 2051-2057.

[26] M. Pannetier-Lecoeur, L. Parkkonen, N. Sergeeva-Chollet, H. Polovy, C. Fermon, C. Fowley, Magnetocardiography with sensors based on giant magnetoresistance. *Appl. Phys. Lett.* **2011**, *98* (15), 153705.

[27] Y. Shirai, K. Hirao, T. Shibuya, S. Okawa, Y. Hasegawa, Y. Adachi*, et al.*, Magnetocardiography Using a Magnetoresistive Sensor Array. *Int. Heart J.* **2019**, *60* (1), 50-54.

[28] H. Ehlers, M. Pelkner, R. Thewes, Heterodyne Eddy Current Testing Using Magnetoresistive Sensors for Additive Manufacturing Purposes. *IEEE Sens. J.* **2020**, *20* (11), 5793-5800.

[29] D.H. Blohm, A. Guiseppi-Elie, New developments in microarray technology. *Curr. Opin. Biotechnol.* **2001**, *12* (1), 41-47.

[30] C. Ren, Q. Bayin, S. Feng, Y. Fu, X. Ma, J. Guo, Biomarkers detection with magnetoresistance-based sensors. *Biosens. Bioelectron.* **2020**, *165*, 112340.

[31] J.I. Paredes, S. Villar-Rodil, M.J. Fernández-Merino, L. Guardia, A. Martínez-Alonso, J.M.D. Tascón, Environmentally friendly approaches toward the mass production of processable graphene from graphite oxide. *J. Mater. Chem.* **2011**, *21* (2), 298-306.

[32] V.B. Mohan, R. Brown, K. Jayaraman, D. Bhattacharyya, Characterisation of reduced graphene oxide: Effects of reduction variables on electrical conductivity. *Mater. Sci. Eng., B* **2015**, *193*, 49-60.

[33] F. Ortmann, A. Cresti, G. Montambaux, S. Roche, Magnetoresistance in disordered graphene: The role of pseudospin and dimensionality effects unraveled. *EPL* **2011**, *94* (4), 47006.

[34] H.N. Fuke, S. Hashimoto, M. Takagishi, H. Iwasaki, S. Kawasaki, K. Miyake, *et al.*, Magnetoresistance of FeCo Nanocontacts With Current-Perpendicular-to-Plane Spin-Valve Structure. *IEEE Trans. Magn.* **2007**, *43* (6), 2848-2850.

[35] R.S. Sundar, S.C. Deevi, Soft magnetic FeCo alloys: alloy development, processing, and properties. *Int. Mater. Rev.* **2005**, *50* (3), 157-192.

[36] M. Kąc, J. Morgiel, A. Polit, Y. Zabila, M. Marszałek, Atomic scale structure investigations of epitaxial Fe/Cr multilayers. *Appl. Surf. Sci.* **2014**, *305*, 154-159.

[37] M. Kąc, A. Polit, A. Dobrowolska, Y. Zabila, M. Krupiński, M. Marszałek, Surfactant influence on interface roughness and magnetoresistance value in Fe/Cr multilayers. *Thin Solid Films* **2013**, *542*, 199-203.

[38] C.-L. Chang, T.-H. Chiou, P.-H. Chen, W.-C. Chen, C.-T. Ho, W.-Y. Wu, Characteristics of TiN/W_2N multilayers prepared using magnetron sputter deposition with dc and pulsed dc powers. *Surf. Coat. Technol.* **2016**, *303*, 25-31.

[39] N. Saoula, S. Djerourou, K. Yahiaoui, K. Henda, R. Kesri, R.M. Erasmus, *et al.*, Study of the deposition of Ti/TiN multilayers by magnetron sputtering. *Surf. Interface Anal.* **2010**, *42* (6‐7), 1176-1179.

[40] E. Schubert, F. Frost, B. Ziberi, G. Wagner, H. Neumann, B. Rauschenbach, Ion beam sputter deposition of soft x-ray Mo∕Si multilayer mirrors. *J. Vac. Sci. Technol., B: Microelectron. Nanometer Struct.--Process., Meas., Phenom.* **2005**, *23* (3), 959-965.

[41] P.-K. Chiu, C.-T. Lee, D. Chiang, W.-H. Cho, C.-N. Hsiao, Y.-Y. Chen, *et al.*, Conductive and transparent multilayer films for low-temperature $TiO_2/Ag/SiO_2$ electrodes by E-beam evaporation with IAD. *Nanoscale Res. Lett.* **2014**, *9* (1), 35.

[42] M. Kąc, J. Żukrowski, M. Toulemonde, R. Kruk, V. Tokman, A. Polit, *et al.*, Swift iodine ion modification of the structural and magnetotransport properties of Fe/Cr systems. *Nucl. Instrum. Methods Phys. Res. B* **2009**, *267* (6), 925-930.

[43] Z.W. Fan, P. Li, E.Y. Jiang, H.L. Bai, Evolution of magnetoresistance mechanisms in granular Co/C films with different conduction regimes. *J. Phys. D: Appl. Phys.* **2013**, *46* (6), 065002.

[44] Z. Quan, X. Zhang, W. Liu, X. Li, K. Addison, G.A. Gehring, *et al.*, Enhanced Room Temperature Magnetoresistance and Spin Injection from Metallic Cobalt in Co/ZnO and Co/ZnAlO Films. *ACS Appl. Mater. Interfaces* **2013**, *5* (9), 3607-3613.

[45] A. Gerber, A. Milner, B. Groisman, M. Karpovsky, A. Gladkikh, A. Sulpice, Magnetoresistance of granular ferromagnets. *Phys. Rev. B* **1997**, *55* (10), 6446-6452.

[46] A.A. Abrikosov, Quantum magnetoresistance of layered semimetals. *Phys. Rev. B* **1999**, *60* (6), 4231-4234.

[47] A.A. Abrikosov, Quantum linear magnetoresistance. *EPL* **2000**, *49* (6), 789-793.

[48] C. Majumder, S. Bhattacharya, S.K. Saha, Anomalous large negative magnetoresistance in transition-metal decorated graphene: Evidence for electron-hole puddles. *Phys. Rev. B* **2019**, *99* (4), 045408.

[49] J. Zhu, Z. Luo, S. Wu, N. Haldolaarachchige, D.P. Young, S. Wei*, et al.*, Magnetic graphene nanocomposites: electron conduction, giant magnetoresistance and tunable negative permittivity. *J. Mater. Chem.* **2012**, *22* (3), 835-844.

[50] B. Song, K. Moon, C. Wong, Recent Developments in Design and Fabrication of Graphene-Based Interdigital Micro-Supercapacitors for Miniaturized Energy Storage Devices. *IEEE Trans. Compon., Packag., Manuf. Technol.* **2016**, *6* (12), 1752-1765.

[51] M.S. Purewal, Y. Zhang, P. Kim, Unusual transport properties in carbon based nanoscaled materials: nanotubes and graphene. *Phys. Status Solidi B* **2006**, *243* (13), 3418-3422.

[52] A.L. Friedman, J.L. Tedesco, P.M. Campbell, J.C. Culbertson, E. Aifer, F.K. Perkins*, et al.*, Quantum Linear Magnetoresistance in Multilayer Epitaxial Graphene. *Nano Lett.* **2010**, *10* (10), 3962-3965.

[53] Z.-M. Liao, H.-C. Wu, S. Kumar, G.S. Duesberg, Y.-B. Zhou, G.L.W. Cross*, et al.*, Large Magnetoresistance in Few Layer Graphene Stacks with Current Perpendicular to Plane Geometry. *Adv. Mater.* **2012**, *24* (14), 1862-1866.

[54] K. Gopinadhan, Y.J. Shin, I. Yudhistira, J. Niu, H. Yang, Giant magnetoresistance in single-layer graphene flakes with a gate-voltage-tunable weak antilocalization. *Phys. Rev. B* **2013**, *88* (19), 195429.

[55] G. Abellán, H. Prima-García, E. Coronado, Graphene enhances the magnetoresistance of $FeNi_3$ nanoparticles in hierarchical $FeNi_3$–graphene nanocomposites. *J. Mater. Chem. C* **2016**, *4* (11), 2252-2258.

[56] Z.-B. Gu, C.-S. Yuan, M.-H. Lu, J. Wang, D. Wu, S.-T. Zhang*, et al.*, Magnetic and transport properties of (Mn, Co)-codoped ZnO films prepared by radio-frequency magnetron cosputtering. *J. Appl. Phys.* **2005**, *98* (5), 053908.

[57] L.Z. Kong, H. Wang, S.Q. Xiao, J.J. Lu, Y.X. Xia, G.J. Hu*, et al.*, Integrated properties of large lateral photovoltage and positive magnetoresistance in Co/Mn/Co/c-Si structures. *J. Phys. D: Appl. Phys.* **2008**, *41* (5), 052003.

[58] Y. Zhang, T.-T. Tang, C. Girit, Z. Hao, M.C. Martin, A. Zettl*, et al.*, Direct observation of a widely tunable bandgap in bilayer graphene. *Nature* **2009**, *459* (7248), 820-823.

[59] Y. Ouyang, J. He, J. Hu, S.X. Wang, A Current Sensor Based on the Giant Magnetoresistance Effect: Design and Potential Smart Grid Applications. *Sensors* **2012**, *12* (11), 15520-15541.

[60] D. Rifai, A.N. Abdalla, K. Ali, R. Razali, Giant Magnetoresistance Sensors: A Review on Structures and Non-Destructive Eddy Current Testing Applications. *Sensors* **2016**, *16* (3), 298.

[61] M. Pelkner, A. Neubauer, V. Reimund, M. Kreutzbruck, A. Schütze, Routes for GMR-Sensor Design in Non-Destructive Testing. *Sensors* **2012**, *12* (9), 12169-12183.

[62] P. Balasubramanian, T.S.T. Balamurugan, S.-M. Chen, T.-W. Chen, Simplistic synthesis of ultrafine $CoMnO_3$ nanosheets: An excellent electrocatalyst for highly sensitive detection of toxic 4-nitrophenol in environmental water samples. *J. Hazard. Mater.* **2019**, *361*, 123-133.

[63] J.-Y. Wang, P.-Y. Kuang, N. Li, Z.-Q. Liu, Y.-Z. Su, S. Chen, Facile hydrothermal synthesis of cobalt manganese oxides spindles and their magnetic properties. *Ceram. Int.* **2015**, *41* (7), 8670-8679.

[64] B.R. Wiston, M. Ashok, Microwave-assisted synthesis of cobalt-manganese oxide for supercapacitor electrodes. *Mater. Sci. Semicond. Process.* **2019**, *103*, 104607.

[65] J. Li, S. Xiong, X. Li, Y. Qian, A facile route to synthesize multiporous $MnCo_2O_4$ and $CoMn_2O_4$ spinel quasi-hollow spheres with improved lithium storage properties. *Nanoscale* **2013**, *5* (5), 2045-2054.

[66] Y. Liang, H. Wang, J. Zhou, Y. Li, J. Wang, T. Regier*, et al.*, Covalent Hybrid of Spinel Manganese–Cobalt Oxide and Graphene as Advanced Oxygen Reduction Electrocatalysts. *J. Am. Chem. Soc.* **2012**, *134* (7), 3517-3523.

[67] X. Ge, Y. Liu, F.W.T. Goh, T.S.A. Hor, Y. Zong, P. Xiao*, et al.*, Dual-Phase Spinel $MnCo_2O_4$ and Spinel $MnCo_2O_4$/Nanocarbon Hybrids for Electrocatalytic Oxygen Reduction and Evolution. *ACS Appl. Mater. Interfaces* **2014**, *6* (15), 12684-12691.

[68] H. Wang, Y. Yang, Y. Liang, G. Zheng, Y. Li, Y. Cui*, et al.*, Rechargeable Li–O_2 batteries with a covalently coupled $MnCo_2O_4$–graphene hybrid as an oxygen cathode catalyst. *Energy Environ. Sci.* **2012**, *5* (7), 7931-7935.

[69] K.B. Shepard, R.D. Priestley, MAPLE Deposition of Macromolecules. *Macromol. Chem. Phys.* **2013**, *214* (8), 862-872.

[70] A. Bonciu, A. Vasilescu, V. Dinca, S.F. Peteu, Interfaces Obtained by MAPLE for Chemical and Biosensors Applications. *Sens. Actuators Rep.* **2021**, 100040.

[71] S. Yang, W.H. Tse, J. Zhang, Deposition of Antibody Modified Upconversion Nanoparticles on Glass by a Laser-Assisted Method to Improve the Performance of Cell Culture. *Nanoscale Res. Lett.* **2019**, *14* (1), 101.

Appendices

A video of the wireless magnetic field sensing process.

As the resistance of the magnetic field sensor is affected by the external electromagnetic radiation source, the data center (i) receives the disturbing of voltage sent from the wireless magnetic field sensing node (ii) and sends a remote command to the wireless signal indicator (iii) to turn on the LED (small inset figure) as an alert.

Curriculum Vitae

Name:	Songlin Yang

Post-secondary Education and Degrees:	Tianjin University Tianjin, China 2011-2015 B.A. The University of Western Ontario London, Ontario, Canada 2015-2017 M.E.Sc. The University of Western Ontario London, Ontario, Canada 2017-2021 Ph.D.
Honours and Awards:	Third Prize of Class Notes Competition, Tianjin University 2013 University Excellent Student Cadre, Tianjin University 2013 Graduate Fellowship, The University of Western Ontario 2015-2021
Related Work Experience	Teaching Assistant The University of Western Ontario 2015-2021

Publications:

Yang, S.; Tan, M.; Yu, T.; Li, X.; Wang, X.; Zhang, J., Hybrid Reduced Graphene Oxide with Special Magnetoresistance for Wireless Magnetic Field Sensor. *Nano-Micro Letters* **2020,** *12* (1), 69.

Yang, S.; Tse, W. H.; Zhang, J., Deposition of Antibody Modified Upconversion Nanoparticles on Glass by a Laser-Assisted Method to Improve the Performance of Cell Culture. *Nanoscale research letters* **2019,** *14* (1), 101.

Yang, S.; Zhang, J., Deposition of YBCO nanoparticles on graphene nanosheets by using matrix-assisted pulsed laser evaporation. *Optics & Laser Technology* **2019,** *109*, 465-469.

Yang, S.; Zhang, J., Matrix-Assisted Pulsed Laser Evaporation (MAPLE) technique for deposition of hybrid nanostructures. *Frontiers in Nanoscience and Nanotechnology* **2017,** *3* (1), 1.

Zhao, X.; Lu, C.; **Yang, S.**; Zhang, J., Bioconjugation of aptamer to fluorescent trimethyl chitosan nanoparticles for bacterial detection. *Materials Letters* **2020,** *264*, 127330.

Balaji, A.; **Yang, S.**; Wang, J.; Zhang, J., Graphene Oxide-Based Nanostructured DNA Sensor. *Biosensors* **2019,** *9* (2), 74.

Gao, X.; Sun, Q.; Yang, X.; Liang, J.; Koo, A.; Li, W.; Liang, J.; Wang, J.; Li, R.; Holness, F. B.; Price, A. D.; **Yang, S.**; Sham, T.-K.; Sun, X., Toward a remarkable Li-S battery via 3D printing. *Nano Energy* **2019,** *56*, 595-603.

Shen, Y.; Deng, K.; **Yang, S.**; Qin, B.; Cheng, S.; Zhu, N.; Ding, J.; Zhao, D.; Liu, J.; Zeng, Q.; Wang, C., Triangular-shaped molecular random tiling and molecular rotation in two-dimensional glassy networks. *Nanoscale* **2014,** *6* (13), 7221-7225.

Conferences:

Songlin Yang, Wai Hei Tse, Jin Zhang*, "*Development of A Suitable Surface by Coating with Antibody Modified Up-conversion Nanoparticles for Improvement of Cell Culture Performance*", Vancouver Nanomedicine Day 2020, September 2020, Vancouver, BC, Canada

Songlin Yang, Wai Hei Tse, Jin Zhang*,"*Biocompatible Protein (IgG) Modified Upconversion Nanoparticles (NaGdF$_4$: Yb^{3+}, Er^{3+}) Deposited by Matrix-Assisted Pulsed Laser Evaporation MAPLE*"(**Nomination for Best Paper award**), 2018 IEEE International Conference on Manipulation, Manufacturing, and Measurement on the Nanoscale (3M-NANO), August 2018, Hangzhou, Zhejiang, China

Songlin Yang, Jin Zhang*, "*Deposited BSA/IgG Conjugated Up-Conversion Nanoparticles by the Matrix-Assisted Pulsed Laser Evaporation (MAPLE)*", Proceedings of the International Conference of Theoretical and Applied Nanoscience and Nanotechnology (TANN'17), August 2017, Toronto, ON, Canada

Songlin Yang, Longyi Chen, Paul Ogilvie, and Jin Zhang*, "*Deposition of YBCO Nanoparticles on Graphene Using Matrix-assisted Pulsed Laser Evaporation*", Proceedings of the 3 rd World Congress on New Technologies (NewTech'17), June 2017, Rome, Italy